Spatial frequency domain imaging towards improved detection of gastrointestinal cancers

Jane Crowley

Supervisor: Dr. George S. D. Gordon

A thesis presented for the degree of
Doctor of Philosophy

Optics & Photonics Group
Faculty of Engineering
University of Nottingham
United Kingdom

30 June 2023

Abstract

Early detection and treatment of gastrointestinal cancers has been shown to drastically improve patients survival rates. However, wide population based screening for gastrointestinal cancers is not feasible due to its high cost, risk of potential complications, and time consuming nature. This thesis forms the proposal for the development of a cost-effective, minimally invasive device to return quantitative tissue information for gastrointestinal cancer detection *in-vivo* using spatial frequency domain imaging (SFDI). SFDI is a non-invasive imaging technique which can return close to real time maps of absorption and reduced scattering coefficients by projecting a 2D sinusoidal pattern onto a sample of interest. First a low-cost, conventional bench top system was constructed to characterise tissue mimicking phantoms. Phantoms were fabricated with specific absorption and reduced scattering coefficients, mimicking the variation in optical properties typically seen in healthy, cancerous, and pre-cancerous oesophageal tissue. The system shows accurate retrieval of absorption and reduced scattering coefficients of 19% and 11% error respectively. However, this bench top system consists of a bulky projector and is therefore not feasible for *in-vivo* imaging. For SFDI systems to be feasible for *in-vivo* imaging, they are required to be miniaturised. Many conditions must be considered when doing this such as various illumination conditions, lighting conditions and system geometries. Therefore to aid in the miniaturisation of the bench top system, an SFDI system was simulated in the open-source ray tracing software *Blender*, where the capability to simulate these conditions is possible. A material of tunable absorption and scattering properties was characterised such that the specific absorption and reduced scattering coefficients of the material were known. The simulated system shows capability in detecting optical properties of typical gastrointestinal conditions in an up-close, planar geometry, as well in a non-planar geometry of a tube simulating a lumen. Optical property imaging in the non-planar, tubular geometry was done with the use of a novel illumination pattern, developed for this work. Finally, using the knowledge gained from the simulation model, the bench top system was miniaturised to a 3 mm diameter prototype. The novel use of a fiber array producing the necessary interfering fringe patterns replaced the bulky projector. The system showed capability to image phantoms simulating typical gastrointestinal conditions at two wavelengths (515 and 660 nm), measuring absorption and reduced scattering coefficients with 15% and 6% accuracy in comparison to the bench top system for the fabricated phantoms. It is proposed that this system may be used for cost-effective, minimally invasive, quantitative imaging of the gastrointestinal tract *in-vivo*, providing enhanced contrast for difficult to detect cancers.

Acknowledgements

The work presented in this thesis would not have been possible without the incredible support from Dr Gordon. Especially in the unprecedented times of lockdowns and lab closures, George's advice, encouragement and enthusiasm made it possible to accomplish so much more than I expected. I don't think many students can say they leave a supervisor meeting feeling more confident both in their work and in themselves than when they went in, which is a testament to George's incredible unmatched supervision skills. I am proud to be his first PhD student here at the University of Nottingham.

I want to thank my fellow OPTIMlab members (the 'OPTIMlads') Fei, Rafael, Amy, and Terry for their friendship, support and for providing well needed treats at group meetings. I am excited to see what's to come out of this talented group in the future. Special thanks to Terry for reading a chapter, and to Rafael for proof-reading and providing comments on several chapters for me, I appreciate it so much.

I am also grateful for my fellow Optics & Photonics group members, for always lending a helping hand when needed. Especially to my B floor office cohorts, for providing daily mind breaks with coffee and baked goods. It has been a pleasure to be surrounded by such an inspiring, wonderful group of people.

I would like to acknowledge my family, my biggest cheerleaders, to whom I owe so much. Thanks to my parents for your never ending support and belief in me. To my sister, Amy, who inspires me daily and is always only a phone call away, I appreciate you. Finally to my partner Rob, who is always encouraging, helpful, and the provider of deliciously cooked meals. This endeavour would have been so much more challenging without your support. Also thanks for teaching me to code all those years ago. You were right, it's pretty helpful.

List of publications

Journal Publications

J. Crowley and G. Gordon, "Designing and simulating realistic spatial frequency domain imaging systems using open-source 3D rendering software", Biomedical Optics Express 14, 2523-2538 (2023); doi: 10.1364/BOE.484286.

A. Osman, **J. Crowley**, and G. S. D. Gordon, "Training Generative Adversarial Networks for Optical Property Mapping using Synthetic Image Data", Biomedical Optics Express 13, 5171-5186 (2022); doi: 10.1364/BOE.458554

F. Phillips, **J. Crowley**, S. Warburton, G. S. Gordon, and A. Parra-Blanco, "Aerosol and droplet generation in upper and lower GI endoscopy: whole procedure and event-based analysis", Gastrointestinal Endoscopy, vol. 96, no. 4, pp. 603–611, (2022); doi: 10.1016/j.gie.2022.05.018

F. Phillips, **J. Crowley**, S. Warburton, K. Staniforth, A. Parra-Blanco, and G. S. Gordon, "Air filtration mitigates aerosol levels both during and after endoscopy procedures", DEN Open, vol. 3, no. 1, (2023); doi: 10.1002/deo2.231

J. Crowley and G. Gordon, "Ultra-miniature dual-wavelength spatial frequency domain imaging for micro-endoscopy", *In review, preprint available*; doi: 10.48550/arXiv.2306.03713

F. Phillips, **J. Crowley**, S. Warburton, A. Parra-Blanco, G. S. Gordon, "Bronchoscopy masks mitigate aerosols during upper gastrointestinal endoscopies", *In review, preprint available*; doi: 10.1101/2022.12.06.22283092

Conference Proceedings

J. Crowley and G. Gordon, "Ultra-miniaturised spatial frequency domain imaging for improved early detection of gastrointestinal cancers", Proc. SPIE 12393, Biomedical Applications of Light Scattering XIII, 1239302 (2023); doi: 10.1117/12.2648766.

J. Crowley and G. S. D. Gordon. "Simulating medical applications of tissue optical property and shape imaging using open-source ray tracing software", Proc. SPIE 11657, Biomedical Applications of Light Scattering XI, 1165707 (2021); doi: 10.1117/12.2576779.

Contents

List of Figures

List of Tables

Nomenclature

Abbreviations

AFI	Autofluroscence imaging
AWB	Auto white balance
BO	Barrett's Oesophagus
BSDF	Bi-directional scattering distribution function
CMOS	Complementary metal oxide semiconductor
cSFDI	Coherent spatial frequency domain imaging
DIS	Double integrating sphere
DMD	Digital micromirror device
DRS	Diffuse reflectance spectroscopy
FFT	Fast Fourier transform
FoV	Field of view
FTP	Fourier transform profilometry
GI	Gastrointestinal
GPU	Graphics processing units
hs-SFDI	Hyperspectal spatial frequency domain imaging
IAD	Inverse adding doubling
IFT	Inverse Fourier transform
LED	Light emitting diode
LSI	Laser speckle imaging
MTF	Modulation transfer function
NaN	Not a Number
NBI	Narrow-band imaging

NIR	Near infrared
OAC	Oesophageal adenocarcinoma
OCT	Optical coherence tomography
PDT	Photo-dynamic therapy
PSF	Point spread function
RTE	Radiative transfer equation
SCC	Squamous cell carcinoma
sd-SFDI	Sub-diffuse spatial frequency domain imaging
SFDI	Spatial frequency domain imaging
SFDS	Spatial frequency domain spectroscopy
SFI	Speckle flow index
si-SFDI	Speckle illumination spatial frequency domain imaging
SLM	Spatial light modulator
SNR	Signal-to-noise
SSOP	Single snapshot of optical properties

Scientific Symbols

μ_a	Absorption coefficient
μ_s	Scattering coefficient
μ_s'	Reduced scattering coefficient
A_ρ	Absorption density
g	Anisotropy factor
Hb	Deoxyhaemoglobin
HbO_2	Oxyhaemoglobin
M_{AC}	AC modulation amplitude
M_{DC}	DC modulation amplitude
n	Refractive index
R_d	Diffuse reflectance
S_ρ	Scattering density

Chapter 1

Introduction

Reflectance optical imaging is a prominent imaging technique in biomedical optics as it can non-invasively return structural, functional and molecular tissue information at high resolution. In this chapter, the propagation of light in biological tissue is reviewed. The understanding of light propagation, which can lead to the extraction of tissue optical properties, absorption and scattering, is looked at. The importance of tissue absorption and scattering is also discussed. Spatial frequency domain imaging (SFDI) as a diffuse optical imaging technique is discussed. The advantages and disadvantages of this imaging technique are discussed, and SFDI systems that are currently in use in the field are compared with one another. With the idea of applying SFDI to gastrointestinal imaging, current gastrointestinal imaging modalities and devices are looked at, noting the advantages and disadvantages to all in relation to the proposed SFDI device.

1.1 Light propagation

The radiative transport equation (RTE) is a fundamental equation describing photon propagation in a medium, such as biological tissue [1]. Solving the RTE for light propagation in biological tissue enables the extraction and isolation of the absorption and scattering properties of the tissue, by using information from the reflected light. There are many possible solutions to the RTE which will be discussed in this section. These methods find the diffuse reflectance for some given illumination conditions and system constraints.

1.1.1 The diffusion approximation

Numerical solutions to the RTE are laborious, time consuming and costly. Therefore, analytical solutions can be readily obtained by use of the diffusion approximation. The diffusion approximation aims to solve a series of differential equations to understand the propagation of light through turbid, highly scattering media, such as tissue, by providing intuitive solutions. *Cuccia et al.* set out to provide a conceptual framework for a spatially modulated photon density standing wave in an experimental set-up with the use of periodic illumination, which will be presented in this section [2]. To start, the time-independent form of the diffusion equation for a homogeneous medium is given by:

$$\nabla^2\varphi - \mu_{eff}^2\varphi = -3\mu_{tr}q \tag{1.1}$$

where φ is the fluence rate (optical energy delivered per unit area), μ_{tr} is the transport coefficient given by $\mu_{tr} = \mu_a + \mu'_s$ where μ_a is the absorption coefficient and μ'_s is the reduced scattering coefficient, μ_{eff} is the effective attenuation coefficient given by $\mu_{eff} = \sqrt{3\mu_a\mu_{tr}}$, q is the illumination source which is given by:

$$q = q_0(z)\cos(k_x x + \alpha)\cos(k_y y + \beta) \tag{1.2}$$

where $k = 2\pi f$, f being the spatial frequency of the illumination, and α and β are the spatial phases in the spatial dimensions x and y respectively, with arbitrary dependence on depth, z. The medium of interest will have a diffuse fluence rate due to this illumination source of the form:

$$\varphi = \varphi_0(z)\cos(k_x x + \alpha)\cos(k_y y + \beta) \tag{1.3}$$

Substituting Eqns 1.2 and 1.3 into 1.1 an equation identical to the diffusion equation for planar illumination is obtained (derived in Appendix A):

$$\frac{\partial^2}{\partial z^2}\varphi_0(z) - \mu'^2_{eff}\varphi_0(z) = -3\mu_{tr}q_0(z) \tag{1.4}$$

where

$$\mu'_{eff} = (\mu^2_{eff} + k_x^2 + k_y^2)^{1/2} = \frac{1}{\delta'_{eff}} \tag{1.5}$$

where δ'_{eff} is the effective penetration depth into the medium. For planar illuminations of a sinusoidal wave, it is assumed that it is only modulating in one direction, x, with constant illumination. Therefore, one can let $k = k_x$ as $k_y = 0$. The source of this planar photon density wave reflectance can be modelled as [3]:

$$q_0(z) = P_0\mu'_s e^{\mu_{tr}z} \tag{1.6}$$

where P_0 is the incident power. Putting Eqn 1.6 into Eqn 1.4 and solving for $\varphi_0(z)$, one gets (derived in Appendix B):

$$\varphi_0(z) = \frac{3P_0a'}{\mu'^2_{eff}/\mu^2_{tr} - 1}e^{\mu_{tr}z} + Ce^{-\mu'_{eff}z} \tag{1.7}$$

where the reduced albedo, $a' = \mu'_s/\mu_{tr}$ and C is a constant of integration dependent on the boundary conditions of the semi-infinite geometry. This constant is determined, in this case, by use of the partial current boundary condition [4], where the flux, j, (optical energy per unit time) is set proportional to the fluence at the material interface (i.e. $z \to 0$):

$$j|_{z\to 0} \equiv \frac{-\nabla\varphi|_{z\to 0}}{3\mu_{tr}} = -A\varphi|_{z\to 0} \tag{1.8}$$

where A is a proportionality constant given by:

$$A = \frac{1 - R_{eff}}{2(1 + R_{eff})} \tag{1.9}$$

where R_{eff} is the effective reflection coefficient, given by:

$$R_{eff} \approx 0.0636n + 0.668 + \frac{0.710}{n} - \frac{1.440}{n^2} \tag{1.10}$$

where n is the refractive index of the diffuse medium e.g. tissue. The diffuse reflectance, also known as the diffuse spatial modulation transfer function (MTF) of the system, for a given set of optical properties can therefore be given by:

$$R_d = \frac{-j|_{z\to 0}}{P_0} = \frac{3Aa'}{(\mu'_{eff}/\mu_{tr}+1)(\mu'_{eff}/\mu_{tr}+3A)} \tag{1.11}$$

So, for a given set of optical properties at a given spatial frequency, Eqn 1.11 will return the diffuse reflectance.

Looking at the denominator of Eqn 1.11, where

$$\frac{\mu'_{eff}}{\mu_{tr}} = \Big(\frac{\mu_{eff}^2 + k^2}{\mu_{tr}^2}\Big)^{1/2} = \Big(\frac{3\mu_a\mu_{tr} + (2\pi f)^2}{\mu_{tr}^2}\Big)^{1/2} \tag{1.12}$$

it is noted that the diffuse reflectance is frequency dependent in the form of an inverse polynomial function of a single, positive valued μ'_{eff}/μ_{tr}. Therefore, the use of low or high frequencies will result in a variance in the diffuse reflectance and hence the ability to accurately resolve optical property values. From Eqn 1.12, it is noted that for low spatial frequencies, $k \ll \mu_{eff}$, absorption has the dominant effect, while for high spatial frequencies, $k \gg \mu_{eff}$, scattering has the maximal effect, as the diffusion approximation assumes that $\mu'_s \gg \mu_a$. For a planar illumination, i.e. $k = 0$, accompanied by an absorption of 0, μ'_{eff} of Eqn 1.12 $\to 0$ and therefore R_d of Eqn 1.11 $\to 1$.

The diffusion approximation suffers from many limitations. Firstly, it is only valid for $\mu'_s \gg \mu_a$, for a semi-infinite medium given the above boundary conditions. However use of different boundary conditions for arbitrary geometries (e.g. slab) would allow for the approximation of a non semi-infinite medium, at the expense of a more complex diffusion approximation. Secondly, the distance from the incident light source to a point on the boundary of the medium, ρ, is expected to be much greater than the transport mean free path, l^*:

$$\rho \gg l^* \tag{1.13}$$

where the l^* is the distance a photon travels within a medium before it changes it's direction, defined by [5]:

$$l^* = \frac{1}{\mu_a + \mu'_s} \tag{1.14}$$

It has been found that the minimum value of ρ for accurate optical property retrieval is $\rho \sim 4l^*$ [6, 7]. There also exists a limitation of maximum possible spatial frequency. The spatial frequency inverse of l^* is the transport spatial frequency ($f_{x,tr}$), which is exactly equal to the transport coefficient $\mu_{tr} = f_{x,tr}$. By thinking of the inverse of ρ as a metric of spatial frequency, it can therefore be said that:

$$f_x \ll \frac{1}{l^*} = \mu_{tr} \tag{1.15}$$

Therefore the maximum spatial frequency that agrees with the diffusion approximation must be less than $\mu_{tr} = \mu_a + \mu'_s$.

The diffusion approximation can be used to accurately determine the optical properties of a homogeneous media, agreeing with the above constraints. However, the generation of Monte Carlo simulations to solutions of the RTE as opposed to using the diffusion approximation has been shown to increase accuracy [2].

1.1.2 Monte Carlo simulations

To overcome the limitations implicit in using the diffusion approximation for optical property specification, e.g. $\mu_a \ll \mu_s'$ and maximum spatial frequency specification ($f_x \ll \mu_{tr}$), an alternate approach is required. Monte Carlo simulations are frequently used to generate solutions that are analytically difficult to solve. This is typically done by modelling an experiment as a series of probability density functions (which in this case are random scattering events over a range of possible scattering angles and random absorption events), sampling these probability density functions repeatedly, and then returning a statistical result of interest (which in this case is the expected distribution of possible reflectance values) [8]. A probability density function is a function which determines the probability of a specific, random variable appearing within a distribution for a continuous variable, and can be used to determine the probability of an observation occurring randomly [9].

Monte Carlo simulations have been used for many years to model light transport in tissue [10, 11], and open-source code is available to perform Monte Carlo simulations of the RTE [12]. There are several quantities to be considered to run a successful simulation of photon propagation within a turbid medium. Firstly, one must consider the probability that a photon will be absorbed within the medium. Secondly, one considers the probability that a photon will reflect at the interface between two media (i.e. air and tissue). Another consideration is the probability that a photon will scatter within the medium, and in doing so change its direction of propagation. A phase function describes this new direction a photon takes after a scattering event. Deciding on a correct phase function is paramount in accuracy of simulation. For biological tissue with multiple scattering events, with a source detector distance between 20 and 30 mm, one can describe photon scattering by the *Henyey-Greenstein* phase function [13, 14]. *Binzoni et al.* discuss the use of the *Henyey-Greenstein* phase function to model photon direction after a scattering event in Monte Carlo simulations [15]. The *Henyey-Greenstein* phase function is given by:

$$P_{HG}(\theta) = \frac{1}{4\pi} \frac{1 - g^2}{(1 + g^2 - 2g\cos(\theta))^{3/2}} \tag{1.16}$$

where g is the anisotropy which defines the direction of scattering within the medium (which will be discussed in Sect 1.2.1) and θ is the deflection angle of the photon after a scattering event. $\theta = 0$ implies that the photon direction is not affected by the scattering event.

Cuccia et al. use 'white' Monte Carlo simulations to generate diffuse reflectance values for a set of input optical properties for a single layered medium [2], while work has been done to show the capability to extend this to multi-layered media [16]. A white Monte Carlo simulation is used to reduce computational time by performing a single simulation with no absorption in the material and scaling the results to predict the light propagation for a range of different absorption and scattering properties [17]. *Kienle et al.* showed that this method compared to the conventional method resulted in errors in absorption and reduced scattering coefficients of $< 1\%$ and $< 2\%$ respectively [18]. For the simulation by *Cuccia et al.*, they simulated a collimated point source of 10^7 photons for the illumination and a detector with a numerical aperture of 0.22. They used values of g and n of 0.71 and 1.33 respectively, in line with known information of the phantom, tissue-mimicking material which was used.

Agreement was found between the diffusion approximation and these white Monte Carlo simulations of 12% for $f_x \leq 0.5\mu_{tr}$ and $a' = 0.99$ [2].

1.1.3 Alternate solutions

Other techniques exist besides Monte Carlo simulations to overcome the limitations of the diffusion approximation. *Erickson et al.* devised a custom, empirically derived look-up table based of tissue-mimicking phantom measurements to overcome the constraints [19]. This was done by taking measurements of reflectance and modulation of 126 varying phantom material properties and comparing the results with that of a 99% reflecting reference standard using the equations:

$$R(x,y) = \frac{I_{DC,sample}(x,y,) \times 0.99}{I_{DC,ref}(x,y)} \tag{1.17}$$

$$M(x,y) = \frac{I_{AC,sample}(x,y)/I_{DC,sample}(x,y)}{I_{AC,ref}(x,y)/I_{DC,ref}(x,y)} \tag{1.18}$$

where $R(x,y)$ is the reflectance, $M(x,y)$ is the modulation, and I_{AC} and I_{DC} are the magnitudes of the AC and DC components of projected pattern, which will be discussed in Sect 1.3.1. They found that, for large absorption coefficient, $\mu_a \geq 0.3$ mm^{-1}, the diffusion approximation produces very large errors and cannot accurately extract an absorption coefficient, while the empirically derived look-up table has an absorption coefficient error of just 7%. For an absorption coefficient of $\mu_a = 0.5$ mm^{-1}, the error in calculated reduced scattering coefficient for the diffusion approximation is 12%, reduced to 6% by using the empirically derived look-up table [19].

Kim describes the use of discrete-ordinate methods to compute the *Green's* function as a solution to the RTE [20]. The *Green's* function is a fundamental solution to the RTE [21]. Plane wave modes are general solutions to the RTE, and an analytical expansion of these is the calculated *Green's* function. The reasoning for using discrete ordinate method is because plane wave modes are not known analytically and therefore must be determined numerically. This method is limited to media with minimum forward scattering, as it can not successfully compute solutions to the RTE for highly forward scattering material.

Post et al. propose an improved model for diffuse reflectance to that of *Cuccia et al.* by obtaining the tissue impulse response through computing the reflectance as a function of radial distance ρ using a narrow pencil beam as an illumination source under the partial current boundary condition (PCBC) [22]. The updated diffuse reflectance is given by:

$$R_{PCBC}(k) = \frac{a'}{\frac{4A}{3}\mu'_{eff}/\mu_{tr}} \frac{\left[1 - \exp\left(-\frac{4A}{3}\mu'_{eff}/\mu_{tr}\right)\right]}{1 + \mu'_{eff}/\mu_{tr}} \tag{1.19}$$

By comparing this new model of diffuse reflectance to the model proposed by *Cuccia et al.* in Eqn 1.11, this new model reduces the median relative error in the extracted absorption coefficient from 0.022% to 0.008% and in the extracted reduced scattering coefficient from 0.029% to 0.026%. The two main differences in the models are source of incident illumination, where *Cuccia et al.* model plane wave illumination while

Post et al. propose a pencil beam illumination, and the improved model replaces μ_{eff} with μ'_{eff}.

Looking at the above models, the diffusion approximation should be used in cases where the discussed constraints are obeyed such as the turbid medium being semi-infinite with $\mu'_s \gg \mu_a$. If the set up does not meet these conditions, a Monte Carlo simulation of diffuse reflectance values should be used to overcome these constraints, at a cost of increased computational time. Non-conventional system geometries, or samples not obeying the previously discussed diffusion approximation limits, would benefit from the use of an empirically derived look-up table. This is due to the look-up table being specific to that imaging system, increasing accuracy in optical property retrieval.

1.2 Tissue optical properties

Optical properties can tell us important information on the material make up of biological tissue. Structural tissue information gives an insight to objects within the tissue that have the potential to be scattered by light, such as cell nuclei, mitochondria, and collagen. Functional tissue information gives details on the work being carried out by the tissue, such as blood oxygenation or cell transport. To understand the functional tissue information, it's often necessary to be aware of molecular tissue information, such as oxyhaemoglobin (HbO_2), deoxyhaemoglobin (Hb), lipids and melanin content [23].

1.2.1 Absorption and scattering

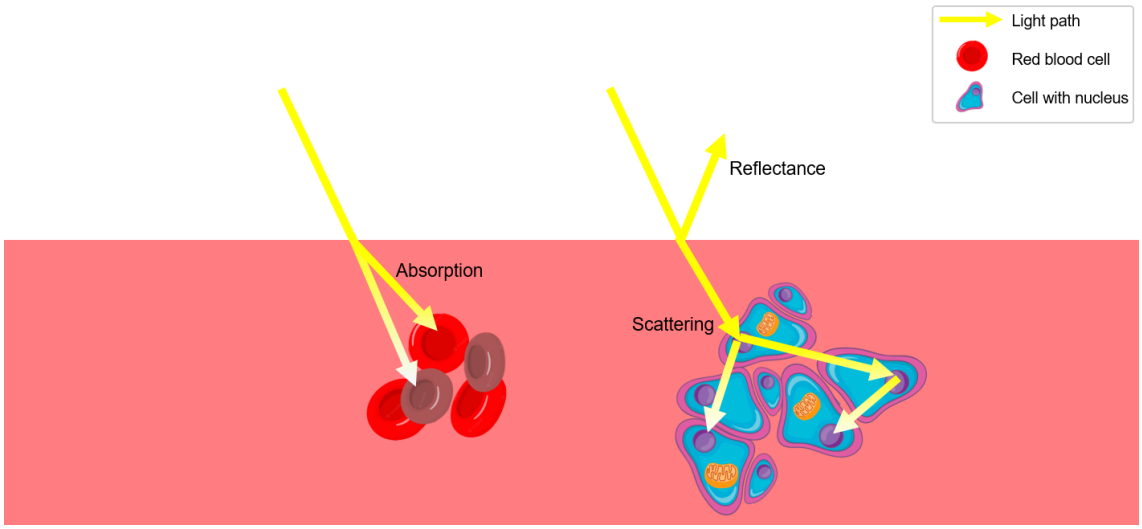

Figure 1.1: Schematic of absorption, reflectance and scattering processes in bulk tissue.

The dominant optical properties of tissue are expressed by the absorption coefficient μ_a, the scattering coefficient μ_s, and the refractive index n. It is typical to use μ_s when investigating thin tissue samples where one to several scattering events take place. For thicker samples where multiple scattering events occur, the angle θ

is introduced which represents the deflection angle of a photon during a scattering event. The anisotropy of a material is represented as:

$$g = \langle \cos\theta \rangle \tag{1.20}$$

and defines the probability distribution of scattering in a sample in terms of forward and backward scattering i.e. $g = 0$ has both forward and backward scattering (isotropic), $g = -0.9$ is dominated by backward scattering with some forward scattering, and $g = 0.9$ is dominated by forward scattering with some backward scattering. Therefore, for a thick sample with multiple scattering events, the reduced scattering coefficient is used instead, given by:

$$\mu_s' = \mu_s(1 - g) \tag{1.21}$$

Scattering within a medium depends on the relative refractive index change from the surrounding medium (typically air) to the medium of interest, the wavelength of the incident light, and the size of particles within the medium of interest. One way to describe optical scattering can be by Mie theory, in which the scattering of particles within a sample is due to the particles having a refractive index different to that of the surrounding sample (e.g. cell nucleus having different refractive index to surrounding cell) [24]. Mie theory assumes the scattering particles are perfectly spherical in shape, and that different sphere sizes simulate the optical scattering behaviour of a material [25]. Mie scattering is dominated by forward scattering, i.e. $g \approx 0.9$. Another type of scattering is Rayleigh scattering in which the scattering is caused by light propagating through a medium in which the particle size is much smaller than the wavelength of incident radiation [26]. Rayleigh scattering is wavelength dependent i.e. the amount of scattering $\sim \lambda^{-4}$ [27]. Therefore, different wavelengths will scatter differently in contrasting samples, and consideration must be taken as to which wavelength used relates to the expected scattering within the sample. By either Mie or Raleigh scattering, bulk scattering refers in a large amount of back scattering from the incident light, whereas multiple scattering and absorption events within the tissue are responsible for the eventual attenuation of the incident light. A depiction of scattering in tissue is shown in Fig 1.1.

Absorption is a process where the incident beam of photons is attenuated by tissue components, also shown in Fig 1.1. Various chromophores in biological tissue absorb light, such as HbO_2, Hb, and melanin [29]. HbO_2 and Hb are important tissue optical properties because they have the potential to differentiate between malignant and benign tumours. As a tumour grows, it rapidly outgrows its blood supply, and therefore proliferated tumours often present with regions of significantly lower oxygen concentration than healthy tissue. These hypoxia conditions often exist in malignant tumours over benign tumours. The vasculature of tumours is directly related to proliferation, growth and metastasis [30]. Therefore, the ability to differentiate between HbO_2 and Hb is invaluable in determining tissue type. HbO_2 and Hb have significantly different absorption spectra at several wavelengths, depicted in Fig 1.2, particularly in the near infrared wavelength range, which is the principle on which pulse oximeters are based [31]. Using the modified Beer-Lambert law, the absorption at particular wavelength is obtained by:

$$\mu_a(\lambda_i) = \sum_{n=1}^{N} \varepsilon_n(\lambda_i) c_n \tag{1.22}$$

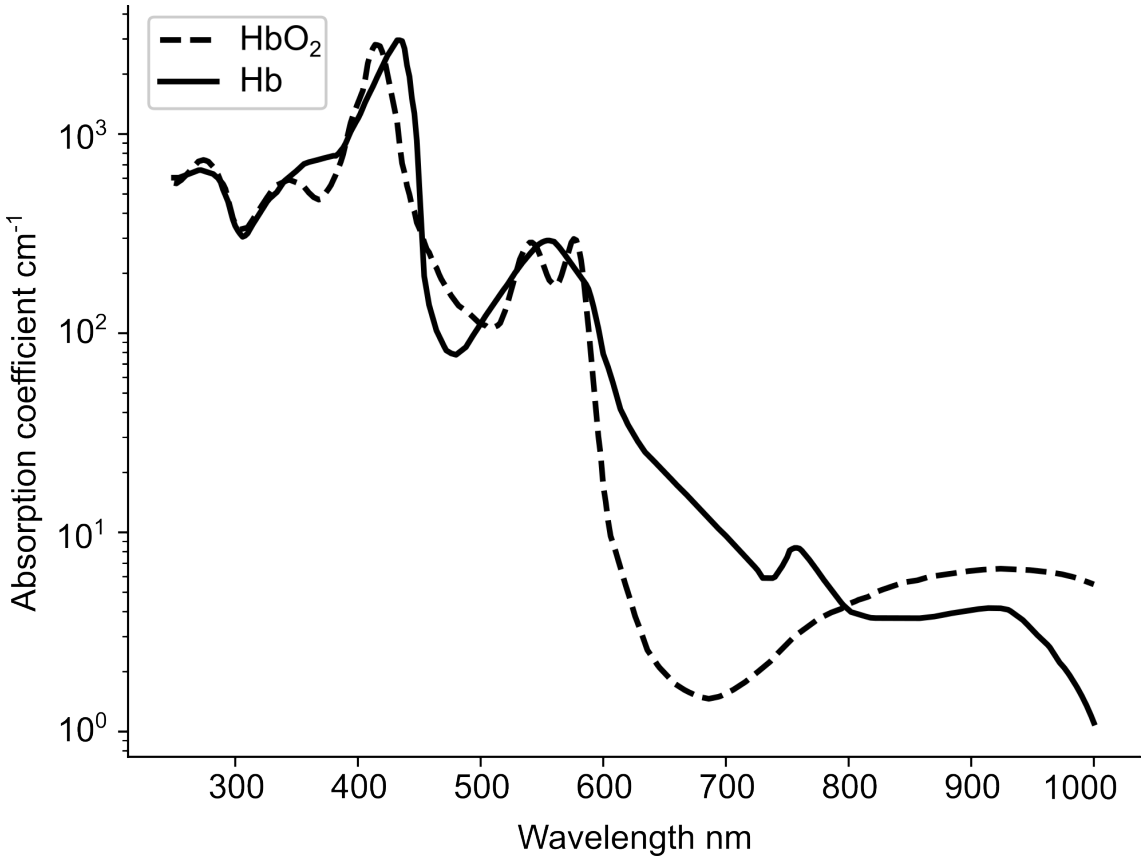

Figure 1.2: Absorption coefficient vs wavelength for oxyhaemoglobin (HbO_2) and deoxyhaemoglobin (Hb). Adapted from [28].

where ε is the chromophore extinction coefficient at a particular wavelength, λ, (which are known values from literature [32, 33]), c is the chromophore concentration and N is the number of chromophores. In this case, the reduced scattering coefficient has been previously determined, and such the pathlength has been inferred for the absorption coefficient calculation. By taking measurements of the absorption coefficient at different wavelengths, the concentration of the chromophores of interest can be calculated via the matrix:

$$\begin{bmatrix} \mu_a(\lambda_1) \\ \vdots \\ \mu_a(\lambda_j) \end{bmatrix} = \begin{bmatrix} \varepsilon_1(\lambda_1) \dots \varepsilon_i(\lambda_1) \\ \vdots \quad \ddots \quad \vdots \\ \varepsilon_1(\lambda_j) \dots \varepsilon_i(\lambda_j) \end{bmatrix} \times \begin{bmatrix} c_1 \\ \vdots \\ c_i \end{bmatrix} \tag{1.23}$$

where i represents the number of wavelengths used and j represents the number of chromophores of interest [34]. For determination of HbO_2 and Hb in tissue, it is typical to use two wavelengths either side of isobestic point of HbO_2 and Hb at 800 nm, as seen in Fig 1.2. *Sato et al.* determine the optimum wavelength pair to use for measurement of tissue HbO_2 and Hb by simultaneously imaging a sample at five wavelengths: $678, 692, 750, 782$, and 830 nm for pairing with 830 nm [35]. The signal-to-noise (SNR) ratios for each wavelength pair was calculated over several sample areas. They found that pairing 692 nm with 830 nm had the highest SNR, and is therefore the optimal choice. It is of note that at this wavelength, the difference in absorption coefficient between HbO_2 and Hb is at it's largest, which may be a contributing factor to the high SNR obtained.

Optical property	Measurable by SFDI
μ_a	✓
n	×
μ_s	×
g	×
μ_s'	✓

Table 1.1: Optical property measurement compatibility with direct measurement from spatial frequency domain imaging.

Optical properties can be measured by different techniques. Table 1.1 depicts the optical properties directly measurable with SFDI, which will be introduced in Sect 1.3.1. As μ_s' can be measured via SFDI, knowledge of the material of interest's anisotropy factor, g, can infer the materials scattering coefficient, μ_s.

1.2.2 Absorption and scattering of typical gastrointestinal conditions

Holmer et al. have shown that cancerous and non-cancerous tissue in the stomach and oesophagus exhibit a variation in measured optical properties [36]. A total of 36 samples of adenocarcinoma and squamous cell carcinoma (SCC) were imaged,as well as several samples of healthy stomach and healthy oesophageal tissue taken from the surgical safety margin. Adenocarcinomas are malignant tumours formed in the glands of the epithelial tissue [37], which is the tissue that lines hollow organs [38]. SCC arises from the proliferation of squamous cells, which are flat cells that line different parts of the gastrointestinal (GI) tract [39]. SCC's are among the most frequent incidences of solid tumours in humans and are a major cause of cancer related deaths [39]. Their main feature is their high degree of cellular heterogeneity. SCC can originate from stratified epithelial cells, which are layers of cells that cover the inside and outside surfaces of the body and have the capability to self-renew, or form pseudo-stratified epithelium cells (which are a single layer of cells tightly packed, appearing as if they are stacked in layers) through the activation of quiescent cells. Quiescent cells are cells that remain out of the cell cycle, but can commence division once activated, resulting in a switch in cell fate determination.

The samples were imaged in an integrating sphere spectrometer over the wavelength range $300 - 1140$ nm. An integrating sphere spectrometer is a device which measures the reflectance and transmission of light through a sample, from which the samples optical properties can be inferred. Further discussion on how an integrating sphere operates will be given in Chapter 3. Over this wavelength range, it was found that the absorption coefficient of both adenocarcinoma and SCC is less than that of healthy oesophageal tissue. The scattering coefficient of adenocarcinoma is greater than that of healthy stomach tissue at wavelengths < 600 nm and less than that of healthy stomach tissue at wavelengths > 600 nm. The scattering coefficient of SCC is comparable to that of healthy oesophageal tissue at wavelengths < 420 nm and less than that of healthy oesophageal tissue at wavelengths > 420 nm. The anisotropy of tissue was also measured, ranging from $0.8 - 0.94$ with no variation between that of healthy and cancerous tissue at wavelengths ≥ 630 nm. *Holmer et*

al. suspects the lower scattering coefficients seen in adenocarcinoma > 600 nm and SCC at > 420 nm compared to healthy tissue can be attributed to the lower content of chromophores, cell nuclei and cell membranes present in tumour tissue. The lower absorption coefficients seen in adenocarcinoma and SCC may be attributed to their rapid proliferation resulting in poorly formed vasculature, described in Sect 1.2.1. However, as oesophageal neoplasia is associated with angiogenesis [40], it might be suspected that these regions of new, abnormal cell growth have a higher absorption coefficient than that of healthy tissue, while regions of abnormal cells present for some period of time will have a lower absorption coefficient compared the healthy tissue. This is because the rapid proliferation will first result in more blood vessels and an increased absorption coefficient, but then the vasculature will rapidly outgrow it's blood supply, decreasing the absorption coefficient.

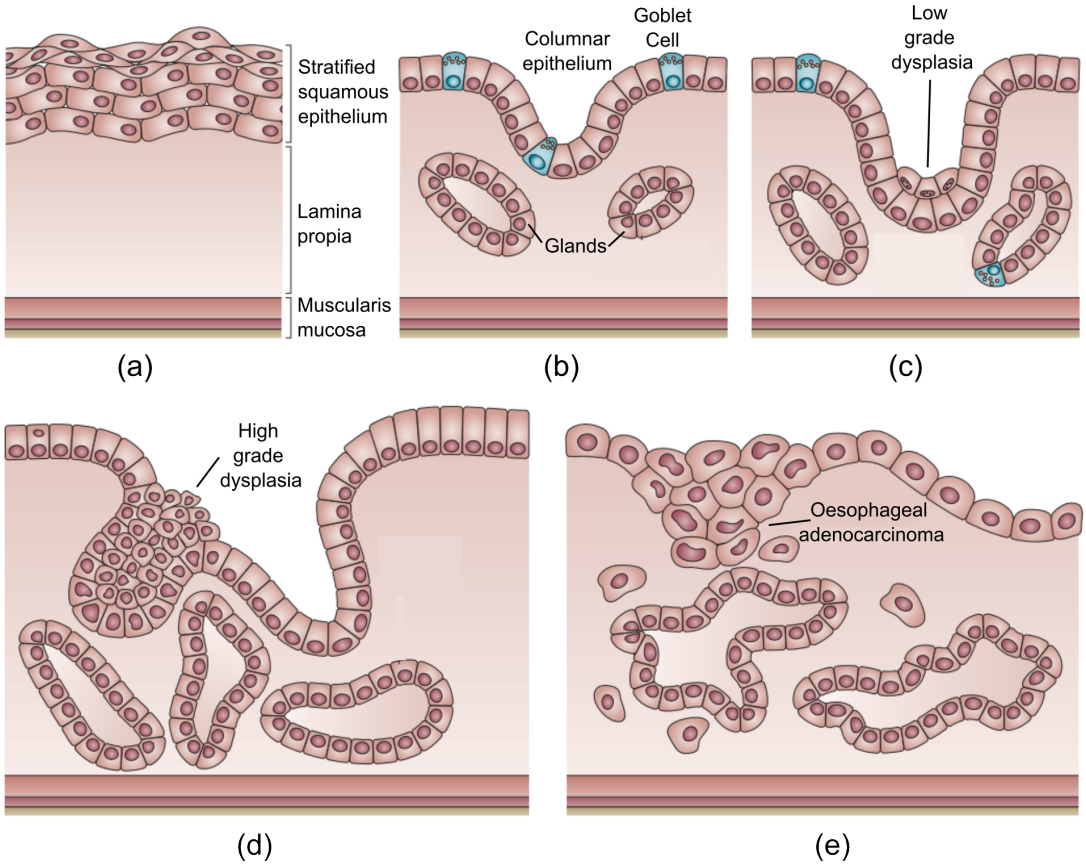

Figure 1.3: Schematic representation of the progression from healthy oesophageal tissue to oesophageal adenocarcinoma (a) normal stratified squamous epithelium in the oesophagus (b) metaplasia occurring, an indication of BO. Goblet cells are intestinal mucosal epithelial cells whose purpose is for nutrient digestion and absorption of mucosa [41] (c) development of low grade dysplasia (d) development of high grade dysplasia (e) neoplastic oesophageal adenocarcinoma. Adapted from [42].

Before detection of adenocarcinoma within the oesophagus, most patients are diagnosed with a precancerous condition termed Barrett's Oesophagus (BO) in which the typical epithelial cells lining the oesophagus (see Fig 1.3 (a)) change to that of columnar cells, which are commonly found in the small and large intestine [42, 43] in a process termed metaplasia (see Fig 1.3 (b)). It is thought that these columnar

epithelial cells arise directly from stromal cells [44]. It can be a result from ongoing acid and bile reflux from the stomach, where dysplasia then occurs at the distal end of the oesophagus (see Fig 1.3 (c & d)). Dysplasia is the development of abnormal cells within tissue, and can lead to a wide range of conditions such as enlarged tissue and precancerous cells. Many people with BO do not develop oesophageal adenocarcinoma. However, there still exists a necessary requirement for patients with BO to undergo regular endoscopies to monitor the conditions progression as up to 13% of patients with BO in the UK will develop oesophageal adenocarcinoma in their lifetime [45]. Detecting changes from BO to neoplastic tissue is invaluable in treating the disease early to prevent progression to adenocarcinoma. There is no evidence toward significant difference in the absorption coefficient between healthy tissue and BO. However, neoplastic tissue in the oesophagus in particular is associated with angiogensis, as previously discussed, and therefore will have a higher absorption coefficient than surrounding healthy tissue (or surrounding BO). The scattering of stromal cells present in BO is significantly greater than that of healthy tissue [46]. However, neoplasia is associated with a slight decrease in the scattering of these stromal cells present in BO, which is attributed to degradation of collagen fibers [46].

Sweer et al. imaged resected oesophageal tissue at several wavelengths from 471 nm to 851 nm [47], which will be discussed in depth in Sect 1.3.4. As shown in Table 1.2 in Sect 1.3.4, it was found that the ratios of absorption coefficient at 471 nm to absorption coefficient at 851 nm for healthy tissue, Barrett's Oesophagus, and squamous cell carcinoma were 13, 25, and 11 respectively. It was also found that the ratios of reduced scattering coefficient at 471 nm to reduced scattering coefficient at 851 nm for healthy tissue, Barrett's Oesophagus and squamous cell carcinoma were 2, 1.2 and 1.7 respectively.

Therefore, it is suspected that as oesophageal tissue progresses from healthy (Fig 1.3 (a)), to BO (Fig 1.3 (b)), to dysplasia (Fig 1.3 (c & d)), to adenocarcinoma (Fig 1.3 (e)), that the absorption coefficient will stay constant from healthy to BO, then a significant increase as it progresses to neoplasia, followed by a significant decrease in adenocarcinoma. As for the scattering coefficient, it is suspected that it will increase from healthy tissue to BO, and then decrease throughout the disease progression. The capability to detect these optical property variances is vital in determining tissue type. The American Society for Gastrointestinal Endoscopy set out guidelines which state that a new technology needs to have 90% sensitivity and 80% specificity to be recommended for targeted biopsy [48].

1.3 Spatial Frequency Domain Imaging

Conventional measurements of the structural and functional properties within a turbid medium (such as tissue), described in Sect 1.2, rely on resolving the behaviour of photon propagation within the medium, discussed in Sect 1.1. In the real spatial domain, a point source illuminates a medium which induces a diffuse reflectance in time with a spatial point spread function (s-PSF), of which the shape of the spatial decay is characteristic of these sub surface structural and functional properties of the medium. Measuring medium properties in the real domain is advantageous as it offers high signal-to-noise ratio (SNR) data. However, to recover optical properties over a large field of view, a point scanning technique is normally required which is

time consuming and not possible for real-time return of material parameters. Therefore, measuring medium properties in the spatial frequency domain is advantageous for wide field, real time imaging.

1.3.1 An Introduction

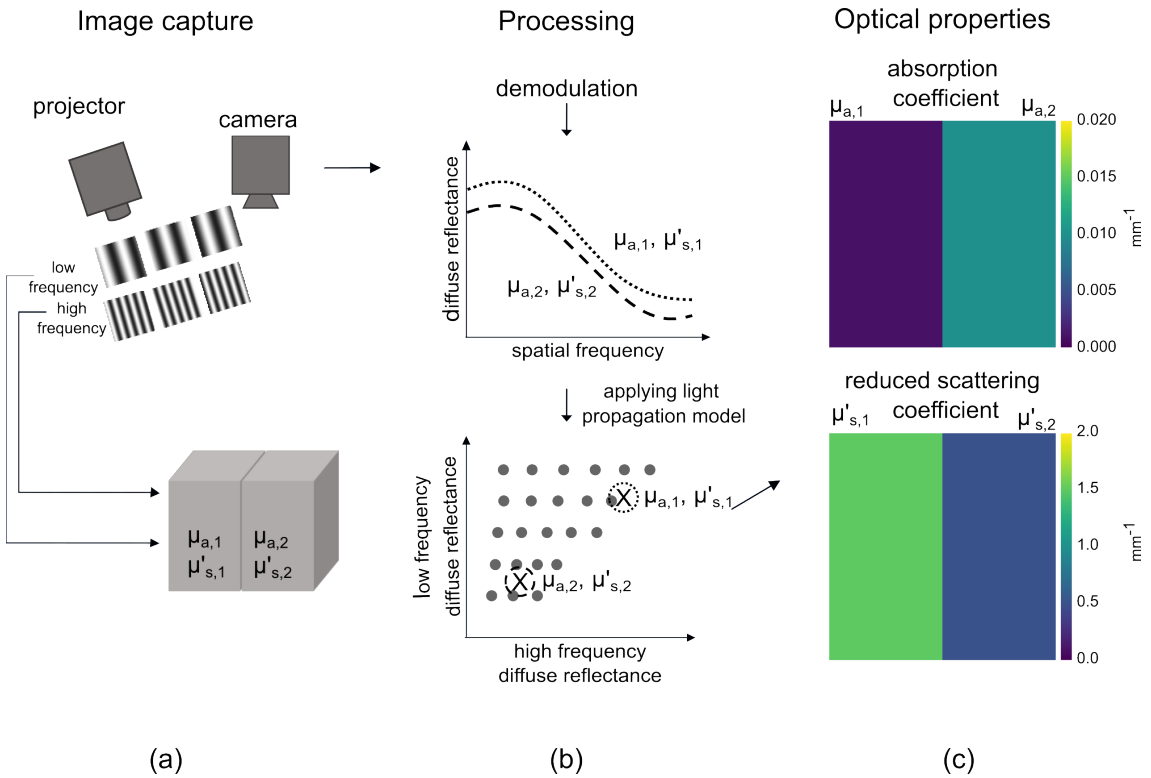

Figure 1.4: SFDI process: (a) a series of high and low frequencies are projected onto a sample of interest. A camera placed directly above the sample captures how the sample reflects/transmits the projected patterns. (b) A demodulation is then performed where the s-MTF i.e. diffuse reflectance of each pixel in the image can be determined for each spatial frequency. Using a light propagation model to relate the diffuse reflectance values to optical properties via a look-up table, (c) optical property maps of the absorption and reduced scattering coefficient may be obtained.

In the spatial frequency domain, a wide 2D intensity sine wave is projected onto the medium and, by a process called demodulation, the spatial modulation transfer function (s-MTF) as a function of spatial frequency is obtained which contains information on the properties of the medium. The s-MTF of the medium is represented by the function $R_d(x, f_x)$, the diffuse modulation transfer function of the system, which can be modelled with any light propagation model described in Sect 1.1. Then, solving the inverse problem allows recovery of optical properties of the medium. Measurements in the spatial domain rely on less complex mathematical models which reduces complexity, as well as providing the capability to image large ($\gtrsim 10 \times 10$ cm) field of views rapidly.

Spatial Frequency Domain Imaging (SFDI) is a well established, low-cost imaging technique that can deliver close to real time quantitative maps of absorption and reduced scattering coefficients, inferring information on the structural and functional

information of the sample of interest [2, 49, 50]. Conventional imaging consists of projecting a 2D sinusoidal pattern of known spatial frequency onto a sample of interest, while work has shown success with square waves and speckle illumination [51, 52]. Typically, the projector is placed at a small angle ($\lesssim 10°$) to the normal in an effort to reduce specular reflections recorded by the camera [53] (See Fig 1.4 (a)). Specular reflections result from light perfectly reflecting off a sample surface due to changes in refractive index, rather than scattering in all directions (diffuse reflectance). This results in the presence of a bright spot of light in captured images and therefore the return of improper optical property values [54]. Another measure to reduce specular reflections is to place cross polarisers in front of the projector and camera. The sample reflects/scatters the incident light, reducing the amplitude of the 2D projection pattern. A camera placed directly above the sample captures the modified amplitude of the illumination pattern due to these reflections/scatterings taking place within the sample. It is assumed that the captured diffusely reflected intensity, I, of the projection pattern is the sum of the modulated (AC) and planar (DC) components of the sinusoid, such that $I = I_{AC} + I_{DC}$, where the intensity components can be modelled as:

$$I_{AC} = M_{AC}(x, f_x) \cdot \cos(2\pi f_x x + \alpha) \tag{1.24}$$

$$I_{DC} = M_{DC}(x) \cdot \cos(\alpha) \tag{1.25}$$

where M_{AC} and M_{DC} represent the modulated amplitude envelope of the reflected photon density wave at position x at frequency f_x, and α is the spatial phase of the illumination pattern. To determine M_{AC}, the sample is illuminated with a sinusoidal pattern of spatial frequency f_x at three spatially shifted phases of $\alpha = 0°, 120°$ and $240°$. A process called demodulation is performed on every pixel in the image using the equations (derived in Appendix C):

$$M_{AC}(x, f_x) = \frac{\sqrt{2}}{3}\Big((I_1(x) - I_2(x))^2 + (I_2(x) - I_3(x))^2 + (I_3(x) - I_1(x))^2\Big)^{1/2} \tag{1.26}$$

$$M_{DC}(x) = \frac{1}{3}\Big(I_1(x) + I_2(x) + I_3(x)\Big) \tag{1.27}$$

where I_1, I_2 and I_3 are the three equiphase shifted images captured of their respective spatial frequency patterns. Conventionally, a minimum of two spatial frequency patterns are required: one of spatial frequency lower than the other (or planar projection with spatial frequency = 0 mm^{-1}) and one with a spatial frequency higher than the first (typically ≥ 0.1 mm^{-1}). This is because the absorption of a sample attenuates the lower spatial frequencies of the MTF more than scattering, and the scattering attenuates the higher spatial frequencies of the MTF more than absorption. Therefore, using two spatial frequencies allows for the decoupling of the optical properties. However for low absorbing samples, as typically required for accurate SFDI, three higher frequency captures may be used to obtain the DC modulation amplitude image by averaging them together, as an AC image is the sum of an AC and DC image. Reducing from six to three images may result in increasing the average noise across the image, imperfections and non-linearities.

The calculated AC and DC modulation amplitudes must be related to diffuse reflectance values, in order to calculate the optical properties. An AC modulation amplitude calculation, as in Eqn 1.26, in the frequency domain is a product of

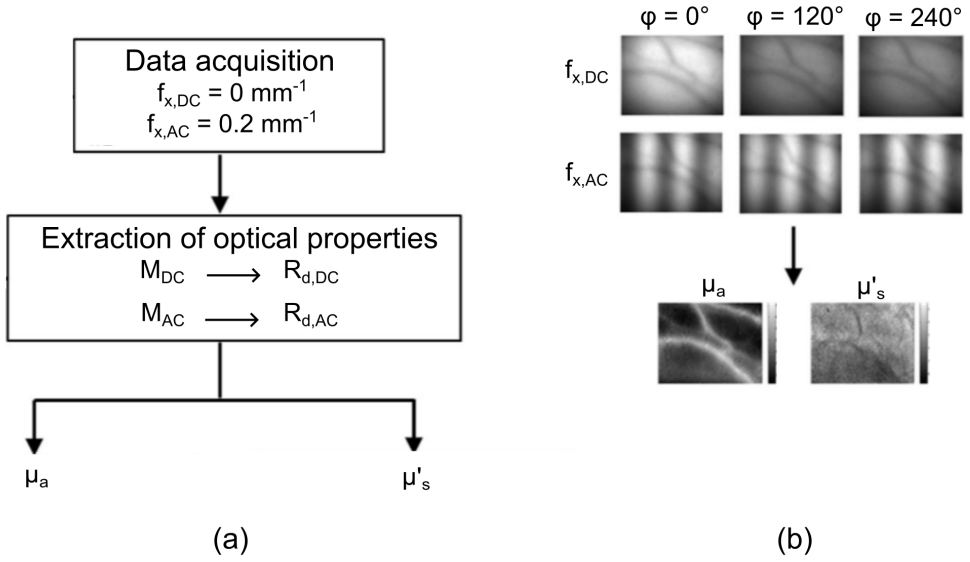

Figure 1.5: Full acquisition workflow of typical SFDI optical property maps (a) schematic of typical workflow from data acquisition through to extraction of optical properties, μ_a and μ'_s (b) raw acquisition images at two spatial frequencies and three equally shifted phases and resultant, processed, optical property maps, μ_a and μ'_s. Adapted from [50].

the source intensity I_0, the modulation transfer function of the system MTF_{system}, and diffuse spatial modulation transfer function of a medium with specific optical properties, also known as the diffuse reflectance R_d:

$$M_{AC}(x, f_x) = I_0 \cdot MTF_{system}(x, f_x) \cdot R_d(x, f_x) \tag{1.28}$$

There is a need to calibrate for the source intensity and MTF of the system. By using a reference material of known optical properties, and hence known diffuse reflectance, this can be achieved. Therefore, the diffuse reflectance of an unknown sample can be found through the equation:

$$R_d(x, f_x) = \frac{M_{AC}(x, f_x)}{M_{AC,ref}(x, f_x)} \cdot R_{d,ref}(x, f_x) \tag{1.29}$$

where M_{AC} and R_d are the AC modulation amplitude and diffuse reflectance of the unknown sample of interest and $M_{AC,ref}$ and $R_{d,ref}$ are the AC modulation amplitude and diffuse reflectance of the reference material of known optical properties. $R_{d,ref}$ is found through use of chosen light propagation model, discussed in Sect 1.1. By substituting M_{DC} in place of M_{AC} in Eqn 1.29 and using R_d calculated at the DC spatial frequency, one then has two values for diffuse reflectance at the high and low spatial frequency of projection (see Fig 1.4 (b)).

To determine the optical properties of a sample of interest, one generates a look-up table (LUT) from a chosen light propagation model as discussed in Sect 1.1. The LUT is a pre-calculated set of DC diffuse reflectance vs AC diffuse reflectance values, where each set of values corresponds to a specific set of optical properties. Then, through an interpolation (typically cubic), the optical properties of the sample of

interest can be determined (see Fig 1.4 (c)). A typical workflow of the SFDI process is depicted in Fig 1.5 (a & b).

1.3.2 Additional techniques to conventional spatial frequency domain imaging

SFDI has several drawbacks associated with it. Translating an SFDI instrument to a clinical environment can be challenging as, conventionally, a minimum of six patterns (two spatial frequencies, three phases) needs to be both projected and captured by the system on the sample of interest, and then processed to obtain the resultant optical properties. This process can be time consuming in a fast-paced clinical setting and it can be challenging for use with real-time acquisition. Increasing the speed of SFDI measurements is paramount in the strive toward their clinical translation. Several techniques exist which make it possible to overcome the drawbacks of SFDI, and enhance it's potential to make it feasible for clinical imaging, which will be discussed here.

Single snapshot of optical properties imaging

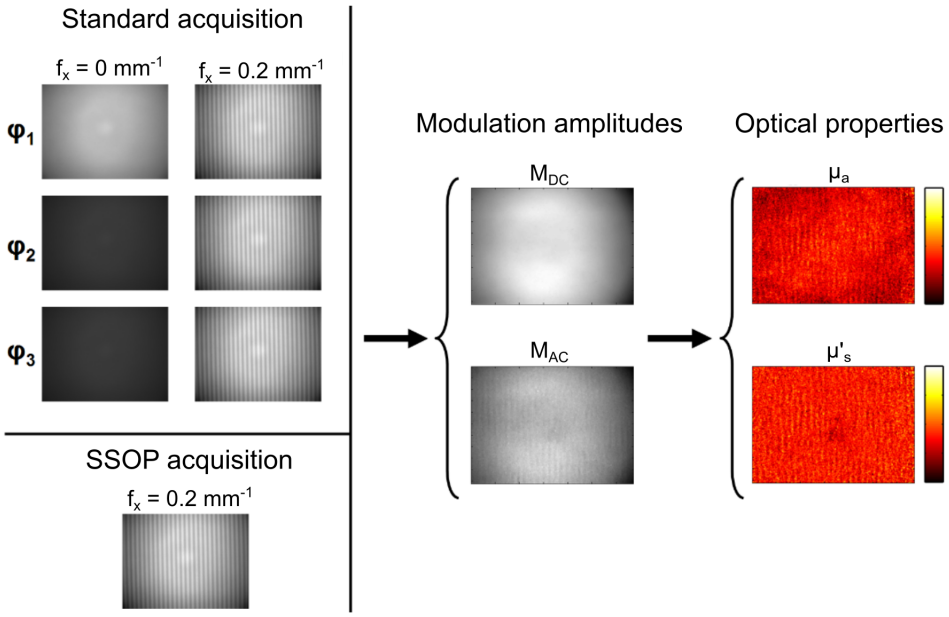

Figure 1.6: Comparison of SFDI and SSOP. Image(s) are acquired, the DC and AC components are extracted, and the optical properties obtained. The standard acquisition process using SFDI requires 6 images (top left) and the SSOP method requires a single image (bottom left). Adapted from [55].

Single snapshot of optical properties (SSOP) imaging is an alternate technique to conventional SFDI with the advantage to potentially image optical properties 3 times as fast. This is due to the fact that SSOP requires the projection of a singular spatial frequency at a singular phase instead of three phase images at two spatial frequencies, as shown in Fig 1.6. As only one, high spatial frequency pattern is projected, the captured illumination pattern must be filtered to extract the low and high frequency information to get the low (DC) and high (AC) modulation amplitudes. The optical

properties are then calculated as before via a light propagation model by knowledge of the diffuse reflectance of the sample [55]. Reducing the necessary number of patterns to project leads to shorter acquisition times. However, as just one image is acquired and filtering is applied, the resultant optical property maps do suffer from reduced image quality due to energy spectrum losses, and hence inaccuracies in optical property values, compared to conventional SFDI.

One method to separate the low and high frequencies proposed by *Vervandier et al.* relies on performing a line by line Fourier transform on each individual line of the single, captured image [55]. The first and last maxima of the line spectrum are separated to get the respective low and high frequency components by a cut-off frequency, calculated by determining the closest local minimum to the highest AC frequency detected in a smoothed line spectrum. An inverse Fourier transform (IFT) is then applied to each separated low and high spectra which corresponds to a row in the resultant DC and AC images respectively.

Another approach to filter an SSOP image proposed by *van de Giessen et al.* makes use of rectangular blocking filters after performing a Fourier Transform to mask out the individual low and high frequencies [56]. Fig 1.7 (a) depicts the raw images captured. While a single spatial frequency may be used to extract optical properties, the additional of a second spatial frequency, orthogonal to the first spatial frequency, may be used to extract height information from the sample of interest. This is because the sample of interest will shift the lateral phase of the projected sinusoid, which can be converted to height. This technique is termed 3D-SSOP, where both optical property and height information can be obtained simultaneously. The spatial frequency required for profilometry imaging is, as a rule, less than that of the spatial frequency used for optical property measurements. The spatial frequency pattern for a profilometry measurement must also be projected orthogonal to the spatial frequency pattern for optical property measurement as a sample with inhomogeneous height will show variation in one pattern orientation and not the other, due to the relative orientation of the projector. This variation can be seen clearly in Fig 1.7 (a). When projecting two patterns simultaneously, the captured image must first be expanded by mirroring the image to reduce image artefacts at the image edges.

Filtering may then be used to extract the individual low and high frequencies, after applying a 2D Fourier transform to the mirrored image. To isolate the DC component, the side high frequencies are masked out, as well as the high frequencies present due to the orthogonally projected pattern for the profilometry measurement, as shown in Fig 1.7 (b). A 2D IFT is then applied to the entire image. The AC component is isolated by masking out the centre low frequency, as well as the high frequencies present due to the orthogonally projected pattern for the profilometry measurement, as was done in isolating the DC component, also shown in Fig 1.7 (b). To obtain the AC image, a 2D IFT is applied, as well as an additional Hilbert transform [57]. A Hilbert transform is used over an inverse Fourier transform as the negative and positive high frequencies are both present after masking, and the Hilbert transform multiplies the negative frequencies by -1 to obtain just the positive, high frequency i.e. it cancels out one of the 'mirrored' spatial frequency components, meaning that the magnitude of the result simply equals the AC modulation. As the captured image was expanded at the beginning, the final image is selected by taking the centre frame from each resulting image. This technique may

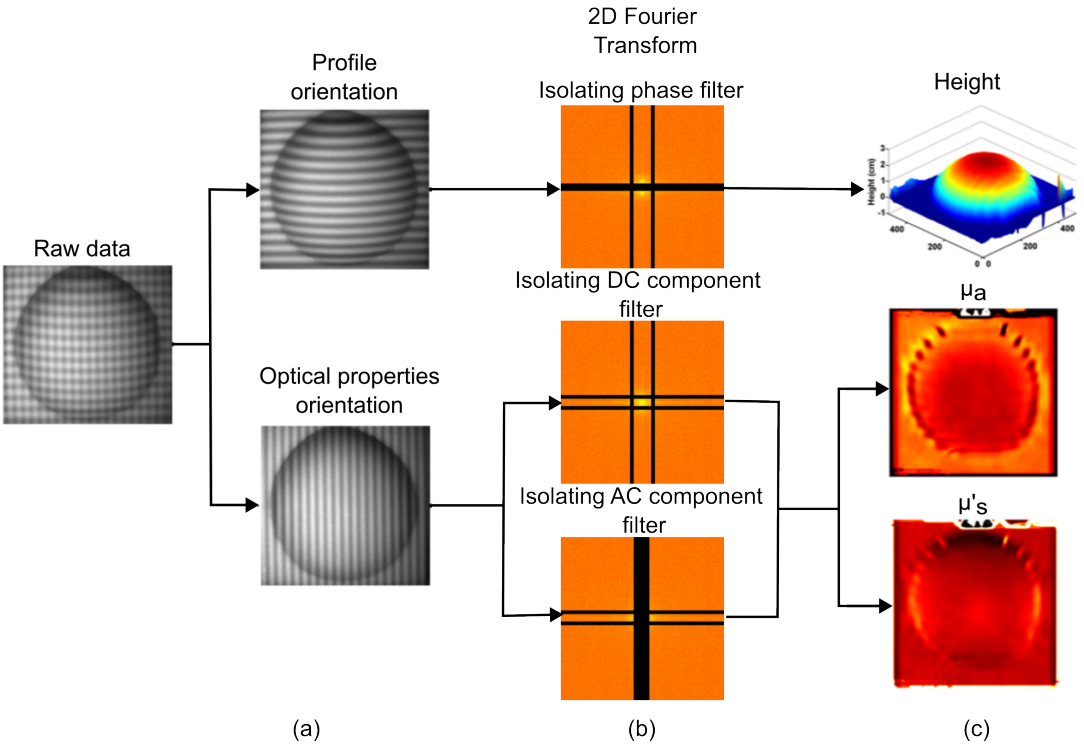

Figure 1.7: 3D SSOP where a dual sinusoid is projected onto a sample, one pattern sensitive to surface profile and an orthogonal pattern sensitive to optical properties. Adapted from [56].

be applied to extract the optical properties of the sample of interest (Fig 1.7 (c)). The phase is isolated by masking out the high frequencies from the optical property projection pattern, as well as masking out the center low frequency for the phase projection pattern, as shown in Fig 1.7 (b). A 2D IFT is then applied, followed by an additional Hilbert transform as before to extract the AC image. This phase information can be converted to height information via fringe profilometry, which will be discussed later in this section.

This method is advantageous to the demodulation method proposed by *Vervandier et al.* as it allows for simultaneous acquisition of both phase and optical property information. If an SFDI system is designed to image samples of highly varying profilometry at various heights, performing a phase calibration on homogeneous flat phantoms is necessary to perform profile correction. Another advantage over the previous approach is an increase in processing speed. The image processing being completed in Fourier space and the use of a novel 2D optical property LUT greatly reduces the needed processing time to 0.125 s. However, this technique suffers from the same image degradation to that as the line by line transform technique. Also, the calculated phase contains noise, which results in artefacts present in the reconstructed 3D image. These artefacts are also present in the optical property maps, particularly in samples where the surface is inhomogeneous.

Aguénounon et al. investigate optimal filtering techniques and optimal spatial frequencies to improve the artefacts present in SSOP optical property maps [58]. The two previously described demodulation techniques suffer from reduced image quality as ideal, discontinuous rectangular filters cause ringing/ripple to occur in

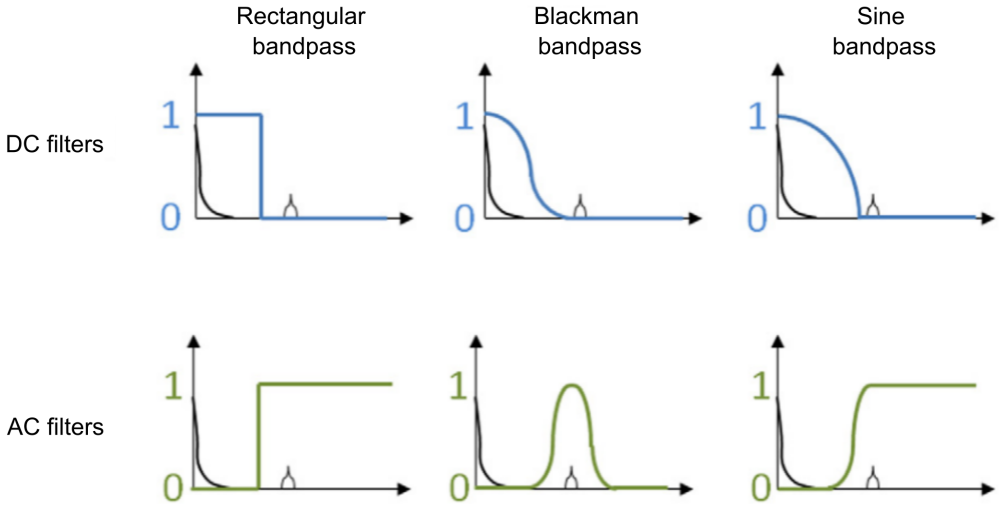

Figure 1.8: Schematics of different DC and AC filters used to separate low and high frequencies in SSOP by *Aguénounon et al.*. Adapted from [58].

the output image, known as the *Gibbs effect* [59], and extracting the AC phase independently can be challenging. *Aguénounon et al.* investigated a variety windows: rectangular, Blackman and sinusoidal, shown in Fig 1.8. In the x direction (i.e. the direction with spatially modulated information), the filters were designed around the zeroth frequency to make the DC filter and around the higher spatial frequency of projection for the AC filter. In the y direction (where there is no spatially modulation information), filters were maximised to encapsulate as much information as possible. These had to be converted to 2D filters, which were created by multiplying the filters in the x and y directions, resulting in anisotropic filters of elliptical shape. Four spatial frequencies from $0.1 - 0.4$ mm^{-1} were used for each combination of AC and DC filters to determine what SSOP result returned the lowest error with respect to conventional 3 phase SFDI. The higher the spatial frequency, the lower the cross talk between the AC and DC component and therefore they should be easier to separate. They found that, using the highest spatial frequency of 0.4 mm^{-1}, filters which gave the lowest optical property error relative to 3 phase SFDI were a rectangular bandpass filter for the DC image and a Blackman bandpass filter for the AC image. These filters also resulted in resultant optical property maps of much higher quality that previous SSOP methods, as the Gibbs effect was eliminated.

Deep learning approaches

Several deep learning approaches have been proposed to improve optical property map generation with SSOP. It is thought that any method which allow operation at $>$ 10 fps will allow real time acquisition of optical properties. *Chen et al.* propose a method to extract the optical properties from a single SSOP image using a generative adversarial network [60]. Generative Adversarial Network Prediction of Optical Properties (GANPOP) is a deep learning framework designed to predict the optical properties directly from a single image. The training set consists of both flat field and structured illumination images, as well as corresponding optical property maps. These images were used to develop a data-driven model that can output optical property maps of previously unknown samples of interest. Resultant

optical property maps were compared to that of conventional 3 phase SFDI and SSOP performed using the demodulation technique proposed by *Vervandier et al.*, which was not corrected for sample height variations or surface angles. *Chen et al.* showed that GANPOP is capable to estimate optical property values with errors of 4.5% and 1.5% for absorption and reduced scattering coefficients respectively, compared to conventional 3 phase SFDI measurements. This offers improvement on the measured reduced scattering coefficient, as the error of SSOP compared to conventional 3 phase SFDI measurements is 2.4% and 2.7% for the absorption and reduced scattering coefficient respectively. A main advantage of GANPOP is that fewer artefacts are present compared to SSOP as no filtering is performed on the images, and therefore the accuracy of the resultant optical property maps is increased. In imaging human gastrointestinal samples, GANPOP estimates optical properties with 58% higher accuracy than SSOP. GANPOP also offers a reduced image processing speed over SSOP of 0.04 s, as the need for a time consuming LUT is no longer required. Therefore, GANPOP has paved the way for SFDI to be used in real time, advantageous in clinical environments.

Aguénounon et al. propose the use of a GPU to accelerate a novel deep learning network at the filtering stage in SSOP, to enable the capability to produce profile corrected optical property maps of non-flat samples in real time [61]. The mean absolute error was calculated in comparison to conventional 3 phase SFDI, and the SSOP deep learning method showed reduced error compared to that of conventional SSOP filtering. For recovering the 3D profile of a non-flat sample, SSOP has an error of 9.8% while SSOP with deep learning gave a slightly lower error of 9.5%. For maps of profile corrected absorption, conventional SSOP has an error of 8.2% while SSOP with deep learning has a reduced error of 7.7%. Finally for the measured reduced scattering coefficient, conventional SSOP has an error of 9.3% while SSOP with deep learning has an error of 7.5%. It has to be noted that significant improvement was noticed in image reconstruction in SSOP with deep learning, particularly at object-background interfaces. However, the computational time for SSOP with deep learning was still longer than that of conventional SSOP with a time of 0.018 s for the deep learning approach compared to 0.001 s for the conventional SSOP approach. However, this processing time of 0.018 s is shorter than that presented by *Chen et al.* above of 0.04 s and has the added benefit of the resultant maps being surface profile corrected.

Zhao et al. have shown promise to reduce computational time using a deep neural network to develop an ultrafast optical property LUT [62]. Values for diffuse reflectance at five different spatial frequencies are input into the model, which then outputs values for μ_a and μ_s' simultaneously. This deep neural network algorithm outperformed the generic iterative method both in optical property determination accuracy and least computational time. The mean error in absorption and reduced scattering coefficients using the generic iterative method is 0.36% and 0.25% respectively, which reduces to 0.025% and 0.14% for the deep neural network model. For 100×100 data points, the computational time required to determine optical properties from diffuse reflectance values reduced from 674 s to 0.005 s when using the deep neural network model. Similar results were seen by *Panigrahi et al.* using a random forest regressor method [63]. Over a 1 megapixel image, the absorption and reduced scattering coefficients were recovered with errors of 0.6% and 0.1% respectively in 0.45 s.

Looking at the available data on expected optical properties in the gastrointestinal tract from *Sweer et al.*, which will be discussed in Sect 1.3.4, the lowest standard error (at 660 nm) in absorption coefficient is between healthy oesophageal tissue and Barrett's Oesophagus which is 24%, and the lowest standard error in reduced scattering coefficient is between healthy tissue and squamous cell carcinoma, which is 16%. These errors reduce to 2% and 15% for absorption and reduced scattering coefficients respectively when the wavelength reduces to 635 nm. Therefore, a proposed system (operating at 660 nm) would require a minimum absorption error of 24% and a reduced scattering coefficient error of 16%, while a system operating at 635 nm would require minimum absorption error of 2% and reduced scattering coefficient error of 15%. As all above methods are $< 24\%$ in absorption coefficient determination and $< 16\%$ in reduced scattering coefficient determination, they would be compatible with gastrointestinal imaging of optical properties at 635 nm. The above models by *Chen et al.* and *Aguénounon et al.* would not be capable to successfully differentiate between healthy oesophageal tissue and Barrett's Oesophagus at 660 nm, however the method proposed by *Zhao et al.* should be capable to do so as the mean error in absorption coefficient is $< 2\%$. As stated above, operation at > 10 fps will allow real time acquisition of optical properties, and thus the processing times discussed above are all compatible.

Coherent spatial frequency domain imaging

Laser speckle imaging (LSI) is the imaging of a random speckle interference pattern from a coherent laser source to measure liquid flow within a sample of interest [64]. The principle behind LSI is that for the same imaging geometry and imaging sample, the integral of the power spectral density (PSD) should be constant for any laser speckle pattern projected onto the sample. Therefore, if the sample of interest is changed, i.e. red blood cells move with blood flow, this movement will cause a blur in the speckle pattern. From this information, one can calculate the speckle flow index (SFI):

$$\mathrm{SFI} = \frac{1}{2TK^2} \tag{1.30}$$

where T is the integration time of the camera capturing the image and K is the speckle contrast defined by:

$$K = \frac{\sigma}{< I >} \tag{1.31}$$

where σ is the standard deviation across a selected region on the image of interest and $< I >$ is the mean intensity in this region. To calculate the velocity of flow and the concentration of, say, red blood cells within the flow, the velocity distribution must be known. This is typically a Gaussian velocity distribution to describe ordered flow, typical within a clinical setting. LSI is advantageous as it allows non-invasive detection of blood flow, which can indicate if a body part is not receiving enough blood. It has been used to image cerebral blood flow [65], blood perfusion in the liver [66] and blood flow in the optical nerve [67].

SSOP has been combined with LSI in a term coined coherent spatial frequency domain imaging (cSFDI), which is basically LSI performed in the spatial frequency domain to extract the absorption coefficient, reduced scattering coefficient, and SFI from a sample using a single image of coherent spatially modulated light [68]. The process for this is outlined in Fig 1.9 (a & b). Using coherent light from a 120 mW

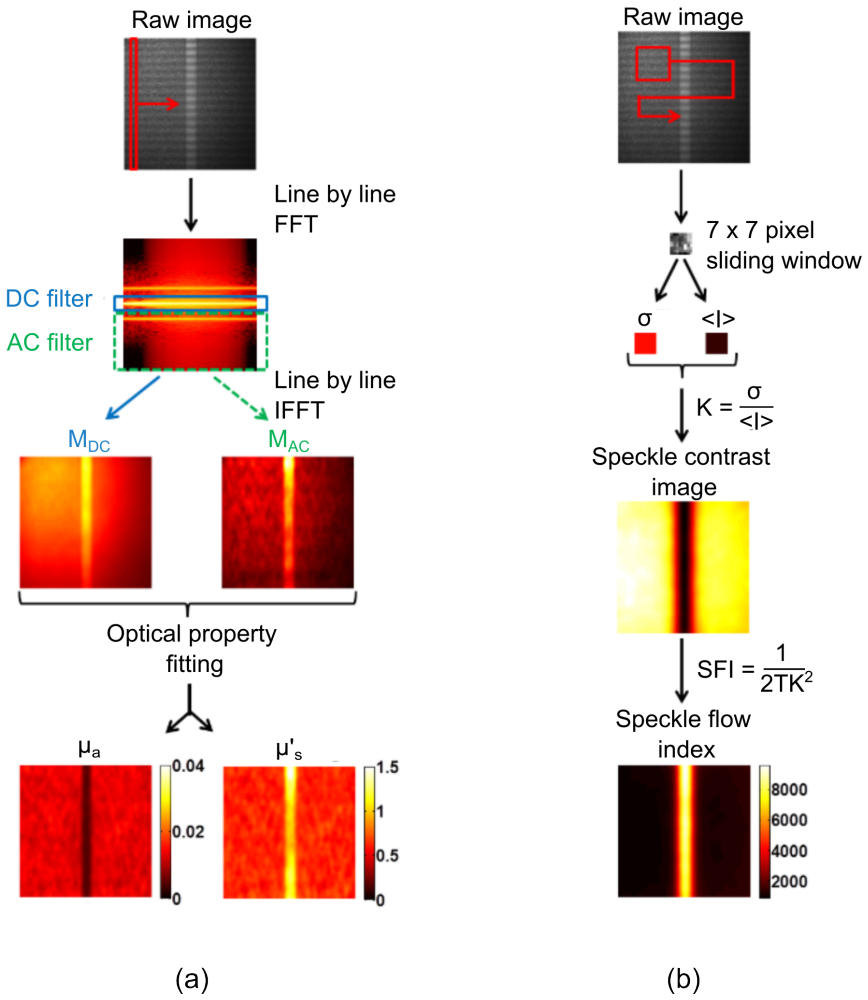

Figure 1.9: Workflow for determining both optical properties and speckle flow index from a single image (a) line by line SSOP to obtain absorption and reduced scattering and (b) LSI performed on the same raw image used to obtain optical properties where the standard deviation σ and mean intensity $< I >$ of a sliding window is determined to infer the speckle contrast, K. From this, with knowledge of integration time T of the camera used, the SFI is determined. Adapted from [68].

660 nm laser diode which was condensed onto a static spatial frequency pattern, homogeneous phantoms were imaged using cSFDI and conventional 3 phase SFDI. cSFDI was performed using the line by line SSOP demodulation method described by *Vervandier et. al.* The average difference in the measured absorption coefficient between cSFDI and 3 phase SFDI was 1.2% and the average difference in the measured reduced scattering coefficient was 0.59%, showing high agreement between the two methods. The SFI is calculated from the same raw image used for the optical property calculation. Analogous to conventional LSI, the standard deviation and mean intensity across the image is calculated using a sliding window filter, and the SFI is calculated using Eqn 1.30. The sensitivity of changes to flow in cSFDI was compared to that of conventional LSI by imaging a phantom with a flow channel with a planar DC image instead of the sinusoidal pattern for cSFDI. *Ghijsen et al.* found that cSFDI has comparable sensitivity to conventional LSI. Therefore, this technique can be used to accurately extract three optical parameters from a single

image, allowing for the possibility to carry out *in-vivo* physiological measurements by incorporating additional wavelengths for the addition of chromophore information [68].

Speckle illumination spatial frequency domain imaging

It has been shown by *Chen et al.* that the random speckle illumination produced from the interference of a coherent laser diode can be used to sample the modulation transfer function of a sample of interest at known spatial frequencies, enabling the successful extraction of sample optical properties, a technique termed speckle illumination spatial frequency domain imaging (si-SFDI) [52]. The laser diode is focused onto a rotating diffuser which is mounted on a stepper motor. The stepper motor randomly rotates the diffuser such that random speckle patterns may be projected. Light leaving the diffuser then passes through a diverging lens to spread the light to match the imaging vergence, such that the projected pattern is spread across the entire field of view of the detector. To obtain diffuse reflectance values, the mean aurocorrelation function is calculated on a sliding window for N speckle images. A fast Fourier transform is taken of the resulting mean image to produce a local power spectral density image, from which the diffuse reflectance values may be obtained after calibration. As with conventional SFDI, a LUT of chosen light propagation model is then used to estimate a sample's optical properties.

Multi spectral spatial frequency domain imaging

Imaging optical properties at more than one wavelength is advantageous as it allows the extraction of functional tissue information, as discussed in Sect 1.2.1. A method proposed to increase the speed of SFDI measurements at multiple wavelengths is proposed by *Applegate et al.*, who developed a high speed SFDI system using temporally modulated light [69]. Following a method proposed by *Domingue et al.* to modulate the different illumination wavelengths at different temporal frequencies [70], they are capable to return optical property maps at three different wavelengths in 2.5 s. This returns average errors of 13% and 8% in absorption and reduced scattering respectively, compared to a commercial SFDI system. Light from three high powered LEDs of wavelengths 519, 652, and 740 nm was modulated using a pulse-width modulation sequence controlled by a microcontroller and sent through a sinusoidal pattern printed on transparency film to produce illumination patterns. A video is recorded of a sequence of images on the sample of interest, which is then demodulated by determining the strength of the reflected signal at each modulation frequency. This results in a single spatially modulated image which is processed via SSOP. This method is advantageous to single wavelength SSOP as is it only sensitive to light modulated at specific frequencies and therefore automatically rejects ambient light, which is not considered in conventional SSOP and is an advantage for translation into a clinical setting.

Torabzadeh et al. propose a method to image tissue optical properties at multiple wavelengths in the spatial frequency domain, in a technique termed hyperspectral spatial frequency domain imaging (hs-SFDI) [71]. With 1000 spectral bins in the wavelength range $580 - 950$ nm, they successfully demonstrated optical property retrieval of optical phantoms with an accuracy of 6.7% and 12.3% for absorption and reduced scattering respectively, compared to spectrophotometer values. They also

imaged samples of beef tissue, and were successfully capable to extract information of five chromophores: Hb, HbO2, methemoglobin (a form of Hb that can carry oxygen but is not capable to dissipate it into tissues successfully [72]), fat and water.

Multi frequency spatial frequency domain imaging

Multi-frequency acquisitions have been shown to greatly improve accuracy of optical property measurements. *Pera et al.* used 13 different spatial frequencies from $0-0.5$ mm^{-1} and found, compared to using just two spatial frequencies ($0, 0.1$ mm^{-1}), that the uncertainty in absorption measurements reduced from 8% to 6% and in scattering measurements reduced from 4% to 2% respectively [73]. These results are the average from measurements taken on four phantoms of optical properties ([μ_a, μ_s'] mm^{-1}): $[0.005, 0.73]$, $[0.005, 1.89]$, $[0.035, 0.73]$, and $[0.035, 1.89]$. While using multiple spatial frequencies increases accuracy, it suffers from long computational times, particularly in the inverse-solving of optical property determination.

Hayakawa et al. show, through Monte Carlo simulations and experimental results on phantoms, that the use of different spatial frequencies can penetrate to different depths within a sample of interest, which can be used for optical depth sampling [74].

McClatchy et al. introduce the use of high frequency illumination to image tissue microstructure in a wide field of view (without the requirement for raster scanning), in a technique termed sub-diffuse spatial frequency domain imaging (sd-SFDI) [75]. This technique enables the detection of microscopic level morphological differences in tissue types, on the scale of several centimetres.

Fringe profilometry

In addition to measuring optical properties, measuring shape has been shown to be an indicator of cancer staging within the colon [76]. Exploiting the fringe profilometry approach to reconstruct 3D shape via Fourier transform profilometry (FTP) is advantageous. Non-contact 3D profilometry is widely used in a variety of sectors, from manufacturing [77, 78] to medicine [79]. *Su et al.* produced a review on different profilometry methods, with the conclusion that FTP is advantageous over other techniques due to its requirement of a single projection pattern (and a single reference projection) with high precision, making it suitable for real-time applications [80]. *Takeda et al.* first introduced FTP, which is a method of processing an image of a projected sinusoidal or Ronchi pattern on a 3D object of interest in the spatial frequency domain to determine the morphology or height of the object [81]. The method for height determination is derived in Appendix D, where the equation for obtaining height is given by:

$$h(x, y) = \frac{\Delta\phi(x, y)l}{\Delta\phi(x, y) - 2\pi df_0} \tag{1.32}$$

where $\Delta\phi$ is the change in phase, l is the distance from the camera to the reference plane, d is the distance between camera and projector, and f_0 is the projected spatial frequency.

The above method is constrained by implicit knowledge of system geometry to calculate height and presence of a small angle between projector and camera as to not cause overlapping in the spatial frequency domain, limiting the maximum height

variation capable of detection. *Guo et al.* propose an improvement to the above technique to overcome these measurement constraints, and expand the possible detectable height variation by ~ 3 times the conventional method [82]. They propose the use of a quasi-sine projection (instead of the previously used Ronchi projection) which reduces frequency components that are higher than the fundamental frequency. They also propose a π phase shifting technique which removes the zeroth component in the frequency domain. Implementing a quasi-sine projection involves moving a Ronchi grating along the projection axis until it is out of focus. This results in the edges of the Ronchi grating image being smoothed and expanded, which approaches a sinusoidal distribution. A quasi-sine projection is used instead of a Ronchi pattern because it expands the distance between peaks in the spatial frequency domain, leaving only the zero component and the fundamental component in the spatial frequency domain. This allows for easier and more accurate phase extraction without overlapping fringes.

Li et al. take this a further step of just requiring a single, grayscale fringe pattern to extract height information [83]. After phase unwrapping from the single shot FTP method discussed above, they construct an artificial absolute phase map based on the geometric constraints of a digital fringe projection system. The final unwrapped absolute phase map is extracted pixel by pixel. Advantages of this method are a single image reduces acquisition time so leads the way to real time acquisition and 3D shape reconstruction which is desired. However, this method assumes that all points imaged do not cause more than a 2π phase difference from the reference plane of the object. In cases where a $> 2\pi$ phase jump occurs from one pixel to the next, an incorrect unwrapped phase could be produced.

Profile correction

Gioux et al. propose the use of FTP to correct for variation in surface profile measurements taken with SFDI [79]. By taking profilometry measurements of a sample as well as SFDI measurements, one can correct for surface profile variations in resultant optical property maps. As previously discussed, the sinusoidal pattern must be rotated by 90° for profilometry measurements such that it is orthogonal to the plane formed by the camera and projector optical axes and maximum sensitivity to surface variations on the sample is imaged. By knowing the measured phase of a reference phantom at various known heights, one can draw a relationship between phase and height and therefore can correct for discrepancies in optical property measurements across a height varying surface. Applying these corrections reduced absorption coefficient error from 10% to $< 1\%$ and the reduced scattering coefficient error from $\sim$ 10% to $< 1\%$ also. *Aguenounon et al.* took this a step further to correct for profile variations with deep learning techniques, showing a variation of $< 10\%$ in both profilometry and resulting optical property measurements [61].

1.3.3 Pre-existing spatial frequency domain imaging system designs

A range of commercial and research SFDI systems exist. The main differences between various systems are source of illumination, method of modulating the illumination, and detector of modulated illumination, which correspond to vast differences

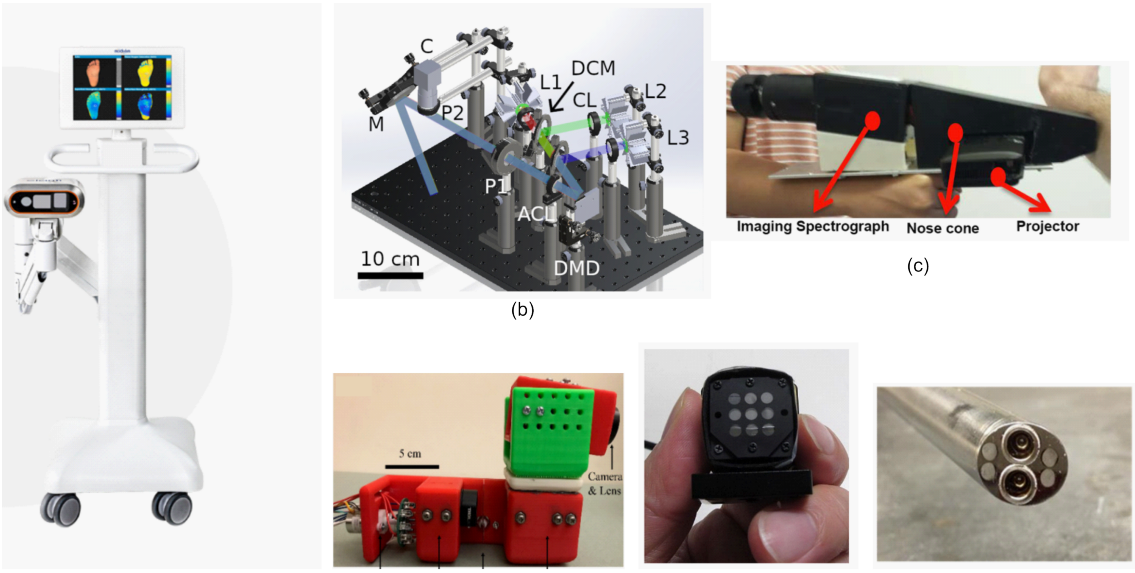

Figure 1.10: Example of existing commercial and research SFDI systems (a) commercial *Modulim* system consisting of imaging head attached to display screen [84] (b) bench top system with three LEDs of different wavelengths (L1 - L3), collimating lens (CL), dichroic mirror (DCM), achromatic lens (ACL), linear polarisers (P1 and P2), mirror (M), camera (C) and digital micromirror device (DMD) [87] (c) handheld probe showing imaging head [88] (d) 3D printed handheld probe [89] (e) multispectral camera imaging head [90] (f) distal end of endoscopic imaging probe using SSOP with two channels for pattern illumination and detection [91].

in system size and cost.

Modulim is the leading developer of commercial SFDI systems, producing large imaging systems with the primary goal of imaging tissue oxygenation and perfusion of limbs to give clinical insight to diabetes, shown in Fig 1.10 (a) [84]. They also look at imaging tissue oxygenation during reconstructive surgery and burn depths. This multi-wavelength system uses a laser diode source to project discrete wavelengths in the range $670 - 980$ nm. A digital micromirror device (DMD) projects the sinusoidal pattern at shifted phases of the incident illumination source. DMDs consist of an array of micromirrors that can be individually accessed and tilted to change the direction of the illumination pattern. Two monochrome cameras capture images at two different wavelengths simultaneously, which is what enables oxygenation imaging. Cross polarisers are placed in front of the light source and cameras. Systems from *Modulim* (previously *Modulated Imaging Inc.*) have been used in many clinical studies. A system analogous to the current one described above has been used to image oxygenation during breast reconstructive surgery following mastectomy, where the DMD has been replaced with a spatial light modulator (SLM) [53]. An SLM is limited by its lower refresh rate than a DMD, making it operationally slower. However, using an SLM it is possible for grey scale and phase modulation, while a DMD only allows binary amplitude modulation [85]. Another system was used to image burn depth in porcine models and showed the capability of SFDI to successfully discern between superficial, partial and full burns [86].

OpenSFDI is an open-source resource consisting of instructions to construct a

bench top SFDI system and how to implement the accompanying image processing software [87]. The system, shown in Fig 1.10 (b), of which a full materials list is available [92], consists of three light emitting diodes (LEDs) in the NIR with centre wavelengths at 660, 730 and 850 nm. These wavelengths were chosen to enable contrast imaging of oxyhaemoglobin and deoxyhaemoglobin, where previous work has shown 670 nm and 850 nm are an optimal pair for imaging these properties [34]. A DMD was used to modulate the illumination. A 1280×1024 pixel monochrome CMOS camera was chosen as the detector. The total cost of the proposed system is \$4717 $\approx$ £3852. The goal of this open-source platform is to increase the accessibility and therefore the use of SFDI systems in research settings.

Saager et al. propose a portable spatial frequency domain spectroscopy (SFDS) device, shown in Fig 1.10 (c) that showed 1% agreement with their bench top system across a range of spatial frequencies of $0 - 0.35$ mm^{-1} [88]. SFDS is a quantitative spectroscopy technique which uses structured illumination patterns across the visible and NIR wavelength regions to extract varying absorption and scattering information across the whole wavelength range. The technique is advantageous in skin measurements as it can image at various depths for varying spatial frequencies. Therefore, it overcomes the issue that melanin is primarily present in the epidermis while blood content is present in the dermis, resulting in typical imaging techniques returning inaccurate, bulk optical properties as a representation of both layers [93]. The system consists of an external 150 W Quartz Tungsten Halogen light source on a mobile cart of dimensions $45 \times 56 \times 76$ cm which is connected to the handheld portable probe via 2 m long liquid light guide. The handheld probe in Fig 1.10 (c) is sat on a base plate of dimensions $6.4 \times 30 \times 0.3$ cm. A liquid light guide is analogous to a fiber bundle in that it transmits lights and is flexible, however it has a liquid core instead of glass. This light is passed to an off the shelf DMD which is the order of 50 times less expensive than a research grade DMD. A CMOS sensor is used as the detector. This device has the advantages of being cost effective, highly portable and easily movable in a clinical setting. However, it has a total acquisition time of $15 - 30$ s, which limits the capability to use the system in real time. Reducing this acquisition time by reducing the number of projected spatial frequencies, reducing the number of wavelengths used, or exploiting SSOP may excel the clinical translation of this device.

Erfanzadeh et al. propose a 3D printed, compact SFDI system (Fig 1.10 (d)) aiming to reduce cost of previously described systems [89]. The illumination consists of nine LEDs with peak emission wavelengths between $660 - 950$ nm on a rotational stepper motor, which when moved changes the LED acting as the illumination source. This light then passes through a sinusoidal pattern printed on transparency paper attached to a linear stepper motor which can be moved to shift the projected phase. A CMOS camera is used as the detector. All components are encased in a 3D printed probe, where the illumination section of the probe has dimensions $17 \times 6 \times 6$ cm and the detection section is held in place in a cube of dimensions $8 \times 5 \times 5$ cm. The total cost of the probe is \$413 $\approx$ £330, the most cost effective device to date. The device was used to image both tissue phantoms and resected ovarian tissue from patients undergoing oophorectomy (surgery to remove one of both ovaries). Benign ovarian tissue and ovarian tissue with a large water filled cyst were imaged. Through use of two wavelengths (660 and 950 nm), the water-collagen content of the tissue was obtained and therefore the capability to

differentiate between the two tissue types. From the tissue phantom measurements, the absolute average error across all wavelengths for reconstructed absorption and reduced scattering coefficients are 6.7% and 4.7% respectively. Samples were imaged < 1 hr after resection and then sent to pathology. The disadvantage of the device is that total acquisition time is ~ 2 mins, which for a handheld device can be challenging as hand/sample movements during this time will result in resultant image artefacts. The group propose to increase motor speed or to change the light source to a broadband source to overcome this issue, however the advantage of keeping the LEDs is keeping the device at a low cost.

Kennedy et al. propose a compact, multispectral camera enabling simultaneous image acquisition at multiple wavelengths, shown in Fig 1.10 (e) [90]. This is to be used instead of the detector in the *Modulim* system previously described [84]. This device is designed to increase image acquisition speed, decrease system cost, and improve portability of previous system. To do this, a commercial CMOS sensor is separated into different regions by placing five 6 mm focal length lenses in different regions and then placing bandpass filters with transmission bands centered at $546 - 966$ nm in front of the lenses. The resultant image size for each section was 630×630 pixels, corresponding to a field of view of 165×165 mm. The dimensions of the multispectral camera are $26 \times 26 \times 24$ mm. By testing on phantoms, the compact imager showed absorption and reduced scattering coefficient errors of 3% and 6% respectively, compared to the commercial *Modulim* system.

Angelo et al. developed an endoscopic probe for improving quantitative surgical guidance with SFDI, shown in Fig 1.10 (f) [91]. The 660 nm laser light source is expanded and collimated onto a transparency film with a sinusoidal pattern of specific phase and spatial frequency via a series of lenses of focal lengths 35 mm. This light is then collimated again and passed through a polariser before being passed through the projection channel of the endoscope. The collected light passes through a polariser, an objective lens and is then imaged onto a CCD. The field of view of detection is limited to that of the collection fiber. All optics of the instrument are located outside the working end of the probe. This device has an 45° angled end, which results in non-uniform spatial frequency with varying distance from probe to sample. The probe is a rigid, Schölly dual-imaging scope from Intuitive Surgical [94]. The specific dimensions and cost of the probe are not stated.

To overcome the issue of limited field of view when miniaturising SFDI systems, groups have developed compressed sensing single pixel spatial frequency domain imaging (cs-SFDI) [95–97]. *Torabzadeh et al.* have shown successful image capture and recovery of absorption and reduced scattering coefficients with errors of just 7.6% and 4.3% respectively to a conventional camera based SFDI system. cs-SFDI has the advantage of exploiting the high bandwidth associated with single pixel detectors and returns a fixed frame rate, compatible for simultaneous multispectral imaging.

Streeter et al. propose a laser line scanning method to achieve high contrast, high dynamic range, sub-diffuse imaging over a wide field of view [98]. Typical SFDI images suffer from low dynamic range and optical properties are not discernible at spatial frequencies > 1.5 mm^{-1}. Active line scanning combined with a spatial frequency projection pattern can be used for localised capture of high-contrast, high dynamic range images of surface layer scatter micro structures over a wide field of view. The proposed system orientates a laser line source perpendicular to the

direction in which the line source will be translated.

Visentini-Scarzanella et. al have developed a structured light illumination probe to image polyp size [99]. A micro patterned chip of a grid pattern of known size is set on the tip of a plastic optical fiber of diamter 2.8 mm. A 532 nm laser is sent through the optical fiber. This optical fiber was then attached externally to a conventional endoscope. Novice endoscopists carried out a study on 392 ex-vivo porcine swine stomach polyps, where accuracy, time and user satisfaction were compared for this new probe against visual inspection, biopsy forceps (of which the size if known), and a ruled snare. They found that this proposed probe can reduce the median estimation error error from 2.2 mm to 1.5 mm compared to visual assessment, while the probe was comparable to results using biopsy forceps as a reference or a ruled snare. The probe took 54.75 s per polyp to generate a result, which is quicker than using a snare (68.5 s), but significantly slower than visual inspection (20.8 s). The user satisfaction was measured on a range of $0 - 10$, with the proposed probe returning the highest mean satisfaction of 7.92, closely followed by visually inspection (7.01), and use of biopsy forceps (7.82). Average user satisfaction for using a ruled snare was 4.42. This probe shows promise of imaging polyp size with structured illumination *in-vivo* during gastrointestinal procedures for accurate polyp size detection.

None of the above described systems have the capability to be used for *in-vivo* gastrointestinal tract imaging due to their large size, rigidity, or non-compatible illumination patterns. Many systems are too complex to miniaturise successfully due to the need for specific components, such as DMDs.

1.3.4 Clinical applications

SFDI has shown applicability to a wide variety of sectors, ranging from healthcare [50] to agriculture [100]. Here the successful application of SFDI to different medical applications in the healthcare field is discussed. SFDI has many medical applications such as imaging blood perfusion during breast reconstructive surgery [53], imaging burn depth [86], imaging bowel ischaemia [101], imaging dental caries [102], and detecting indicators of cancer [91].

Sweer et al. have shown the successful imaging of resected human oesophageal tissue with SFDI [47]. Eight resected tissues were imaged at seven wavelengths from $421-851$ nm using a commercially available system from *Modulim*, described in Sect 1.3.3. The imaging process was as follows: samples were taken from patients who were scheduled to undergo an oesophagectomy as oesophageal adenomcarcinoma was determined to be present. Resected samples were opened, pinned flat to a substrate, and imaged with the SFDI system. The samples were then sent to a pathologist for characterisation. The pathologist annotated the tissue samples and they were compared to the SFDI results. A region of healthy oesophageal tissue was also identified and imaged from each of the eight samples. *Sweer et al.* found that, across all wavelengths, the reduced scattering coefficient of healthy oesophageal tissue is greater than that of invasive SCC and BO with mild chronic inflammation (see Table 1.2). Slight histological changes in tissue structure may be the reason for these scattering differences. They also found that the absorption coefficient of healthy oesophageal tissue is less than that of invasive SCC across all wavelengths, while comparable to BO with mild chronic inflammation (see Table 1.2). It was found that the sen-

Tissue type	471 nm		635 nm		851 nm	
	μ_a mm^{-1}	μ_s' mm^{-1}	μ_a mm^{-1}	μ_s' mm^{-1}	μ_a mm^{-1}	μ_s' mm^{-1}
Healthy tissue	0.21	1.18	0.058	0.75	0.016	0.58
SCC	0.32	0.77	0.120	0.64	0.029	0.46
BO	0.28	0.53	0.057	0.51	0.011	0.44

Table 1.2: Comparing optical properties of healthy oesophageal tissue, invasive squamous cell carcinoma and Barrett's oesophagus with mild chronic inflammation at three wavelengths. Adapted from [47] Fig 4.

sitivity of determining healthy tissue from squamous cell carcinoma at 659 nm is 99% and 95% for the absorption and reduced scattering coefficients respectively, which is in accordance with the American Society for Gastrointestinal Endoscopy guidelines, as discussed in Sect 1.2.2. The sensitivity of determining healthy tissue from Barrett's Oesophagus does not meet these requirements, with 70% sensitivity for differentiating absorption coefficients and 80% sensitivity for differentiating reduced scattering coefficients. The specificity of determining absorption coefficient between healthy tissue and squamous cell carcinoma meets the guidelines at 100%, but is only 73% for determining reduced scattering coefficient. The specificity for determining healthy tissue from Barrett's Oesophagus is 31% for absorption coefficient measurements and 87% for reduced scattering coefficient measurements. *Sweer et al.*'s work is invaluable in determining previously unknown optical properties of different types of healthy and diseased tissue found in the oesophagus, however it suffers from several limitations. Firstly, all SFDI data was taken 30 minutes after resection. This may result in a drop in measured absorption coefficients across all tissue types due to a drop in haemoglobin content, and the oxygenation of the tissue cannot be measured. Also, all tissues imaged had previously undergone some form of treatment e.g. radiation or chemotherapy, which may alter the optical properties of tissue. A study is needed to image *in-vivo*, both diseased and healthy oesphageal tissue (as a control) to determine more accurate optical properties.

Nandy et al. imaged resected human colon tissue using an SFDI system consisting of a mini projector and a CCD camera at three wavelengths of 460, 530 and 630 nm [103]. Fifteen tissue regions from nine patients undergoing either a colectomey or hemicolectomy were imaged. A hemicolectomy is the removal of either the right or left part of the colon, while a colectomy is the removal of the entire colon. Resected tissue was sectioned longitudinally, rinsed with sterile water and pinned to a backing such that the mucosal surface could be imaged with the system. The samples were then sent to histology for characterisation. *Nandy et al.* found that generally the absorption coefficient of healthy colon tissue was less than malignant colon tissue, and the reduced scattering coefficient of healthy colon tissue was higher than malignant colon tissue. The higher absorption coefficient seen in malignant tissue is thought to be due to tumour angiogenesis, where the tumour forms it's own new blood vessels. These results match that seen by *Sweer et al.* in the oesophagus, comparing healthy oesophageal tissue to the malignant invasive squamous cell carcinoma. However, this study of colon optical properties suffers from the same limitations as *Sweer et al.'s* oesophageal tissue optical property study as the imaged tissue was resected and therefore one expects a variation in *in-vivo* optical properties.

Rodríguez-Luna et. al have successfully used multi-spectral SSOP in a pre-clinical study to quantify bowel ischaemia [101]. Bowel ischaemia occurs when the arteries harden and narrow, or a blood clot presents in the arteries, reducing the blood flow to the region. Multi-wavelength SSOP allows for the characterisation of tissue oxygenation, a useful biomarker of tissue viability, by computing the ratio of oxygenated to total haemoglobin in real time. SSOP with GPU accelerated deep learning was compared to normalised capillary lactate, which acted as a validated perfusion biomarker and was measured via a portable analyser, in the small intestines of 6 swine. Two wavelengths, 665 nm and 860 nm, were used for the multi spectral measurements to calculate the oxygen saturation in the tissue, as discussed in Sect 1.2.1. These wavelengths were chosen as *Mazhar et al.* determined the optimum dual wavelength pair for hemodynamic tissue measurements in SFDI to be 670 and 850 nm [34].

Bounds et al. have shown, for the first time, capability to detect early stage dental caries in dental tissue with near-infrared SFDI, using cost-effective LEDs and detectors [102]. Dental caries are the demineralisation of tooth structure resulting from bacteria build up in the tooth. Early stage dental caries are difficult to diagnose and not typically visible on x-ray. Diagnosis of dental caries is normally at their late stage where the treatment option is a necessary filling, which can deteriorate over time. However, if caries could be detected in an earlier stage, the mineral loss may be able to be reversed, removing the need for a filling. Dental caries disrupt the optical scattering of local enamel and therefore have a higher optical scattering. However, caries typically present as a white spot and are not visible under white light. Absorption at NIR wavelengths is negligible and therefore omitted. SFDI shows the capability to detect cavities or demineralisation which are not present through visible light through just the reduced scattering coefficient map.

LSI has shown its potential in imaging burn depth in comparison with SFDI [104, 105]. *Ponticorvo et al.* carried out a controlled study of imaging burn depth on a porcine model, and found that LSI and SFDI offered diagnostic accuracies of 75% and 85% respectively, compared to a histology analysis. *Milstein et al.* have shown the capability of the technique in detecting ischemic areas on gastric tube reconstructions following oesophagectomy [106].

There is a need for a system to image *in-vivo* optical properties using SFDI.

1.4 Clinical state of the art endoscopy in use

Waterhouse et al. has produced a review on endoscopic imaging devices, specifically for surveillance of BO [107], and *Tang et al.* has produced a review on advances in optical gastrointestinal endoscopy [108], which will both be discussed here.

1.4.1 White light imaging

High definition white light endoscopy accompanied with random biopsy is the primary diagnosis of neoplasia, the uncontrolled growth of abnormal cells, in patients with BO [113]. Conventional, forward facing, endoscopes use white light imaging as their primary imaging modality, such as the *EVIS X1* from *Olympus*, a leading brand in endoscopes, shown in Fig 1.11 (a). These endoscopes are expensive, reusable through decontamination protocols, and require to be used by trained clinicians in a

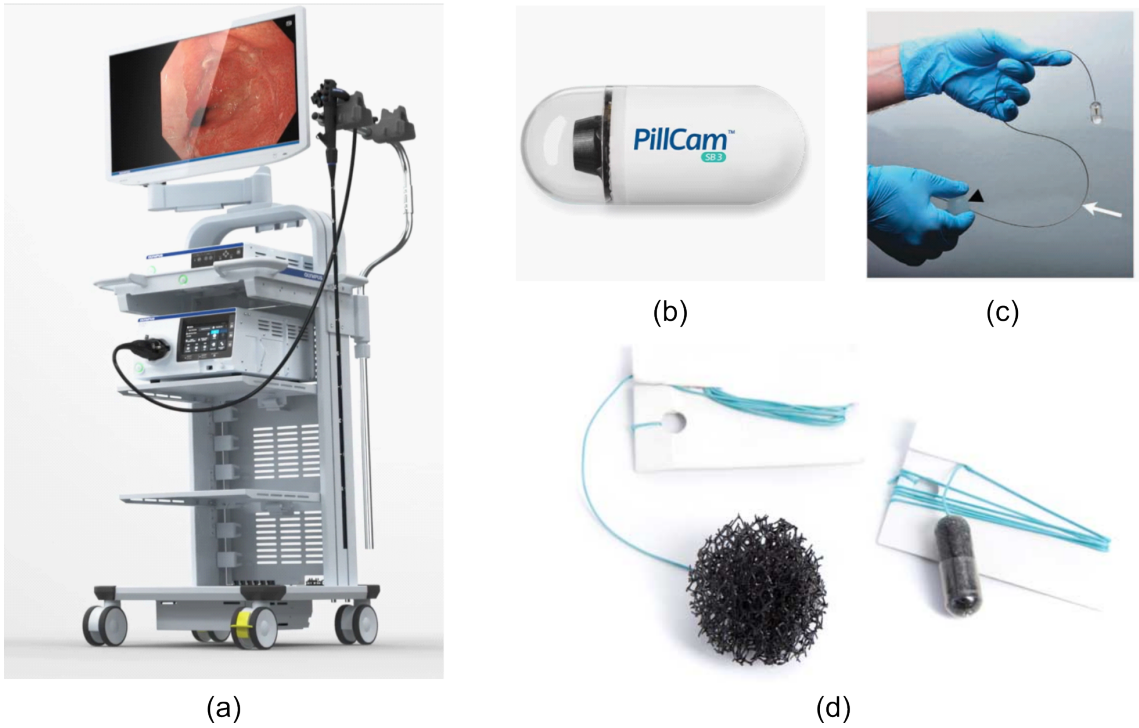

Figure 1.11: Current endoscopic systems in use (a) Typical endoscope *Olympus EVIS X1* [109] for upper and lower gastrointestinal imaging (b) capsule endoscope *Medtronic PillCam SB 3* [110] for upper and lower gastrointestinal imaging (c) tethered capsule endoscope [111] for upper gastrointestinal imaging with OCT (d) tethered capsule cytosponge [112] for upper gastrointestinal histology.

controlled, hospital setting. Companies such as *IQ Endoscopes* are working toward a cost-effective, disposable endoscope which eliminates the time needed for decontamination protocols, and therefore reduces time between procedures as a low-cost, working toward recyclable, new endoscope can be used each time [114]. These endoscopes would be advantageous in a screening environment as the lack of expensive, harmful chemicals required for decontamination would be eliminated, and capacity of patients seen could be increased. The transportability of the device would also see it's use outside the hospital setting, in a point-of-care environment. Standard definition endoscopes produce images with a pixel resolution of $100,000 - 300,000$ pixels, where typical high definition endoscopes produce images with a pixel resolution of up to $1,000,000$ pixels [115].

Capsule endoscopes are advantageous over typical endoscopes as they do not require the patient to be sedated or to be present in a hospital as the capsule passes through the GI tract. *Medtronic*'s latest capsule is the *PillCam SB 3* (Fig 1.11 (b)), with a framerate of $2 - 6$ s depending on the patient's movements, and high image quality allowing great diagnostic confidence [110]. Successful comparison has been shown in the use of capsules to detect oesophageal varices (enlarged veins) with 85.8% agreement to conventional endoscopy [116].

Chromoendoscopy involves the addition of an exogenous dye onto the patients tissue to aid in improved contrast visualisation of neoplastic tissue with white light. The addition of exogenous dyes increases toxicology risk to the patient [117], are difficult to disperse uniformly within the GI tract [118], and increases the procedure

time [119]. There is a desire for using endogenous contrast agents instead, performing at the same sensitivity. This is possible with imaging in modalities other than white light.

1.4.2 Narrow-band imaging

Narrow-band imaging (NBI) is an optical method to enhance mucosal tissue structures and microvascular patterns through the use of wavelength filters to modify white light endoscopy [120]. Two filters are used: a blue filter ($400-430$ nm) which highlights the capillaries in tissue mucosa due to the peak absorption of haemoglobin at 415 nm and a green filter ($525-555$ nm) which penetrates into the mucosa and returns a high clarity visual of the structural surface of the mucosa. These vascular and mucosal patterns are useful in predicting tissue type. The *Olympus* endoscope previously discussed and shown in Fig 1.11 (a) makes use of NBI. It combines texture and colour enhancement imaging from white light, AI techniques to characterise potential lesions within tissue, red dichromatic imaging (which is used to enhance the appearance of deep blood vessels), as well as NBI [109].

Blue laser imaging (BLI) endoscopy is a technique similar to NBI used, again, to improve contrast imaging within the GI tract. BLI uses two laser light sources: 410 nm and 450 nm to produce high resolution, bright images of the mucosa of the GI tract, of which certain cancer indicators are not typically visible with white light, such as vasculature or mucosa surface patterns [121]. The 410 nm laser produces a clear BLI image of surface micro structure and micro vasculature on the mucosa, while the 450 nm laser produces images of deep vasculature and structures deeper within the tissue. 450 nm also acts as an excitation wavelength on the tissue, resulting in fluorescent images. BLI is capable of detecting the boundary between BO and healthy tissue, as well detecting malignant lesions surrounded by intestinal metaplasia.

1.4.3 Autofluorescence imaging

Autofluorescence imaging (AFI) in an optical method that produces images of fluorescence from tissue generated from natural, endogenous fluorophores within the tissue [122]. When tissue is exposed to light of specific wavelengths, endogenous fluorophores within the tissue (such as collagen) are excited and emit fluorescent light at a wavelength longer that the incident wavelength. Different tissue types have different autofluorescent characteristics, and therefore will fluoresce differently, enabling differentiation between normal and neoplastic tissue. During AFI, tissue which appears different in colour to surrounding mucosa is defined as suspected neoplasia. The reason for different tissues fluorescing differently may be accounted for by several parameters. First is the increase in nucleus to cytoplasm ratio in neoplastic tissue, which decreases the autofluorescence as nuclei show no autofluorescence. Second, neoplastic tissue has less collagen than healthy tissue, and collagen is highly fluorescent. Third, angiogenesis associated with rapid growth increases the concentration of haemoglobin, which gets absorbed by autofluorescent light [123].

1.4.4 Optical coherence tomography

Optical coherence tomography (OCT) is a an non-invasive, cross sectional, micron resolution imaging technique [124]. It's premise is based on interferometry, where an infrared light is divided into two components: the first enters the tissue and gets scattered, and the second is reflected off a mirror. The two light beams produce an interference pattern, from which the echo time delay and amplitude can be obtained, giving enough information to produce an *A-scan*. Obtaining several *A-scan*s at different transverse spatial locations enables the capture of a 2D image [125]. Typical OCT systems are bulky, however work has been done towards their miniaturisation through use of optical fibers [126] and photonic integrated circuits [127]. OCT is advantageous as it delivers micron resolution, 2D information on tissue structure. However, it is not capable to return quantitative tissue optical properties.

NinePoint Medical have produced a commercial endoscopic OCT probe called *The NvisionVLE® Imaging System, with Real-time Targeting™*, which can produce high resolution (7 μm) cross-sectional images of tissue micro structure in real time, up to 3 mm deep [128]. It also has the capability to mark the tissue, such that regions of interest non-detectable by white light can be easily identified for biopsy and histological analysis.

1.4.5 Diffuse reflectance spectroscopy

Diffuse reflectance spectroscopy (DRS) is a simple technique for studying biological tissue, where light that is delivered to the tissue undergoes multiple scattering and absorption events, and the detected light contains quantitative information of the tissue [129, 130]. Analogous to SFDI, an analytical model for the diffusion approximation is needed, but in typical DRS situations this model is constrained by the geometry of the setup, where an optical fiber probe is used to collect the diffusely reflected light. The quantitative tissue information is then extracted by comparison of the collected data to a diffuse reflectance model. DRS can be thought of as a subset of SFDI for $f_x = 0$ mm^{-1}.

A comparative study of DRS and SFDI was carried out on optical phantoms, and it was found that DRS is inferior to SFDI for detecting fabricated tumour margins and in determining fabricated tumour depth [131]. DRS has been used in differentiating between dysplasia and metaplasia in BO *in-vivo* [132], and in determining tumour margins in the upper GI [133]. In imaging BO, wide-field illumination was provided by a halogen lamp, delivered through an endoscope with a fiber bundle placed down the endoscope instrument channel collecting the reflected signal. By analysis of the diffuse reflectance spectra at the wavelengths $485, 513, 598$ and 629 nm, *Douplik et al.* were able to provide statistically different differentiation between BO and dysplasia [132].

1.4.6 Tethered capsule endoscopy

Tethered capsule endoscopes hold the same advantage of capsule endoscopes that they do not require patient sedation, however they also allow the capability for optical chromoendoscopy, which is advantageous. A tethered capsule, example shown in Fig 1.11 (c) which uses OCT, is typically swallowed by a patient with a small amount of water, and the capsule is lowered to the stomach via peristalsis. The

capsule is then pulled back up through the oesophagus and it captures images of the tissue [134]. Several research tethered capsule endoscopes exist. *Liang et al.* have developed an OCT capsule endoscope [135, 136]. For the clinical requirement of imaging Barrett's oesophagus for which this probe was fabricated, it would require resolution approaching the scale of columnar epithelial cells to be comparable with histology. A micrometer enables fast rotary scanning and an actuator enables precision in longitudinal scanning. The device enables high resolution (30 μm transverse and 8 μm axial, comparable with the size of columnar epithelial cells), 2D scanning over a small field of view ($\sim$ 1 cm^2), with large field of views ($\sim$ 30 cm^2) obtained by proximally pulling and advancing the capsule as it scans. The probe is capable of imaging 10 cm of oesophageal tissue in 10 s. Results were obtained *in-vivo* in swine models, where cross sectional OCT images were obtained of the upper and lower GI tract. The sensitivity/specificity of the probe was not assessed in this study, however it is assumed a device would require $>$ 80% sensitivity and specificity to be comparable to other methods used to detect Barrett's oesophagus [136]. *Sharma et al.* have developed a low-cost capsule endoscope to be used with a smartphone in low-resource settings [137]. This device makes use of multiple imaging modalities; white light imaging, NBI, and AFI.

1.4.7 Cytosponge

A tethered capsule consisting of a cytosponge, example shown in Fig 1.11 (d), has shown promise is surveillance of BO [138]. A cytosponge is encapsulated in the capsule which disintegrates when it comes into contact with the acid within the stomach, allowing the sponge to expand. As the capsule is pulled back up through the oesophagus, the sponge scrapes the wall of the oesophagus and collects cells, which can then be sent for histological analysis after sponge removal. Combining a cytosponge with a tethered capsule that can perform one of the optical chromoendoscopy techniques described above would return two diagnosis results, which could both be compared to improve accuracy of patient diagnosis.

1.4.8 Unmet clinical need

The imaging methods described above return qualitative variation in tissue, allowing for trained, experienced gastroenterologists to discern between healthy and malignant tissue. To employ widespread endoscopic screening, there is a requirement for the procedure to be carried out by healthcare workers who are not necessarily qualified gastroenterologists. Therefore, there is a need for an imaging technique to return *quantitative* tissue information, such that determining tissue staging is not opinion or experience based, but deterministic.

Therefore, there is a need for a system that can be deployed endoscopically to carry out SFDI on tissue. There is a lack on *in-vivo* gastrointestinal tissue optical property information. Past work by *Holmer et al.* and *Sweer et al.*, discussed in Sect 1.2.2, have imaged gastrointestinal tissue after it has been resected and (in some cases) treatment has been applied, making the results not accurate for comparing to *in-vivo* optical properties [36, 47]. Current SFDI systems, discussed in Sect 1.10, are not compatible with endoscope instrument channels as they are too large and rigid, and therefore there is a need for a miniature SFDI system to either be deployed

through endoscope working channels or be packaged into a tethered capsule. A miniature SFDI system is required to image the optical properties of gastrointestinal tissue *in-vivo* to determine the tissue state in a move to detect abnormal changes in tissue at an early stage so that it may be resected and prevent progression to cancer. Such a system will require miniaturisation of existing materials (e.g. the bench top SFDI system presented in Chapter 2) and also new design tools to aid in the adaption to different imaging geometries, lighting conditions, and camera angles present in the gastrointestinal tract, which have been explored in Chapter 3.

1.5 Thesis outline

Following on from this introduction and overview of spatial frequency domain imaging, the rest of this thesis will comprise of 3 chapters on related works (each presenting their own methods, results and discussion), a chapter on the future work possible from the proceeding 3 chapters, and a final supplementary chapter discussing a clinical study investigating the measurements of aerosols and droplets during gastrointestinal procedures in relation to Covid-19.

Chapter 2 discusses the development of a cost-effective, bench top SFDI system and its use for characterisation of tissue-mimicking phantoms. First, a bench top system using low-cost components is constructed. Then, tissue-mimicking phantoms with varying absorption and scattering properties are fabricated, using Nigrosin dye and Titanium(IV) oxide anatase (TiO_2) respectively. These phantoms are imaged in the constructed bench top system and their optical properties extracted using a pre-calculated look-up table. Phantoms of different shape are then fabricated, and imaged in the bench top system. Capability of the system to successfully extract phantom optical properties, as well as shape, is shown.

Chapter 3 shows the novel use of open source graphics software *Blender* to simulate a realistic SFDI system, with a material of variable optical properties and shape. First, a material of variable absorption and scattering properties is simulated by changing the density of the absorption and scattering volume nodes respectively. Then, this material is characterised by simulating a double integrating sphere in the software and obtaining the optical properties via an inverse adding doubling algorithm. The material is then imaged in an SFDI configuration and the optical properties between two measurement techniques are compared. Successful measurement of shape and optical properties of typical gastrointestinal conditions in up-close planar geometry is shown. A novel projection pattern for optical property measurement in non-planar geometries, such as in a tube simulating a lumen, is also shown. This simulation was used to test various illumination schemes and projection-camera angles compatible with miniaturisation of SFDI. This chapter is based on [139, 140].

Chapter 4 presents an ultra-miniature (> 900 times smaller than the bench top system presented in Chapter 2) SFDI system, using a novel illumination scheme of a fiber array with interfering fibers producing the desired spatial frequency pattern. The proposed prototype is of 3 mm diameter, with a < 0.125 mm fiber and 1×1 mm camera at the distal end. Successful agreement between the ultra-miniature system and the bench top system is shown. Successful imaging of the optical properties of two phantoms with different optical properties placed adjacent to one another, mimicking the typical gastrointestinal condition of squamous cell carcinoma adjacent to

healthy oesophageal tissue, is shown. This chapter is based on [141] and a manuscript in review, preprint available: https://doi.org/10.48550/arXiv.2306.03713.

The penultimate chapter, Chapter 5, discusses the future advances of the work presented. The primary future works are identified, with the main aim of using the simulation model to advance further development of the proposed prototype. Further work is also needed on the prototype packaging to make it feasible for endoscopic deployment. A final conclusion for the thesis is also drawn.

Finally, Chapter 6 is a supplementary chapter which presents clinical trial work done with collaborators at Queens Medical Centre, Nottingham during the Covid-19 pandemic. This work investigates the generation of aerosols during gastrointesintal procedures in relation to Covid-19. This chapter is based on [142, 143].

Chapter 2

Imaging tissue-mimicking phantoms with a bench top SFDI system

This chapter will explore the fabrication and successful characterisation of tissue-mimicking co-polymer in oil phantoms with a bench top spatial frequency domain imaging (SFDI) system. This step was crucial to understand the mechanisms and limitations of SFDI, and to validate the fabrication of tissue-mimicking phantoms. A cost-effective, bench top SFDI system was constructed, consisting of a Raspberry Pi camera, a mini projector, inexpensive optical components and use of 3D printed materials. The system is desired to have a pixel resolution matching that of standard endoscopes, from $100,000 - 300,000$ pixels, as discussed in Sect 1.4. The fabrication of phantoms was optimised and their optical properties were successfully calculated, with 19% and 11% error for absorption and reduced scattering coefficients respectively. This corresponds to an absorption coefficient measurement sensitivity and specificity of $\geq 99.5\%$ and $\geq 86\%$ respectively, for absorption variances which are $> 0.003\,\text{mm}^{-1}$, and a reduced scattering coefficient measurement sensitivity $\geq 99.5\%$ and specificity $\geq 81\%$, for reduced scattering variances which are $> 0.22\ \text{mm}^{-1}$. These values are, as discussed in Sect 1.2.2, meeting the guidelines of the American Society of Gastrointestinal Endoscopy (ASGE) for a new endoscopic imaging device. The system would be capable to differentiate between reduced scattering coefficients of all desired tissue types, capable to differentiate between absorption coefficients of healthy tissue and squamous cell carcinoma and Barrett's Oesophagus and squamous cell carcinoma, but *not* capable to detect differences in absorption coefficient between healthy tissue ($\mu_a = 0.058\ \text{mm}^{-1}$ at 635 nm) and Barrett's Oesophagus ($\mu_a = 0.057\ \text{mm}^{-1}$ at 635 nm). Phantoms mimicking the variation in tissue optical properties in healthy and pre-cancerous/cancerous oesophageal tissue were fabricated and their optical properties and morphology were imaged in the bench top system. Development of the phantom fabrication protocol and imaging of phantoms in a double integrating sphere was carried out by collaborators at the University of Cambridge. Phantoms used in this study were all self-fabricated following this protocol.

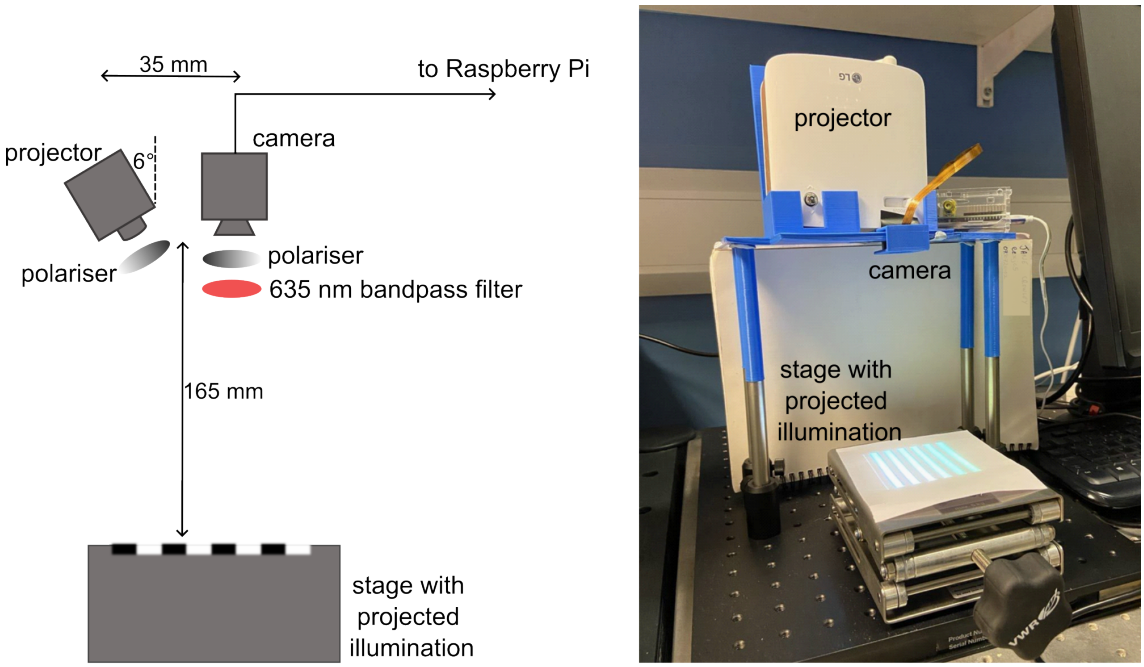

Figure 2.1: bench top SFDI imaging system consisting of a raspberry pi camera detector at a 6° angle to projector shown in (a) photograph and (b) schematic. Polarisers and filters shown in schematic are housed in 3*D* printed material in (a)

2.1 Building a bench top SFDI system

As discussed previously in Sect 1.3.3, many commercial and research SFDI systems exist. A cost effective, bench top SFDI system was built to image the optical properties of tissue-mimicking phantoms. A schematic and picture of the bench top system is shown in Fig 2.1 (a & b) respectively. Building a bench top SFDI system was crucial to validate an SFDI set-up and image acquisition process such that development of a ultra-miniature system would be possible.

2.1.1 Component selection

The bench top set-up consists of a Raspberry Pi (*2011.12*) with a Raspberry Pi camera (Camera module v1), a miniature projector (*LG Minibeam PH150g HD ready mini projector*), a movable z stage (*VWR*), linear polariser (LPNIRE100-B, *Thorlabs*, UK), polarising sheet, 635 nm bandpass filter (FL635-10, *Thorlabs*, UK), and 3D printed materials. The camera was chosen as it was low-cost (£20 [144]) and had potential for use in system miniaturisation with dimensions 25 × 25 × 9 mm. The camera has a resolution of 2592 × 1944 pixels, with horizontal and diagonal fields of view of 53.5° and 41.4° respectively. The projector was chosen as it is low-cost (£209), has a rechargeable battery such that it could be used without direct connection to a power source (which is useful in a clinical setting), and has the capability to project any desired illumination pattern. It has manual focus adjustment via an exterior knob, a resolution of 1280 × 720 pixels, an RGB LED as its light source and a throw ratio of 1.57 [145]. Throw ratio is the ratio of distance

from projector to screen to the width of the projected image.

The components are placed in a 3D printed stand, shown in Fig 2.1 (b), such that the projector is placed at a 6° angle to the plane of the camera, the projector-camera distance is fixed at 35 mm, and the distance from the projector-camera plane to the base breadboard (stage removed) is 220 mm. The stage has a minimum height of 55 mm from its base, and a maximum height of 280 mm from its base when fully extended. A linear polariser is placed in front of the camera, and polarising sheet is cross polarised and placed in front of the projector (i.e. at 90° to the camera polariser). Cross-polarisation was ensured by viewing light passing through both polarisers simultaneously and orientating them such that the coupled light power was minimised, meaning the light passing through is being polarised by both components. The cross polarisers are important for removing any specularly reflected light and in ensuring just diffusely reflected light is imaged. Specularly reflected light will just have reflected once from the air-sample interface and therefore have little to no information on the absorption and scattering properties of the sample of interest, whereas diffuse reflections will have undergone multiple scattering events. The 635 nm filter was placed in front of the camera and linear polariser to ensure only red light was captured by the camera. It was decided to focus on red light for several reasons. First, red light penetrates deeper into tissue than blue or green light, which is advantageous for sub-surface imaging of tissue optical properties, as discussed in Sect 1.2.1. Second, as typical gastrointestinal tissue appears red/pink, it is assumed that red light has good reflectivity on this tissue type. Finally, as shown in Table 1.2 in Sect 1.3.4, tissues of interest such as Barrett's oesophagus and squamous cell carcinoma have variable optical properties at this wavelength.

equipment	**cost (£)**
projector	209
camera	20
stage	62
linear polariser	96
filter	121
total:	508

Table 2.1: Approximate costing for bench top SFDI system

The total cost of the system is £508, with individual item costs outlined in Table 2.1. This system is 7 times cheaper than a conventional bench top SFDI system proposed by *OpenSFDI* for £3852 [87], as discussed in Sect 1.3.3. This considerably lower cost opens the possibility of the system to be used in low-resource settings.

2.1.2 Detector characterisation

Raspberry Pi cameras typically operate from the *picamera* module, which has extensive documentation on various camera settings such as for exposure, gamma correction, and white balance [146]. It is expected that the Raspberry Pi camera will not be linear with respect to power due to such settings, for example automatic exposure control. To determine which settings are required for the Raspberry Pi camera to be linear with respect to power, an experiment was set up, shown in Fig

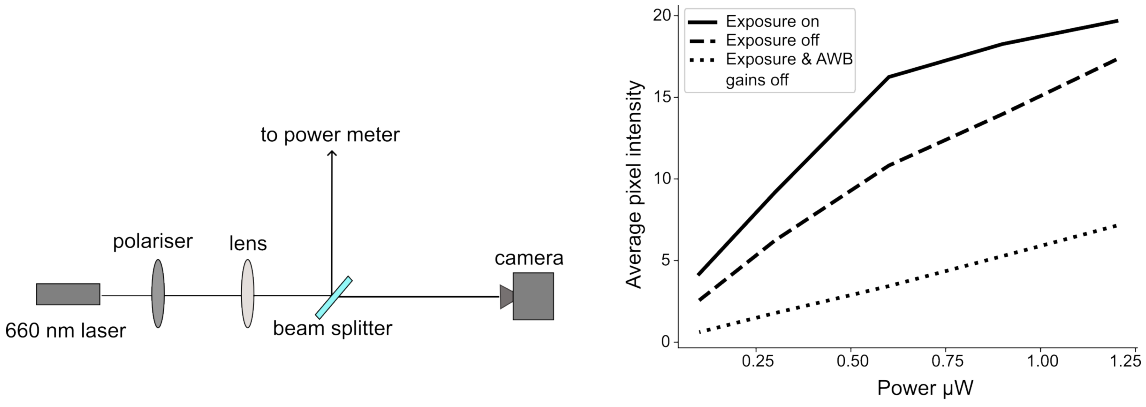

Figure 2.2: Schematic of set up used to calibrate camera properties. A 660 nm laser passes through a polariser, a lens, and then into a beam splitter, where part of the beam is transmitted forward to the camera and part is reflected toward a power meter

2.2 (a). A 660 nm laser diode (LPS-660-FC, *Thorlabs*, UK) was passed through a linear polariser (LPNIRE100-B , *Thorlabs*, UK) and a biconvex lens of focal length 100 mm (LB1187, *Thorlabs*, UK), which was placed 100 mm from a 50 : 50 beamsplitter (CCM1-BS014/M, *Thorlabs*, UK) where 50% of the light passes to the Raspberry Pi camera and 50% of the light passes to a power meter (PM100USB, *Thorlabs*, UK). Using the Pi camera, images were taken of the transmitted laser light and the average intensity of resultant pixels was calculated. The first measurement was taken with laser power (as measured at the power meter) of 0.1 μW. Then, the current to the laser was increased, resulting in a power increase from $0.3 - 1.2$ μW in equal increments of 0.3 μW, giving a total of 5 different intensity measurements. The entire field of the camera was illuminated with a random speckle pattern. As the intensity measurements were obtained by taking an average of all pixels in the resultant image, this speckle was not taken to be an issue. Images were captured with various settings on the camera: with normal exposure on, with automatic exposure turned off, and with both automatic exposure and automatic white balance (AWB) mode turned off. When the exposure mode of the camera is turned off, the camera's automatic gain control is disabled. This fixes the values for the analog and digital gain. When the AWB mode is turned off, the camera's AWB is disabled. This white balance is then controlled via the AWB gains property. Setting the AWB gains determines the red and blue balance of the camera. The results in Fig 2.2 (b) show that in order for the camera to be linearly proportional to the intensity of light, appropriate settings for the camera are for the exposure and AWB to be turned off.

2.1.3 Illumination characterisation

Input sinusoidal patterns project varying spatial frequencies at varying working distances from the camera and projector plane to the sample plane. For the same input projection pattern (shown in Fig 2.3 (a)), the measured spatial frequency at the imaging plane will decrease for increasing working distances (as shown in Fig 2.3 (b)). The spatial frequency of the projected sinusoidal pattern in the imaging

plane of interest was calculated manually via the equation:

$$\text{spatial frequency mm}^{-1} = \frac{\text{No. of line pairs in } x \text{ mm}}{x} \tag{2.1}$$

where a line pair refers to the distance between adjacent maxima or minima on a sinusoidal pattern, shown in Fig 2.3 (a). The measured spatial frequencies were then fitted to a 2D polynomial using the function *numpy.polyfit()* in *Python*. The resultant fit is shown in Fig 2.3 (b).

The projector had to be calibrated with respect to the camera due to several illumination effects inherent to a projector. Effects include the vignetting at the projection edges (projected image appearing with a low intensity blur at image edges) and the gamma correction built into the projector used to mimic the dynamic response of the human eye, which is highly non linear. These illumination effects of the projector are corrected for by determining the modulation transfer function (MTF) of the system as a whole, as discussed in Sect 1.3.1, by dividing by a reference material of known optical properties, calibrating for the MTF.

Sinusoidal patterns were generated in *Python* using the equation:

$$y = A\sin(2\pi f_x x + \alpha) + C \tag{2.2}$$

where A is the amplitude of the sinusoidal pattern with $A_{min} = -1$ and $A_{max} = 1$, such that $A = \frac{1}{2}(A_{max} - A_{min})$, f_x is the spatial frequency of the projection pattern, x is the size of the projection pattern (in pixels) in the x direction, α is the spatially shifted phase of the projection pattern, and C is a constant where $C = \frac{1}{2}(A_{max} + A_{min})$. It is noted that $A = -1$ corresponds to an output pixel value of 0 and $A = 1$ corresponds to an output pixel value of 255. This pattern is repeated a total of n times to create a 2D image using the *Python* function *numpy.matlib.repmat()*, where n is the size (in pixels) of the projection pattern in the y direction. It was found that sinusoidal projections required a lower intensity offset in order to be successfully demodulated using Eqns 1.26 & 1.27 in Sect 1.3.1. Therefore, an offset was applied to the projected patterns, such that instead of having a sinusoid with $A_{min} = -1$, a sinusoid with $A_{min} = -0.75$ was created. The offset was applied as the demodulation was not successful without it. This is assumed to be due to the projectors lowest pixel value of 0 not being exactly 0 and thus the full range of pixel values was not utilised in the projected pattern.

2.2 Image acquisition & processing

2.2.1 Acquisition

To take a measurement, the projection patterns of interest are loaded on a USB memory stick which is put into the projector. The desired illumination pattern is selected, and the focus knob of the projector is adjusted until the projected pattern is in focus in the imaging plane of interest. The sample to be imaged is placed in the center of the projected pattern. A black sheet cover is placed over the system and sample being imaged, to remove the effect of any background room lights. It is desired to obtain an image that has not undergone any form of image correction. Therefore, the raw Bayer image is extracted using the *picamera* module. A raw

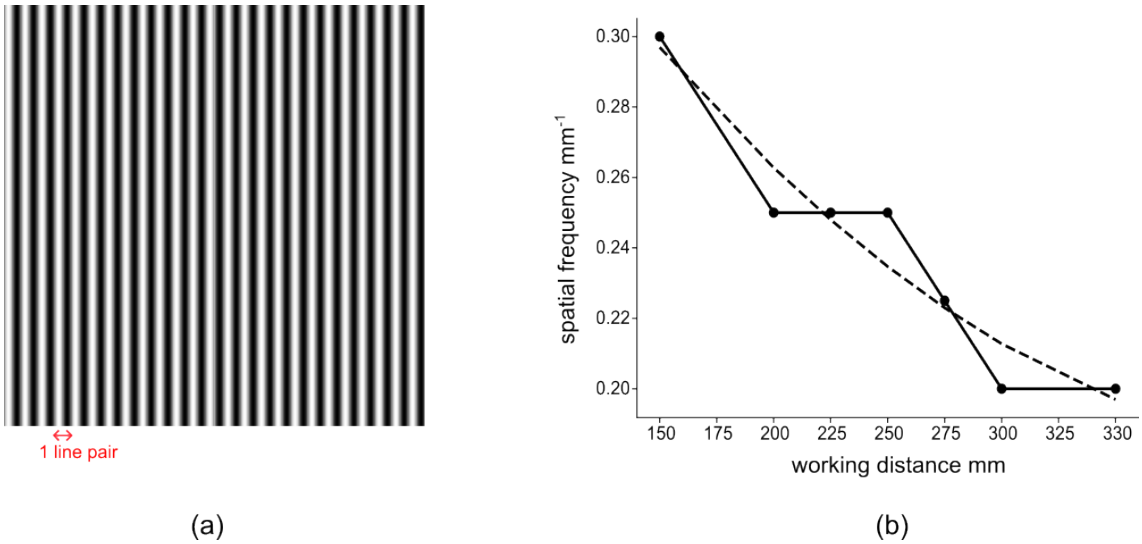

Figure 2.3: Projected spatial frequency varies with working distance i.e. distance from projector to imaging plane (a) image of input sinusoidal projection pattern indicating what one line pair corresponds to (b) measured spatial frequency of this projection pattern at varying working distances.

Bayer image is a captured image before any form of processing has been performed, where the pixels of the captured image are more heavily weighted to green pixels than to red and blue pixels in a $2:1:1$ ratio [147]. Therefore, a step called demosaicing has to be performed where the weighted average of a pixel is calculated based on its surrounding pixels. This will result in an output RGB image of equally weighted pixels. The red channel is then extracted, for reasons previously discussed.

When interested in imaging the morphology of a sample, the projection pattern must be rotated 90° to ensure maximum distortion to surface variations. This was simply done with inbuilt projector settings to rotate the desired patterns.

2.2.2 Processing

The resulting images are put into *Python* code to correct for the effect of distortion from both the camera and projector. Slight distortions are present due to the projected pattern being projected at an angle onto the sample of interest, while the camera is placed orthogonal to the sample. To correct for these distortions, first the perspective transform matrix is computed using the *OpenCV-Python* function *cv2.getPerspectiveTransform()*. Two sets of coordinates are input into the function: the first set are the four desired corner coordinate points in the distorted image and the second are the four corner coordinate points of the new, cropped image. The transform matrix is then input into the *OpenCV-Python* function *cv2.warpPerspective()* where it is applied to the captured image of interest. The shape of the distortion corrected image is also input into this function, where the output is the distortion corrected image.

These images are then input to *Python* code where the optical properties are calculated either via a diffusion approximation or a Monte Carlo generated look-up table, by comparison to a reference phantom of known optical properties (and hence known diffuse reflectance values), using Eqn 1.29. Look up tables (LUTs) are a rapid

processing technique that match a set of pre-computed values to a complex equation. The standard LUT used in SFDI makes use of a selected light propagation model to model the diffuse reflectance for a given set of optical properties at a specific spatial frequency. The simulation is run over multiple optical properties for at least two spatial frequencies. Then, determining the optical properties of a sample replies on determining the diffuse reflectance of the sample at the two spatial frequencies and cycling through the pre-calculated diffuse reflectance values via an interpolation to find the corresponding optical properties.

A diffusion approximation LUT was generated in *Python* using equations from Sect 1.1.1. The LUT had parameters: $\mu_a : 0.001 - 0.03$ mm^{-1} with a stepsize of 0.0001 mm^{-1} and $\mu_s' : 0 - 3$ mm^{-1} with a stepsize of 0.01 mm^{-1}. These optical properties were chosen such that the full range of optical properties for the fabricated phantoms, which will be discussed in Sect 2.3, were encapsulated. The refractive index, n, was set to 1.4 inline with literature values for mineral oil, from which the phantoms are fabricated [148]. Final optical properties are determined via a cubic interpolation within the *Python* function *scipy.interpolate.griddata()*.

A Monte Carlo LUT was generated using open-source Monte Carlo software *Virtual Photonics* [12]. A photon packet of 1×10^4 photons was simulated. For the absorption and reduced scattering coefficients, three different ranges of which the desired optical properties would lie within were simulated, which will be discussed in Sect 2.3. The first range had $\mu_a : 0.01 - 0.15$ mm^{-1} with a stepsize of 0.02 mm^{-1} and $\mu_s' : 0.3 - 9.9$ mm^{-1} with a stepsize of 1.2 mm^{-1}. The second range explored lower optical properties, with $\mu_a : 0.002 - 0.008$ mm^{-1} with a stepsize of 0.002 mm^{-1} and $\mu_s' : 0.3 - 1$ mm^{-1} with a stepsize of 0.1 mm^{-1}. The third, and final, range had $\mu_a : 0.012 - 0.018$ mm^{-1} with a stepsize of 0.002 mm^{-1} and $\mu_s' : 0.3 - 1$ mm^{-1} with a stepsize of 0.1 mm^{-1}. Final optical properties are again determined via a cubic interpolation within the *Python* function *scipy.interpolate.griddata()*.

As discussed, to calculate the optical properties of an unknown sample, a reference material of known optical properties is required. As the exact optical properties of the fabricated phantoms are not certain due to potential variations in fabrication protocol, outlined in Sect 2.3.1, each individual phantom was used as a reference, such that for each phantom a total of n optical property maps were obtained, where n is the total number of fabricated phantoms. These n maps were then averaged together to get a final optical property map. A smoothing Gaussian filter of standard deviation 3 was applied to the AC and DC modulation amplitudes of both the phantom of interest and the reference phantom using the *Python* function *scipy.ndimage.gaussian_filter()*. This filtering creates a more uniform optical property image and reduces the amount of NaNs present in the final optical property image. NaNs may be present in the resultant optical property image due to interpolations occurring outside the convex hull of the generated LUT. A data point may lie outside the hull as a result of some speckle noise being present, which may be due to imperfect cross-polarisation of the polarisers in the set up.

This is currently a non-automated process, and so the time from commencement of first acquisition to final optical property maps is on the order of several minutes. Advances toward automation of fringe projection with captures feeding directly into optical property measurement code would speed up the process to be on the order of several seconds.

2.3 Fabrication & imaging of tissue-mimicking phantoms

Phantoms are materials which are designed and fabricated to act as a substitute for human tissue such that their properties can be analysed to calibrate, test or optimise the performance of optical systems [149, 150]. Phantoms exist in several diverse forms; such as liquid phantoms optimised for microwave and ultrasound imaging [151], rubber phantoms for ultrasonic imaging [152], gelatinous phantoms for visible and infrared imaging [153], 3D printed phantoms to fabricate complex geometries [154, 155], multi-layer phantoms for depth imaging in the visible and NIR wavelength regions [156], and fluorescent phantoms for use in photo-dynamic therapy and fluorescence spectroscopy [157]. *Pogue and Patterson* produced a concise and all-inclusive review on tissue-mimicking phantoms [158].

2.3.1 Fabrication protocol

Low-cost, tissue-mimicking, co-polymer in oil phantoms were fabricated with the aid of collaborators at the University of Cambridge [159], who carried out optical property measurements of 5 mm thick phantoms using a double integrating sphere (DIS) on several of the fabricated phantoms. The phantoms had been previously optimised to have tunable photo-acoustic and optical characteristics of human tissue. The base material consists of mineral oil (*Sigma Aldrich-330779-1L*), copolymers low-density polyethylene (*Alfa Aesar 43949.30*) and polystyrene-block-poly(ethylene-ran-butylene)-block-polystyrene (*Sigma Aldrich 200557-250G*) and butylated hydroxytoluene as a stabaliser (*Sigma Aldrich W218405-1KG-K*). Titanium(IV) oxide, anatase (TiO_2) (*Sigma Aldrich 232033*) and Nigrosin dye (*Sigma Aldrich 211680-100G*) were added to introduce optical scattering and absorption respectively.

The following process was followed for the fabrication of a 100 mL phantom (slight variation in volume arises from varying dye stock solution volumes):

1. A stock solution of Nigrosin dye and mineral oil was required to use as an absorbing agent. 0.1 g of Nigrosin and 40 mL of mineral oil were sonicated for 60 minutes at $80°C$. This solution was kept for multiple batches, and such was sonicated for ~ 60 minutes each time before use to ensure uniform dispersion of Nigrosin in the mineral oil.

2. The desired amount of TiO_2 and Nigrosin dye stock solution (Table 2.2, determined from *Hacker et al.* [159]) were weighed, put in a beaker with 83.8 g of mineral oil and sonicated for 60 minutes at 80°C, as shown in Fig 2.4 (a).

3. While this was sonicating, a glass dish containing silicone oil was secured onto a hot plate and the temperature was set to 200°C. A magnetic stir bar was placed in the oil bath to heat the oil uniformly, with the revolutions per minute (rpm) set to 100. Tin foil was placed around the oil bath to prevent heat loss.

4. When sonication was complete, a magnetic stir bar was introduced to the solution and it was put into the silicone oil bath as shown in Fig 2.4 (b). A thermometer was placed in the beaker and the solution was heated until it reached 170°C.

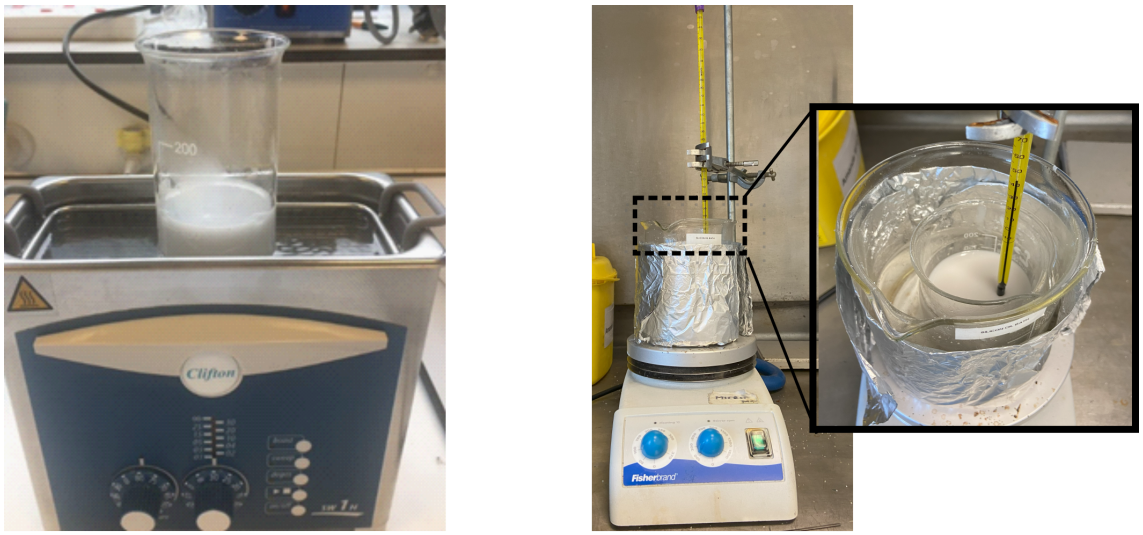

(a) (b)

Figure 2.4: Protocol for phantom fabrication (a) solution in beaker in sonicator (b) sonicated solution in beaker in silicone oil bath on a hot plate.

5. Once this temperature was reached, 20 g of polystyrene-block-poly(ethylene-ran-butylene)-block-polystyrene, 4 g of low-density polyethylene and 3 g of butylated hydroxytoluene were added to the solution. The rpm of the magnetic stir bar was increased to 200 rpm and the solution was stirred until the polymers had mostly dissolved. As the polymers reduced the temperature of the solution, the solution was left to heat back up to 170°C.

6. Once this temperature was reached again, the magnetic stir bar was reduced to 100 rpm and the solution was left at 170°C for $\sim$ 15 minutes. Throughout this time, the solution was also gently stirred manually every several minutes such that no lumps would be present in the solution from the polymers.

7. The beaker was then removed from the oil bath and carefully poured from a low height into a vessel of interest using heat-protective gloves.

TiO_2 (w/v%)	**TiO_2** (g)	**$\mu_s\prime$** (mm^{-1})	**Nigrosin** (w/v%)	**Dye stock** (g)	**μ_a** (mm^{-1})
0.03	0.03	0.34	0.0007	0.2364	0.002
0.07	0.07	0.54	0.0015	0.5028	0.008
0.10	0.10	0.79	0.0022	0.7374	0.012
0.13	0.13	1.02	0.0030	1.0056	0.018

Table 2.2: TiO_2 and Nigrosin dye stock solution values to use for a 100 mL sample to obtain given optical properties at 635 nm (Data from *Hacker et al.* [159])

In Table 2.2, the values of TiO_2 and Nigrosin in weight per volume (w/v%) which give corresponding optical properties at 635 nm are noted. For a 100 mL phantom, the TiO_2 amount in w/v% equates to an equal amount in grams as it follows from

the equation:

$$\text{Solution concentration (w/v\%)} = \frac{\text{Weight of solute (g)}}{\text{Volume of solution (mL)}} \times 100 \tag{2.3}$$

However the Nigrosin concentration is given as the amount of Nigrosin in the phantom solution, so a conversion was required to calculate the amount of stock solution needed for each absorption coefficient. Given that the stock solution is made by putting 0.1 g of Nigrosin in 40 mL of mineral oil, it has a concentration of 0.0025 g mL^{-1}. By dividing the Nigrosin concentration in w/v by the concentration of Nigrosin in the stock solution, the volume of the stock solution needed for each Nigrosin concentration is obtained. Knowing that the density of the mineral oil is 0.838 g mL^{-1}, the mass in grams of the Nigrosin dye stock solution needed to give the corresponding absorption coefficients can be calculated.

To obtain optical properties outside of these specific range of values, a second order polynomial was fitted to the TiO_2 data and a linear equation to the Nigrosin dye stock solution, data giving R^2 values of 0.9973 and 0.9995 respectively. Therefore, optical properties outside of the specific values in Table 2.2 were obtained following the equations:

$$\mu_s'(\lambda = 635 \text{ nm}) = 23.246 \times (\text{TiO}_2 \text{ (g)})^2 + 3.2054 \times (\text{TiO}_2 \text{ (g)}) + 0.2191 \tag{2.4}$$

$$\mu_a(\lambda = 635 \text{ nm}) = 0.027 \times (\text{Dye stock solution (g)}) - 0.0026 \tag{2.5}$$

In step 7 of the phantom fabrication protocol, the phantom mixture is poured slowly and steadily into a heat-proof vessel to let it set. Ideally, this vessel containing the solution would be placed in a vacuum oven to remove any air bubbles. As a vacuum oven was not available, several different techniques were trialled in an attempt to reduce and remove air bubbles. In the first attempt, the solution was taken directly from the silicone oil bath and poured steadily and from a low height into the vessel. While these phantoms appeared visibly satisfactory, they still had many air bubbles trapped inside making them highly inhomogeneous, and it was not possible for their optical properties to be measured in a DIS. The second attempt involved pouring steadily and from a low height as before, and then placing the vessel containing the solution into a vacuum chamber. This was also unsuccessful as the phantom mixture sets rapidly, and had somewhat set by the time the vacuum chamber was closed and turned on. Therefore, this method just shrivelled up the phantom. The final, and successful, approach was to pour the phantom mixture steadily from a low height into a heat-proof vessel and placing that vessel into an oven. The oven was heated up to 170°C, let sit at 170°C for 60 minutes, and then the oven temperature was gradually decreased by 1° every 3 minutes until the oven reached room temperature. This technique made air bubble free samples, capable of being measured in a DIS.

Several iterations of phantoms batches were fabricated before successful imaging in the bench top SFDI system. For the first and second batch of fabricated phantoms, each phantom mixture was poured into two glass petri dishes to give two $\sim$ 5 mm thick phantoms. The first batch of phantoms were not put into an oven after fabricated, as discussed above. Once poured into the petri dishes, one sample was imaged in the system, and the other, once set, was cut to size ($60 \times 25 \times 5$ mm) and sent to be imaged in the DIS. Due to air bubbles in this first batch, these

Phantom (Batch)	**TiO_2**	**$\mu_s'_{exp}$**	**$\mu_s'_{meas}$**	**Dye stock**	**$\mu_{a,\,exp}$**	**$\mu_{a,\,meas}$**
	(g)	(mm^{-1})	(mm^{-1})	(g)	(mm^{-1})	(mm^{-1})
I(1)	0.2	1.79	1.44	1.5	0.028	0.017
A(2)	0.03	0.34	0.29	0.25	0.003	0
B(2)	0.03	0.34	0.32	1	0.018	0
C(2)	0.07	0.54	0.59	0.75	0.013	0.006

Table 2.3: Comparison of expected (exp) optical property values to measured (meas) optical property values in DIS system at 635 nm. Data obtained by collaborators.

phantoms were highly inhomogenous and the optical properties of only one phantom were successfully measured in the DIS system (see Table 2.3, phantom I batch 1). Phantoms in the second batch were placed in the oven after pouring as described above, and so were all capable of being measured in the DIS. The results from the DIS measurements are shown in Table 2.3. It is noted that for phantoms A and B in batch 2, the IAD (inverse-adding doubling) algorithm used to calculate the optical properties from the DIS measurements did not converge as the absorption was too low. The optical property measurements of these phantoms are therefore less accurate than the others. It is noted that the amount of dye stock solution added to phantom B2 was 1 g, which indicates an expected absorption coefficient of 0.018 mm^{-1} at 635 nm. The DIS measured an absorption coefficient of 0 mm^{-1} over the range $570-900$ nm for this phantom. For all phantoms successfully measured in the DIS, the measured absorption coefficient is significantly lower than the expected value. The conclusion is therefore that the Nigrosin dye stock solution was not sonicated sufficiently for these phantom fabrications, implying that the Nigrosin was not dispersed homogeneously throughout the mineral oil dye stock solution and that a diluted dye stock solution was added to the phantom mixtures. For future phantom fabrications, the Nigrosin dye stock solution is always sonicated for 60 minutes, and stirred manually, before introducing it to the mixture.

The third batch, batch 3, consisted of four widely optically varying phantoms, with Nigrosin dye stock solution ranging from $0-2$ g and TiO_2 ranging from $0-0.2$ g, representing an optical property range of absorption coefficients from $0-0.039$ mm^{-1} and reduced scattering coefficients from $0-1.79$ mm^{-1} at 635 nm respectively. For these phantoms, the mixture was poured to a ~ 5 mm height in a heat-proof petri dish and placed in an oven to remove any air bubbles, as previously described in Sect 2.3.1. With a white sheet of paper as the background, all phantoms were imaged in the bench top system, and the AC and DC modulation amplitudes of each sample were calculated using Eqns 1.26 and 1.27 in Sect 1.3.1 respectively. This was repeated with a black plastic sheet in place of white paper as the background and the differences in results were analysed. For a phantom with 0.2 g of TiO_2 and 2 g of Nigrosin dye stock solution, there is minimal difference $< 1\%$ when the imaging background material is changed, as expected. For phantoms with no TiO_2 present, it is noted that there is a vast difference $> 100\%$ in the calculated DC modulation amplitude when the imaging background material is changed. This is because the phantoms which had no TiO_2 present were visibly transparent, and so the incident photons were passing directly through the sample, reflecting of the

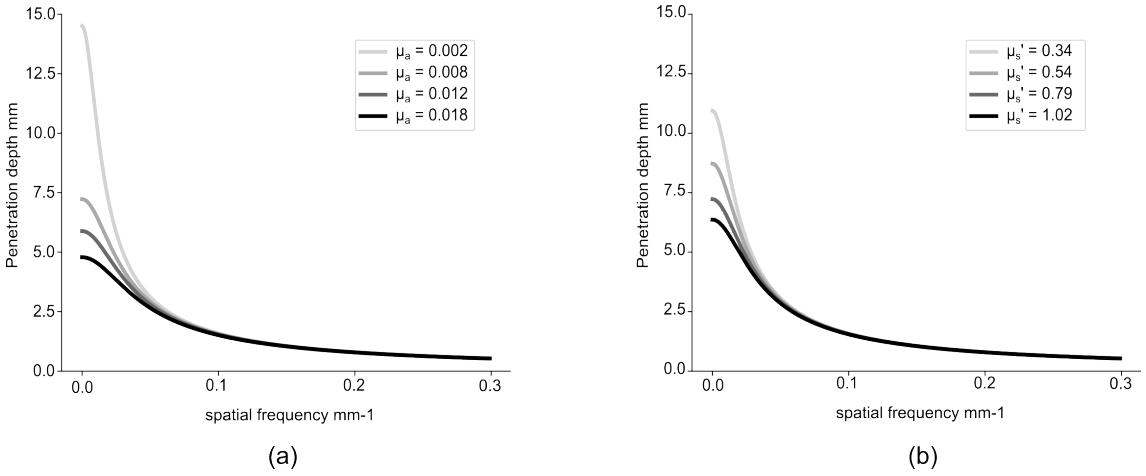

Figure 2.5: Calculated penetration depth over spatial frequency range $0-0.3$ mm^{-1} for (a) phantoms with $\mu_s' = 0.79$ mm^{-1} and (b) phantoms with $\mu_a = 0.008$ mm^{-1}. Legend optical properties are of unit mm^{-1}.

sample background, and travelling back into the camera. For an SFDI measurement to be successful, an opaque sample is required such that only the diffuse reflectance of the material of interest is captured and not information about the background material. These phantoms did not meet the semi-infinite thickness requirement for SFDI and therefore returned inaccurate optical properties.

To overcome this issue, the minimal thickness a required phantom must have was determined. The penetration depth of the bench top SFDI system was investigated. SFDI is capable of penetrating tissue at different depths by utilising different spatial frequencies [160]. The depth at which light can penetrate into tissue is given by the equation [161]:

$$\delta = \frac{1}{\sqrt{\mu_{eff}^2 + (2\pi f)^2}} \tag{2.6}$$

where $\mu_{eff} = \sqrt{3\mu_a(\mu_a + \mu_s')}$ and f is the spatial frequency of the projection pattern. While this equation depends on knowing the exact optical properties of the tissue of interest, *Hayakawa et al.* propose a solution to calculate penetration depth for arbitrary optical properties [74]. For phantoms with optical properties of those in Table 2.2, the typical calculated penetration depth is calculated using Eqn 2.6 to be ~ 0.8 mm for a spatial frequency of 0.2 mm^{-1}, as shown in Fig 2.5 (a & b). The optical penetration depth ranges from $5-15$ mm for planar illumination. It can be seen from Fig 2.5 (a) that as the absorption coefficient of the imaging sample is increased, the penetration depth decreases, and from Fig 2.5 (b) that as the reduced scattering coefficient of the imaging sample is increased, the penetration depth decreases also.

Therefore, future fabricated phantoms must be visibly opaque and have a thickness > 15 mm to be successfully imaged in the bench top SFDI system presented in Sect 2.1.

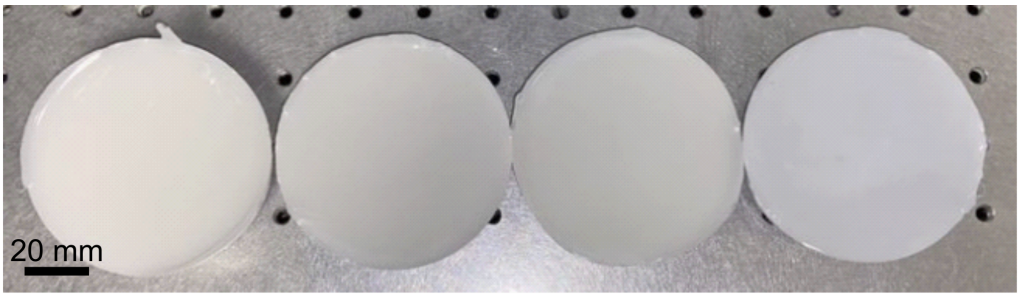

(a)

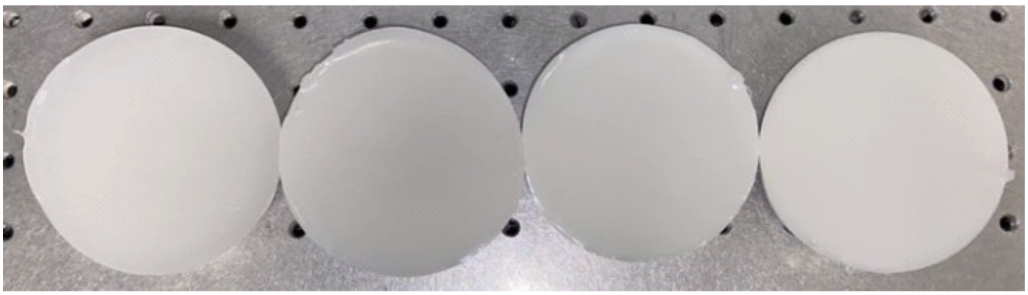

(b)

Figure 2.6: Top down image of fabricated phantoms. (a) Phantom batch 5: constant TiO_2 with increasing (from left to right) Nigrosin dye stock solution. (b) Phantom batch 6: constant Nigrosin dye stock solution with increasing (from left to right) TiO_2. Images captured with phone camera

2.3.2 Phantoms with absorption and scattering variation

Following the phantom fabrication protocol outlined in Sect 2.3.1, two more batches of phantoms were fabricated, each consisting of four phantoms. The first batch had a constant amount of TiO_2 and increasing amounts of dye stock solution, shown in Fig 2.6 (a), and the second batch had a constant amount of dye stock and increasing amounts of TiO_2, shown in Fig 2.6 (b). Actual Nigrosin dye stock and TiO_2 values used are given in Table 2.4. The phantoms were poured into cylindrical silicone moulds to a height of 30 mm, with a bottom diameter of 65 mm and a top diameter of ~ 78 mm. These phantoms were placed in an oven after fabrication to remove air bubbles. Once set, the phantoms were imaged in the bench top system. Sinusoidal patterns of spatial frequency 0.2 mm^{-1} were projected onto the sample of interest at three equi-shifted phases of 0°, 120° and 240°. The distance from top of phantom to projector was 200 mm.

As 8 phantoms were fabricated, a total of 8 optical property maps were determined for each phantom using a Diffusion approximation LUT, with the final optical property map obtained by averaging all 8 maps together, as discussed in Sect 2.2.2. A 300×300 pixel region at the centre of the phantom optical property map was taken, corresponding to a phantom area of $\sim 22 \times 22$ mm. This area size was chosen as it covered the central region of each phantom. The mean pixel value taken from this region was calculated to obtain the optical properties of the phantom. The resultant measured optical properties are shown in Sect 2.4 Figs 2.10 & 2.11.

The optical properties of these phantoms were calculated using a diffusion ap-

Phantom	TiO_2 (g)	Dye stock (g)	Phantom	TiO_2 (g)	Dye stock (g)
A5	0.10	0.25	A6	0.03	0.50
B5	0.10	0.50	B6	0.07	0.50
C5	0.10	0.75	C6	0.10	0.50
D5	0.10	1.01	D6	0.13	0.50

Table 2.4: Weight of TiO_2 and Nigrosin dye stock solution used to make 100 mL phantoms, for phantom batch 5 and 6.

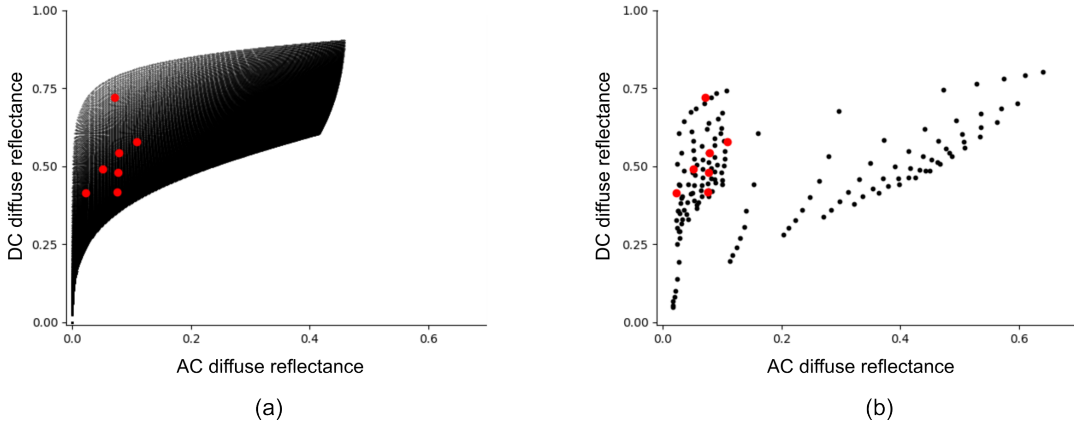

Figure 2.7: Look up tables generated from (a) diffusion approximation and (b) Monte Carlo simulations of the radiative transport equation. The black markers indicate the respective light propagation model generated diffuse reflectance values and the red markers indicate the expected diffuse reflectance values of the 8 fabricated phantoms.

proximation generated LUT with parameters $\mu_a : 0.001 - 0.03$ mm^{-1} with a stepsize of 0.0001 mm^{-1} and $\mu_s' : 0 - 3$ mm^{-1} with a stepsize of 0.01 mm^{-1}, as discussed in Sect 2.2.2. The resultant LUT is shown in Fig 2.7 (a). The optical properties of these phantoms were also calculated using a Monte Carlo generated LUT using *Virtual Photonics* software [12]. The data from this simulation is shown in the LUT in Fig 2.7 (b). The Monte Carlo generated LUT is significantly less dense than the diffusion approximation LUT as it requires significantly more computational time. The differences in optical property measurements from using each LUT were compared and the results are shown in Sect 2.4.2.

2.3.3 Phantoms of biologically relevant optical properties

Tissue mimicking phantoms simulating expected optical property variation seen in typical gastrointestinal conditions such as squamous cell carcinoma (SCC) and Barrett's Oesophagus (BO) were fabricated. As discussed in Sect 1.2.2, SCC's are among the most frequent incidences of solid tumours in humans and are a major cause of cancer related deaths [39], and there has been an increased incidence in carcinomas in the gastrointestinal tract in recent years [162]. Therefore it was selected as a tissue type of interest to fabricate optical property variations of and image. Also in

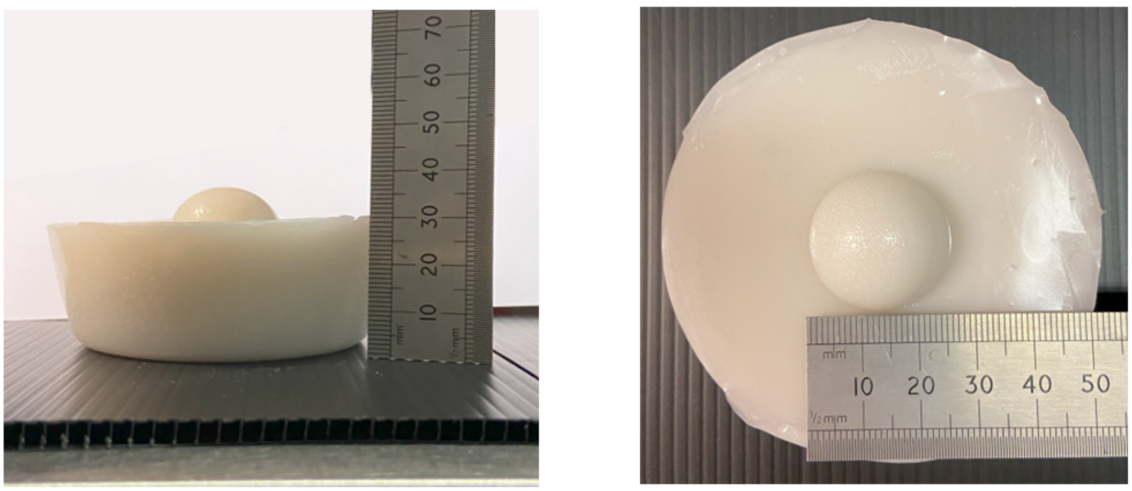

(a) (b)

Figure 2.8: Images of hemispherical phantom, simulating a colon polyp, on top of cylindrical phantom, simulating background tissue (a) side view (b) top down view. Images captured with phone camera.

Sect 1.2.2, BO is discussed and how it is a known important precursor to the development of cancer cells in the oesophagus, oesophageal adenocarcinoma (OAC) [42]. It was for this reason that BO was selected as a significant tissue type to fabricate optical property variations of and image also.

Sweer et al. imaged resected oesophageal tissue using SFDI at seven wavelengths in the range $471 - 851$ nm, and compared the calculated absorption and reduced scattering properties to histopathology determinations of the resected tissue type, as discussed in Sect 1.3.4. Here, three conditions that were imaged in this study are focused on; healthy oesophageal tissue, invasive SCC and BO with mild chronic inflammation. *Sweer et al.* found that across all wavelengths used, the absorption coefficient of healthy oesophageal tissue was lower than that of SCC and the reduced scattering coefficient of healthy oesophageal tissue was higher than that of invasive SCC. The absorption coefficient of healthy oesophageal tissue is less than that of BO with mild chronic inflammation in the lower wavelength range, and switch orientation from 630 nm onwards, where the absorption coefficient of healthy oesophageal tissue is greater than that of BO with mild chronic inflammation in the higher wavelength range. At 635 nm, which is the current wavelength of interest, *Sweer et al.* determined the absorption coefficient of healthy oesophageal tissue to be comparable to that of BO. The reduced scattering coefficient of healthy oesophageal tissue is higher than that of BO with mild chronic inflammation across the entire wavelength range.

Tissue-mimicking phantom were fabricated as described previously in Sect 2.3.1 in cylindrical silicone moulds as well as fabricating phantoms in hemispherical silicone moulds of diameter 27 mm and height 10 mm. The hemispherical phantoms were then placed on top of the larger cylindrical phantoms once set to simulate an abnormal region of tissue on top of background, healthy tissue, as seen in Fig 2.8 (a & b).

To simulate SCC on top of healthy oesophageal tissue, a hemispherical phantom with a TiO_2 amount of 0.03 g and dye stock solution of 1 g was placed on top of

a cylindrical sample with TiO_2 of 0.13 g and dye stock solution of 0.25 g. These concentrations should show the absorption coefficient of the SCC significantly higher than that of the background phantom and the reduced scattering coefficient lower than the background phantom. To simulate a situation of BO with mild chronic inflammation, a hemispherical phantom with $TiO_2 = 0.03$ g and dye stock solution of 0.5 g was placed on top of a cylindrical phantom with TiO_2 0.1 g and dye stock solution 0.25 g. These values should show the two phantoms to have comparable absorption and the hemi-spherical phantom to have a lower reduced scattering coefficient than the background tissue.

Analogous to image acquisition and processing outlined in Sect 2.3.2, optical property maps were calculated in the same manner via a diffusion approximation LUT where 8 optical property maps were obtained using each phantom from Sect 2.3.2 as a reference such that the resultant optical property map was an average of all 8 measured optical property maps. The phantom area was increased from 300×300 pixels to a 600×600 pixel region corresponding to an area of $\sim 45 \times 45$ mm. The expected and measured optical property maps are shown in Sect 2.4 Figs 2.13 & 2.14.

2.3.4 Imaging morphology

Fringe profilometry, as discussed in Sect 1.3.2, can be used to extract height information from a sample of interest by knowledge of the system geometry. By rotating the projected fringe pattern by 90°, phase information was obtained of a hemispherical phantom which was converted to height information via Eqn 1.32. The projection pattern is rotated as one orientation is more sensitive to surface profile variations than the other. The hemispherical phantom is simulating a polyp, which is any mass protruding from the walls of the gastrointestinal tract [163] and their size and shape can be indicative of cancer staging [76]. The pipeline for extracting height is discussed in Appendix D. Here, three sinusoidal patterns of spatial frequency 0.15 mm^{-1} at three equi-shifted phases of 0°, 120° and 240° were projected onto a hemispherical phantom on top of a cylindrical phantom. A 600×600 pixel region was selected corresponding to a phantom surface area of $\sim 45 \times 45$ mm. Following the steps in Appendix D, the phase is first extracted from Eqn D.7, with the resultant map shown in Fig 2.9 (a). In order to remove the $-\pi$ to π pattern seen, several processing steps must be applied to the image. First, an inverse fast Fourier transform is performed on the the imaginary part of the exponential of Fig 2.9 (a) using the *Python* function *numpy.fft.ifftshift*. A 2D discrete Fourier transform is then applied using the function *numpy.fft.fft2*. The zero frequency component is then shifted to the center using the function *numpy.fft.fftshift*. A shift is then performed in the Fourier domain using the function *scipy.ndimage.shift* by the number of phase shifts present in Fig 2.9 (a), which in this case is a float of value 6.55. Then to obtain the actual, wrapped phase, an inverse fast Fourier transform, followed by a 2D discrete Fourier transform, and finally a fast Fourier transform is performed on the image. The resultant wrapped phase is shown in Fig 2.9 (b). To unwrap this phase, a *Python* wrapper package [164] is used, with the result shown in Fig 2.9 (c). This unwrapped phase may then be converted to height using Eqn 1.32, where the distance from projector to the top of cylindrical phantom (i.e. base of hemispherical phantom) is 200 mm and the distance between the projector and camera is 35 mm.

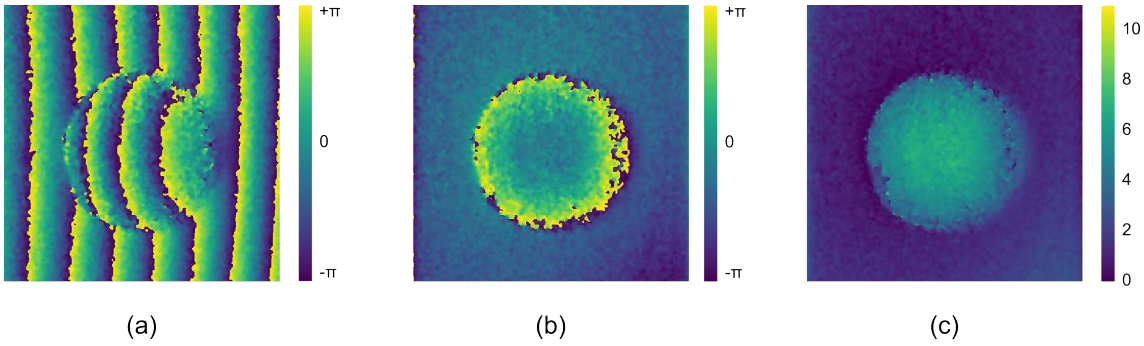

Figure 2.9: Pipeline for extracting phase (a) wrapped phase (b) wrapped phase, shifted to remove multiple $-\pi$ to π shifts (c) actual, unwrapped phase

When extracting height information, an increasing gradient was present in the resultant maps. This gradient was present because the function used to shift the phase image, *numpy.roll()*, was only shifting by integer values, and the necessary shift was somewhere in between two integers (6.55 as stated above). Therefore, by replacing *numpy.roll()* with *scipy.ndimage.shift()*, it was possible to shift the image in float increments, removing the gradient and allowing for a flat background.

2.4 Resultant phantom optical properties

Here the results from imaging phantoms in the bench top SFDI system are presented. Average standard errors of 19% and 11% for absorption and reduced scattering coefficient's respectively were achieved. Variation in optical properties from two different phantoms in the same capture was successfully imaged. The height of a hemispherical phantom, simulating the morphology of a colon polyp on a background of healthy tissue, was also successfully imaged and reconstructed.

2.4.1 Results for absorption and scattering variation

Fig 2.10 (a & b) represent the measured absorption and reduced scattering coefficients of phantoms with a constant 0.1 g of TiO_2 and increasing amounts of dye stock solution (0.25, 0.5, 0.75, 1 g). It can be seen that as the dye stock solution is increased, the measured absorption coefficient also increases and the reduced scattering coefficient remains relatively constant. The phantom with 0.25 g of dye stock solution (phantom A5) is measuring an absorption coefficient relative to the phantom with 0.5 g of dye stock solution. Potential reasons for the inaccurately measured absorption coefficient for this phantom will be discussed in Sect 2.5.4.

Fig 2.11 (a & b) represent the measured absorption and reduced scattering coefficients of phantoms with a constant dye stock solution of 0.5 g and increasing amounts of TiO_2 (0.03, 0.07, 0.1, 0.13 g). It can be seen that as TiO_2 is increasing, the reduced scattering coefficient increases and the absorption coefficient remains relatively constant.

For all 8 phantoms, the average standard error from SFDI measured optical properties to their expected values from reported DIS measurements is 43% and 11% for the absorption and reduced scattering coefficient respectively. This 11% error in reduced scattering coefficient is within the expected range of error between

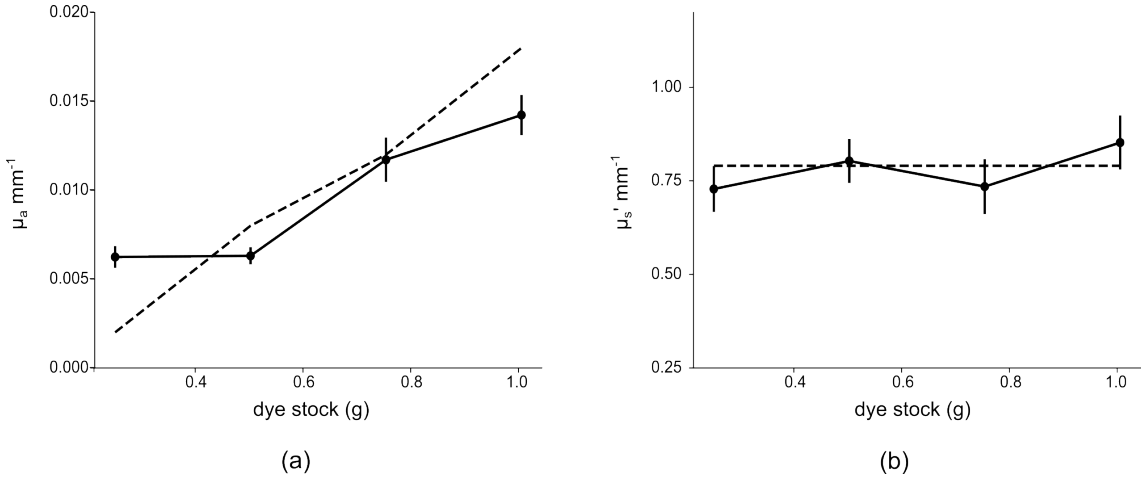

Figure 2.10: Phantom batch 5 with constant TiO_2 and varying Nigrosin dye stock solution (a) absorption coefficient and (b) reduced scattering coefficient. Errors bars represent the standard deviation across a 300×300 pixel region corresponding to phantom area of $\sim 22 \times 22$ mm. Dashed line depicts expected optical properties.

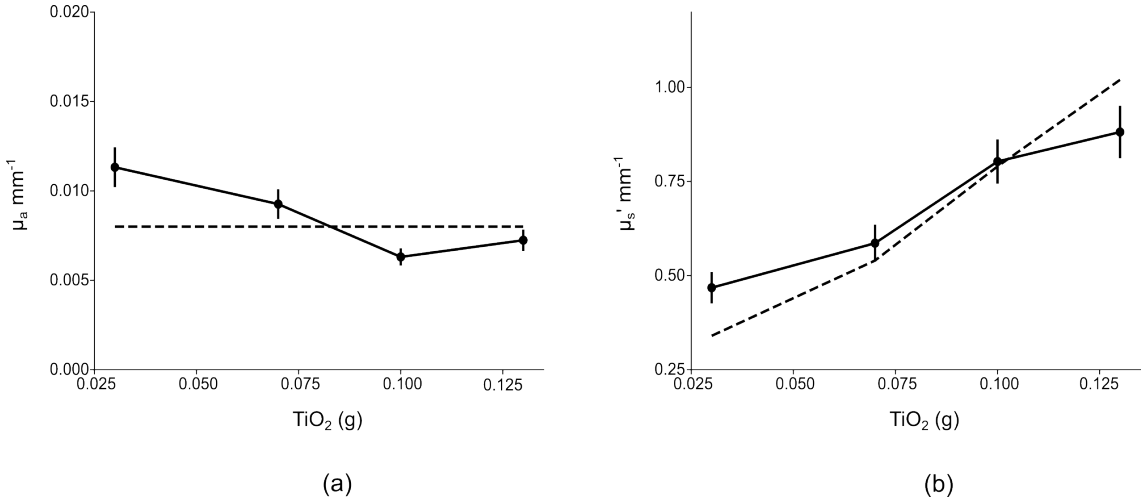

Figure 2.11: Phantom batch 6 with constant Nigrosin dye stock solution and varying TiO_2 (a) absorption coefficient and (b) reduced scattering coefficient. Errors bars represent the standard deviation across a 300×300 pixel region corresponding to phantom area of $\sim 22 \times 22$ mm. Dashed line depicts expected optical properties.

SFDI and DIS measurements, as will be later discussed in Sect 2.5.1. However, the 43% error in absorption coefficient is unexpectedly high. This high error is attributed to phantom A5, with 0.25 g of dye stock solution. The standard error of measured absorption coefficient for this phantom by itself is 212%. This is over 5 times higher than the next highest error present in the data set, and over 10 times higher than the median standard error over all measured absorption coefficients, which is just 21%. Therefore, it is assumed that this 212% error is an outlier, and the average standard error for measured absorption coefficient can be reduced from 43% to 19% by removing this data point. This 19% error for measured absorption coefficient is within the expected range of error between SFDI and DIS measurements, as will be discussed in Sect 2.5.1.

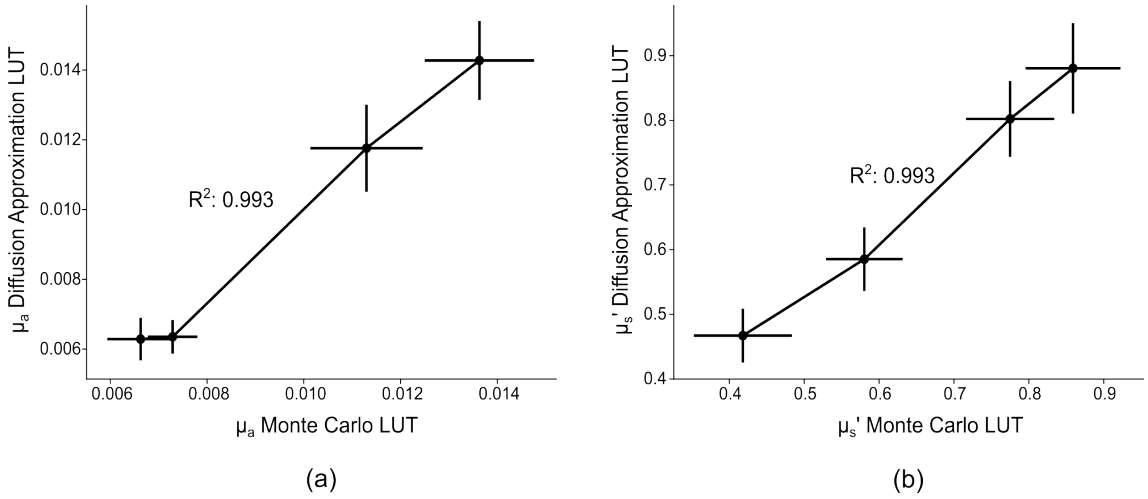

Figure 2.12: Comparing optical property calculations using a Monte Carlo generated LUT (x axis) and a diffusion approximation LUT (y axis) for (a) absorption coefficient and (b) reduced scattering coefficient. The error bars represent the standard deviation across a 300×300 pixel region.

2.4.2 Comparing look-up tables

The optical properties of phantoms fabricated in Sect 2.3.2 are calculated with two look-up tables: a diffusion approximation LUT and a Monte Carlo generated LUT. Both methods return optical properties within acceptable limits, returning R^2 values of 0.993 for both absorption and reduced scattering coefficient measurements. The use of a diffusion approximation LUT was chosen as it requires less computational power than Monte Carlo simulated diffuse reflectance values. The absorption and reduced scattering coefficients are shown in Fig 2.12 (a & b). Neither LUTs return an absorption coefficient < 0.006 mm^{-1}.

2.4.3 Results for imaging typical gastrointestinal conditions

Two typical gastrointestinal conditions were fabricated by placing a hemispherical phantom on top of a cylindrical phantom, mimicking the optical property variation of squamous cell carcinoma (SCC) or Barrett's Oeosphagus (BO) on top of healthy oesophageal tissue. First, SCC on top of healthy oesophageal tissue was fabricated and imaged. A white light image of the two phantoms, captured with the same Raspberry Pi camera used for SFDI acquisition, is shown in Fig 2.13 (a). It is noted that the hemispherical phantom is visually darker in appearance, indicating that it will have a higher absorption coefficient. While this is visually detectable, the *quantitative* absorption and reduced scattering coefficients are not known from this image. The expected optical property maps are shown in Fig 2.13 (b & d), and the measured absorption and reduced scattering coefficients are shown in Fig 2.13 (c & e) respectively. The measured absorption coefficient of the hemispherical phantom in Fig 2.13 (c) appears less than its expected, high value shown in Fig 2.13 (b). However, the measured absorption coefficient of the hemispherical phantom (simulating SCC) is much greater than the absorption coefficient of the background phantom (simulating healthy oesophageal tissue), as expected in SCC. In Fig 2.13 (e), the reduced scattering coefficient is measuring as expected from Fig 2.13 (d), where the

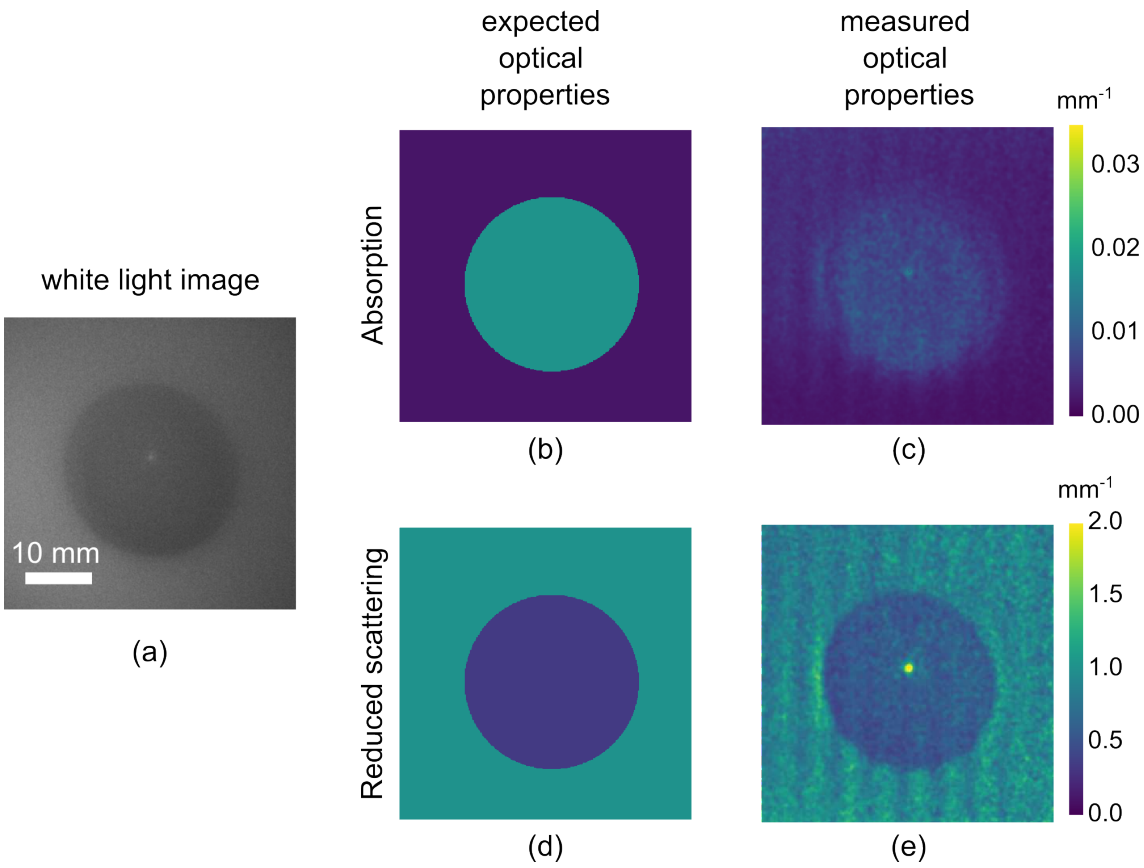

Figure 2.13: Phantoms simulating SCC on top of healthy oesophageal tissue showing (a) white light image (b) expected and (c) measured absorption coefficients (d) expected and (e) measured reduced scattering coefficients.

reduced scattering coefficient of simulated SCC is lower than the simulated healthy oesophageal tissue. Fig 2.13 (e) shows a region of specularly reflected light in the centre of the hemispherical phantom, resulting in an inaccurate reduced scattering coefficient measurement in that region. This may be due to slight movements in the cross polarisers in the system, which should be ensured stable in future system designs. The residual pattern seen in Fig 2.13 (c & e) may be due to the depth of focus of the illumination part of system not being equivalent to that of the imaging part of system and requires further investigation.

To simulate BO, a hemispherical phantom on top of a cylindrical phantom mimicking the optical property variation typically see in BO, was also imaged. A white light image of the two phantoms is shown in Fig 2.14 (a), from which it is difficult to visually detect any differences in optical properties between the two phantoms. The expected optical property maps are shown in Fig 2.14 (b & d), and the measured absorption and reduced scattering coefficient maps are shown in Fig 2.14 (c & e) respectively. The measured absorption coefficient of the background phantom is measuring higher than expected. It is of note that this phantom background phantom is phantom A5, which was found to measure a higher absorption coefficient than expected above in Sect 2.4. While this absorption coefficient is higher than expected, the absorption coefficient of the hemispherical phantom, i.e. BO is not differentiable from the background phantom i.e. healthy oesophageal tissue, as is expected with BO. Some artefacts of higher absorption coefficient are present where

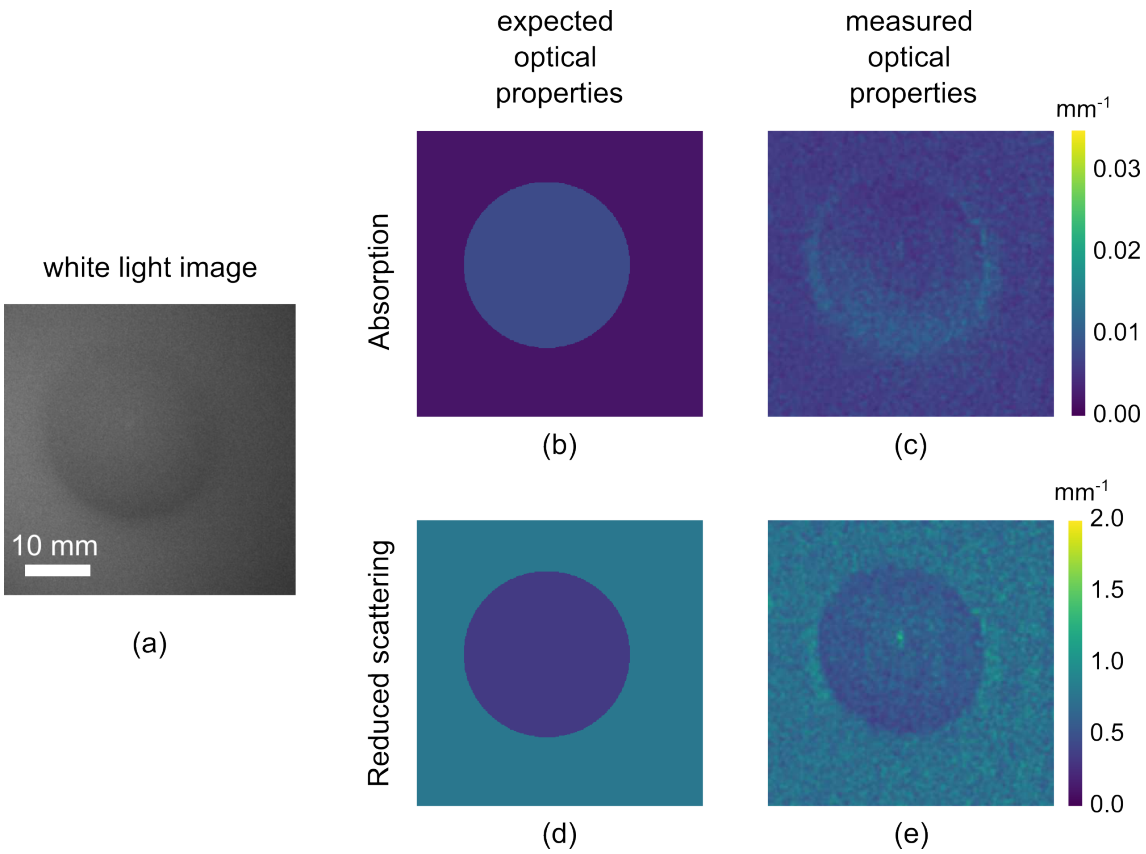

Figure 2.14: Phantoms simulating BO on top of healthy oesophageal tissue showing (a) white light image (b) expected and (c) measured absorption coefficients (d) expected and (e) measured reduced scattering coefficients.

the hemispherical phantom meets the cylindrical phantom, as seen in the absorption map in Fig 2.14 (c). This may be due to a slight air gap caused by uneven surfaces between the two phantoms. The measured reduced scattering coefficient, shown in Fig 2.14 (e) of simulated BO is distinctively lower than that of the surrounding simulated oesophageal tissue, which is seen in BO, and is equivalent to the expected reduced scattering coefficient map.

Fig 2.13 and Fig 2.14 show the capability of the cost effective, bench top SFDI system to successfully detect optical property variances typically seen in SCC and BO in the oesophagus. The background tissue simulating healthy oesophageal tissue in Fig 2.14 is phantom A5, which previously measured a higher absorption coefficient than expected. The absorption coefficient map in Fig 2.14 (c) is therefore as expected from previous bench top SFDI results.

In addition to the above optical property measurements, the morphology of the fabricated phantoms simulating BO was also successfully obtained. The white light image of the configuration is shown Fig 2.14 (a). By performing fringe profilometry, the height of the hemispherical phantom was measured, and the results are shown in Fig 2.15. Fig 2.15 (a) shows a top down view of the height map obtained. The x and y axis also show the width and length of the phantom. Fig 2.15 (b) shows a reconstructed side view of the measured height, width and length of the hemispherical phantom. The hemispherical phantom has a height of 10 mm as measured with a ruler, which was shown previously in Fig 2.8 (a). The resultant

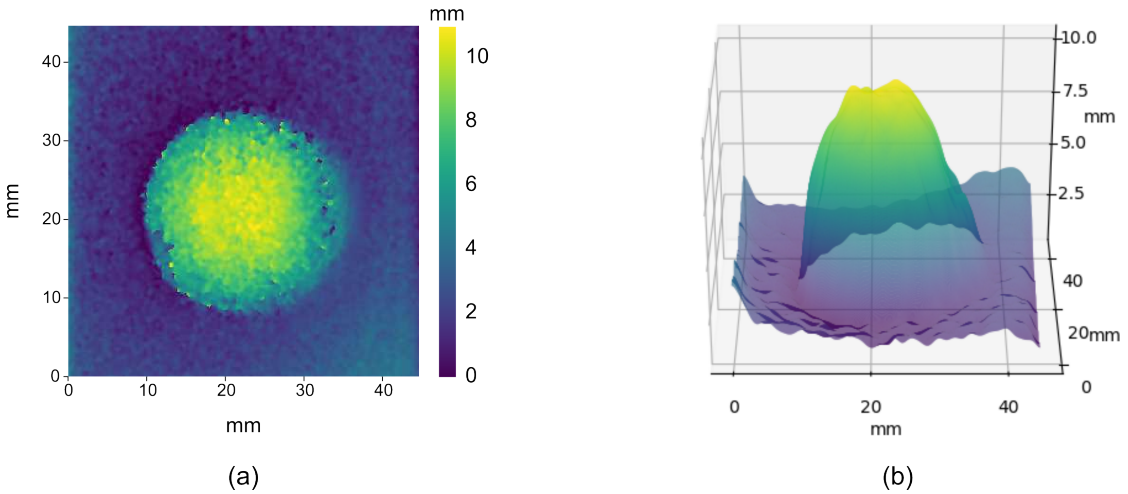

Figure 2.15: Height of hemispherical phantom (a) top view map of height (b) 3D reconstructed height map.

height maps agree with this measurement. These results show the capability of the bench top system to correctly measure morphology of 3D objects within the field of view, which is crucial in the colon for deciding resection potential.

2.5 Discussion

Tissue-mimicking phantoms simulating typical gastrointestinal conditions have been successfully imaged in the cost-effective bench top SFDI system. Using the diffusion approximation, the absorption and reduced scattering coefficients of the phantoms are measured within 19% and 11% accuracy respectively. These errors are a representation of the standard deviation in pixel values across the final optical property maps and do not account for errors in the set-up of the bench top system, inaccuracy in phantom fabrication, surface profile corrections and the use of look-up tables, all of which will be discussed in this section. Using fringe profilometry, the approximate height maps of hemispherical phantoms are also obtained.

2.5.1 Absorption and reduced scattering coefficients

Many tabulated values of optical properties of gastrointestinal tissue exist, as discussed previously in Sect 1.2.2 & Sect 1.3.4. The variation in measured absorption coefficient between malignant and healthy gastrointestinal tissue found by *Holmer et al.* using a double integrating sphere spectrometer [36] contradicts results from *Sweer et al.* and *Nandy et al.* using SFDI [47, 103]. *Holmer et al.* found SCC to have a lower absorption coefficient than healthy tissue, while *Sweer et al.* and *Nandy et al.* found it to have a higher absorption coefficient. This may be due to the fact that integrating sphere measurements and SFDI measurements are not always complimentary, with *Chen et al.* showing that inaccuracies in measured diffuse reflectance in integrating sphere measurements of just 5% can lead to to up to 25% relative change in measured absorption coefficients [165]. *Hu et al.* show experimental differences in SFDI and integrating sphere measurements of up to 20%

and 14% in absorption and reduced scattering coefficients respectively, at 675 nm [166]. Therefore, the average standard errors for absorption and reduced scattering coefficients obtained with the bench top system in this chapter of 19% and 11% respectively may be due to differences in SFDI and DIS measurements.

Also, these tabulated values are taken from *ex-vivo* samples, and it is suspected that there will exist a variation in *in-vivo* optical properties due to differences in blood oxygenation, water, and collagen content. The measurement of true optical properties may also be variable from previously measured due to measurement artefacts within the different imaging systems, such as noise and non-linearities.

Therefore, it is understood that knowledge of the exact optical properties is not possible, and understanding the expected *variation* of optical properties of different tissue types is advantageous to anticipate what the variation in optical properties will look like *in-vivo* rather than exact, quantitative values [167].

The sensitivity and specificity of the phantom measurements for increasing absorption and increasing scattering were calculated, at the operating wavelength of 635 nm. As discussed in Sect 1.2.2, the required sensitivity and specificity for a new endoscopic imaging technology are 90% and 80% respectively. From the measurements taken, it was found that the bench top system is compatible with the American Society of Gastrointestinal Endoscopy (ASGE) guidelines for absorption variances which are > 0.003 mm^{-1} (sensitivity $\geq 99.5\%$ and specificity $\geq 86\%$) and for reduced scattering variances which are > 0.22 mm^{-1} (sensitivity $\geq 99.5\%$ and specificity $\geq 81\%$). If the variation in absorption coefficient is ≤ 0.003 mm^{-1} and in reduced scattering coefficient is ≤ 0.22 mm^{-1}, the bench top system may not successfully detect the optical property variance.

2.5.2 Phantom fabrication

It was decided to fabricate the phantoms based on work by *Hacker et al.* for several reasons. Firstly, the fabrication requires low-cost, readily available materials, with a total costing per 100 mL phantom of $\sim$ £10. Second, the phantom optical properties are easily tunable and, once fabricated, remain stable over time without the requirement for specialist storage, with *Hacker et al.* determining optical property stability over a period of 11 months [159]. Third, once a phantom is fabricated, it can be easily recast by reheating the solid phantom until it is viscous and re-pouring the phantom into a desired mould, without altering the phantoms optical properties. TiO_2 (particle diameter $\lesssim 5$ μm [168]) was chosen as the scattering agent as it it is highly scattering and has negligible absorption in the NIR [169]. The particle size indicates Mie scattering is taking place, as discussed in Sect 1.2.1, which indicates highly forward scattering material due to refractive index changes within the bulk material, indicative of typical scattering in biological tissue e.g. cell nuclei scattering incident light due to difference in refractive index to surrounding cytoplasm. Nigrosin was chosen as the absorbing agent as it has a flat absorption spectrum over the visible wavelength range [170]. This allows for easy tuning of the absorption coefficient with different Nigrosin concentrations.

2.5.3 Reproducibility of phantom fabrication protocol

A batch of four phantoms was made twice in an attempt to determine the reproducibility of the fabrication process, as it can be challenging to get precise TiO_2 and Nigrosin dye stock solution concentrations into a sample. Nigrosin powder proved particularly challenging to weigh accurately, and therefore the concentration of Nigrosin in the dye stock solution may not have been exact. The fabricated phantoms had concentrations of (Nigrosin dye stock, TiO_2): (0.25 g, 0.1 g), (0.25 g, 0.13 g), (0.5 g, 0.1 g), and (0.5 g, 0.13 g). The optical properties of the phantoms were calculated using each of the 4 phantoms fabricated within that batch as a reference, such that 4 optical property maps were obtained for each phantom and averaged together to get a final optical property map. It was found that the average standard error in absorption and reduced scattering coefficients between batches was 15% and 5% respectively. This discrepancy in measured absorption coefficient may be accounted for by non-homogeneous dye stock solution as the Nigrosin powder tends to settle at the bottom of the dye stock solution and it has to be sonicated and stirred sufficiently before use. However, by following the fabrication protocol precisely one should be able to fabricate phantoms without much variation between batches of same Nigrosin dye stock solution and TiO_2.

2.5.4 Measured absorption coefficients of phantom

As previously discussed, in Fig 2.10 (a) phantom A5 which has the lowest concentration of dye stock solution, 0.25 g, is measuring an absorption coefficient comparable to the phantom with 0.5 g of dye stock solution. This may be for several reasons.

The first possible reason is that the dye stock solution made in Step 1 of the fabrication protocol was not sonicated sufficiently before putting the desired concentration into the phantom mixture. This would result in Nigrosin powder not being distributed uniformly throughout the mineral oil, and hence more Nigrosin powder may have been put into the phantom mixture than desired. Another reason for the measured difference may be due to the known difference in DIS and SFDI measurements, as previously discussed. The phantom protocol followed measures optical properties in a DIS, and therefore it is suspected that SFDI measurements will have a slight offset. Correcting for this may be possible by knowing the exact absorption of a phantom with the fabricated dye stock solution used, either through use of a double integrating sphere (from which some error may be present) or by using a spectrometer and calculating the ratio of incident to transmitted intensity to determine the absorption coefficient. As neither of these equipment were available in house, it was not possible to measure each fabricated phantoms optical properties via another method than SFDI. It is also possible that the range of reference phantoms used for optical property calculation was not sufficient. As discussed in Sect 2.5.3, two of the phantoms within each batch had Nigrosin dye stock concentrations of 0.25 g (the same concentration as phantom A5). Over the 4 phantoms fabricated between both batches with this Nigrosin dye stock concentration, the average absorption coefficient measured for phantoms with this dye stock concentration was 0.003 mm^{-1}. This implies that either phantom A5 which has been extensively discussed above was incorrectly fabricated, or the increase of phantoms with this low absorption coefficient as a reference made it more likely for the system to detect a low absorption coefficient. For phantoms batch 5 and 6, the optical properties were

determined by using each as a reference, but only one low absorbing reference phantom was used. Additional low absorbing reference phantoms may therefore generate more accurate low-absorption results. One possibility to aid the fabrication may be in the use of a small amount of a solvent e.g. ethanol with the Nigrosin to aid in the dispersion of Nigrosin in the oil. This aspect of the bench top system requires further investigation and is beyond the scope of this work.

However, as previously stated, primary interest lies in determining the localised contrast in optical properties, rather than exact quantitative optical properties. As this localised contrast has been successfully shown in Sect 2.4.3, this work is acceptable for potential *in-vivo* contrast-enhanced imaging applications, which is the goal here.

2.5.5 Surface profile

Several SFDI techniques require the correction of optical properties due to the presence of an objects varying surface profile. *Gioux et al.* imaged a phantoms optical properties and phase at height translations of $0 - 3$ cm [79]. They then obtained a relationship between known height and measured phase, and a surface height correction model was obtained. This returned optical property maps with 23% and 6% improved accuracy compared to uncorrected optical property maps. For height differences of 1 cm, the difference in measured optical properties between corrected and uncorrected measurements was found to be $< 14\%$. Therefore, for the clinical application of imaging gastrointestinal optical properties and polyp height *in-vivo*, the need to perform surface profile correction is negated as polyps ≥ 6 mm will be excised independent of what optical properties they posses [171].

2.5.6 Look-up tables

Minimal differences were noted in phantom optical property measurements determined from a diffusion approximation LUT and a Monte Carlo generated LUT, as shown in Sect 2.4.2. Using the Monte Carlo generated LUT improved absorption coefficient accuracy by 5% and reduced scattering coefficient accuracy by just 2%. Therefore, use of the diffusion approximation over Monte Carlo LUT is acceptable in this case.

Angelo et al. propose different forms of LUTs which do not require the time consuming interpolations present in typical LUTs [172]. One of these LUTs linearly samples diffuse reflectance values instead of optical properties as is typically done. This showed error in measured absorption and reduced scattering coefficients with respect to Monte Carlo simulations as low as 0.2% and 0.09% respectively. It also has a quick processing speed in comparison with a 100×100 pixel region taking 6×10^{-4} s to measure. Exploration of this quick LUT in the future to improve bench top optical property measurement accuracy is desired.

2.6 Conclusion

This chapter demonstrates the capability of a cost-effective, bench top SFDI system to measure the absorption and reduced scattering coefficients of tissue-mimicking phantoms with 19% and 11% accuracy respectively. As discussed in Sect 2.5.1, the

sensitivity and specificity of absorption coefficient measurements with the bench top system were determined to be $\geq 99.5\%$ and $\geq 86\%$ respectively for an absorption coefficient variation > 0.003 mm^{-1}. The sensitivity and specificity of reduced scattering coefficient measurements were determined to be $\geq 99.5\%$ and $\geq 81\%$ respectively for a reduced scattering coefficient variation > 0.22 mm^{-1}. Therefore, this system is capable of imaging variation in absorption coefficient between healthy tissue and squamous cell carcinoma and variation in reduced scattering coefficient between healthy tissue and Barrett's Oesophagus in accordance with ASGE guidelines and expected optical properties presented in Sect 1.3.4, Table 1.2. However, it may not be capable to differentiate the absorption coefficient of healthy oesophageal tissue (0.058 mm^{-1} at 635 nm [47]) from the absorption coefficient of Barrett's Oesophagus (0.057 mm^{-1} at 635 nm [47]) or to differentiate the reduced scattering coefficient of healthy oesophageal tissue (0.75 mm^{-1} at 635 nm [47]) from the reduced scattering coefficient of squamous cell carcinoma (0.64 mm^{-1} at 635 nm [47]). The capability to image tissue-mimicking phantoms simulating typical gastrointestinal conditions has also been successfully demonstrated. This work demonstrates the capability this system to deployed in low-resource environments, where knowledge of optical properties on *ex-vivo* tissue is desired.

However, the goal of this work is to miniaturise this system, to demonstrate the capability to use SFDI to image gastrointestinal optical properties *in-vivo*. There are many challenges associated with miniaturisation of such a system. First is the physical capability of components to be miniaturised, for example the bulky projector must to be replaced with a much smaller mechanism. Second is the capability of these miniature mechanisms to perform on par optical property measurements with the bench top system. Third is the constrained system geometry associated with imaging *in-vivo*. To aid in the miniaturisation of the system and to over come some of these challenges, an SFDI system was simulated in the ray tracing software *Blender*, which will be explored in the next chapter.

Chapter 3

Simulating an SFDI system

A spatial frequency domain imaging (SFDI) design and simulation tool using open-source 3D modelling and rendering software *Blender* is presented in this chapter. The model can simulate SFDI for recovery of absorption, scattering and shape in a wide range of geometries. First, the capability to use *Blender* to model a customisable absorbing and scattering material using inbuilt material nodes is shown. Then, the construction of a virtual characterisation system for the absorption density, A_ρ, and scattering density, S_ρ, of this material is shown using two approaches: a double integrating sphere (DIS) and an SFDI system. For both approaches, the accuracy of retrieved optical properties is validated and it is shown how this can be improved by generating an empirically derived look-up table (LUT) from the DIS *in-situ* data. Next, two illustrative example cases for the system are presented. First, the simulated SFDI system is shown to enable reconstruction of absorption, scattering and shape of planar geometry samples mimicking cancerous and pre-cancerous conditions such as squamous cell carcinoma and Barrett's Oesophagus. Second, a novel illumination scheme tailored for non-planar tubular geometries (such as inside a lumen) is presented, where the spatial frequency is constant throughout the length of the tube such that the optical properties can be accurately obtained. To improve accuracy, the tube is longitudinally sectioned and separate look-up tables are created for each section, a straight-forward task in the system. This customised illumination can detect changes in absorption and scattering properties within a tube of biologically relevant material properties, providing a potential design for future SFDI systems. The work presented in this chapter is based on [139, 140]. Virtual Photonics Monte Carlo simulation software [12] and *Prahl*'s inverse adding-doubling (IAD) algorithm [173] were utilised in this work.

3.1 Need for a new SFDI simulation tool

A range of commercial [84] and research [50, 87, 89] SFDI systems exist, as previously discussed in Sect 1.3.3. However, these systems are almost exclusively designed for *planar* imaging geometries, where the sample is relatively uniform in morphology and the camera and projector are located above it at near-normal incidence (see Fig 3.1 (a)). Yet, many important clinical applications exhibit *non-planar* geometries: for example imaging inside tubular lumen such as the gastrointestinal (GI) tract, blood vessels, or the biliary system (Fig 3.1 (b)). SFDI imaging *in vivo* in such organs is challenging due to miniaturisation needs, and because the surfaces are

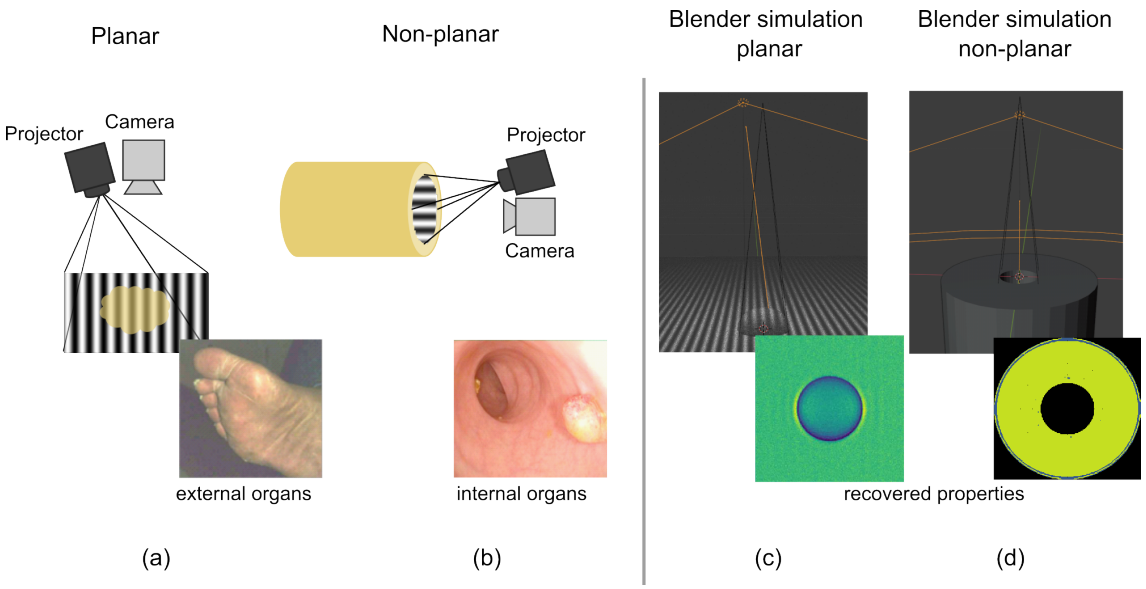

Figure 3.1: Future SFDI systems, especially those for *in vivo* clinical use, may require significantly different geometries from conventional SFDI: (a) conventional 'planar' SFDI imaging geometry with projector at a small angle to planar sample, with real-world application of measuring diabetic foot shown in inset [175], (b) SFDI operating in a tubular (lumen) geometry, that may be required for use in future endoscope systems where projection is no longer approximately planar, with example usage for imaging polyps in the colon shown inset [176], (c) screenshot of presented *Blender* SFDI model applied to a planar geometry, with reconstructed scattering properties of tumour like sample shown inset, (d) a screenshot of presented *Blender* model applied to a non-planar tubular geometry, with reconstructed scattering properties of inner tube wall shown inset.

cylindrical, creating non-planar illumination conditions and sample geometries. This means that illumination and imaging may no longer be normal (or nearly normal) to the surface being imaged, and so different scattering behaviour will be observed [174], and specular reflections will be altered.

The use of 3D modelling or computer-aided design (CAD) software to simulate conventional optical imaging with a light source, 3D objects and a camera is well-established [177, 178]. SFDI simulation systems have several necessary requirements for successful, accurate modelling of real-world SFDI systems. Such requirements are ease of use in complex geometries and provision of photo-realistic renderings, including effects such as vignetting, specular reflections, shadows. Other requirements include varying the incident lighting, refractive index, and non-normal incidence angles. The capability to easily produce large data sets to train AI models is also desired as SFDI datasets have been shown to successfully train neural networks, as previously discussed in Sect 1.3.2. Currently, a number of open-source software packages relevant to SFDI exist such as *AppSFDI* (Open SFDI [92]), *Toast++* (Schweiger and Arridge [179]), *ValoMC* (Leino et al. [180]), *OptgenSim* (Professor Steven Jacques's Lab at Oregon Health and Science University, BIST Lab at the University of Wisconsin at Milwaukee, and the LOCI group at the University of Wisconsin at Madison [181]) and *FullMonte* (Medical biophotonics research group and the computer engineering group of the University of Toronto [182]), which will

be discussed here.

AppSFDI can perform SFDI demodulation for a set of input images taken at specific spatial frequencies of 0 and 0.2 mm^{-1} [92]. It can also produce maps of absorption and reduced scattering coefficients if images of a reference phantom of known optical properties are also input. This package is limited by use of specific spatial frequencies, and input data must be either taken experimentally or from another SFDI simulation software. There exists another software capable of performing SFDI demodulation and production of absorption and reduced scattering coefficient maps using deep learning [61]. However, this software also requires input data to be taken experimentally or from another SFDI simulation software. Perhaps of more relevance to this work is software that simulates the optical behaviour of materials under conditions of varying absorption and scattering properties. *Toast++* is widely used for forward and inverse modelling in diffuse optical tomography [179]. However, because the software is designed for diffuse optical tomography, it typically simulates a small number of sources and detectors which are placed on the surface of a sample. It is thus less well-suited to considering the effects of complex illumination patterns and high-resolution detectors placed some distance away from the sample, as is required for SFDI. There are numerous specialised pieces of Monte-Carlo simulation software such as *ValoMC*, *OptogenSIM* and *FullMonte* [180–182]. However, these packages also suffer from a variety of limitations. *ValoMC* can perform Monte Carlo simulations of light in tissue for large samples, however it requires meshes to be imported from other softwares and has limited detector positioning. *OptogenSIM* is a simulation platform to estimate light delivery for heterogeneous optical properties in brain tissue. It is limited in application as the sample geometry is specific to the brain. *FullMonte*, which also requires meshes to be imported from other softwares, is currently limited to a maximum of 32 different material configurations of varying optical properties within one simulation, and does not offer wide-field illumination.

None of the above models are capable of providing all of the necessary requirements for realistic, end-to-end SFDI simulation. Therefore, there is a need for a design and simulation tool to accelerate the design of new SFDI systems. An SFDI design and simulation tool has been created in the open-source, 3D modelling software *Blender* (Fig 3.1 (c & d)), which will be presented in the rest of this chapter.

3.2 Development of SFDI & fringe profilometry imaging system in Blender

Blender is an open-source, 3D modelling software. It is typically used to create animations, 3D models for printing, and for visual effects. *Blender* simulates realistic optical properties and geometries while naturally accounting for realistic features of SFDI systems, which is why it was chosen for this work. *Blender* can be used for both geometry specification (i.e. design) via constructing materials of any desired shape, and simulation via ray-tracing with its engine Cycles, which will be discussed in depth in Sect 3.2.2. Shapes or geometries can be simulated with specific material properties of in-built shader nodes, of which different types will be presented in Sect 3.2.1 & 3.2.2. Different lighting conditions can be simulated with different intensities, colours, and shading, which will be further discussed in Sect 3.2.3. Rendering settings may be applied to a scene to make graphics more visually appealing, or

more realistic, which will be discussed in Sect 3.2.4. *Blender* has previously been used for three-dimensional shape measurement of additive manufacturing parts with complex geometries [183], for the development of anatomically accurate meshes to use in Monte Carlo light simulations [184], and for the generation of SFDI image data sets to train neural networks [185].

This section will discuss the development of an SFDI and fringe profilometry simulation in *Blender* (v 2.93). First the limitations of the initial material, using a subsurface scattering model, are discussed and why it was necessary to improve the model with volume absorption and scattering shaders. Next, the improved material model and simulated system are introduced, and methods for characterising the material are discussed. A robust method for morphology determination through fringe profilometry is then introduced. Finally, the development of a novel illumination scheme for imaging inside tubular geometries is presented.

3.2.1 Subsurface absorption & scattering material model

The initial simulation model was created by applying custom material properties to 3D objects in *Blender* [139]. The absorption and scattering were varied by the absorption factor and scattering factor, shown in Fig 3.2 (a). Absorption was implemented using a custom material simulating transmissivity of light through the material, calculated from the Lambert Beer Law [186]:

$$T = \frac{I}{I_0} = e^{-\mu_a L} \tag{3.1}$$

where I and I_0 are the transmitted and incident light respectively, L is the path length of light travelled and μ_a is the absorption coefficient of the material, which is set to 1 mm^{-1}. This was implemented with a transparent bi-directional scattering distribution function (BSDF) shader equally mixed with a refraction BSDF shader with a refractive index of 1.43. A weight factor termed the 'absorption factor' varied the observed colour of the refraction BSDF block from 0 (black, fully absorbing) to 1 (fully transparent). The structure of the absorption material is shown in Fig 3.2 (b).

Scattering was simulated by mixing two of Blender's prebuilt shaders: the transparent BSDF shader (which adds transparency to the material without adding refraction) and the subsurface scattering shader (which simulates light rays penetrating the surface of the material and bouncing around inside until they either escape or are absorbed). A weight factor termed the 'scattering factor' was varied between 0 and 1 to control how much of the composite materials' properties arise from the subsurface scattering component vs the BSDF component, which was implemented using a 'mixing' shader. A scattering factor of 0 resulted in a fully transparent material whilst a scattering factor of 1 resulted in fully subsurface scattering material. The subsurface scattering material has a scattering radius and scale properties that were adjusted in advance such that the total scattering is very high, which then represents the maximum scattering that can be achieved by this mixing approach. The structure of the scattering material is shown in Fig 3.2 (b).

The 'final factor' was a weighted mix of the absorbing and scattering components, where a factor of 0 simulated a material only dependent on the scattering component and a factor of 1 simulated a material only dependent on the absorption component.

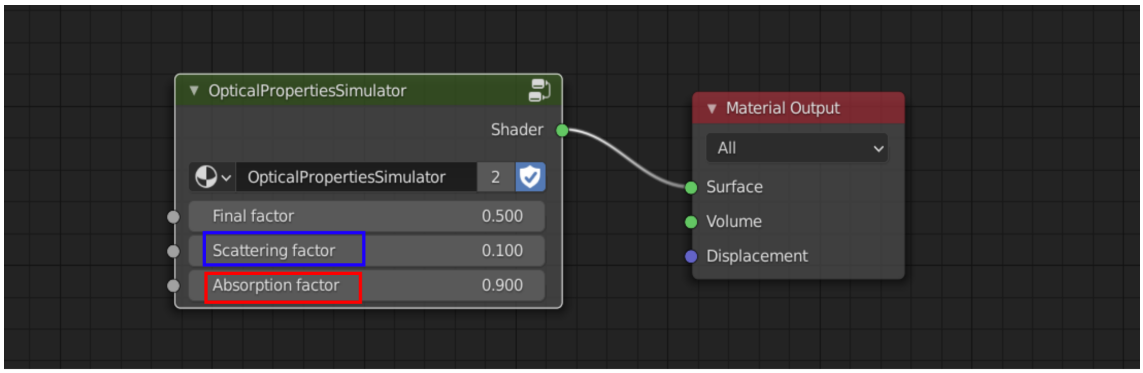

(a)

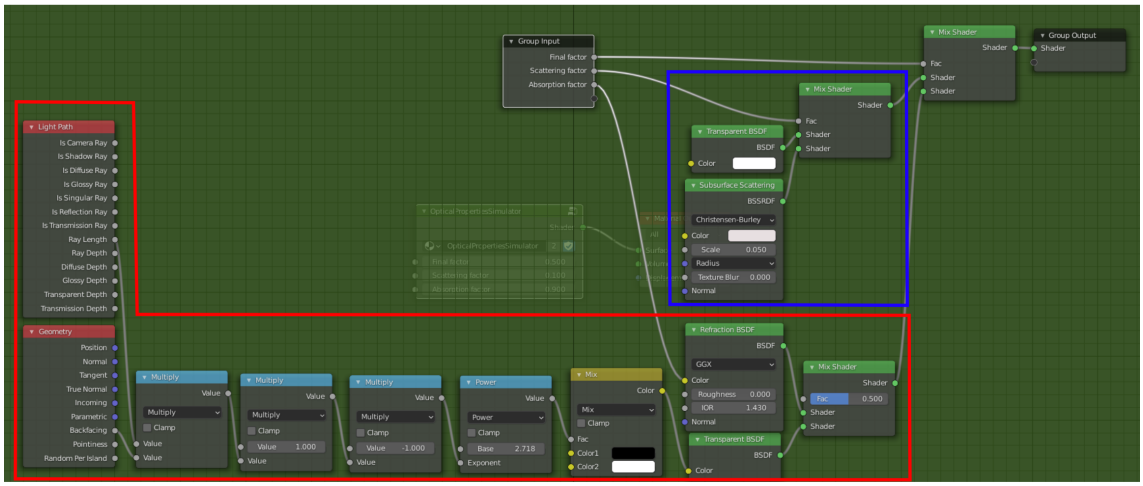

(b)

Figure 3.2: Material nodes in *Blender* to simulate the subsurface absorption and scattering material (a) final factor alters the weighted mix between absorption and scattering material, scattering factor alters the weighted mix of the nodes simulating scattering within the material and absorption factor alters the weighted mix of material colour. (b) showing the input to the *OpticalPropertySimulator* shown in (a) where the absorption material simulation is boxed in red and the scattering material simulation is boxed in blue.

Though this approach works in many realistic operating regimes (in reflectance imaging), it is limited because the sub-surface approximation applies only at surfaces and not in the entire material volume. Therefore, the detection of transmitted light through a sample is not possible with this model, which is necessary for DIS calibration, which will be discussed in Sect 3.2.5.

3.2.2 Volume absorption & scattering material model

The model described in Sect 3.2.1 is improved upon be modelling the material using a volume shader instead of surface shader, exploiting Blender's built-in volume absorption and volume scattering functionalities. This was done using the built-in ray-tracing engine Cycles. Cycles is a physically based path tracer, in which rays of light are randomly generated and traced from each camera pixel into the scene. Here, it can be absorbed, reflected, refracted or scattered, analogous to a Monte Carlo simulation [8]. Cycles simulates volume scattering inside objects using a Henyey-

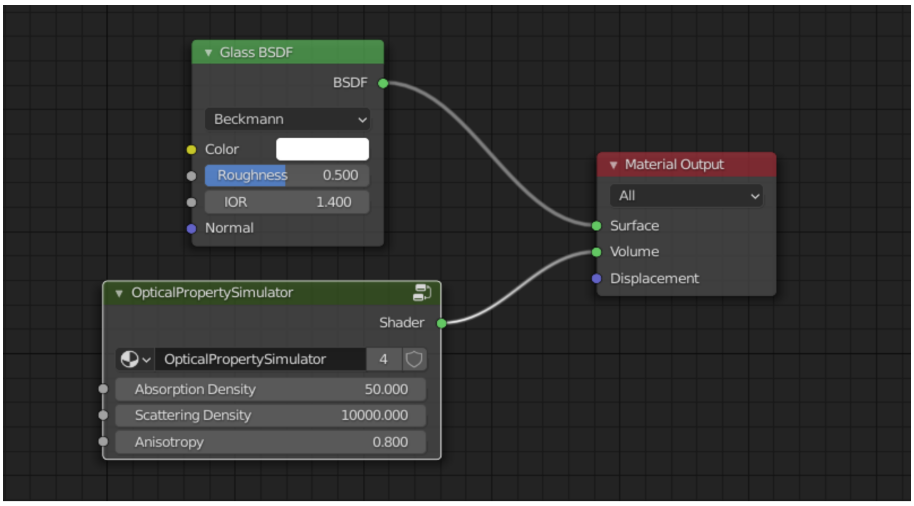

(a)

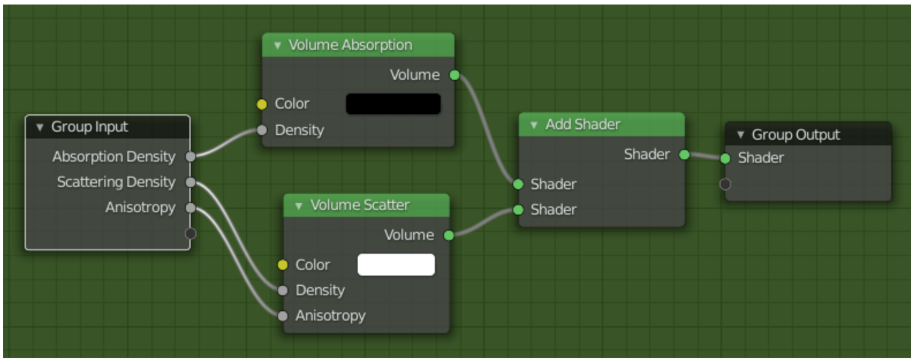

(b)

Figure 3.3: Material nodes in *Blender* to simulate the material (a) where the index of refraction (IOR) is set to 1.4, absorption density alters the material absorption, scattering density alters the materials scattering, and anisotropy is set to 0.8. (b) showing the input to the *OpticalPropertySimulator* shown in (a) where the in-built absorption and scattering volume shaders are input

Greenstein Phase function, which is commonly used in Monte Carlo simulations of tissue [11, 187], as discussed in Sect 1.1.2. Therefore, it is expected that the results from Cycles will broadly match those from Monte Carlo simulations.

The absorption and scattering are varied by changing the density parameters of the nodes: absorption density A_ρ and scattering density S_ρ respectively, as shown in Fig 3.3 (a). The anisotropy, g, in the volume scatter node was set to 0.8. This value is representative of typical anisotropy values measured for tissue at the GI junction [36]. The refractive index of the material is set to $n = 1.4$ by connecting a glass bi-directional scattering distribution function (BSDF) shader node to the surface input of the material. This shader was set to have a surface roughness of 0.5. This was set as a roughness of 0 implemented a perfectly smooth surface on which visualisation of projection patterns was not possible. Fig 3.3 (b) shows the inputs to the node tree in Fig 3.3 (a).

The anisotropy set in the volume scattering shader does not entirely determine the overall anisotropy of the material as it is mixed with the volume absorption shader, which assumes an anisotropy of 1 as light is not scattered. The impact of this inaccuracy in anisotropy cause by the mixing of these shaders was investigated,

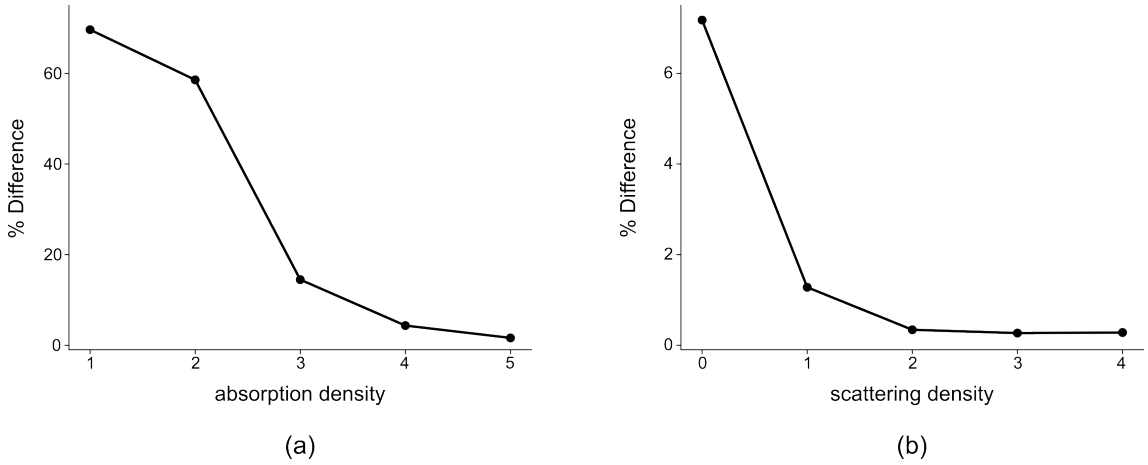

Figure 3.4: Setting requirements for semi-infinite material. Percentage difference from red sphere region to bulk material region for (a) increasing absorption density with no scattering density and (b) increase scattering density with no absorption density present.

and will be discussed in Sect 3.2.5.

Blender supports tri-colour operation so it can provide physically realistic scattering at green and blue wavelengths if desired. However, the volume absorption, scatter and surface reflectance was configured to be equal in these three bands, simulating a white material. In Blender, this is achieved by setting the colour parameter of the shader nodes to white (RGB $= (1.0, 1.0, 1.0)$). Further, when capturing image data, the red channel of the RGB colour images was extracted.

In order to use a LUT generated from a Monte Carlo simulation or the diffusion approximation, both of which will be discussed in Sect 3.2.5, the semi-infinite thickness requirement must be met [188]. To set an appropriate thickness for the material to meet this property, a red sphere was placed behind the bulk material with variable A_ρ and S_ρ properties, as discussed above. A camera directly above the bulk material captured an image of bulk material such that when $A_\rho = S_\rho = 0$, the red sphere was visible in the centre of the image. The A_ρ and S_ρ parameters of the bulk material were then varied until the difference in intensity between a 20×20 pixel region within the red sphere boundary and a 20×20 pixel region outside the red sphere boundary was $\leq 1\%$. For a material of 2 m thickness (to meet the semi-infinite thickness requirement of the diffusion approximation as discussed in Sect 1.1.1), this threshold was achieved for $A_\rho > 5$ when $S_\rho = 0$, shown in Fig 3.4 (a), and for $S_\rho > 4$ when $A_\rho = 0$, shown in Fig 3.4 (b). These are therefore the lower bounds of the material parameters in the simulation, which is agreeable as the material simulated had values much larger than these limitations, as shown in Sect 3.3.1. However, this limitation could be circumvented by using an empirically derived LUT calibrated to a particular physical thickness. The scene was illuminated by a sun light source of strength 10.

3.2.3 System & sample geometries

The simulated SFDI and fringe profilometry system consists of a camera placed 0.5 m above the sample of interest and a projector, placed at a 4° offset to the camera

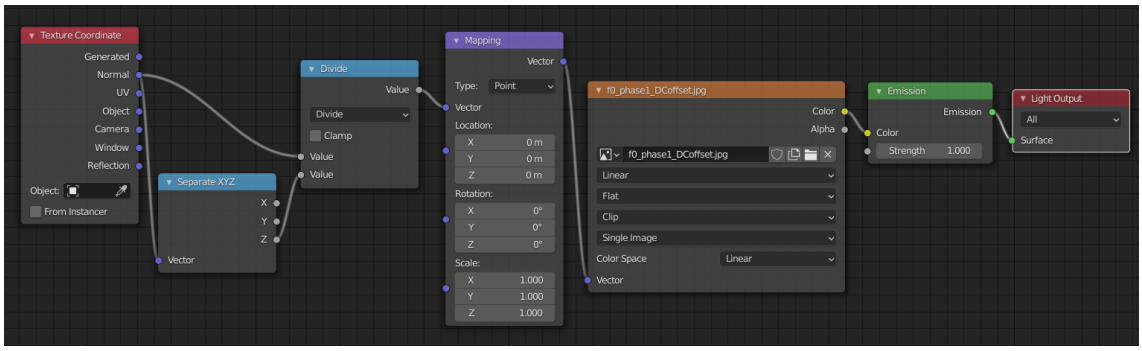

Figure 3.5: Nodes creating a projector in *Blender*.

to reduce any specular reflections. The camera and projector were placed at the same height from the sample, at 0.035 m apart. The projector is a spot light source that has been converted to be capable to project an image of interest into the scene, as shown in Fig 3.5. It has a power of 5 W (where this calculated in *Blender* by watts per square meter per steradian), a spotlight angle beam of 126° and a blend of 0.15, which is the softness of the spotlight edge. The texture coordinate normal of the spot light is divided by the z of the normal and this is mapped into vector format. An image texture is then applied, the emission strength is set, and the output light acts as a projector, projecting the image texture that had been input. It was ensured that the colour space in the image texture node was always set to linear after inputting a new image texture.

The aim was to create a simulation of an SFDI system with biologically relevant samples, and so two disease states relevant for detection of cancer in the upper GI tract were identified: squamous cell carcinoma (SCC) and Barrett's Oesophagus (BO) [42]. SCC was modelled as tumour spheroids using sphere meshes scaled to be 80 mm in diameter (40 mm height from the base material), as shown in Fig 3.6 (a). This large size is for demonstrative purpose and is not indicative of the actual physical size of tumour spheroids. It is noted that the *'scale'* parameter of the object in Blender should be reset when the desired size is reached to ensure proper behaviour with regard to scattering length scales. At 635 nm (i.e. data from the red channel), the absorption coefficient of SCC is 0.12 mm^{-1}, which is much greater than that of healthy oesophageal tissue, 0.058 mm^{-1}, and the reduced scattering coefficient of SCC, 0.64 mm^{-1}, is less than that of healthy oesophageal tissue, which is typically 0.75 mm^{-1} [47]. To simulate BO, two materials were placed adjacent to one another: one with the optical properties of healthy oesophageal tissue and the other with the optical properties of BO, as shown in Fig 3.6 (b). At 635 nm, the absorption coefficient of BO with mild chronic inflammation is 0.057 mm^{-1}, which is similar to that of healthy oesophageal tissue, while the reduced scattering coefficient of BO with mild chronic inflammation, 0.51 mm^{-1} is much less than that of healthy oesophageal tissue [47].

More in depth information on using the simulated model is given in Appendix F.

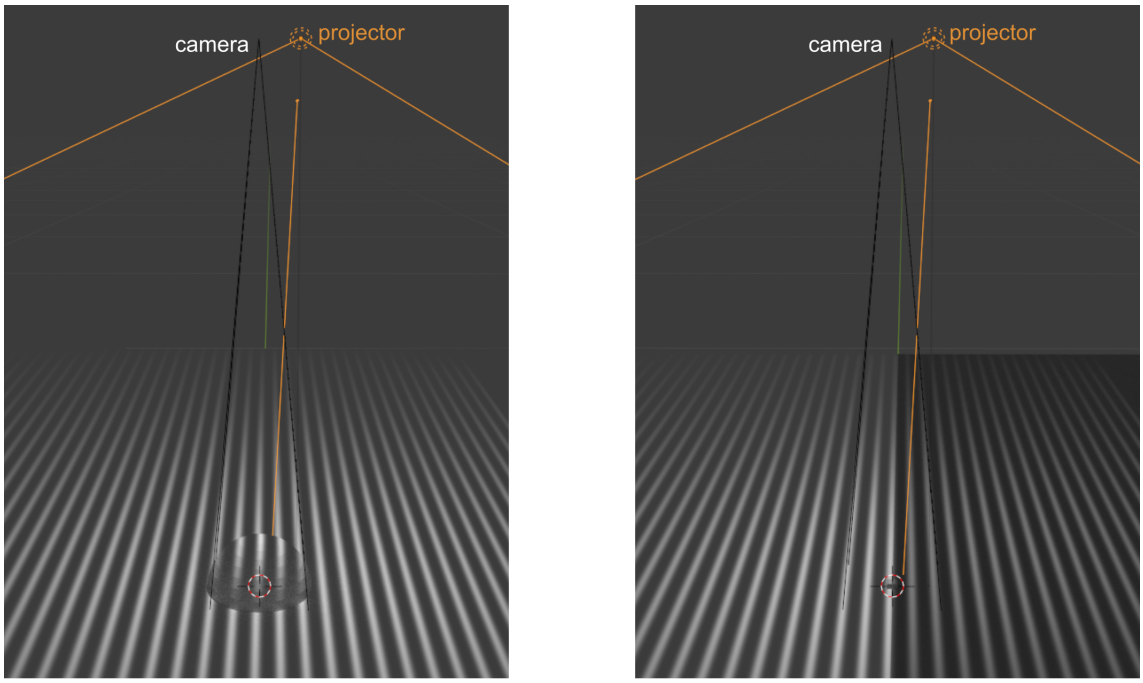

(a) (b)

Figure 3.6: Captured image of simulated system of (a) a spheroid simulating squamous cell carcinoma on top of a background of healthy oesophageal tissue and (b) two optically varying materials adjacent to one another simulating Barrett's Oesophagus (right) adjacent to healthy oesophageal tissue (left)

3.2.4 Render settings

To achieve the most physically realistic ray-traced renders in *Blender*, some optimisation of the render settings is required. Within the ray-tracing engine Cycles, the maximum number of bounces a light ray can travel before the simulation terminates can be set. This value is set to 1024, the highest allowed. It was found that, for a semi-infinite material simulating healthy oesophageal tissue (for which characterisation will be discussed in Sect 3.2.5), halving the maximum number of bounces from 1024 to 512 resulted in a minimal decrease in the AC and DC modulation amplitudes of 0.03% and 0.2% respectively, as depicted in Fig 3.7 (a & b). This shows that a limit of 1024 is likely to be sufficient for most important practical cases. Clamping of direct and indirect light, which limits the maximum intensity a pixel can have, was disabled by setting both to 0. Colour management, which is typically used to make visually appealing images but introduces unwanted artefacts such as gamma correction, was disabled by setting the display device to *'None'*. View transform was set to *'Standard'* to ensure no extra processing is applied to the resulting images. The sequencer, which sets the the colour space, was set to *'Raw'* to avoid unwanted colour balancing or further gamma correction. For all images rendered, the camera exposure is adjusted in accordance with *Blender* documentation [189] to avoid saturation while maximising power of detected signal, but the images must then have their intensities corrected by following the equation:

$$I_{output}(x, y) = I_{render}(x, y) \times 2^{t_{exposure}} \tag{3.2}$$

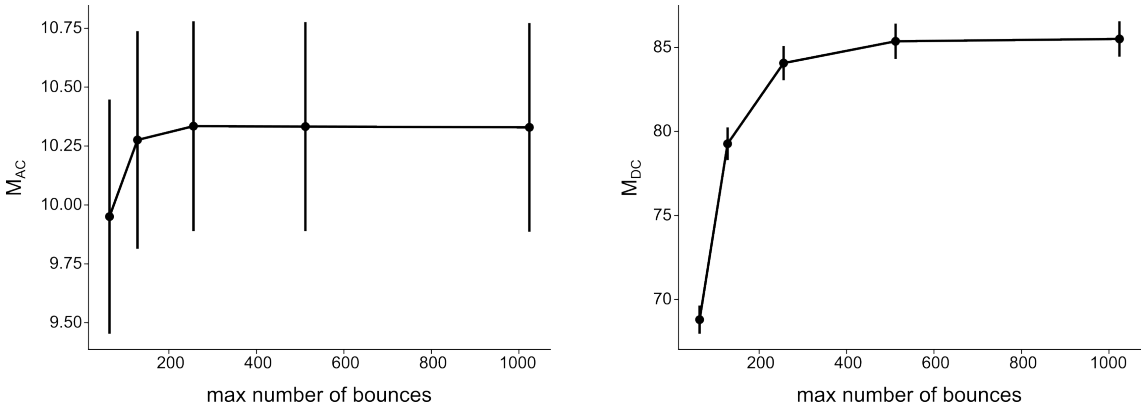

Figure 3.7: Increasing maximum number of bounces in Cycles and calculated (a) AC modulation amplitude and (b) DC modulation amplitude. The errors bars represent the standard deviation across a 500 × 500 pixel region.

where I_{output} is the exposure-corrected intensity required, I_{render} is the raw value obtained following the render, and $t_{exposure}$ is the exposure setting.

Rendering a single frame may take some time, especially if the max bounces of light in render properties is set to the maximum value. Therefore, the animation feature within *Blender* is used to allow parameter sweeps in individual settings, such as in the camera, projector, sample position, sample absorption and sample scattering, as an example. This allows a render to be left running for several hours, without need of intervention. Here, the animation of the projector to project phase shifted patterns sequentially is explained. This set up is analogous to Fig 3.5 except the vector mapping goes into several different image textures which are then set to the light output through using multiple *Mix shader* nodes. *Mix shader* works by having a weighted mixture of its two inputs; where 0 returns an output of the first material, 0.5 returns an output of 50% of each material and 1 returns all the second material. Therefore if, say, two different image textures are desired to be projected sequentially, one must first go to the animation tab in *Blender* and set the start and end number of animations in the bottom right (in this case 1 is the start and 2 is the end number of animations). One then goes back to the shading element where the mix shader is added between the two image textures. The mixing factor must be set to 0 and this element is right clicked on to insert a keyframe. This tells the animation that when one is this frame, the mix shader mixing factor will be 0, indicating that the first inputted image will be projected. Back in the animation tab, the selected frame must be changed from 1 to 2. Then one must go back to the shader nodes for the projector and change the mixing factor from 0 to 1 and repeat the insertion of a keyframe, described above. Now, when one is in frame two, the second image texture inputted to mix shader will be projected. Therefore, when an animation is rendered, two frames will be output: the first with a capture of the first projected image texture and the second with a capture of the second projected image texture.

3.2.5 Calibrating material properties

For SFDI measurements, a reference material of known optical properties is required to correctly calibrate the system response (as discussed in Sect 1.3.1). This requires

determining the relationship between the material parameters in *Blender* and the recovered absorption and reduced scattering coefficients. This can be done directly with an SFDI system through a 'trial and error' approach [139] but this is imprecise and laborious. Therefore, a more accurate approach is desired.

Double integrating sphere

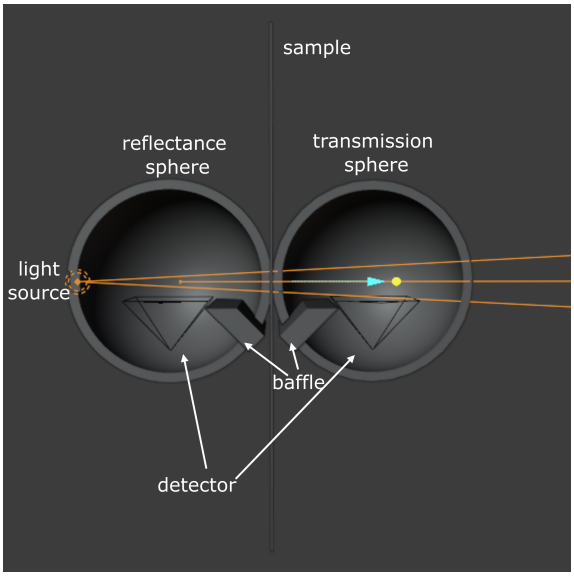

Figure 3.8: Double integrating sphere (DIS) set-up in *Blender* with light source entering a reflectance sphere, passing through a thin sample of material of interest and entering the transmission sphere. Baffles are placed to block specularly reflected sample rays.

A DIS system was simulated in *Blender*, shown in Fig 3.8. A double integrating sphere captures the reflected and transmitted light from within two spheres placed either side of a sample of interest, from which the optical properties of that sample can be inferred [190]. Absorption and reduced scattering coefficient measurements from DIS and SFDI are expected to show errors of up to 20% and 14% respectively, at 675 nm [166]. Nonetheless, it was decided to be an acceptable starting point for system calibration. The simulated DIS consists of two hollow spheres, termed the 'reflectance' sphere and 'transmission' sphere, each with 100 mm diameter and 10 mm wall thickness. The material of these spheres is set to be highly reflective using the diffuse BSDF shader with 0 roughness and reflectance of 0.99 (configured by setting the colour parameter to white, with a brightness value of 0.99). The reflectance sphere has an entry port and an exit port, with the sample located at the exit port. The ports are square in shape with a 10 mm side length. The transmission sphere has only an entry port, where the sample is located, of the same shape and size as the reflectance sphere exit port. The sample has a thickness of 1 mm. The material of the sample is that of the material described in Sect. 3.2.2. The input light source is a spot light of power 5 W, with a beam radius of 0.5 mm and a beam expansion angle of 6°. The light is placed at the entry port of the reflectance sphere. Cameras are placed at the base of each of the spheres to act as detectors, with all pixels summed together (i.e. integrated over the detector area) to give a power value. For initial tests, only the red channel is considered. Baffles

are placed between the sample ports and the cameras to block specularly reflected light from the sample entering the cameras. To perform normalisation, a reflectance standard sample is simulated using the diffuse BSDF shader with roughness set to 0 and reflectance of 0.7 to improve accuracy in absorption coefficient determination [173]. For each captured image, the camera exposure was varied until the average intensity was approximately in the middle of the $0 - 255$ range (i.e. 8-bit colour). This exposure was noted and corrected for using Eq 3.2.

To determine the absorption and reduced scattering coefficients, a series of images in the reflectance sphere and the transmission sphere are captured. From these images, the normalised reflectance, M_R, and transmission, M_T, are calculated for varying sample material properties using the equations [173]:

$$M_R = r_{std}\frac{R_2(r_s^{direct}, r_s, t_s^{direct}, t_s) - R_2(0,0,0,0)}{R_2(r_{std}, r_{std}, 0, 0) - R_2(0,0,0,0)} \tag{3.3}$$

$$M_T = \frac{T_2(r_s^{direct}, r_s, t_s^{direct}, t_s) - T_2(0,0,0,0)}{T_2(0,0,1,1) - T_2(0,0,0,0)} \tag{3.4}$$

where

- r_{std} is the normalised reflectance of the reflectance standard. A reflectance standard is a highly reflective diffuse material which exhibits isotropic diffuse reflection, with a typical normalised reflectance value of 1 [191].

- $R_2(r_s^{direct}, r_s, t_s^{direct}, t_s)$ is a reflectance measurement when the sample material is in place, where r_s^{direct} indicates reflection off the sample of interest is present, r_s indicates reflection off the reflectance sphere is present, t_s^{direct} indicates transmission from the sample of interest is present and t_s indicates the presence of reflected light within the transmission sphere is present.

- $T_2(r_s^{direct}, r_s, t_s^{direct}, t_s)$ is a transmission measurement when the sample material is in place.

- $R_2(r_{std}, r_{std}, 0, 0)$ is a reflectance measurement when the reflectance standard previously described is simulated in between the two spheres instead of the sample material, where the 0 values in brackets represent the removal of the transmission sphere.

- $R_2(0,0,0,0)$ is a reflectance measurement when there is no sample present and the transmission sphere is removed. The first two 0 values in brackets indicate the lack of a sample or reflectance standard and therefore lack of reflection in the reflectance sphere, and the second two 0 values in brackets indicate the removal of the transmission sphere.

- $T_2(0,0,1,1)$ is a transmission measurement when there is no sample present and therefore light passes straight through the reflectance sphere into the transmission sphere. The first two 0 values in brackets indicate the lack of a sample or reflectance standard and therefore lack of reflection in the reflectance sphere. The two 1 values in brackets indicate the presence of the transmission sphere and presence of reflections off the inner transmission sphere surface.

- $T_2(0,0,0,0)$ is a transmission measurement when the incident light beam is blocked and there is no sample in the port. The first two 0 values in brackets indicate the lack of a sample or reflectance standard, and also the lack of reflections in the reflection sphere due to the blocked beam of incident light. The second t 0 values represent the lack of transmission measurements and reflections off the inner transmission sphere due to the blocking of incident light

These normalised values are then input into an inverse adding-doubling (IAD) algorithm to determine the sample material optical properties [192]. The adding-doubling method is an accurate solution to the radiative transport equation, which was introduced in Sect 1.1, and is used to calculate reflectance and transmittance values. Therefore, the *inverse* adding-doubling method determines the optical properties of a sample from reflectance and transmittance values. It does this through an iterative approach, where first a set of optical properties are guessed and values for M_R and M_T from above are calculated. If these calculated values match the measured values, then the guessed optical properties are a match for the optical properties of the measured sample. If these calculated values do not match, a new set of optical properties is guessed and the process is repeated [173].

For a material of $A_\rho = 1$, the absorption coefficient measured from the DIS was > 0.1 mm^{-1}, for a material that should be measuring close to no absorption. This may be for several reasons. First it may be due to the difficulty in the DIS set-up in detecting low absorption coefficients due to the loss of light at the sample-sphere interface, causing a higher, false absorption coefficient to register [193, 194]. It may also be due to an inaccuracy in transmission measurements due to high forward scattering of the sample, resulting in inaccurate retrieval of low absorption coefficients [195]. While experimental work has been done on altering the sample thickness and DIS configuration to improve optical property measurements [196], a different approach was taken here. It was assumed that the unaccounted light lost causes an offset in the measured absorption coefficient. Therefore, as a first approximation, for all bulk material optical properties determined, the IAD measured absorption coefficient of the material with an absorption density of 1 (averaged over all scattering densities measured) was subtracted from the measured absorption coefficient to account for this offset.

Retrieval of optical properties from the IAD algorithm was obtained for different bulk material values of A_ρ : $50, 75, 100$ and S_ρ : $5000, 10000, 20000$, totalling 9 material optical property values. From the IAD algorithm, these material values correspond to optical property values in the range $\mu_a = 0.08$ to 0.22 mm^{-1} and $\mu_s' = 1.4$ to 6.5 mm^{-1}, with the absorption correction discussed above applied. These values represent a very wide range of optical properties over which to evaluate the model. From these values, it was possible to determine the A_ρ and S_ρ values needed to simulate the optical properties of squamous cell carcinoma (SCC) and Barrett's oesophagus (BO), as discussed in Sect 3.2.3. Healthy background tissue was configured with $A_\rho = 37$ and $S_\rho = 2591$ and SCC polyps was configured with with $A_\rho = 69$ and $S_\rho = 2253$. BO material was configured to have $A_\rho = 37$ and $S_\rho = 1855$.

To evaluate the performance of SFDI, images were captured in the SFDI set-up using a projected spatial frequency of 0.2 mm^{-1}, described in Sect 3.2.3, for these same 9 material parameters of A_ρ : $50, 75, 100$ and S_ρ : $5000, 10000, 20000$. The

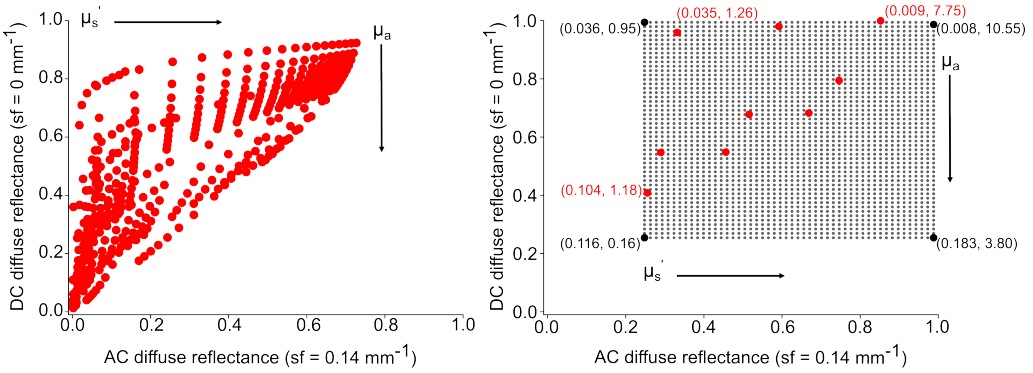

Figure 3.9: (a) DC vs AC reflectance showing values sampled for MC LUT. (b) DC vs AC reflectance showing values sampled for empirically derived LUT. Red dots represent simulated optical properties and black dots represent extrapolated sample points for larger LUT. Optical properties of selected points are displayed as (μ_a, μ_s') with units mm^{-1}.

optical properties of these SFDI captures were calculated using two different LUTs: a Monte Carlo generated LUT and an empirically-derived LUT.

SFDI: Monte Carlo LUT

The Monte Carlo (MC) LUT was generated using Virtual Photonics MC simulation software [12]. This allows the capability to sample a large range of μ_a and μ_s' values, so a range that covers the same 9 material samples measured in the DIS, and also covers the range of chosen biomedical examples of imaging SCC and BO, is selected. The ranges of the LUT are therefore $\mu_a = 0.001$ to 0.3 mm^{-1} and $\mu_s' = 0.1$ to 8.5 mm^{-1}. The spacings within these ranges are variable, but are depicted in Fig 3.9 (a). For comparison with the IAD algorithm, the optical properties of the 9 material values were calculated using a reference material of $A_\rho = 100$ and $S_\rho = 20000$ with the corresponding reference optical properties determined from the IAD algorithm.

SFDI: Empirically-derived LUT

The empirically-derived LUT is able to correct for discrepancies between the SFDI and DIS measurements which arise from the different assumptions made in the models [166]. To generate an empirical modulation vs reflectance LUT, the process described by *Erickson et al.* [19] was used. The reflectance and modulation are calculated via the equations:

$$R(x,y) = \frac{M_{DC,sample}(x,y) \times R_{std}}{M_{DC,std}(x,y)} \tag{3.5}$$

$$M(x,y) = \frac{M_{AC,sample}(x,y)/M_{DC,sample}}{M_{AC,std}/M_{DC,std}} \tag{3.6}$$

where M_{AC} and M_{DC} are calculated via Eqs 1.26 and 1.27 respectively and $M_{DC,sample}$ represents the DC modulation amplitude of the sample of interest and $M_{DC,std}$ is the DC modulation amplitude of a reference standard with known reflectivity of R_{std}.

The modulation and reflectance of planar samples with absorption and scattering densities the same as the 9 data points used for the IAD were obtained. Then, a first order linear extrapolation was performed using these data points to increase the LUT from 9 data points to 100×100 data points, improving granularity of final optical properties. This is shown in Fig 3.9 (b). Given the relative smoothness of the surface sampled by the original 9 points, it was found that this extrapolation gives reliable and consistent results for later optical property estimation including of SCC and BO samples. When applying the LUT, a further interpolation step, this time using bicubic interpolation, is carried out to determine the optical properties of a sample of interest.

Effective anisotropy

As previously discussed, the set anisotropy of the material does not entirely determine the overall anisotropy due to the volume absorption and volume scatter nodes being mixed. To examine the impact this inaccuracy in anisotropy has, data is first taken with the DIS. The bulk material anisotropy, g, is kept constant at 0.8, and the assumed anisotropy input into the IAD algorithm was varied. This was repeated for anisotropy values from $0.65 - 0.95$ in increments of 0.5. Next, several MC LUTs over the same anisotropy range $(0.65 - 0.9)$ were simulated using Virtual Photonics software [12]. SFDI data was taken where the bulk material anisotropy was kept constant at 0.8 and the reduced scattering coefficient was measured using the generated LUTs of different anisotropy values. The recovered reduced scattering coefficient for the SFDI method was compared to the reduced scattering coefficient from the IAD algorithm for various different assumed values of anisotropy. When the reduced scattering coefficients of both the SFDI and IAD measurements intersected, the corresponding value of anisotropy was determined to be the effective anisotropy, g_{eff}, of the simulated system.

3.2.6 Robust shape determination

In addition to measuring optical properties, the 3D shape of objects was reconstructed via fringe profilometry. For proof-of-principle, a generalised approach is executed of using 3 phase-shifted images to reconstruct height maps, though if speed is desired a single image is sufficient [197]. To do this, the possibility of using N frames is considered (see Appendix E). Once the phase ϕ is extracted, it can be converted to height for each pixel in the image (given that the geometry of the system is precisely known) using the equation [81]:

$$h(x, y) = \frac{l_0 \Delta\phi(x, y)}{\Delta\phi(x, y) - 2\pi f_0 d} \tag{3.7}$$

where l_0 is the distance from the projector to the reference material, $\Delta\phi$ is the phase difference between the actual phase (calculated) and the phase of the background reference plane, f_0 is the spatial frequency of the projected pattern and d is the separation distance of the projector and camera. Because of the geometrical assumptions made in mapping phase to height, this approach cannot be straightforwardly applied to non-planar geometries for shape reconstruction. In non-planar geometries, reconstruction of exact physical height could be approximately deduced

by comparison with a reference phantom, e.g. perfectly straight tube for a lumen geometry, or advanced techniques such as deep-learning could be applied [198].

3.2.7 Projection pattern for tubular geometry

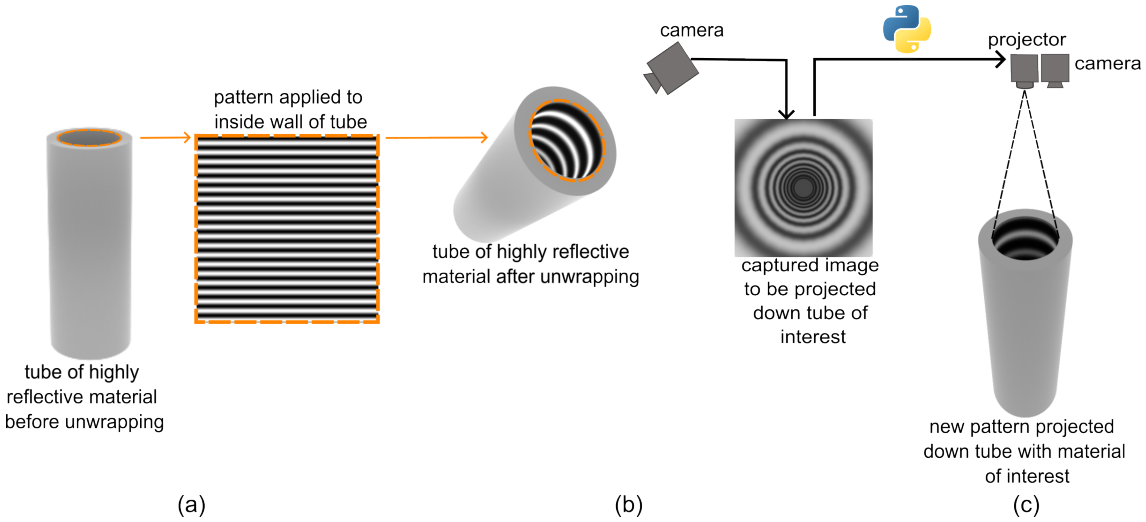

Figure 3.10: Pipeline of obtaining novel illumination pattern. First a tube of desired length and diameter is simulated. The inside wall of the tube is unwrapped such that it is flat, and the desired pattern is applied, in this case a sinusoid modulating in y. The inside of the tube is then wrapped with its new pattern. An image is captured of this new pattern, which is then post-processed in *Python* before being input to a projector to project down a tube with material properties of interest.

To simulate realistic gastrointestinal imaging, two imaging geometries are considered. The first, as previously discussed, simulates an 'up-close' view of a tumour on the wall of a large lumen and can be approximated by a planar geometry. However, for *in-vivo* endoscopic use, it is also necessary to consider a tubular geometry with a forward-facing wide field-of-view. The scenario of an SFDI system pointing down a tube simulating a lumen such as the GI tract is therefore also considered. Using the *Blender* simulation it is relatively straightforward to explore such a situation.

A tube of length 250 mm with an outer diameter of 80 mm and an inner diameter of 20 mm was first simulated. Epithelial layers of oesophageal tissue may be thinner than this [199], but for initial calibration it was desired to ensure the semi-infinite thickness requirement was met. The distal end of the tube is covered by the same material as the walls of the tube. A spot light source was placed at a distance of 100 mm from the top of the tube and projected a 2D sinusoidal pattern down the tube. This naive approach creates a non-uniform spatial frequency pattern throughout the length of the tube which makes reconstructing accurate optical properties challenging. Therefore, a process was developed to create a more suitable illumination pattern for other imaging geometries and demonstrated for the test case of a tube.

First, the material of the tube was set to be highly reflective using a pre-existing diffuse BSDF material node with a roughness of 0 and a shade of pure white. Next, the surface of the tube was 'unwrapped' within *Blender* using the UV mapping tool, resulting in a flattened map of the inside tube wall, shown in Fig 3.10 (a). A sinusoidal pattern of the desired phase and spatial frequency was then applied to

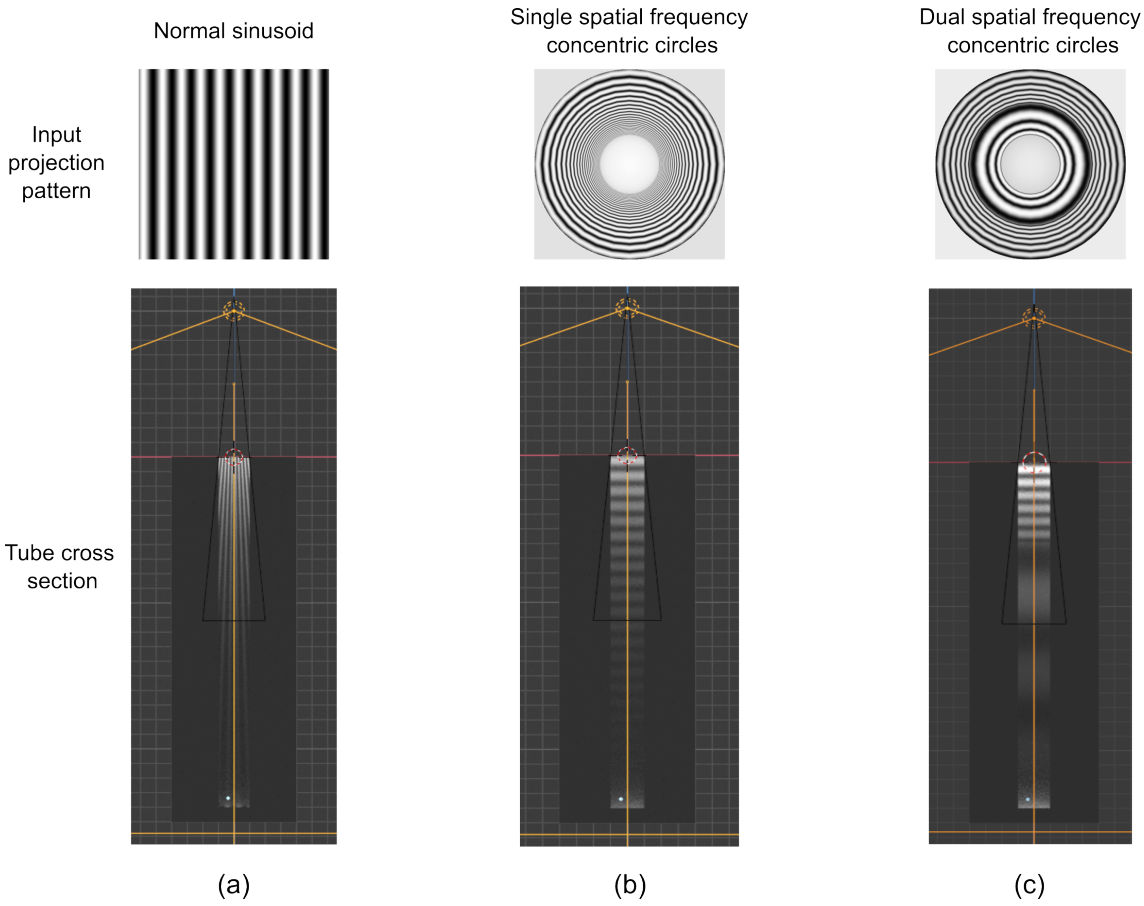

Figure 3.11: Comparing tubes with (a) planar sinusoidal pattern exhibiting varying spatial frequency along the length of the tube and (b) illumination pattern with two areas of constant spatial frequency in different lengths of tube (c) presented novel illumination pattern with constant spatial frequency down the length of the tube. Top insets show image being projected. Bottom insets show view of projected pattern down tube by view of tube cross sections.

this flat surface. Once applied, the material is then wrapped, such that the inside of the tube now has a uniform spatial frequency throughout its length. 40 1 W light sources were then placed equally throughout the tube length such that the intensity is uniform looking down the tube from the top. A camera placed 110 mm above the top of the tube then captured an image of the concentric circle illumination pattern (see Fig 3.10 (b)). This image was then exported to *Python* where a normalisation was applied to ensure that the sinusoid pixel values vary across the maximum range for projection $(0-255)$. This process was carried out for sinusoidal patterns of a fixed spatial frequency at 3 equal phase shifts. These normalised images are then used as the new projection patterns, which are projected into the tube which has the material of interest with a 5 W light source. A camera captures the reflected patterns, shown in Fig 3.10 (c). This process can be considered a 'pre-distortion' of the projected pattern to produce more uniform spatial frequencies and could alternatively be computed using analytically-derived formulae, or by direct inverse computation using a ray-tracing engine. These modified projection patterns can then be used for SFDI imaging as there is a now a uniform spatial frequency pattern within the geometry length. Fig 3.11 (a) depicts the projection of

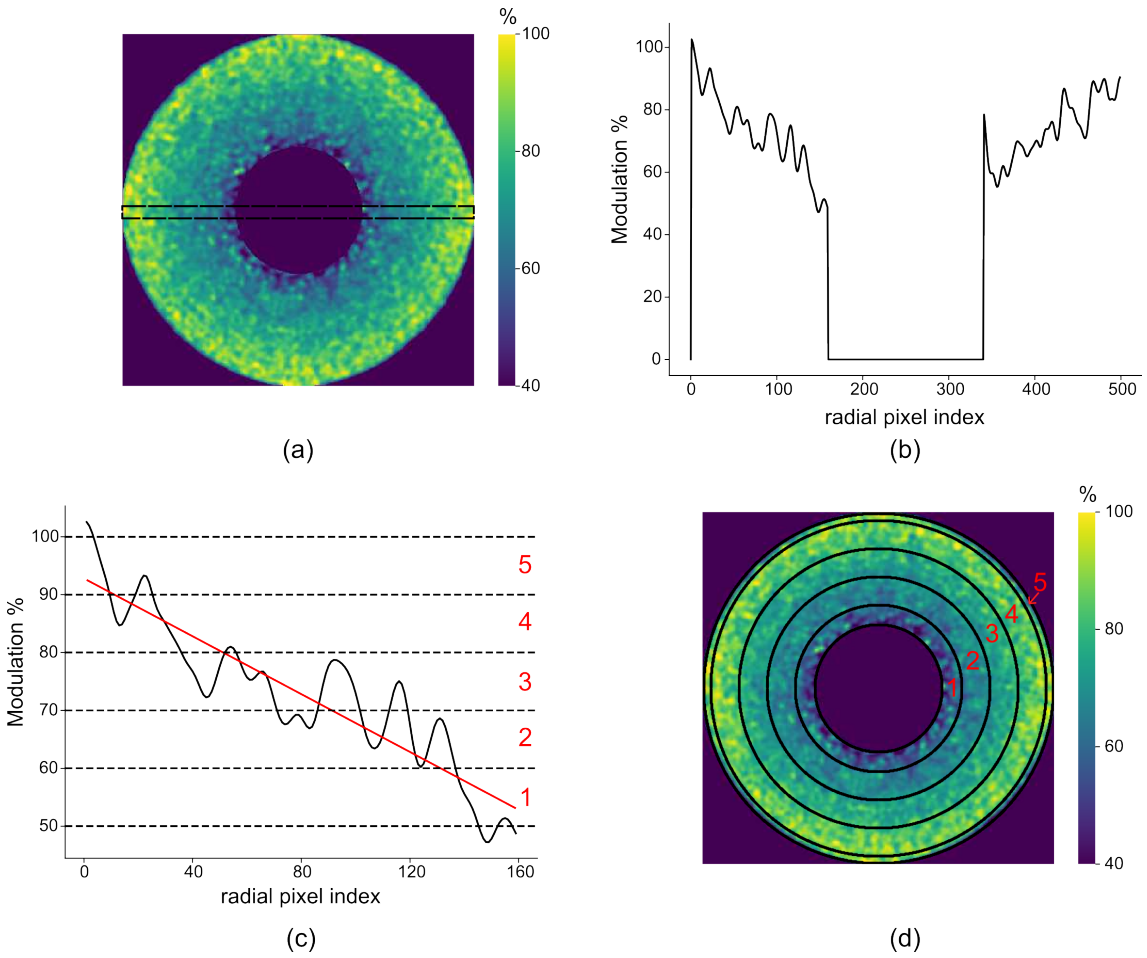

Figure 3.12: Tube sub-sectioning for multi LUT optical property measurement (a) top down image of modulation variation on inner tube wall of tube with optical properties typical of healthy oesophageal tissue. (b) Cross section of (a). (c) Left hand side cross section of (a) where a first order polynomial has been fitted to aid in subdivision of sections. (d) Modulation variation on inner tube wall showing 5 different subsections using different LUTs.

a conventional, 2D sinusoidal pattern down a tube, resulting in non-uniform spatial frequency pattern down the tubes length, while Fig 3.11 (b) depicts the projection of the above described, modified illumination pattern, resulting in a uniform spatial frequency pattern throughout the tube length.

The spatial frequency is visually difficult to detect at the distal end of the tube when looking from the proximal end, shown in Fig 3.11 (b). Therefore, a sinusoidal pattern with two different spatial frequencies was tested such that the spatial frequency in the upper quadrant of the tube is higher than the spatial frequency in the rest of the tube, as shown in Fig 3.11 (c). Two different LUTs were then used for the two different regions with discrete, different spatial frequencies. This projection pattern may be advantageous for different analyses in different lengths of the tube, for example viewing smaller features up close at the top of the tube and examining larger features further down the tube.

However, the tubular geometry inherently allows less light to reach the distal end of the tube and less light to be reflected back as only a small range of angles can escape the tube via the proximal opening. Light cannot escape through the

distal end of the tube as it is covered with the material of interest. The projector placement, at a large angle to the normal of the tube surface, also creates different incidence angles along the length of the tube. As such, many of the assumptions of the standard MC LUT do not apply in this geometry. It is therefore necessary to apply the empirically derived LUT approach in this case to account for these effects. Further, to account for variation along the tube, a longitudinal sectioning approach was developed: the tube is divided in 5 different longitudinal subsections, each with its own LUT. Fig 3.12 (a & b) show a top down image of the modulation variation within the tube and a cross section of this view respectively. The modulation can be seen to vary from 40% to 100% along the length of the tube wall. The five sections were selected as regions that showed a mean modulation difference $> 10\%$ relative to other sections, as shown in Fig 3.12 (c). A view of the five separate LUT sections within the tube is shown in Fig 3.12 (d).

3.3 Simulated system performance

Here the results are presented for the simulated SFDI and fringe profilometry system. First, the optical properties determined from the IAD algorithm, obtained from DIS data, are compared with SFDI measured optical properties of the same material using two different LUTs: a Monte Carlo LUT and an empirically-derived LUT. The effective anisotropy of the material is also determined and presented. Next, the successful imaging of typical gastrointestinal conditions is shown, again via the two LUT approaches. The minimal effect of altering the projector and camera angle with respect to one another is shown. Finally, images of optical property measurements in a tubular geometry from use of the novel illumination pattern are shown.

3.3.1 Material simulation

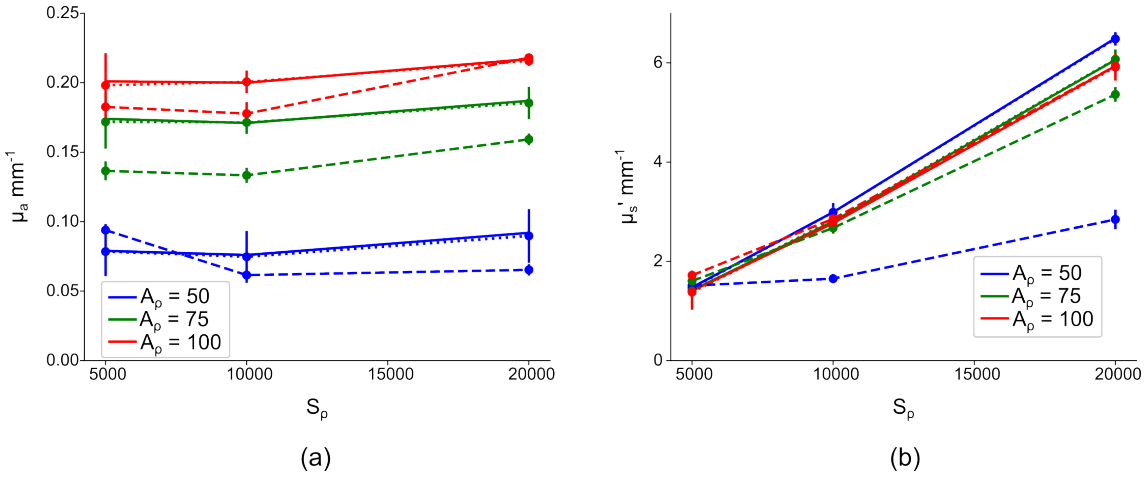

Figure 3.13: (a) Absorption and (b) reduced scattering coefficient vs scattering density, S_ρ, calculated for varying absorption densities, A_ρ, via IAD algorithm (solid line), SFDI Monte Carlo LUT (dashed line) and SFDI empirically derived LUT (dotted line). The error bars represent the standard deviation across the calculated 500×500 pixel optical property map.

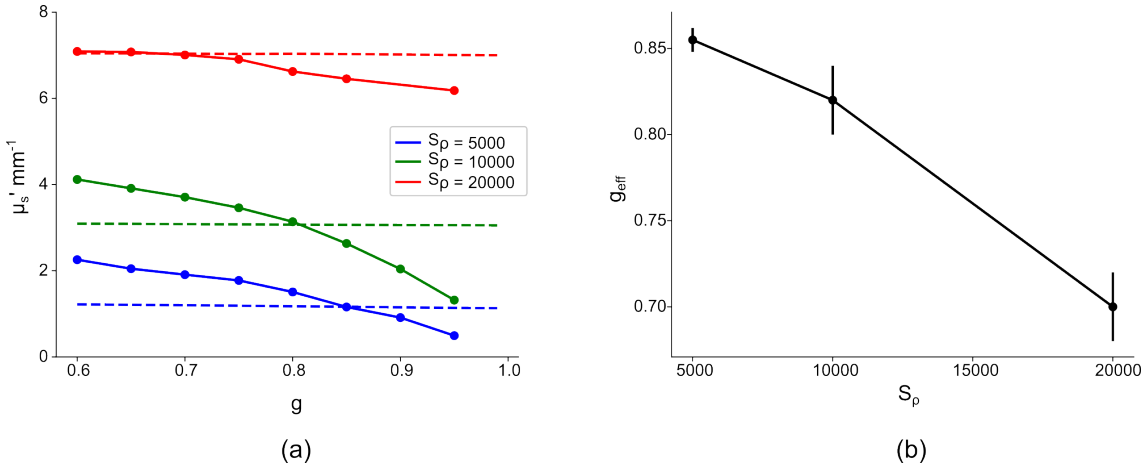

Figure 3.14: Determining g_{eff} (a) reduced scattering coefficient measured from SFDI Monte Carlo LUT (solid lines) and from IAD algorithm (dashed lines) for varying anisotropy g values, for $A_\rho = 50$. (b) Effective anisotropy found to correct for reduced scattering coefficient i.e. intersects from (a). Error bars represent standard deviation across g_{eff} over all bulk material absorption densities

By repeated DIS simulation, it was found that appropriate parameter ranges to produce the desired optical properties were $50 \leq A_\rho \leq 100$ and $5000 \leq S_\rho \leq 20000$. Material of $A_\rho = 100$ and $S_\rho = 20000$ with optical properties $\mu_a = 0.217$ mm^{-1} and $\mu_s' = 5.94$ mm^{-1} was selected to be the reference material for the SFDI measurements.

The results from the SFDI measurements are compared with the DIS results in Fig 3.13 (a & b). It is noted that there are discrepancies between the absorption and reduced scattering results from the IAD (solid lines) and the SFDI Monte Carlo LUT (dashed lines) calculations, with an average standard error of 16% and 18% respectively. This is caused in part because the different methodologies rely on different assumptions and have different sources of error, which will be discussed in Sect 3.4.2. However, these results can be improved by using the empirically derived LUT (dotted lines), reducing relative error in optical property measurements in comparison to IAD (solid lines) calculations to 1% and 0.7% for absorption and reduced scattering coefficients respectively.

The sensitivity and specificity of the *Blender* system using the Monte Carlo LUT results were assessed. It was found that the system is capable to differentiate absorption and reduced scattering coefficients with $\geq 99.5\%$ sensitivity and specificity, for absorption coefficient variances ≥ 0.04 mm^{-1} and reduced scattering coefficient variances ≥ 1.1 mm^{-1}. For $A_\rho = 50$, $S_\rho = 5000 - 10000$, the sensitivity and specificity for differentiating the reduced scattering coefficients is just 67% and 62% respectively, which corresponds to a reduced scattering coefficient variation of just 0.1 mm^{-1}. This in line with the American Society of Gastrointestinal Endoscopy guidelines, as discussed in Sect 1.2.2.

To examine the impact of inaccuracies in anisotropy caused by the mixing of *Blender* shaders, the reduced scattering coefficient measured from the IAD algorithm and SFDI measurement using Monte Carlo generated LUT for varying values of g was plotted. The results for one absorption density, $A_\rho = 50$, are plotted in Fig 3.14 (a), however other absorption densities produce similar results. Where the

measured reduced scattering coefficients intersect is where the effective anisotropy, g_{eff}, is determined to be, shown in Fig 3.14 (b). This is because this is where the DIS and SFDI data intersect and thus is assumed to be correct. For low scattering values, where the absorption shader is dominant, g_{eff} is observed to be greater than the anisotropy value of 0.8 specified in the scattering shader settings, but decreases to 0.7 for high scattering. This characterisation could be expanded to compute g_{eff} for a wider range of scattering values and hence increase accuracy of simulation. However, the use of an empirically-derived LUT naturally accounts for these discrepancies.

3.3.2 Simulation of typical gastrointestinal conditions in up-close planar geometry

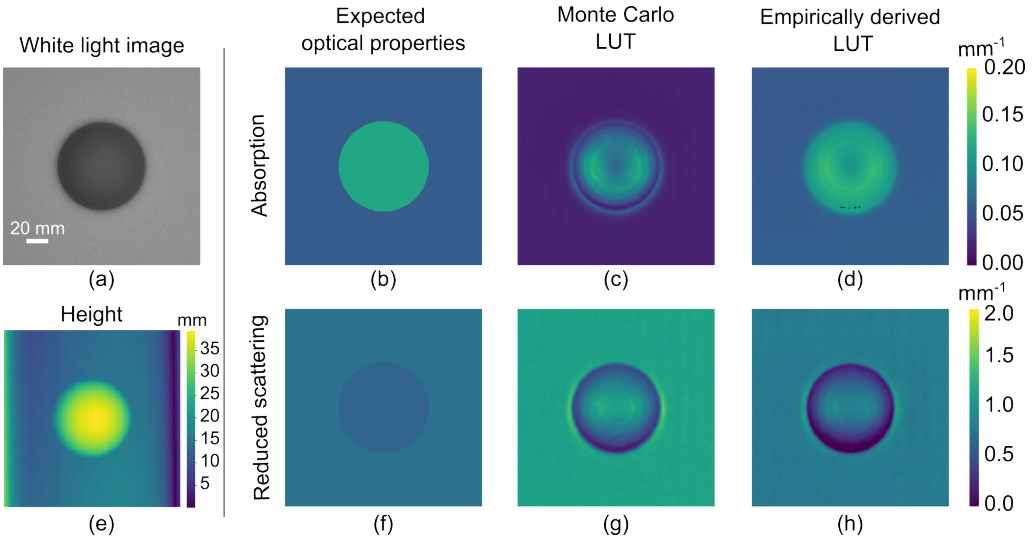

Figure 3.15: Simulated squamous cell carcinoma (SCC) as a spheroid on a background of healthy oesophageal tissue (HT) showing (a) white light image and (e) reconstructed height map with (b) expected absorption coefficient where, $\mu_{a,SCC}/\mu_{a,HT} \approx 2$, (c) μ_a recovered with MC LUT (d) μ_a recovered with empirically derived LUT (f) expected reduced scattering coefficient, where $\mu'_{s,SCC}/\mu'_{s,HT} \approx 0.85$, (g) μ'_s recovered with MC LUT and (h) μ'_s recovered with empirically derived LUT. Scale bar = 20mm.

The results for simulating typical gastrointestinal conditions in an up-close, planar geometry are presented here. Fig 3.15 shows the optical property and height maps generated for a 80 mm diameter simulated polyp, with an absorption coefficient higher than that of surrounding healthy tissue and a reduced scattering coefficient lower than that of surrounding healthy tissue, simulating squamous cell carcinoma. Fig 3.15 (a) shows a conventional white light image of the simulated sample, where quantitative variation in absorption and scattering is not-detectable. Fig 3.15 (b & f) depict the expected absorption and reduced scattering coefficient maps from IAD algorithm recovered material optical properties. Fig 3.15 (c & g) demonstrate successful recovery of optical properties using the Monte Carlo LUT, with average standard errors across the entire images of 62% and 51% respectively. Fig 3.15 (d & h) demonstrate successful optical property recovery using the empirically derived LUT, with average standard errors across the entire images of 5% and 16% respec-

tively. The empirically derived LUT produces results closer to the expected values, which is because it accounts for discrepancies in the tissue simulation as described earlier. However,the Monte Carlo LUT still provides high contrast between the squamous cell carcinoma and background, which is arguably more important for wide-field diagnostic applications. Fig 3.15 (e) shows a successful height map generation from fringe profilometry measurements. It is noted that because the surface profile information is available, the optical property accuracy may be improved by the addition of surface profile correction for optical property determination [79].

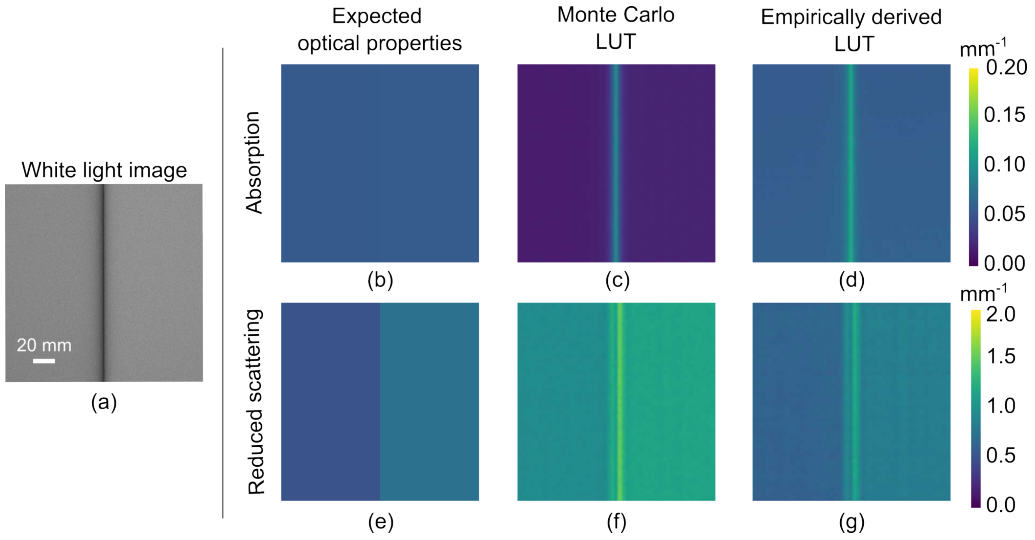

Figure 3.16: Simulated Barrett's Oesophagus (BO) with mild chronic inflammation (left half of sample) adjacent to healthy oesophageal tissue (right half of sample) showing (a) white light image (b) expected absorption coefficient, where $\mu_{a,BO}/\mu_{a,HT} \approx 0.99$, (c) μ_a recovered with MC LUT and (d) μ_a recovered with empirically derived LUT (e) expected reduced scattering coefficient, where $\mu'_{s,BO}/\mu'_{s,HT} = 0.68$, (f) μ'_s recovered with MC LUT and (g) μ'_s recovered with empirically derived LUT. Scale bar = 20mm.

Fig 3.16 shows the optical property maps generated for a segment of Barrett's oesophagus adjacent to a segment of healthy oesophageal tissue. The tissue properties are designed to exhibit similar absorption coefficients, while the reduced scattering coefficient of the simulated BO is less than that of the adjacent healthy oesophageal tissue. Fig 3.16 (a) shows a conventional white light image of the simulated tissue, from which it is difficult to visually detect any variation between the two material types. Fig 3.16 (b & e) represent the expected absorption and reduced scattering coefficient maps from IAD algorithm recovered material optical properties. Fig 3.16 (c & f) represent the measured absorption and reduced scattering coefficient maps using a Monte Carlo LUT, where the variation between simulated tissue types is as expected with average standard errors of 65% and 75% respectively. Fig 3.16 (d & g) represents a more accurate recovery of absorption and reduced scattering coefficient maps through use of the empirically derived LUT, with average standard errors of 10% and 22% respectively. It is noted that at the intersection region of the two simulated tissue types, there is a spike in both the optical properties, which results from effects at the interface and a small air gap that is present.

These results show the capability of the simulated system to successfully differ-

entiate between typical tissue types.

3.3.3 Effect of no DC projection

A planar sample of healthy oesophageal tissue with $\mu_a = 0.058$ mm^{-1} and $\mu_s' = 0.75$ mm^{-1} was imaged at two spatial frequencies: 0 and 0.2 mm−1. The optical properties of the sample were measured via two methods. The first method used Eqn 1.26 for the high frequency image captures and Eqn 1.27 for the low frequency image captures to determine the AC and DC modulation amplitudes respectively. The second method used Eqns 1.26 & 1.27 with just the high frequency image captures to determine the AC and DC modulation amplitudes respectively. This was done to investigate the effect of projections on optical property variation for experimental work which will be discussed in Chapter 4. For a sample simulating healthy oesophageal tissue, it was found that this variation in M_{AC} and M_{DC} resulted in absorption and reduced scattering coefficient differences of just 0.13% and 0.03% respectively.

3.3.4 Effect of projector & camera angle

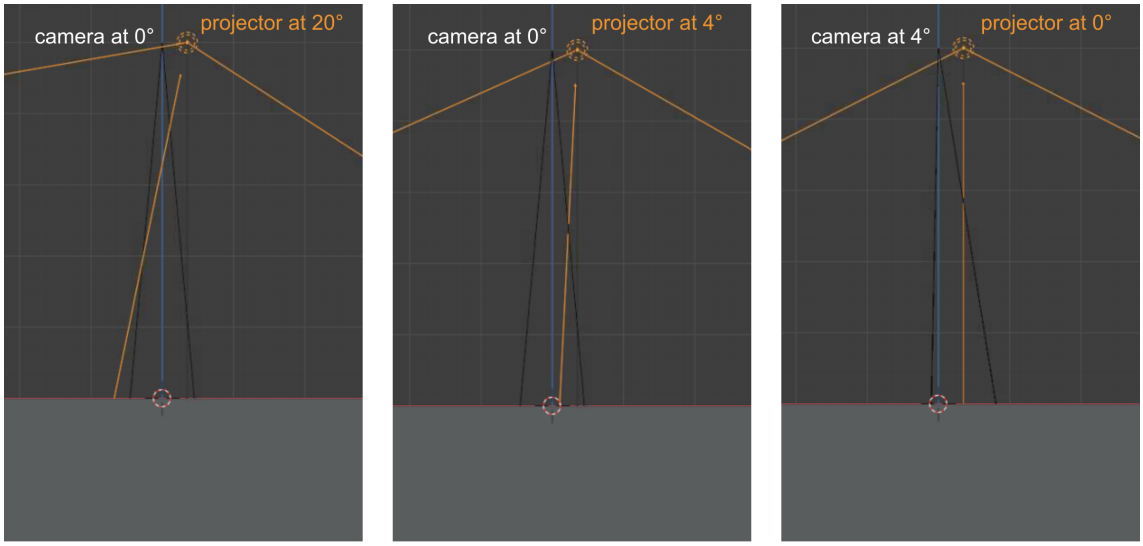

Figure 3.17: Various projector and camera angles tested with simulated system (a) conventional projections seen in SFDI system with projector at 20° angle to the camera (b) testing smaller projector angles, useful for miniaturisation of SFDI systems, with the projector at 4° angle to camera (c) the camera placed at 4° angle to the projector which is not-angled.

A planar sample of healthy oesophageal tissue was simulated and imaged with the projector at a 20° (Fig 3.17 (a)) and a 4° (Fig 3.17 (b)) angle to the camera. Images of a reference material of $A_\rho = 100$ and $S_\rho = 20000$ simulated in both system geometries were also generated. By calculating the optical properties of the sample simulating healthy oesophageal tissue via a Monte Carlo generated LUT, the relative standard error in optical properties was measured to be just 2% for both the absorption and reduced scattering coefficient. The projector was then placed at a 0°

angle to the camera, with the camera instead placed at a 4° angle to the projector (Fig 3.17 (c)). Again, images of a reference material of $A_\rho = 100$ and $S_\rho = 20000$ were simulated in the new system geometry. The resultant standard error in optical properties was just 1% for both absorption and reduced scattering coefficients, in comparison to the projector at a 20° angle.

3.3.5 Simulation of optical property variation in tubular geometry

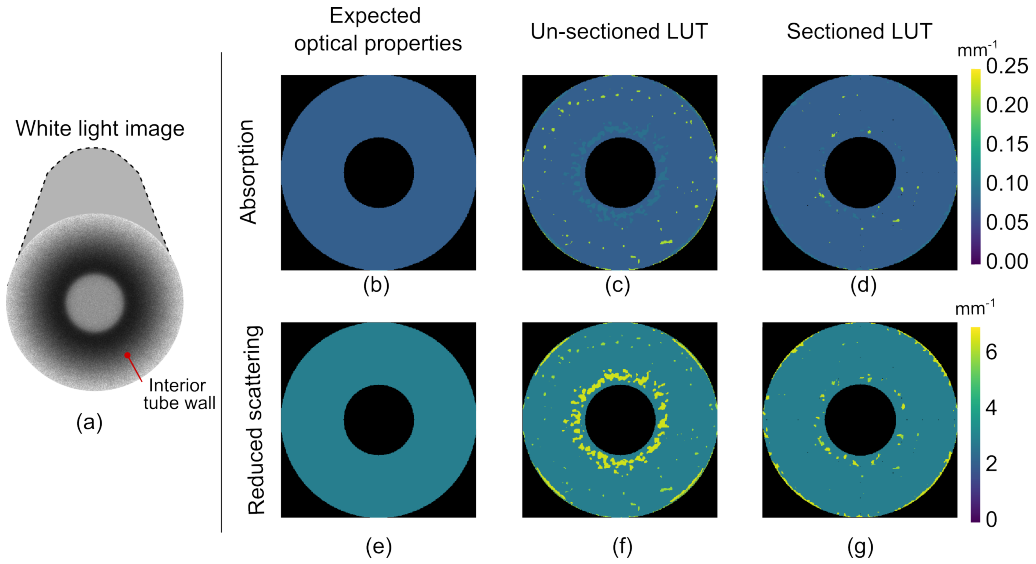

Figure 3.18: Comparison of sectioned and un-sectioned empirically derived LUT for tube wall material of $\mu_a = 0.076$ mm^{-1} and $\mu_s' = 2.99$ mm^{-1} (a) white light image of tube (b) expected absorption coefficient, μ_a, (c) simulated μ_a using un-sectioned LUT (d) simulated μ_a using *sectioned* LUT (e) expected reduced scattering coefficient, μ_s', (f) μ_s' simulated using un-sectioned LUT, (g) μ_s' simulated from *sectioned* LUT. Tube inner diameter = 20mm.

The custom projection pattern modified for a tube, introduced in Sect 3.2.7, was next used to produce Fig 3.18 and Fig 3.19. The optical property maps have a quantized appearance due to the use of nearest-neighbour interpolation, which was found to increase robustness for points outside the convex hull of the LUT. A larger LUT could be generated with more sample images from *Blender* to mitigate this effect using bicubic interpolation. The simulated AC modulation amplitude was observed to be higher than expected, which may be due to the high incidence angle of the light creating substantially different scattering and reflectance behaviour. Though this is corrected for to a large degree using empirically-derived LUTs, there is still a residual increase in AC modulation amplitude and therefore an offset in reduced scattering coefficient.

Fig 3.18 (a) shows a white light image looking down the tube from a top-down view point. It is noted that at the center of the image (the distal end of the tube) the tube wall is considerably darker than the outer, upper edges (the top of the tube which closest to the camera and projector). The expected optical properties of the inner tube wall are shown in Fig 3.18 (b & e). Without applying a sectioned LUT to

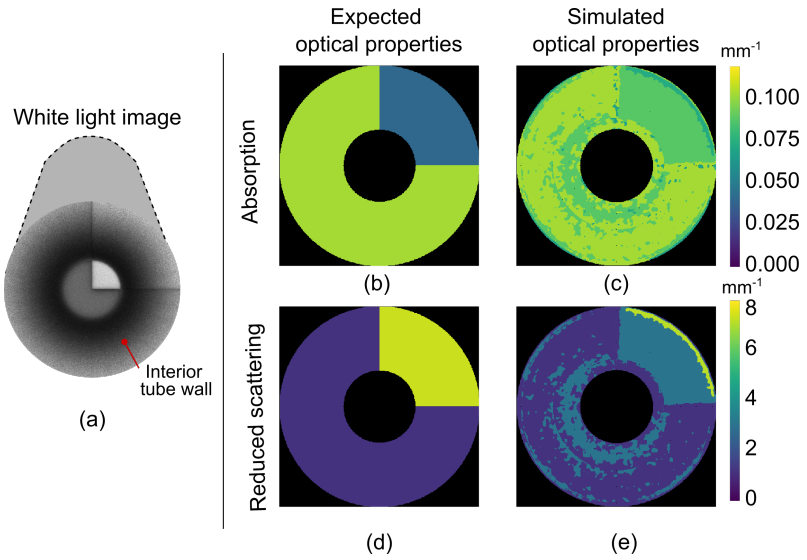

Figure 3.19: Imaging different material types within complex geometry, analogous to a lumen showing (a) white light image of the tube (b) expected absorption coefficient of tube material (c) simulated absorption coefficient (d) expected reduced scattering coefficient of tube material and (e) simulated reduced scattering coefficient. Tube inner diameter = 20mm.

different lengths throughout the tube, as discussed in Sect 3.2.7, this non-uniformity of illumination results in discrepancies in measured optical properties, as shown in Fig 3.18 (c & f). Significant improvement is achieved when longitudinally sectioning the LUT shown in Fig 3.18 (d & g). Over six varying material values, it was determined that the sectioned LUT method reduced both the calculated absorption and reduced scattering coefficients relative error from 5% to 2% compared to the SFDI global LUT, within a tubular geometry.

Finally, to simulate detection of disease inside a lumen, a tube with one quadrant exhibiting a large variation in optical properties compared to the remaining three quadrants was simulated. The results are shown in Fig 3.19. Fig 3.19 (a) depicts a conventional white light image looking down the tube from a top-down view point. A distinct difference in material in the top right quadrant is observed. The expected, quantitative difference of optical properties on the inner wall of the tube are shown in Fig 3.19 (b & d).The measured optical properties are shown in Fig 3.19 (c & e). These optical property maps show a clear variation in measured optical properties from the top right quadrant to the rest of the tube. However, the quantitative variation in optical properties in the right upper quadrant are not as expected. Fig 3.19 (c) shows the absorption coefficient of the top right quadrant is higher than expected and Fig 3.19 (e) shows the reduced scattering coefficient of the top right quadrant is lower than expected. It is suspected that light rays are reflecting off the other three quadrants of the tube and reflecting off the top right quadrant, causing the measured optical properties to lean toward that of the larger three quadrants within the tube. Overcoming this issue may require projecting the pattern within the tube at different angles and averaging the final result.

3.4 Discussion

An SFDI and fringe profilometry simulation model in the graphics software *Blender* has been presented. This section will discuss the accuracy of the simulation model in measuring optical properties, as well as its limitations. Next, potential applications of the simulated system are discussed. Finally, alternate implementations to conventional SFDI explored in this work is discussed.

3.4.1 Relationship between absorption and reduced scattering coefficients measured with DIS and SFDI

Over 9 varying material values, the standard errors in absorption and reduced scattering coefficients between SFDI and DIS data are 16% and 18% respectively (using a MC LUT). Fig 3.13 (a & b) in Sect 3.3.1 shows this difference in results graphically. It can be seen that the discrepancy observed between DIS and SFDI results is particularly high at low absorption values. It is known that DIS and SFDI measurements do not exactly match for several reasons. Firstly, different methodologies rely on different assumptions. For example, an SFDI measurement is obtaining information solely from diffusely reflected light, while a DIS measurement is obtaining information both from diffusely reflected light *and* transmitted light. It is also well known that DIS measurements can have poor accuracy for absorption coefficient recovery. Some examples reasons for this include light being lost at the sample edge in the integrating sphere measurement [200], and non-optimization of diffuse reflectance standard [173].

Previous work by *Hu et al.* has shown relative errors of 20% and 14% for absorption and reduced scattering coefficients measured from DIS and SFDI data at 675 nm [166], as previously discussed in Sect 2.5.1. This 20% error in absorption coefficient between DIS and SFDI measurements was obtained using a more accurate method of obtaining the absorption coefficient than the conventional IAD algorithm used is this work. *Hu et al.* obtained the absorption coefficient via a collimated transmittance measurement using the Lambert-Beer law, as discussed in Sect 1.2.1. The errors observed between the presented simulated SFDI and DIS systems of 16% and 18% for absorption and reduced scattering respectively are consistent with results obtained by *Hu et al.*. As such, it is assumed that the obtained errors are a result of the different underlying assumptions of the two approaches.

However, the simulation can successfully differentiate between material types in both planar and tubular geometries with great accuracy. Therefore, the use of a DIS for characterising material properties for measurements with SFDI is justified.

3.4.2 Limitations

There are a few key limitations of the presented model. The first limitation is the variation in effective anisotropy as a function of scattering. As the anisotropy cannot be set in the volume absorption node, and the bulk material is an equally weighted mixture of the volume absorption and the volume scatter node, the exact anisotropy of the material had to be determined. However, it has been shown in Sect 3.3.1 that this can be characterised for by determining the effective anisotropy of the material. Therefore, LUTs could have an extra dimension added to them containing effective

anisotropy, enabling this parameter to be controlled independently. This would result in an increased accuracy in measurement of optical properties with the MC LUT.

The second limitation is the presence of some artefacts in the tubular geometry configuration. It is speculated that these may be caused by light reflecting off multiple surfaces before reaching the camera, or are residual errors due to large, spatially varying angles of incidence that are not entirely corrected by the empirical LUT approach. Further work is required to increase accuracy, perhaps by the addition of more longitudinal sections in the empirically derived LUT. Since the position of the camera and projector are not fixed, they could also be advanced into the tube to characterise how optical property accuracy changes when features such as polyps move closer. The animation feature of *Blender* could be used to straightforwardly simulate this scenario, producing multiple video frames as the camera and projector move along the tube.

The final limitation is that *Blender* is only capable to operate in 3 wavelengths: red, green and blue. This is a fundamental limitation of *Blender*, but scattering at other wavelengths could be simulated by adjusting the material scale to change the scattering length scales. However, this tool is intended as a geometrical design tool for SFDI systems that should be used in combination with Monte Carlo simulators for more accurate design at other wavelengths.

3.4.3 Potential applications

The results presented in Sect 3.3 demonstrate the capability of the *Blender* SFDI simulation system to recreate various tissue types in various shapes and imaging geometries, and then reconstruct these optical properties using standard SFDI algorithms. The presented SFDI simulation model can overcome many of the limitations of existing software, discussed in Sect 3.1, by enabling custom configuration of illumination source, camera position and orientation, spatial frequency, illumination patterns, as well as the addition of real world artefacts such as specular reflection, vignetting and distortion. SFDI can have various sources of errors arising from assumptions made with selected light propagation model, differences in optical properties dependent on depth, divergence of the projection beam, how the spatial frequency may change with distance from projector to sample, and different probing depths achieved by different spatial frequencies [201, 202]. This model could also allow exploration of some of these typical sources of error in SFDI, such as noise. The introduction of these real-world artefacts will help to test the limitations and robustness of new SFDI system design. It is therefore envisaged that the *Blender* model could accelerate development of novel SFDI systems for applications such as endoscopy or manufacturing.

Another potential application of this system could be to generate large SFDI data sets that may be used in lieu of or in addition to experimental data. Such data sets could be used to improve optical property uncertainty measurements by creating large look up tables for specific system setups [73] or to train deep-learning SFDI recovery systems [61, 203]. The capability of the subsurface absorption and scattering material model of this system (described in Sect 3.2.1) has shown capability to train a generative adversarial network for the prediction of optical property maps from SFDI images [185].

3.4.4 Alternate SFDI implementations

This simulation models allows one to investigate different implementations of SFDI at ease, such as use of projection patterns and system geometries, which will be discussed here.

Projections utilised

The use of a planar DC projection was investigated. *Pera et al.* found that by not including a DC projection, the uncertainty in measured absorption coefficient increases to $\sim$ 13% (from 6% including a DC projection) [73]. The uncertainty in reduced scattering coefficient is much less severe, increasing from 1.85% to 2.05% for including and excluding a DC projection. They note that the absorption coefficient uncertainty is more significant for materials with lower absorption coefficients, with the uncertainty increasing from 6% to 19.5% for phantoms with $\mu_a = 0.035$ mm^{-1} to $\mu_a = 0.005$ mm^{-1}. This is accounted for by the fact that DC projections propagate deeper into a sample, as found in Sect 2.3.1, and therefore its presence is significant for sampling rarer absorption events.

By imaging a sample simulating healthy oesophageal tissue, it was found that the error in absorption and reduced scattering coefficients was 0.13% and 0.03% respectively, as shown in Sect 3.3.3. Therefore, it can be assumed the use of non-planar projection was sufficient within the system geometry for the materials of interest.

Smaller camera and projector angles

For development of an SFDI system in a space-constrained geometry, projector-camera angles of $10 - 20°$ seen in typical SFDI systems are not feasible. Therefore, the use of smaller projector-camera angles is investigated, compatible with realistic miniaturisation of SFDI systems. Previous experimental work has shown SFDI systems can work with small projector-camera angles of 8° [88]. Sect 3.2.2 discusses the simulated SFDI system with a projector-camera angle of 4°. It was desired to determine the error in measured optical properties when using a smaller angle.

It was found, as shown in Sect 3.3.4, that reducing the angle of the projector from 20° to 4° resulted in a difference in absorption and reduced scattering coefficients of just 2%. Therefore, the use of a smaller projector-camera angle is feasible for use on samples simulating tissue optical properties within our range of interest.

3.5 Conclusion

The capability of the open-source graphics software *Blender* to be used to simulate SFDI and fringe profilometry systems has been shown. First, quantitative agreement between Monte Carlo simulated absorption and reduced scattering coefficients to those simulated from the Blender system is demonstrated, achieving 16% discrepancy in absorption coefficient and 18% in reduced scattering coefficient, which correspond to sensitivity and specificity values of $\geq 99.5\%$ for absorption coefficient variances ≥ 0.04 mm^{-1} and reduced scattering coefficient variances ≥ 1.1 mm^{-1}. These results make the system compatible with guidelines new endoscopic imaging modalities suggested by the American Society of Gastrointestinal Endoscopy under

these constraints, as discussed in Sect 3.3.1. Further work is needed to acquire more data to determine the minimum compatible constraints. However, it is shown that using an empirically derived look-up table reduced these errors to 1% and 0.7% respectively. Next, SFDI mapping of absorption, scattering and shape is simulated for tumour spheroids, demonstrating enhanced contrast. The software enables the simulation of typical gastrointestinal conditions with specific absorption and reduced scattering coefficients in tubular imaging geometries relevant for endoscopy in the gastrointestinal tract. SFDI mapping is demonstrated inside a tubular lumen, which highlighted a important design insight: custom look-up tables must be generated for different longitudinal sections of the lumen. With this approach errors of 2% are achieved for both absorption and reduced scattering coefficients. It is anticipated that these results will aid in the design of future SFDI systems, e.g. miniaturised systems, by enabling the testing of different illumination geometries and patterns.

Chapter 4

Constructing an ultra-miniature SFDI system

This chapter presents an ultra-miniature ($>$ 900 times smaller than the bench top system presented in Chapter 2) spatial frequency domain imaging (SFDI) system. The system is comprised of an optical fiber array (tip diameter 0.125 mm) displacing the conventionally bulky projector and a micro camera ($1\times1\times2$ mm package) instead of a regular detector. The prototype has an outer diameter 3 mm, but the individual components dimensions could permit future packaging to $<$ 1.5 mm diameter. As the fiber array projects interference fringes at different phase shifts, a phase-tracking algorithm was developed to rapidly extract video frames with fringe projections at 3 equispaced phase shifts in order to perform SFDI demodulation. To validate performance, comparable recovery of quantitative absorption and reduced scattering coefficients between the ultra-miniature system and the conventional bench top SFDI system presented in Chapter 2 was demonstrated, with agreement of 15% and 6% respectively. Next, imaging of absorption and reduced scattering coefficients of phantoms mimicking typical gastrointestinal conditions was demonstrated. This provides enhanced contrast between simulated tissue types (healthy and tumour), and is done simultaneously at wavelengths of 515 nm and 660 nm. This device shows promise as a cost-effective, quantitative imaging tool to detect variations in optical absorption and scattering as indicators of cancer. This chapter is based on works [141] and https://doi.org/10.48550/arXiv.2306.03713 (in review).

4.1 Motivation

Gastrointestinal (GI) cancers account for one quarter of the global cancer incidence and over one third of all cancer related deaths [204]. Wide population based endoscopic screening has shown promise in significantly decreasing mortality rates [205]. However, the high cost of GI procedures, associated risk, and high miss rates for some types of polyps during diagnostic colonoscopies [206] makes wide population based screening for GI cancers not feasible. Therefore, there is a need for a cost-effective, minimally invasive and improved contrast imaging device that can be deployed endoscopically. The instrument channel has diameter ranges of $2.8-4.2$ mm in standard colonoscopes and $2-3.8$ mm in conventional endoscopes [207]. Therefore, a device is desired to be within these sizes to have potential to be deployed down the instrument channel. To be suitable for population screening programmes, it must also be

relatively low-cost to manufacture and operate.

SFDI is an attractive choice for an improved contrast imaging modality because it does not require high-powered lasers, sensitive detectors or complex optical components [50]. It is therefore relatively low-cost to manufacture and operate, and systems can be miniaturised easily. As a result, a number of SFDI systems exist (as discussed in Sect 1.3.3), such as large commercial systems [84] to portable handheld systems [88]. However, in most existing systems the projector element remains costly and difficult to miniaturise, being typically comprised of either a digital micromirror device (DMD) projector [88] or a motorised grating [89, 90].

There have been two main approaches in miniaturising fringe projection systems: rigid scopes (Fig 4.1 (a & b)) and flexible optical fibers (Fig 4.1 (c-f)). A rigid endoscope has been used to achieve single snapshot of optical properties (SSOP) [91], a technique previously discussed in Sect 1.3.2. While SSOP is advantageous as it reduces acquisition times, it poses several disadvantages, with the main disadvantage being reduced image quality due to the use of filtering a single image. As discussed in Sect 1.3.3, the exact dimensions of this rigid Schölly dual-imaging scope from Intuitive Surgical are not stated [94]. This set up, shown in Fig 4.1 (a), is only capable of projecting a single illumination pattern at a single spatial phase. *Le et al.* overcome this issue by the use of a DMD to modulate the phase of the projection pattern, as shown in Fig 4.1 (b). This system has been used for *ex-vivo* imaging of bowel anastomosis [208]. Both the illumination and imaging scopes have diameters of 4 mm each. As both the probes developed in [91] and [208] are rigid in nature, they are not suitable for imaging in the GI tract.

Flexible approaches to miniaturising fringe projection systems conventionally rely on the use of optical fiber bundles [209–213]. Fig 4.1 (c) shows the projection of a Ronchi ruling pattern (square wave pattern) through a fiber bundle, and the imaging of this projected pattern through the same fiber bundle onto a CCD [209]. The Ronchi pattern allows for a single spatial frequency and phase to be projected, analogous to the rigid scope SSOP system previously discussed. The fiber bundle has a diameter of 2.7 mm at the distal end. The system proposed by *Supekar et al.* in Fig 4.1 (d) overcomes the use of a single phase pattern by using a DMD to generate the projection pattern. This pattern is then also transmitted through a fiber bundle [210]. Instead of imaging the projected pattern back through the fiber bundle as previously described, a series of lenses focuses the image of the projected pattern on a CMOS sensor. This device has a height of 30 mm, with an approximate diameter of 10 mm at the device's base. *Matthias et al.* developed an endoscopic fringe projection system by using two fiber bundles: one for pattern projection and one for imaging [213] (see Fig 4.1 (e)). Again, the pattern is generated via a DMD and transmitted through the fiber bundle. The resultant pattern is imaged with a separate fiber bundle and focused onto a CMOS sensor. Both fiber bundles have a diameter of 1.7 mm each, giving a total minimal diameter of 3.4 mm at the distal end of the system.

Fiber bundles have disadvantages for both imaging and projection, such as their high sensitivity to vibrations, cross coupling and fiber movements [215]. These effects make the reconstruction of images through a fiber bundle challenging, and therefore the use of a micro camera instead is advantageous [216]. Commercial fiber bundle projection typically only supports high fidelity fringes at green wavelengths due to increased cross-coupling between cores at red wavelengths [217]. Fringe pro-

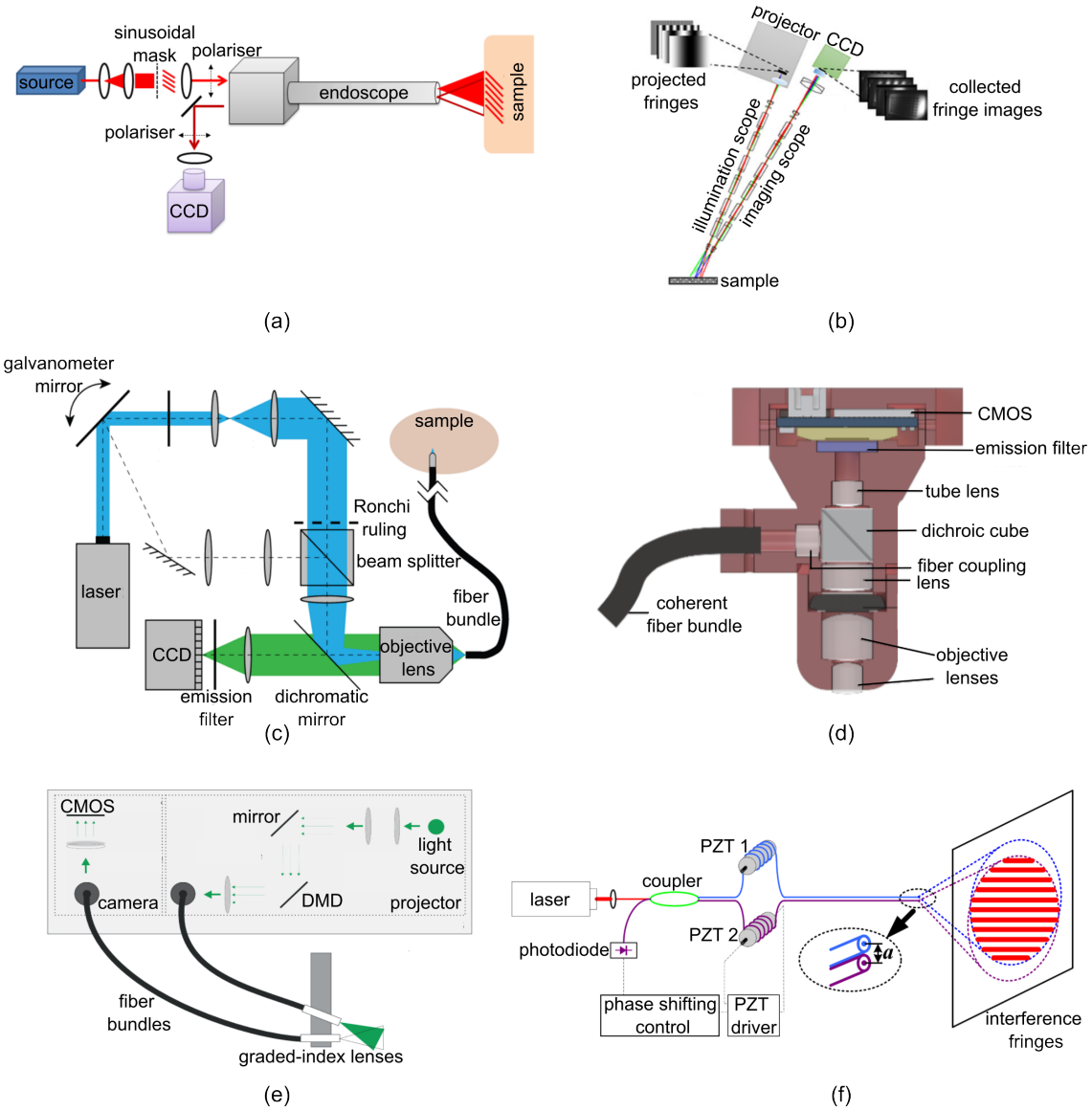

Figure 4.1: Schematics of advances in miniaturising fringe projection systems from literature (a) Rigid endoscopic SSOP imaging system projecting a sinusoidal mask and imaging the projected pattern through a separate channel in the surgical scope, adapted from [91]. (b) Rigid laparoscopic 3D imaging system projecting patterns generated from a DMD through a surgical scope and imaging the patterns through a secondary surgical scope, adapted from [208]. (c) Flexible fiber bundle for fluorescence endomicroscopy projecting a Ronchi ruling and imaging pattern through same fiber bundle, adapted from [209]. (d) Flexible fiber bundle transmitting pattern generated from DMD for optical sectioning and imaging pattern onto a CMOS sensor, adapted from [210]. (e) Flexible fiber bundles transmitting pattern generated from DMD with a second fiber bundle imaging the projected pattern onto a CMOS sensor, adapted from [213]. (f) Interferometric interference pattern produced by illuminating two single mode fibers, controlling the phase with piezoelectric transducers (PZT), adapted from [214].

jection at more than one wavelength is desired, typically in SFDI, for several reasons. Firstly, it has the capability to reduce speckle noise by averaging it out over several

wavelengths. Secondly, it gives the opportunity to penetrate to different depths in the sample of interest with different wavelengths [93]. Third, it introduces the capability to obtain chromophore information, such as oxyhaemoglobin and deoxyhaemoglobin concentration, by measuring the variation in absorption coefficient at more than one wavelength [34, 218], as discussed in Sect 1.2.1. Blood oxygenation SFDI systems often operate in the Red/IR e.g. [219], but, as previously stated, most fiber bundle systems operate in the green to avoid too much cross-coupling between fibers [217].

Ultra-thin fiber arrays have been used to create fringe patterns interferometrically for profilometry with a wavelength of 633 nm [214] (see Fig 4.1 (f)). An optical fiber array is a 1 or 2 dimensional array of optical fibers, where the array is only formed for the very distal end of a bundle of fibers, rather than over the whole fiber length as in a fiber bundle. The system shown in Fig 4.1 (f) stabilises the phase and controls the modulation by use of piezoelectric transducers. Fiber arrays have also been used in combination with photonic chips for generating standing wave interference patterns needed for structured illumination microscopy [220]. Photonic chips that are made of dielectric materials can generate uniform illumination patterns over a large field of view, making them desirable for use in *in-vivo* imaging.

None of these existing systems are suitable for routine endoscopic deployment in the GI tract because they either use DMD-based projectors which are costly and cannot be sufficiently miniaturised; use fiber bundles which produce low-quality fringe patterns at a limited set of wavelengths and only record low resolution images; or use rigid endoscopes which are not flexible. There is a need for a cost-effective, quantitative imaging tool that can be deployed endoscopically to better detect early stage GI cancers.

Therefore, an ultra-miniature SFDI system has been developed, with an outer diameter of 3 mm. The system uses a fiber array to interferometrically produce fringe patterns feasible for SFDI at green (515 nm) and red (660 nm) wavelengths both individually and simultaneously. Images of the fringe patterns are recorded at 320×320 pixel resolution using a micro camera. The prototype packaging is sufficiently small that it could be compatible with the instrument channel of standard colonoscopes and endoscopes.

4.2 System design & development

The primary components needed for an SFDI system are a source of pattern projection and a detector to capture the projected patterns on a sample of interest. For the development of this system, a spatial frequency projection in the range of $0.15 - 0.3$ mm^{-1} [50, 74] was desired, with a large field of view operating at a working distance ≤ 50 mm to be compatible with endoscopic imaging. An optical fiber array was chosen as the source of projection patterns as it is relatively low cost and has a small tip diameter (≤ 0.125 mm). The design of the optical fiber array will be discussed in Sect 4.2.1. A micro camera was chosen as the detector because it is also relatively low cost, has a small diameter (1 mm), and has a pixel resolution of $320 \times 320 = 102,400$ pixels, compatible with standard definition endoscopy as discussed in Sect 1.4. The subsequent section will discuss design of the fiber array, it's specifications, and the incorporation of the fiber array and micro camera to develop an ultra-miniature SFDI system.

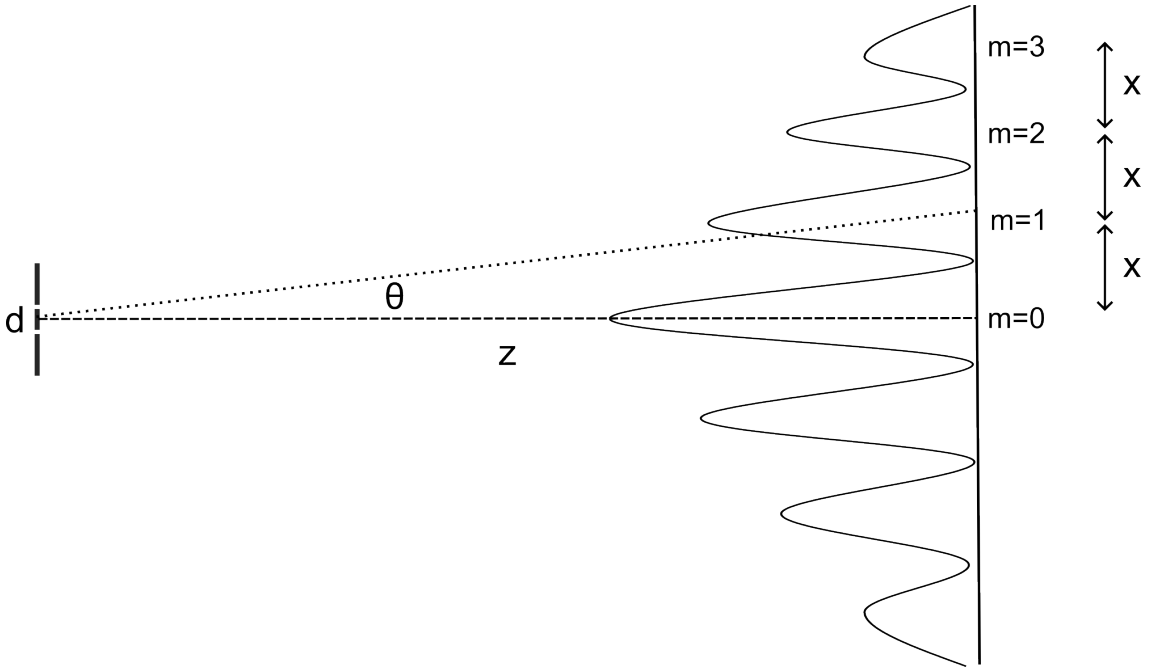

Figure 4.2: Young's double slit schematic for determining minimum spacing required to produce interference patterns within the range of interest, where d is the spacing between fibers required, z is the working distance, θ is the angle of projection, m is the number of interference line spacings from the central point and x is the distance between adjacent maxima such that the spatial frequency of the projection pattern is $1/x$.

4.2.1 Component design & selection

To create an ultra-miniature fringe projector without using a bulk projector or DMD elements, a customised two-dimensional pitch-reducing optical fiber array (PROFA™, *Chiral Photonics*, NJ) was designed to create fringes interferometrically. The fiber array was designed to initially produce interference patterns within a widely used spatial frequency range ($0.15 - 0.3$ mm^{-1} [50, 74]) at an initial test working distance of 50 mm when two adjacent channels are illuminated by the same laser source of 660 nm. However, later work showed the capability of the system to also operate at 515 nm. To compute the required fiber spacings, the double slit equation was used:

$$m\lambda = d \sin\theta \tag{4.1}$$

where m is the number of the interference line spacings from the central point, λ is the wavelength of light, d is the distance between slits and θ is the angle of projection, depicted in Fig 4.2. As previously stated, the desired wavelength was chosen to be 660 nm, however the fiber array also operates efficiently at 515 nm, enabling dual-wavelength imaging. The distance from slit to projection pattern, i.e. the working distance, was chosen initially to be 50 mm, which is the maximum working distance of the camera. Using Eqn 4.1, the spacing d required to produce the spatial frequencies of interest ($0.15-0.3$ mm^{-1}) was determined to be $4.99-9.92$ μm (see Appendix G). Specifications of the fabricated fiber array will be discussed in Sect 4.2.4.

A schematic and image of the system is shown in Fig 4.3 (a & b) respectively. The

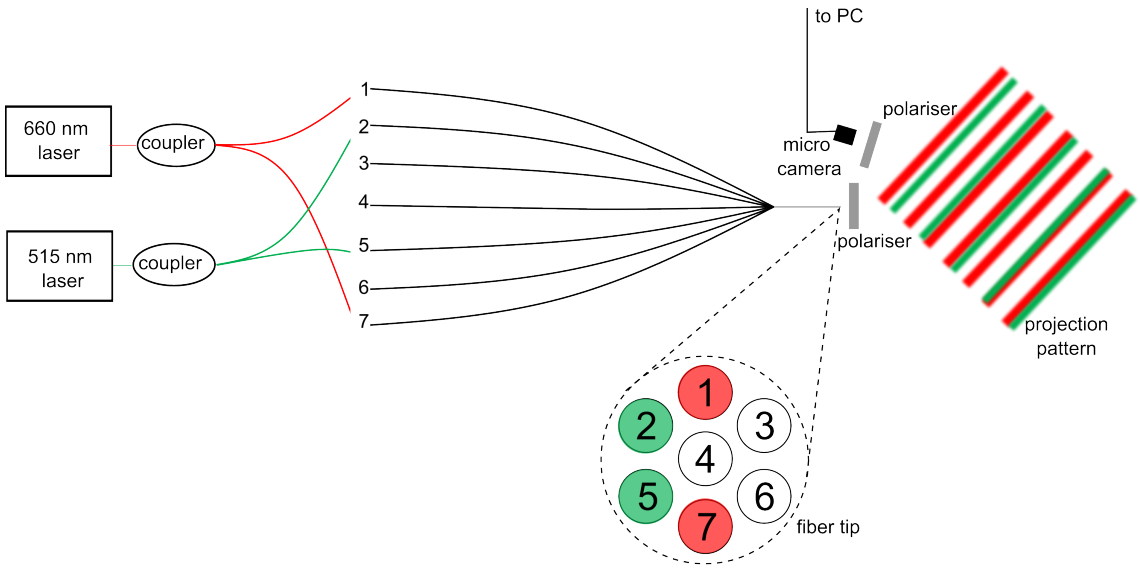

(a)

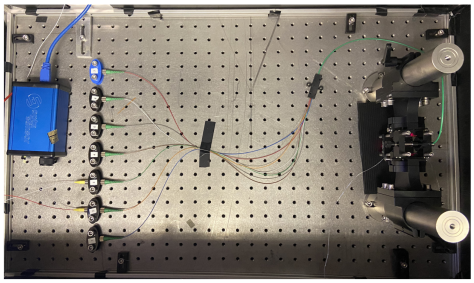

(b)

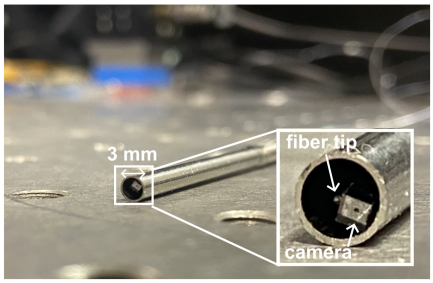

(c)

Figure 4.3: Proposed ultra-miniature SFDI system (a) Schematic of fiber array in ultra-miniature SFDI system showing dual wavelength illumination simultaneously. Light passes from the two lasers into the fiber array via a selection of 7 single-mode fiber input ports. At the tip of the fused taper, the fibers are spaced in a hexagonal array, providing three possible spacings. Crossed polarisers are placed in front of the fiber tip and the micro camera to reduce specular reflections from the imaging sample. (b) Photograph of experimental set up. (c) Prototype device package of 3 mm diameter with inset showing zoomed in view of fiber tip and camera.

camera chosen is a 1×1 mm micro camera module (Osiris M module, *OptaSensor*, Germany). The camera has a resolution of 320×320 pixels, with an individual pixel size of 2.4 μm. An in-built 'lens', made of a single surface droplet of polymer in front of the sensor, provides horizontal and diagonal field of views of 68° and 90° respectively, accompanied by a depth of focus of $5 - 50$ mm. The camera module produces a 12 bit BGR raw image output. The camera is accompanied by software to control camera parameters such as exposure, gamma correction and black level correction. The automatic exposure correction was disabled so that all image frames contain the same optical power ranges. The micro camera has a frame rate of 10 fps, which is the minimum rate required for proper endoscopic visualisation [221].

To minimise specular reflections present on the imaging sample, adhesive-backed polymer polariser sheets are cross-polarised and placed in front of the camera and

fiber tip. The camera is also placed at a small angle of 4° to the fiber to further limit specular reflections on the imaging sample. This angle is smaller than conventional SFDI systems [53], but is more amenable to miniaturisation. Previous work has shown that this angle, and the fact that the camera is at an angle instead of the projector, can still produce high quality optical property maps [140], as discussed in Sect 3.3.4.

The distal end of the system has the capability to be packaged in 3 mm diameter tubing, as shown in Fig 4.3 (c). Further discussion on developing this prototype will be in Sect 4.2.5.

4.2.2 System cost

Cost is an important factor in device development, particularly if that device is being proposed for screening processes. The main cost of a medical device may lie in paying for clinician's time to use it. Therefore, the development of a point-of-care device that can be operated by non-specialised medical practitioners is desired. The single fiber array cost \$1800 ≈ £1444, however it is assumed that bulk order of fiber arrays would significantly reduce the cost. The opta sensor camera has a cost of €219 ≈ £189, while the camera driver which can be reused has an initial cost of €1380 ≈ £1188. The 660 nm laser cost £338 and the 520 nm laser cost £349.

Therefore, the initial, one time cost of the entire system is ∼£3508. The capability to purchase low cost cameras and fiber arrays in bulk and the re-usability of the camera driver and lasers would significantly reduce the cost of a single device. The micro camera and fiber array will require either the deployment of decontamination protocols after each use *or* to be single use. Future work will weigh cost, time and waste to decide the optimum outcome.

4.2.3 Detector characterisation

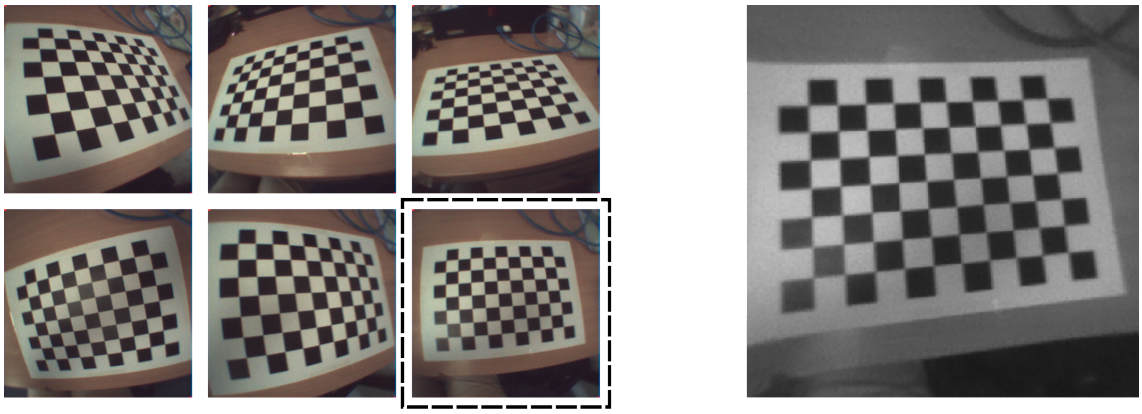

Figure 4.4: Calibrating camera distortion (a) set of example input distorted images captured from different angles (b) corrected image of highlighted capture from (a)

As discussed in Sect 4.2.1, the chosen camera has a drop of polymer in front of the sensor, acting as a lens. By contrast, microscopes have multi-surface complex lenses to minimise distortion [222]. Therefore, owing to its simplicity, this polymer lens creates a distortion in captured images, as shown in Fig 4.4 (a). This

distortion was corrected based on work from *Zhang* [223], utilising the *OpenCV* imaging processing library in *Python*. First, a checker board grid pattern of black and white squares was printed and placed on a flat surface. Images of this pattern were captured with the camera at several different angles, and their corners identified with the function *cv2.findChessboardCorners()*. For increased accuracy, the function *cv2.cornerSubPix()* then takes these corners and iteratively searches the image area of the given point to find the sub-pixel, accurate location of the given corners. These points are passed to the function *cv2.calibrateCamera()* which returns the data needed for the undistorted image, camera matrix and the distortion coefficients. The function *cv2.getOptimalNewCameraMatrix()* then refines the camera matrix, returning a cropped region of interest. Finally, the camera matrix, distortion coefficients, and cropped region of interest are input to the function *cv2.undistort()*, returning the undistorted result, as shown in Fig 4.4 (b).

The resolution of the detector was characterised by imaging a resolution target (R3L3S1N - Negative 1951 USAF Test Target, $3'' \times 3''$, *Thorlabs*, UK). The target was placed 50 mm from the detector and illumination was provided with a white light torch. The results are shown in Sect 4.4.1.

4.2.4 Illumination characterisation

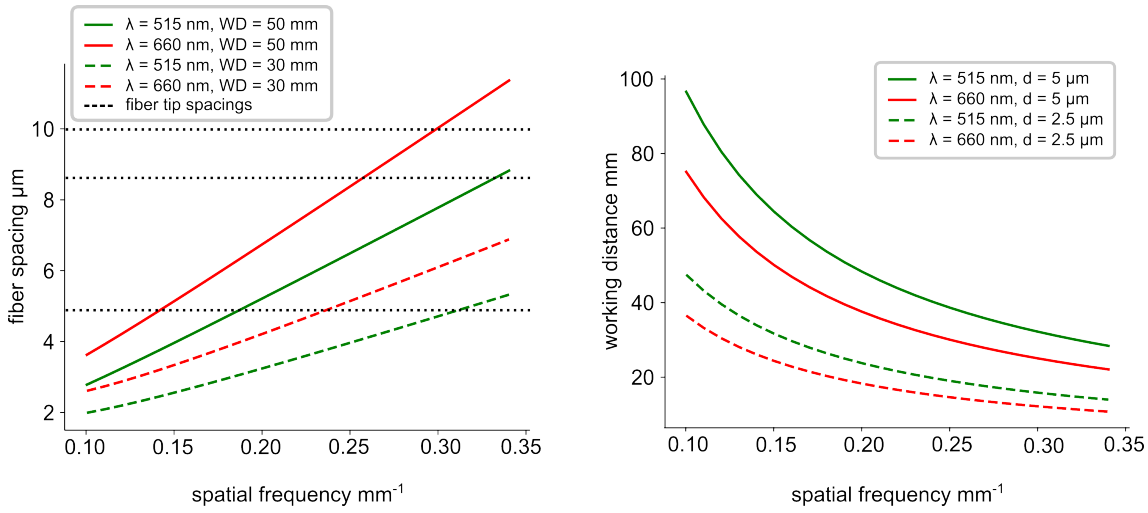

Figure 4.5: Determining desired fiber spacing to produce spatial frequencies within the range of interest $0.15 - 0.3$ mm^{-1} (a) Addressable spatial frequency projection at working distances (WD) of 50 mm (solid lines) and 30 mm (dashed lines). The black dotted lines represent the three possible fiber tip spacings of 5, 8.66 and 10 μm (b) proposed design of spatial frequency projection at various working distances for fiber tip spacing (d) of 5 μm (solid lines) and 2.5 μm (dashed lines), useful for smaller working distances.

The fabricated fiber array has a pitch of 5 μm with an average error of 0.11 μm and a maximum error of 0.14 μm. The 7 fiber channels are spaced at the tip as shown in Fig 4.3 (a). Therefore, the fiber array has three possible spacings of 5, 8.66 and 10 μm. At a working distance of 50 mm, these spacings will produce

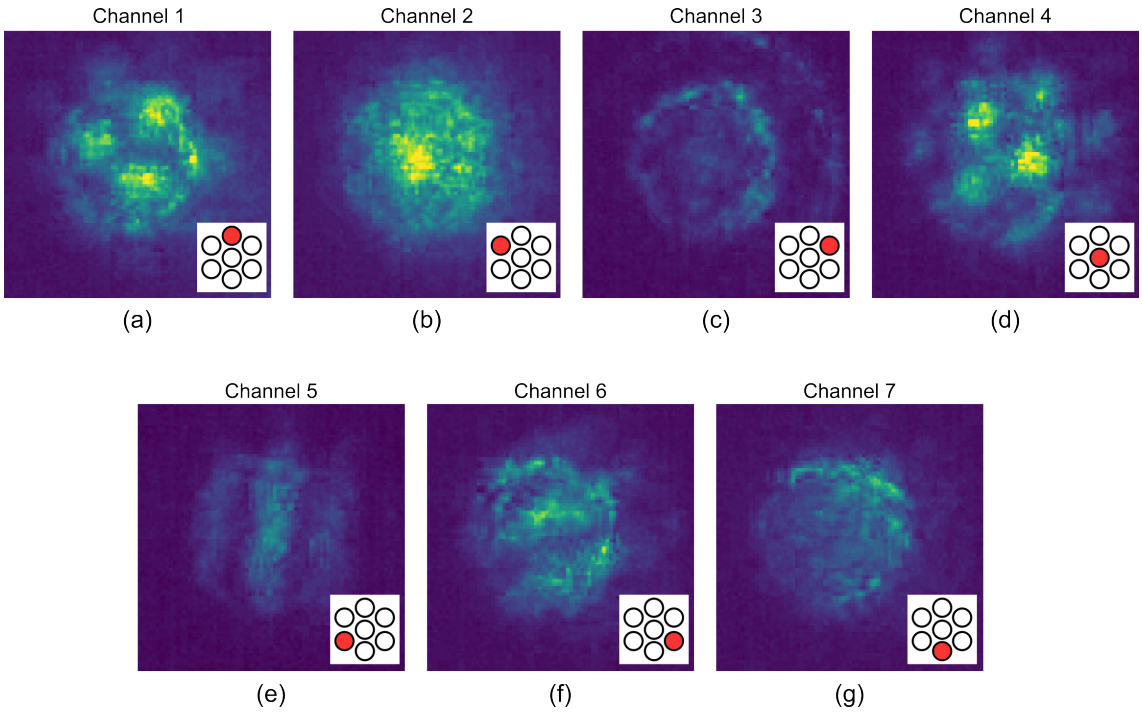

Figure 4.6: Illuminating each channel of fiber array individually with 660 nm and capturing image of projection pattern with mini camera (a)-(g) channels (1)-(7). Each inset shows the arrangement of the 7 channels, with channel illuminated shown in red.

spatial frequencies of 0.15, 0.25, and 0.3 mm^{-1} at 660 nm and 0.19, 0.33 and 0.38 mm^{-1} at 515 nm, as shown in Fig 4.5 (a).

The spatial frequency projection at varying fiber to sample working distances was then determined, shown in Fig 4.5 (b). Typical endoscope working distances are $20-30$ mm [224], which is achievable using the 5μm spacing option of the array, producing a spatial frequency pattern of 0.3 mm^{-1} at 660 nm, though in future designs a $2.5\mu m$ spacing could enable even shorter working distances. The light sources used are a 5 mW 660 nm laser diode (LPS-660-FC, *Thorlabs*) and a 3 mW 515 nm laser (LP515-SF3, *Thorlabs*). These lasers were selected as they were cost effective and readily available. Light was coupled from the lasers to the desired fiber array channels using a fiber optic coupler (TW630R5F1, *Thorlabs*).

Each channel of the fiber array was illuminated individually with the 660 nm laser diode to assess the projection quality. Since each channel is a single mode fiber, it is expected that transmitting laser light through just one channel will result in the projection of a Gaussian spot. However, as shown in Fig 4.6, cross-coupling between fibers in the fiber array can result in some channels producing projections with some interference patterns. For example, when just channel 1 or channel 4 is illuminated (Fig 4.6 (a) & (d) respectively), there are several bright spots present in the projection. When channel 5 and channel 6 are illuminated individually (Fig 4.6 (e) & (f) respectively), an interference pattern is detected, a probable result from cross talk between channels. Channel 2, 3 and 7 illuminated independently (Fig 4.6 (b), (c) & (g) respectively) show relatively uniform projections, meaning these channels have low cross talk from others. Even with such abnormalities present from cross talk in the projections, their presence is constant and relatively stationary with time.

Therefore, these abnormalities are removed from resultant optical property maps by the calibration of the modulation transfer function of the system, as discussed in Sect 1.3.1. However, it must be ensured that when calibrating the system, the reference material is illuminated by the same two channels as the sample of interest.

Multi-wavelength imaging is possible with this system in two ways. First, the fiber array consists of seven channels and illuminating two channels from the same source will produce a spatial frequency projection at the source wavelength. This allows up to three different wavelengths and spatial frequencies simultaneously for the 7 channel fiber array presented here. Second, two wavelengths could be projected down the same channel by use of a dichroic splitter, enabling more wavelengths to be projected simultaneously. For ease of control of projected spatial frequency, projecting just one wavelength down two channels is done in this work. Expanding the existing system to tri-colour would be possible by adding an additional laser of, say ~ 450 nm, to two available illumination channels which will produce a spatial frequency of ~ 0.22 mm^{-1} (at a working distance of 50 mm). This could then be analysed from the blue channel of the captured video. Multi-wavelength imaging would probe different depths and could be used to image depth-varying optical properties of a layered medium.

4.2.5 Prototype development

To package the device from Fig 4.3 (b) to (c), the angle between the projector and camera present in conventional SFDI systems to minimise specular reflections had to be considered. The initial proposed design was a hollow cylinder of outer diameter 6 mm made of 3D printed materials, with a 3D drawing shown in Fig 4.7 (a). At the base of the cylinder, a slope angled at 4° was constructed to hold the camera. Then, the camera and fiber were held in place with UV curing glue (NBA107, *Thorlabs*), as shown in Fig 4.7 (b).

This prototype was not small enough to be compatible with colonoscope and endoscope instrument channels, as previously discussed. The main challenge in SFDI miniaturisation is ensuring an offset angle between the projector and camera is present to minimise specular reflections. To do this, a 2×1 mm, 4° angled wedge is proposed to be 3D printed, as shown in Fig 4.7 (c). This wedge should be placed between the camera and fiber to create that offset angle of 4°. Stainless steel tubing of outer diameter 3 mm and inner diameter 2 mm was purchased and cut to size in length to encase the camera and fiber, as shown in Fig 4.7 (d). The length of the distal end of the prototype which is rigid is 70 mm. This is due to the rigidity of the fiber array and may be reduced by further tapering the fiber array tip to increase its flexibility and enable a prototype capable of deployment *in-vivo*. This initial prototyping was done on a fiber array where several channels had been broken, and hence experiments were done with an operational fiber array without this packaging. This simply demonstrates the principle behind SFDI miniaturisation.

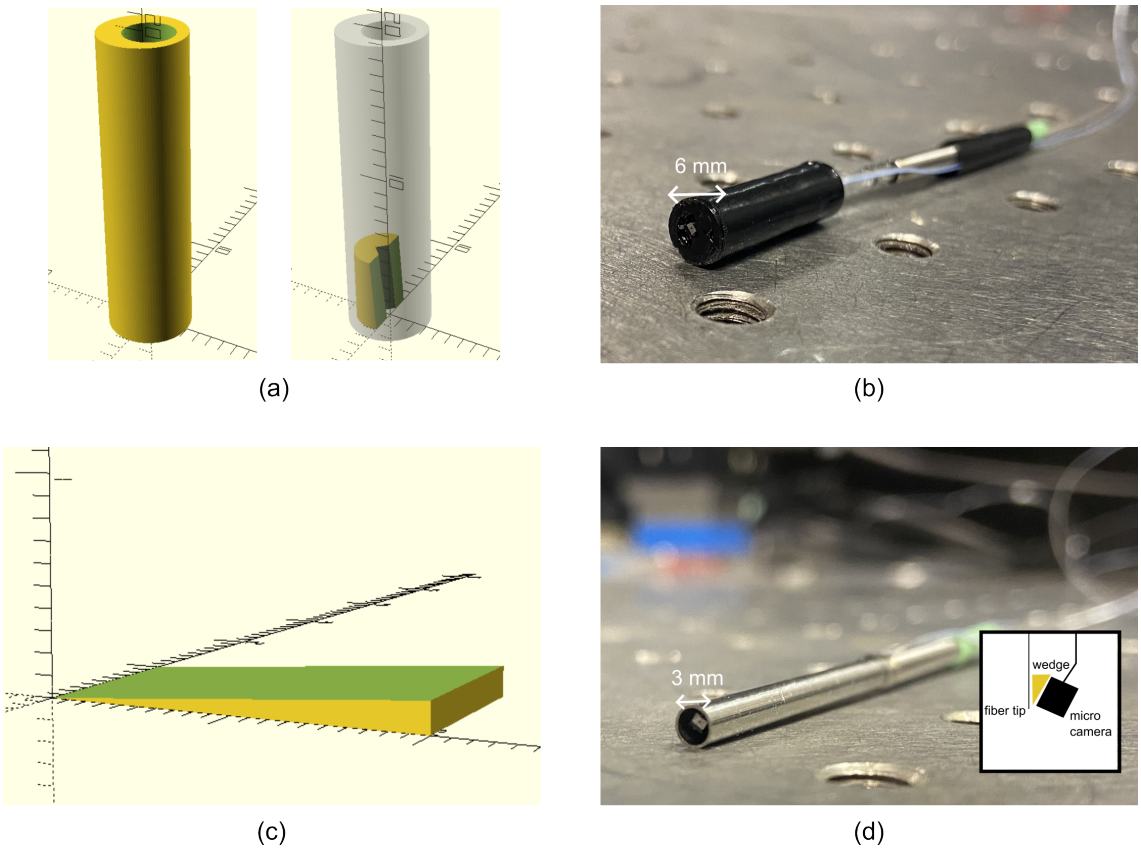

Figure 4.7: Development of prototype ultra-miniature SFDI device (a) *OpenSCAD* drawing of 6 mm diameter, 20 mm height prototype casing with angled camera holder at base (b) image of initial prototype cased in 3D printed housing (c) *OpenSCAD* drawing of 2 mm height wedge at 4° angle camera from fiber tip (d) image of final prototype in 3 mm diameter stainless steel housing with inset showing schematic of fiber tip, wedge, and micro camera.

4.3 Image acquisition & processing

4.3.1 Fabrication of imaging samples

In order to perform initial validation of the ultra-miniature SFDI system, optically homogeneous tissue mimicking co-polymer in oil phantoms were fabricated, with optical properties tunable by controlling concentrations of TiO_2 and Nigrosin dye [159], as discussed in Sect 2.3. The fabricated phantoms had a thickness of 30 mm and were ensured to be non-transparent so as to meet the the semi-infinite thickness requirement of SFDI [1]. Two phantom batches were fabricated; one with increasing amounts of dye stock solution from $0.5 - 1$ g corresponding to an absorption coefficient range of $0.006 - 0.017\ mm^{-1}$ at 660 nm and the second with increasing amounts of TiO_2 from $0.07 - 0.13$ g corresponding to a reduced scattering coefficient range of $0.52 - 0.99\ mm^{-1}$ at 660 nm, as shown in Table 4.1. The batch with increasing dye stock solution each had 0.1 g of TiO_2 and the batch with increasing TiO_2 each had 0.5 g of dye stock solution to ensure the semi-infinite material requirement was met. These optical property ranges were chosen as they lay within optical properties of interest of typical gastrointestinal tissue samples [47] and they had previously been calibrated in literature using a double integrating

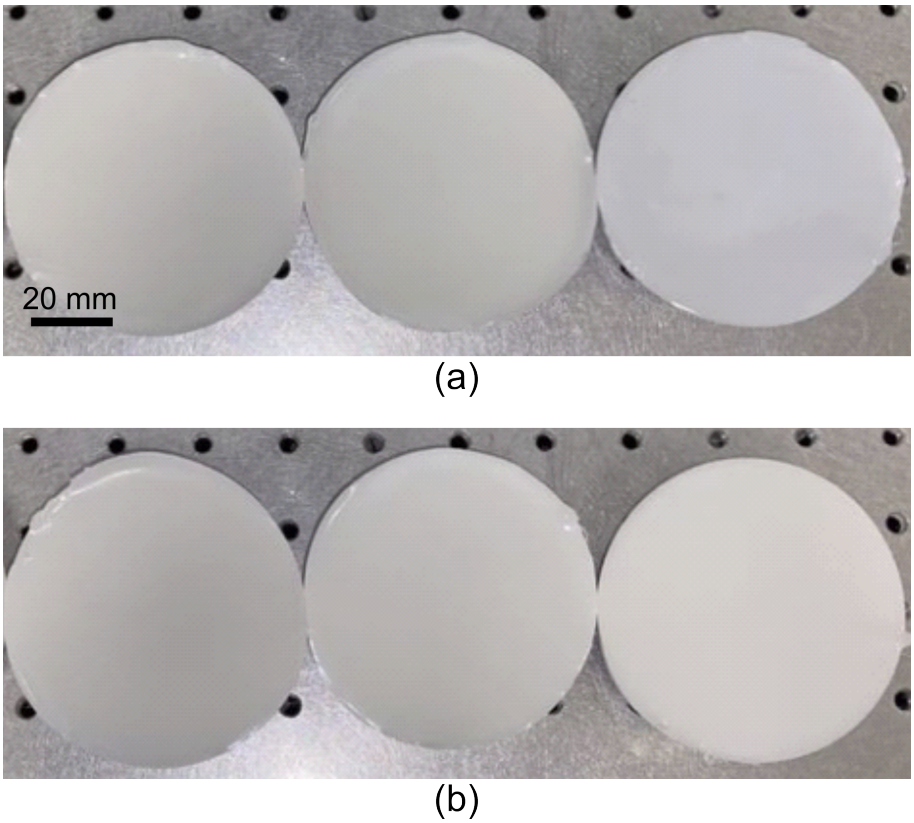

Figure 4.8: Top down view of fabricated phantoms with (a) increasing Nigrosin dye stock from left to right and (b) increasing TiO_2 from left to right. Images captured on phone camera.

sphere (DIS) [159].

4.3.2 Image acquisition

Phantoms were imaged in the bench top SFDI system, which is described in Sect 2.1, and in the ultra-miniature SFDI system, discussed in this chapter. As a 635 nm bandpass filter is placed in front of the bench top system camera and a 660 nm laser is used in the ultra-miniature system, the offset in optical properties had to be accounted for. The difference in optical properties at different wavelengths is shown in Table 4.1. For these particular phantoms, the absorption and reduced scattering coefficients decrease by 14% and 3% respectively from 635 nm 660 nm (taken from pre-determined DIS measurements [159]). This difference was determined to be minimal enough to be capable to successfully compare the two systems. The reference optical properties were adjusted for optical property calculation depending whether the bench top or miniature system were in use. When imaging phantoms at 515 nm in the miniature system, the reference optical properties were also adjusted accordingly. The absorption and reduced scattering coefficients increase by 65% and 20% respectively from 635 nm to 515 nm (again, taken from pre-determined DIS measurements [159]). Therefore, there is no advantage in comparing phantom optical properties imaged with the 515 nm laser in the ultra-miniature system to bench top system results. The addition of a 515 nm bandpass filter in the bench top system would make this possible.

Dye stock (g)	$\mu_{a,660}$ mm^{-1}	$\mu_{a,635}$ mm^{-1}	$\mu_{a,515}$ mm^{-1}	**TiO_2** (g)	$\mu'_{s,660}$ mm^{-1}	$\mu'_{s,635}$ mm^{-1}	$\mu'_{s,515}$ mm^{-1}
0.5	0.006	0.008	0.014	0.07	0.52	0.54	0.63
0.75	0.011	0.013	0.019	0.1	0.77	0.79	0.92
1	0.017	0.018	0.026	0.13	0.99	1.02	1.17

Table 4.1: Absorption and reduced scattering coefficients determined via DIS for phantoms with given Nigrosin dye stock and TiO_2 concentrations at 660, 635 and 515 nm, determined from [159].

For acquiring images with the ultra-miniature system, the phantoms were placed such that the top of the phantom was 50 mm from the distal end of the imaging probe and the projection pattern was in the center of the sample. Videos were taken of the shifting projection pattern on the phantom for $10 - 20$ s to ensure all phases were captured, however it is shown in Sect 4.4.2 that all three phases of interest can be captured in < 1 s of video.

Imaging phantoms with one wavelength

First, to determine the agreement between bench top and ultra-miniature systems, the 6 phantoms described in Sect 4.3.1 were imaged in the ultra-miniature SFDI system. Imaging was done at just 660 nm, for reasons previously discussed. Each phantom was imaged at three different spatial frequencies (0.15, 0.25 and 0.3 mm^{-1} for 660 nm illumination at 50 mm working distance) by illuminating three different fiber channel combinations sequentially. Two phantoms with variable absorption and scattering properties which were placed adjacent to one another were also imaged.

Imaging phantoms with two wavelengths

Next, three phantoms (fabricated as discussed in Sect 4.3.1) were imaged with 660 nm projection only (single spatial frequency 0.3 mm^{-1} at 50 mm working distance), then 515 nm projection only (single spatial frequency 0.2 mm^{-1} at 50 mm working distance), and finally with 660 nm and 515 nm projected simultaneously. Dual-wavelength imaging was performed by illuminating channels 1&7 with 660 nm and channels 2&5 with 515 nm, producing spatial frequency patterns of 0.3 mm^{-1} and 0.2 mm^{-1} respectively at a 50 mm working distance. A video was captured of both illumination patterns simultaneously, and analysis is carried out by extracting the red and green channels from the video capture. Dual-wavelength imaging was also done on two phantoms with variable absorption and scattering properties which were placed adjacent to one another.

Increasing number of equiphase shifted captures for a single wavelength

The projection pattern from the fiber array shifts through an entire sinusoidal period ($0° - 360°$) over time, as it is essentially an interferometer. Therefore, the use of more than 3 equiphase shifted images for demodulation and optical property extraction was investigated in an effort to reduce noise in resultant optical property maps. This can be achieved simply, as in a video capture of $10 - 20$ s, the camera will

capture several full period phase shifts, encapsulating all phases. To do this, an improvement on Eqn 1.26 is needed for N phases instead of 3 (see Appendix E). The same 6 phantoms described above in Sect 4.3.1 are imaged, but instead of the phase tracking algorithm extracting 3 equiphase shifted images it extracts 6 equiphase shifted images. The resultant optical property maps for both 3 and 6 equishifted phases were compared.

4.3.3 Phase tracking algorithm

An inherent property of an interferometer such as the fabricated fiber array is that the sinusoidal pattern produced will shift over time due to mechanical drifts, vibrations, temperature and intensity variations [225]. Conventional wisdom may suggest using a complex set up consisting of a phase-shifting control system and a piezoelectric transducer driver to stabilise and control this phase shift [214]. However, in this work the natural phase drift is exploited as an advantage via a phase-tracking algorithm.

A video, typically $10-20$ s, is first recorded of the shifting sinusoidal pattern on a sample of interest. To determine which frames to use for demodulation, an average of all frames within the video is first taken and subtracted from each individual frame. This allows visualisation of the spatial frequency pattern with reduced noise (see Fig 4.9 (a)). Then, an average is taken across center rows within the frame, a 1D Gaussian smoothing filter of standard deviation 3 applied with the *Python* function *scipy.ndimage.gaussian_filter*, and the sinusoidal pattern is plotted. A zeroth frame is selected, for which the designated phase of the extracted sinusoid is 0°. Next, the average distance between adjacent maxima of this sinusoid is calculated in pixels. This value gives the period of the pattern, in pixel units, as shown in Fig 4.9 (b). Custom *Python* code then cycles through all frames in the captured video and selects frames of equal intensity variation whose sinusoidal projections have relative phases of $(120\pm10)°$ and $(240\pm10)°$ from the selected zeroth frame (see Fig 4.9 (c)). Frames where the sine wave is non-discernible or the intensity variation between peak and trough is low relative to the zeroth frame are disregarded. This eliminates frames where coherence is temporarily disturbed while perturbations are still in progress. Then these frame numbers from the initial video are selected and the images are demodulated using Eqns 1.26 and 1.27 from Sect 1.3.1.

4.3.4 Image processing

For each phantom imaged with just 660 nm at 3 different spatial frequencies, the optical property maps are calculated a total of 18 times, using every other phantom as a reference in turn for each spatial frequency (6 phantoms $\times3$ spatial frequencies $=$ 18). This approach helps to average out errors arising from mismatches in expected optical properties of phantoms, which arises in turn due to discrepancies between DIS and SFDI measurements. Finally, the mean of all 18 optical property maps is used to determine the absorption and reduced scattering coefficients. A 2D Gaussian filter with standard deviation of 5 pixels is applied to resultant optical property maps using the function *scipy.ndimage.gaussian_filter*.

As 3 phantoms were imaged with both 515 and 660 nm simultaneously, the optical property maps are calculated a total of 3 times, using each phantom as

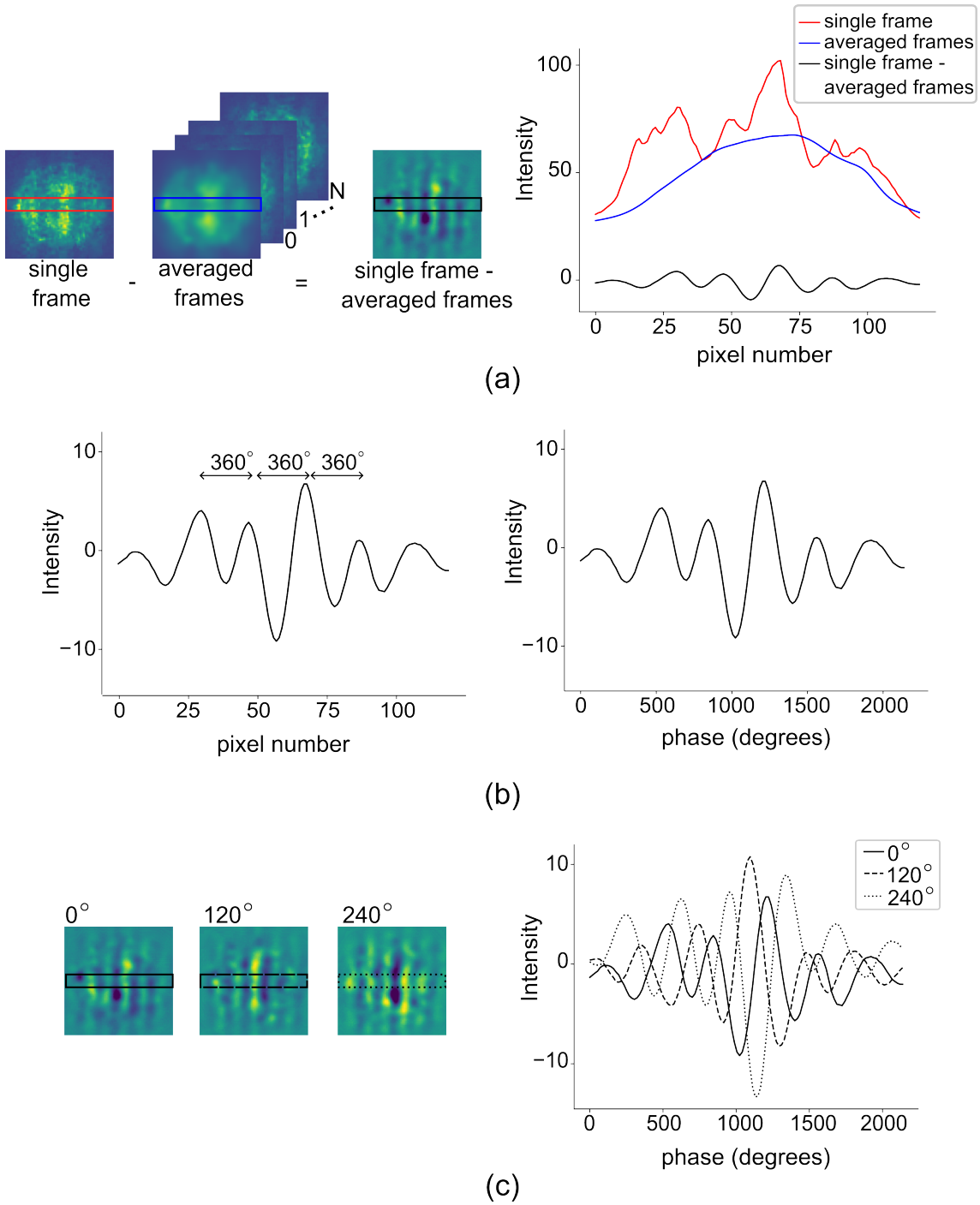

Figure 4.9: Characterisation of fringes and phase tracking (a) image of selected zeroth frame, average of all frames (where N is the total number of all frames within video capture) and the averaged frames subtracted from the selected zeroth frame, and corresponding cross sections (b) cross section of selected zeroth frame, depicting the conversion from number of pixels to phase shift in degrees (c) image of zeroth frame, 120° shifted frame and 240° shifted frame and corresponding cross sections.

a reference. The mean of all 3 optical property maps is used to determine the absorption and reduced scattering coefficients. A 2D Gaussian filter with standard deviation of 5 pixels is applied to resultant optical property maps using the function *scipy.ndimage.gaussian_filter*. It is important to note different reference values were used for red and green channel captures, as previously discussed.

The optical properties are calculated using a look-up table generated from the diffusion approximation, of parameters $\mu_a : 0 - 0.035$ mm^{-1} with a stepsize of 0.0001 mm^{-1} and $\mu_s' : 0.28 - 2.28$ mm^{-1} with a stepsize of 0.01 mm^{-1}.

4.4 Resultant system performance

Here, the results from the ultra-miniature SFDI system are presented. Detector and illumination performance are first presented. Then, the measured optical properties of phantoms imaged with the ultra-miniature system are shown. Average standard errors of 15% and 6% for absorption and reduced scattering coefficients, respectively, were obtained in comparison to the bench top system introduced in Chapter 2. Successfully variation in optical properties from two adjacent, optically variable phantoms was also obtained, for both single and dual wavelength projections. Finally, comparison of optical properties measured from 3 equiphase shifted captures to 6 equiphase shifted captures is presented.

4.4.1 Detector performance

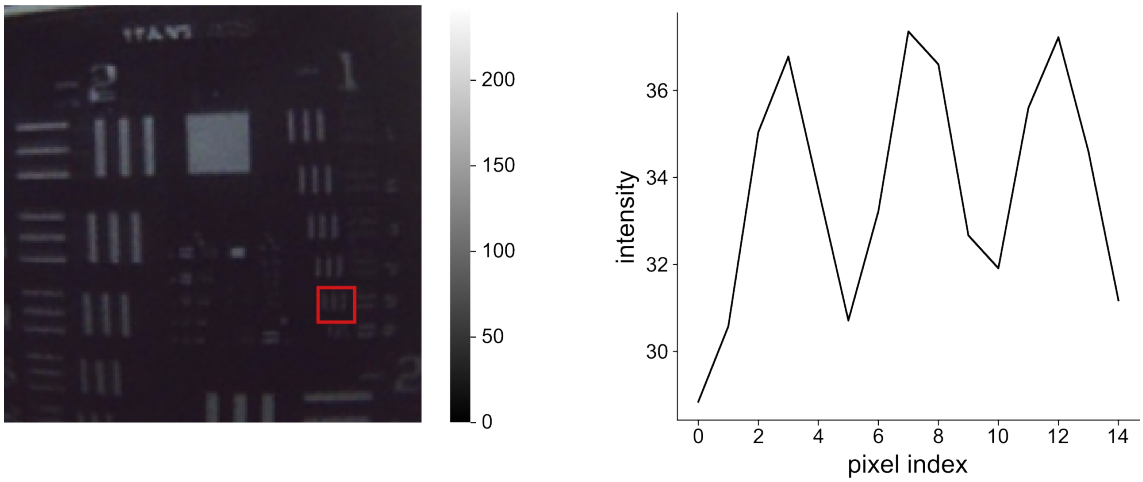

Figure 4.10: Determining the resolution of the detector (a) image of resolution target, uncorrected for distortion with red square denoting group -1, element 5. (b) averaged cross section of line pairs from group -1 element 5 of resolution test target

The performance of the micro camera is determined through imaging a resolution target, as discussed in Sect 4.2.3. An example captured image of the resolution target is shown in Fig 4.10 (a). Using documentation from [226], the resolution of

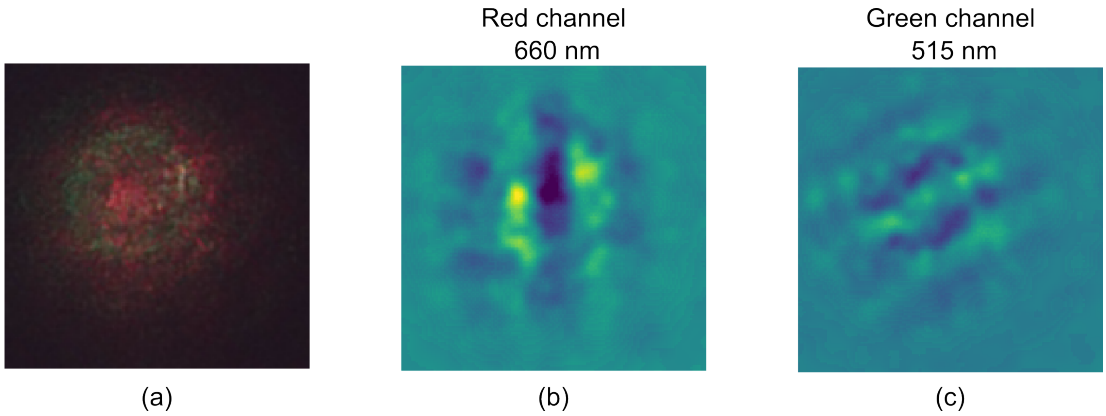

Figure 4.11: Investigating raw performance of detector when fiber array is on (a) image of dual wavelength projection pattern. (b) extracted red channel from (a). (c) extracted green channel from (a).

the imaging system was determined using the equation:

$$\text{Resolution}\left(\frac{\text{line pair (lp)}}{\text{mm}}\right) = 2^{\text{Group} + \left(\frac{\text{Element}-1}{6}\right)} \tag{4.2}$$

where a *group* is a set of 6 horizontal and vertical line pairs on the target, and the *element* refers to the number next to the adjacent horizontal and vertical line pairs within that group. The resolution is determined from the smallest element in which the line pairs are discernible from one another. The cross section of the smallest element discernible on the resolution target for the detector is shown in Fig 4.10 (b) for group -1, element 5. Therefore, the maximum resolution was determined using equation 4.2 to be 0.793 lp/mm, at a working distance of 50 mm. This result implies that the micro camera used will not be capable to detect interference fringes produced by the fiber with spatial frequencies ≥ 0.793 mm^{-1}.

Fig 4.11 (a) shows a frame capture of dual wavelength projection of 515 and 660 nm on a white background. The camera records a BGR image, which can be separated into the different channels in post processing, effectively separating the two wavelengths in the green and red channels respectively. As discussed in Sect 4.3.2, an experiment was performed comparing optical properties of phantoms measured with both wavelengths projecting interference patterns individually and simultaneously. Minimal cross talk from red and green channels was detected, which will further be discussed in Sect 4.4.5. While interference patterns are difficult to discern from the original image capture shown in Fig 4.11 (a), extracting the green and red channels individually enables effective fringe pattern detection, shown in Fig 4.11 (b & c) respectively. The interference pattern produced from the 515 nm laser is at an angle to the interference pattern produced from the 660 nm laser due to different channel illuminations for each wavelength.

4.4.2 Projector performance

The expected spatial frequency of the projected illumination pattern is comparable to the measured spatial frequency with 7% and 12% error for 515 and 660 nm respectively. This is determined from Fig 4.12, which shows the expected spatial frequency projection vs the measured spatial frequency actually projected at a working

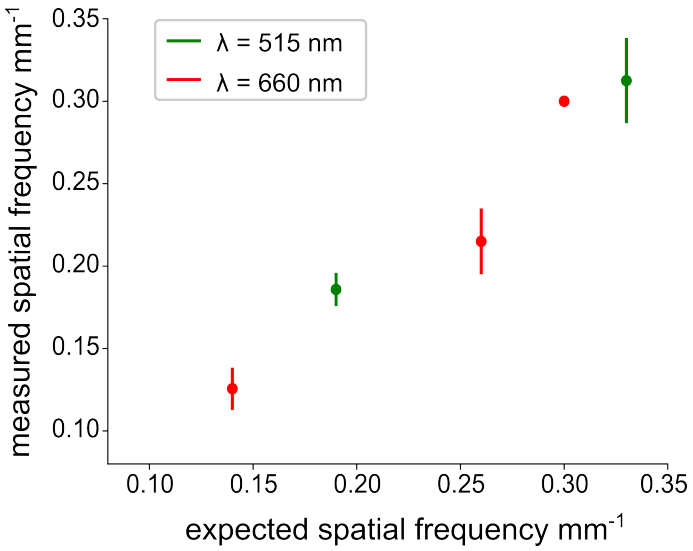

Figure 4.12: Expected vs measured spatial frequency projection from fiber array at a working distance of 50 mm for 515 and 660 nm. The error bars represent the standard deviation across measurements of different channel combination illuminations.

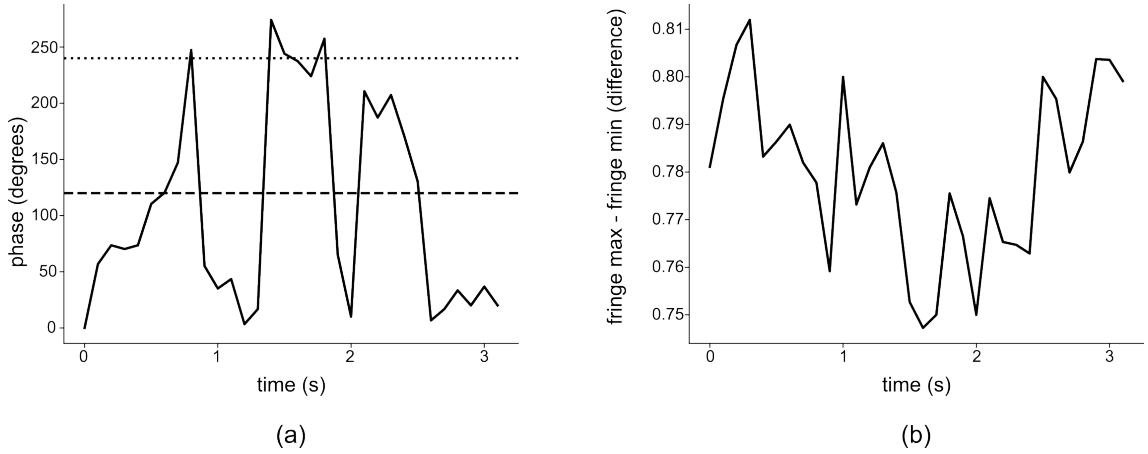

Figure 4.13: fiber array performance

distance of 50 mm. The spatial frequency of each channel pair (that was capable of producing a measurable spatial frequency) was recorded at 660 nm. Only two channel spacings, and hence two spatial frequencies, were recorded with the 515 nm laser for fiber tip spacings of 5 μm and 8.66 μm. Projected patterns at 515 nm at a fiber tip spacing of 10 μm will result in a spatial frequency ~ 0.4 mm^{-1} which is visually difficult to detect in the system, and also not within the range of interest. The average spatial frequency for each fiber tip spacing was recorded, and the error bars in Fig 4.12 represent the standard deviation of recorded spatial frequencies.

Some channels produce clearer interference patterns than others, as previously shown in Fig 4.6, due to cross talk between fibers. This also results in the interference pattern from some channels being more stable than others in time. Interference patterns tend to be stable for < 1 s under typical operating conditions, but for $\gtrsim 10$ s if the fibers are kept still. Fig 4.13 (a) shows the phase shift of fringes vs time for illuminating channels 2 and 5 with 660 nm laser, which results in a spatial frequency pattern of 0.15 mm^{-1} at 50 mm working distance. The video captured was during

a period when the fiber array was being manually moved. It can be seen that the camera records fringes of 120° and 240° phase shifted from the zeroth frame in < 1 s.

Fig 4.13 (b) shows the calculated difference from maximum to minimum of the interference fringes as a function of time. The difference from maximum to minimum appears relatively stable over the 3 s time interval.

4.4.3 Comparison of bench top and ultra-miniature system

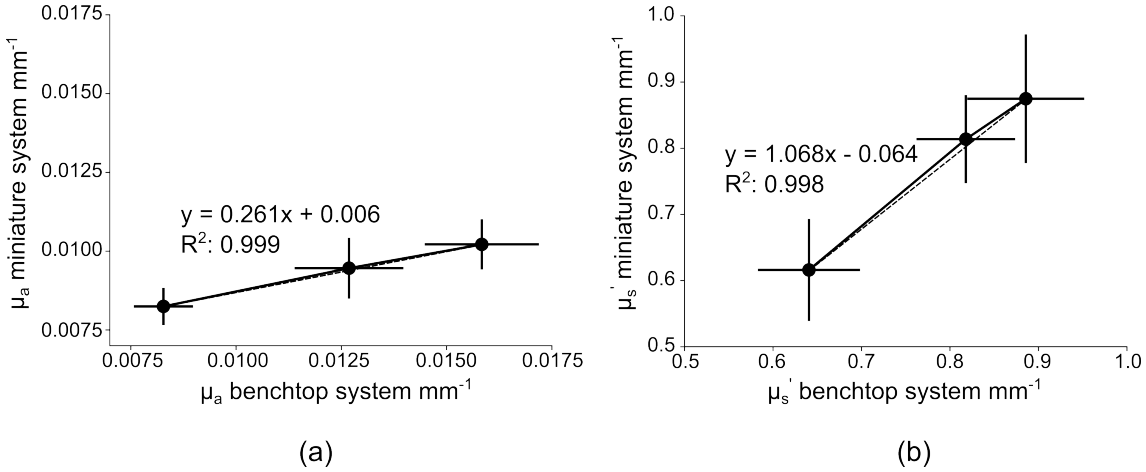

Figure 4.14: Comparison of bench top SFDI system and ultra miniature system: (a) absorption coefficient and (b) reduced scattering coefficient measured from bench top system (x axis) and miniature system (y axis). Error bars represent the standard deviation across the image. Dashed line represents fit of linear equation.

		Bench top		**Miniature**		**Error**	
Nigrosin	**TiO2**	μ_a	μ_s'	μ_a	μ_s'	μ_a	μ_s'
g	g	mm^{-1}	mm^{-1}	mm^{-1}	mm^{-1}	%	%
0.50	0.10	0.008	0.82	0.008	0.82	0.3	0.2
0.75	0.10	0.012	0.77	0.010	0.74	25.0	3.3
1.00	0.10	0.016	0.83	0.010	1.04	35.2	25.4
0.50	0.07	0.010	0.64	0.011	0.62	8.9	3.5
0.50	0.10	0.008	0.82	0.008	0.82	0.3	0.2
0.50	0.13	0.008	0.88	0.007	0.88	21.2	1.0
						15.1	5.6

Table 4.2: Comparing optical properties measured from bench top system and miniature system, showing standard % error calculation

The optical property measurements from the ultra-miniature system are compared with optical property measurements taken with the conventional bench top SFDI system, presented in Chapter 2. The results are shown in Fig 4.14 (a & b). It was found that the average standard error in the absorption and reduced scattering coefficients between the ultra-miniature system and the bench top system were 15%

and 6% respectively, shown in Table 4.2. The bench top system images were filtered using a 635 nm filter and the ultra-miniature images used a laser source at 660 nm laser. Therefore, the 15% error in absorption may be largely accounted for by the expected 14% difference in optical properties due to the wavelength shift [159]. The phantom which showed the greatest % error from the ultra-miniature system to the bench top system had 1 g of Nigrosin dye stock solution and 0.1 g of TiO_2. This phantom gave 35% and 25% error for absorption and reduced scattering respectively.

The sensitivity and specificity of the ultra-miniature system is poorer than the bench top system (which was found to have sensitivity $\geq$ 99.5% and specificity $\geq$ 86% for absorption variances which are > 0.003 mm^{-1}, and sensitivity $\geq$ 99.5% and specificity $\geq$ 81% for reduced scattering variances which are > 0.22 mm^{-1}, as discussed in Sect 2.5.1). The mini system has an average sensitivity of 67% for measuring absorption coefficients and 69% for measuring reduced scattering coefficients, with an average specificity of 63% for measuring absorption coefficients and 67% for measuring reduced scattering coefficients. These results are much less than the 90% sensitivity and 80% specificity required to comply with the American Society of Gastrointestinal Endoscopy as discussed in Sect 1.2.2.

4.4.4 Imaging typical gastrointestinal condition phantoms with ultra-miniature system

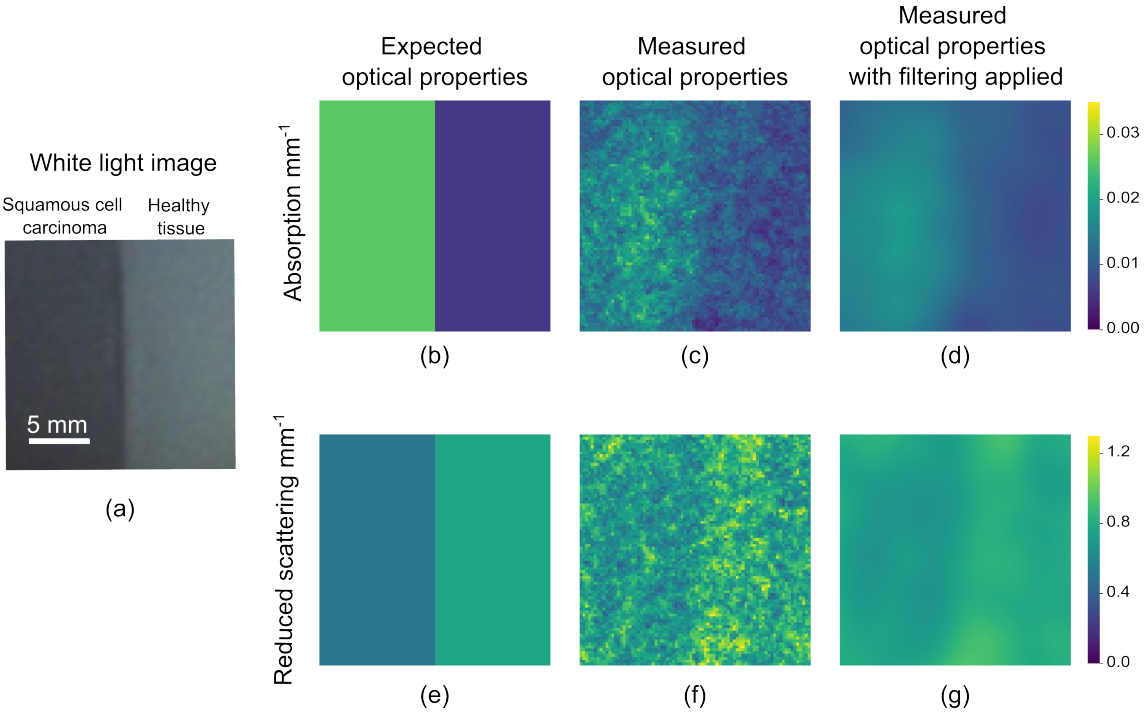

Figure 4.15: Imaging a phantom simulating oesophageal tissue at 660 nm: (a) white light image of two phantoms with different optical properties side by side (b) expected and (c) measured absorption coefficient of phantoms (d) measured absorption coefficient with smoothing filter applied (e) expected and (f) measured reduced scattering coefficient of phantoms (g) measured reduced scattering coefficient with smoothing filter applied. Expected optical properties are mean of the individual phantoms measured in bench top SFDI system.

Two phantoms to simulate typical gastrointestinal tissue states were fabricated: one with optical properties mimicking squamous cell carcinoma, and the second with optical properties mimicking healthy oesophageal tissue. The phantoms were cut and placed side by side, as shown in Fig 4.15 (a). The variance in absorption between the phantoms is optically detectable from this white light image, but a quantitative difference in absorption coefficient is not. SFDI imaging of this sample was then performed at 660 nm, with the expected absorption and reduced scattering coefficients shown in Fig 4.15 (b & e) respectively. Fig 4.15 (c & f) shows that the system can successfully image variation in absorption and reduced scattering coefficients between a simulated healthy and malignant sample, with the presence of some noise, with average standard errors across the two images of 42% and 38% respectively. This noise is averaged by the addition of a filter to the final optical property maps, however this comes at the cost of accurate edge detection between the two phantoms (see Figs 4.15 (d & g)), where the average standard errors are reduced to 35% and 27% respectively. This filtering was a Gaussian filter of standard deviation 3, as discussed in Sect 4.3.4.

The number of pixels each sub figure in Fig 4.15 is 150×150 pixels as a cropped region of the entire 320×320 pixels is selected. This cropping reduces the pixel resolution to $< 100,000$ pixels, making it incompatible for standard definition endoscopy, as discussed in Sect 1.4. Future work is required to reduce the working distance of the system such that the projected pattern takes up the entire field of view of the camera, ensuring all pixels are utilised.

4.4.5 Dual-wavelength imaging

The system performance was characterised across the two wavelengths: 515 and 660 nm. It was found that the recovered optical properties varied by $\leq 10\%$ when the two wavelengths are projected simultaneously, compared to projecting them sequentially. This demonstrates the capability of the system to image optical properties at two wavelengths simultaneously with relatively low cross-coupling. The use of an 850 nm laser was trialled with this set up. However, the ratio of laser power in to laser power detected from fiber tip was 200 : 1. Also the camera was not capable to detect IR light as it has an IR filter in front of it, which will be further discussed in Sect 4.5.2.

Two phantoms with different optical properties placed adjacent to one another were imaged, one mimicking the optical properties of squamous cell carcinoma and the other mimicking the optical properties of healthy oesophageal tissue. The results are shown in Fig 4.16. The expected optical properties are shown in Fig 4.16(a),(d),(g) and (j). The optical properties measured from the red and green channel are not expected to be the same as the phantom properties shift with wavelength [159]. It is expected that the phantom optical properties measured from the green channel are higher than phantom optical properties measured from the red channel.

The difference in optical properties from adjacent phantoms is visible from both the red and green channels. Visually, the measured optical properties from the green channel are higher than from the red, as expected. The average standard errors of absorption and reduced scattering coefficient measured in Fig 4.16 (b & h) are 58% and 40% respectively, reducing to 52% and 31% when filtering is applied as shown in

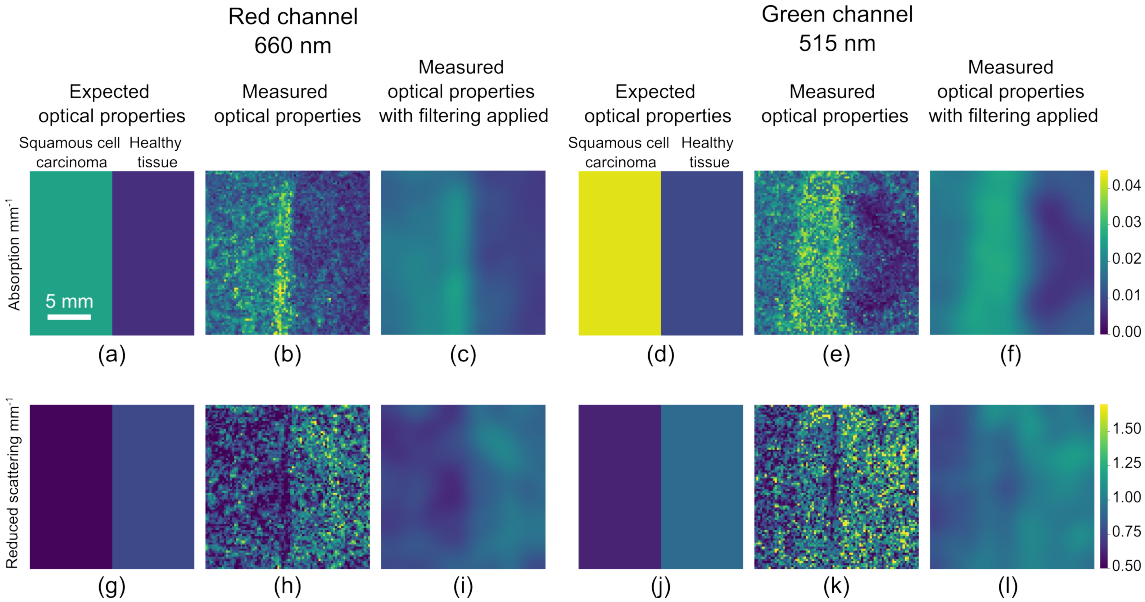

Figure 4.16: Optical properties measured from dual-wavelength imaging experiment: (a) expected absorption coefficient from red channel (b) measured absorption coefficient from red channel with (c) filtering applied (d) expected absorption coefficient from green channel (e) measured absorption coefficient from green channel with (f) filtering applied. (g) expected reduced scattering coefficient from red channel (h) measured reduced scattering coefficient from red channel with (i) filtering applied (j) expected reduced scattering coefficient from green channel (k) measured reduced scattering coefficient from green channel with (l) filtering applied.

Fig 4.16 (c & i) respectively. The average standard errors of absorption and reduced scattering coefficient measured in Fig 4.16 (e & k) are 55% and 31% respectively, reducing to 44% and 14% when filtering is applied as shown in Fig 4.16 (f & l) respectively.

4.4.6 Noise reduction

Two techniques are investigated for noise reduction: increasing from 3 phase to 6 phase imaging and increasing the number of spatial frequencies averaged over. The advantage of the fiber array system is the ability to project different spatial frequencies are different angles with the same illumination source. The results are shown in Fig 4.17. Fig 4.17 (a) & (e) show the expected absorption and reduced scattering coefficient maps respectively. Fig 4.17 (b)-(d) and (f)-(h) show the absorption and reduced scattering coefficient maps for using the conventional 3 phase image approach, increasing to 6 phase images, and then the conventional 3 phase images averaged over three different spatial frequencies. There is a visually detectable increase in accuracy from 3 phase captures to 6 phase captures. However, the image with most clarity is when averaging over three different spatial frequency projections. This is thought to be the case due to increased averaging of speckle noise present from the illumination, increasing accuracy, and was used for the above results presented in Sect 4.4.3 & 4.4.4. The standard deviation across the images reduces by $> 50\%$ from 3 phases, 1 spatial frequency to 3 phases with 3 spatial frequencies.

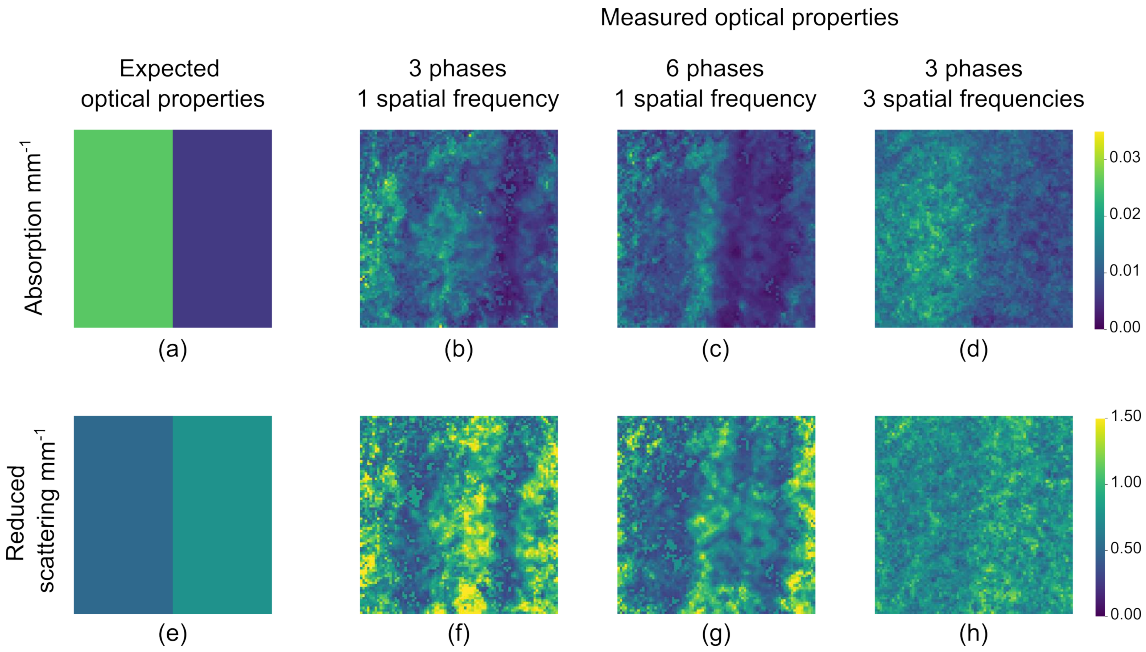

Figure 4.17: Different processing techniques for optical property measurement (a) expected absorption coefficient (b) measured absorption coefficient using conventional 3 equi-spaced phase captures at a single spatial frequency (c) measured absorption coefficient using 6 equi-spaced phase captures at a single spatial frequency (d) measured absorption coefficient using conventional 3 equi-spaced phase captures averaged over three spatial frequencies from different fiber channel illumination combinations (e) expected reduced scattering coefficient (f) measured reduced scattering coefficient using conventional 3 equi-spaced phase captures at a single spatial frequency (g) measured reduced scattering coefficient using 6 equi-spaced phase captures at a single spatial frequency (h) measured reduced scattering coefficient using conventional 3 equi-spaced phase captures averaged over three spatial frequencies from different fiber channel illumination combinations.

4.5 Discussion

An ultra-miniature SFDI system capable of imaging quantitative differences in optical properties of typical gastrointestinal conditions simulated in tissue-mimicking phantoms has been developed. It is sufficiently small to fit in the instrument channel of a standard colonoscope and endoscope ($\lesssim 3$ mm). This work could therefore form the the basis of a new device suitable for cost-effective, endoscopic deployment for population based screening of gastrointestinal cancers.

4.5.1 Comparison of developed system to bench top system

System size

The bench top SFDI system, discussed in Chapter 2, sits on a breadboard of base dimensions 300×450 mm, with a total system height of 385 mm from the breadboard base to the top of the projector. The size of this system makes it not compatible for *in-vivo* imaging. The proposed prototype of the ultra-miniature SFDI system is of 3 mm diameter. However, the length of the rigid distal end is currently 70 mm

in length, due to the rigid nature of the fiber tip. For potential *in-vivo* endoscopic imaging, this length should be on the order of that of the camera height, which is 2 mm. This would allow the whole system to be bendable *in-vivo*, and the potential to do so will be discussed in Sect 5.4.

System cost

In Sect 2.1.1, the cost of the bench top system is given as £508. This is considerably less than the proposed ultra-miniature system, which as discussed in Sect 4.2.2, has an initial cost of £3508. This is on the order of a typical bench top SFDI system proposed by *OpenSFDI*, as discussed in Sect 1.3.3, of £3852 [87]. Costing information on the miniature fringe projection systems discussed in Sect 4.1 was not available. The main cost of operating the device proposed in this chapter would come from paying clinicians salaries. Therefore, the capability of the device to be used easily and effectively by non-gastroenterologists is a desired feature.

Optical property measurements

The main comparison of interest between the two systems is their accuracy in optical property retrieval. As discussed in Sect 2.5.1, there are differences in SFDI and DIS measurements, and therefore the accuracy of the ultra-miniature system is compared against optical properties measured from the bench top system. However, as discussed in Sect 4.3.2, a 635 nm bandpass filter is placed in front of the bench top system camera and a 660 nm laser is used in the ultra-miniature system. Therefore, there will be a small offset in the measured optical properties as they are being measured at two different wavelengths. Different wavelengths were used for the bench top and ultra-miniature system as they were readily available for use, and future work lies in the purchase of a 660 nm bandpass filter for the bench top system for increased accuracy. For a set of phantoms with increasing Nigrosin dye stock concentration of $0.5, 0.75, 1$ g, the standard error in absorption coefficient measured via double integrating sphere from 635 to 660 nm (as obtained from [159]) is 19, 13 and 9% respectively. So one can expect that as the Nigrosin dye stock solution concentration is increased, the error between absorption coefficient measurements at the two wavelengths decreases. The error in reduced scattering coefficient measured via double integrating sphere from 635 to 660 nm (as obtained from [159]) remains roughly constant at 3% for a set of phantoms with increasing concentrations of TiO_2 of $0.07, 0.1, 0.13$ g.

The absorption and reduced scattering coefficient measurements of 6 phantoms from the ultra-miniature system were compared to measurements from the bench top system, obtaining average standard errors of 15% and 6% respectively. These errors correspond to sensitivity and specificity values which are not compatible with the American Society of Gastrointestinal Endoscopy requirements, as discussed in Sect 1.2.2. Further work is required on increasing the sensitivity and specificity of the device, which may lie in increasing the pixel resolution of the optical property maps. While these errors are in line with the expected errors between optical property measurements at the two different wavelengths used as discussed above, the expected differences of some phantoms are not as expected.

Firstly, across all 6 phantoms, the absorption coefficient measured with the ultra-miniature system is less than or comparable to that measured with the bench top

system, as expected. However, as shown in Sect 4.4.3, the ultra-miniature system struggles to measure high absorption coefficients. Table 4.2 shows that phantoms with Nigrosin dye stock solution > 0.5 g have an increased standard error than phantoms with 0.5 g of Nigrosin dye stock solution, which is the inverse of what is expected. To investigate this disparity, the DC and AC modulation amplitudes of the measured phantoms were investigated. It is known that significant inaccuracies in DC modulation amplitude result in inaccurate absorption coefficients and significant inaccuracies in AC modulation amplitudes result in inaccurate reduced scattering coefficients [2]. Because the bench top and ultra-miniature system results were measured in two different systems, it is not possible to directly compare modulation amplitudes due to the difference in system responses. Therefore, a ratio of modulation amplitudes is obtained for all phantoms in comparison to a reference phantom. The reference phantom was selected to be the phantom with minimal error in absorption and reduced scattering coefficients from Table 4.2, with a Nigrosin dye stock concentration of 0.5 g and a TiO_2 concentration of 0.1 g. Two ratios were calculated for all phantoms measurements from both the bench top and ultra-miniature systems: DC modulation amplitude/DC modulation amplitude of reference and AC modulation amplitude/AC modulation amplitude of reference. The phantoms with 0.75 g and 1 g of Nigrosin dye stock solution measured DC modulation amplitude ratios 5% and 21% greater than their corresponding phantom bench top system DC ratios. An increase in the estimation of DC modulation amplitude directly corresponds to a reduction in the absorption coefficient. Therefore, it can be deduced that the ultra-miniature system is over estimating the DC modulation amplitude for high absorbing phantoms, resulting in a lower measured absorption coefficient.

Secondly, as shown in Table 4.2, the standard error in reduced scattering coefficient for 5 of the 6 phantoms is $\leq 3.5\%$, where the miniature system is measuring a reduced scattering coefficient *lower* than the reduced scattering coefficient measured from the bench top system, as expected. However, for a high absorbing phantom with 1 g of Nigrosin dye stock solution and 0.1 g of TiO_2, the reduced scattering coefficient measured in the miniature system is 25% *higher* than the reduced scattering coefficient measured from the bench top system. The ratio of modulation amplitudes was again looked at, and a 50% increase from miniature system AC modulation amplitude ratio to bench top system AC modulation amplitude ratio was found for this phantom. As an increase in AC modulation amplitude results in in increase in reduced scattering coefficient [2], it is thought that the overestimation of AC modulation amplitude is the reason for this high reduced scattering coefficient.

The reason for the miniature system measuring a higher DC and AC modulation amplitude than expected for high absorbing phantoms is not known and requires further investigation. However several potential reasons are speculated here. The first is that it may be a result of improper fringe projection from the fiber array or slightly off phase shifts of selected frames. The second is the difference in system geometries. As the bench top and ultra-miniature systems have different geometries e.g. different working distances, projection angles, projector to detector spacings etc., it's possible that errors will arise between the two system geometries. It is proposed that generating a Monte Carlo look-up table with specific distances of the ultra-miniature system may increase the accuracy of absorption coefficient measurements. A third possibility is the lack of DC planar projections is preventing the

system from accurately sampling the absorption of the phantoms, as the absorption of a sample attenuated the low spatial frequencies of the modulation transfer function and the scattering attenuates the high spatial frequencies of the modulation transfer function.

However, from Fig 4.14 (a & b) it can be clearly seen that the ultra-miniature SFDI system is capable to distinguish between phantoms of varying Nigrosin dye stock solution and TiO_2 respectively. This is desired as detecting the correct variation in expected optical properties is more advantageous than exact optical property values as optical properties in tissues may change depending on their location and state (i.e. *in-vivo* or *ex-vivo*).

4.5.2 Limitations

This work has limitations that need further investigation before clinical translation. The first limitation is the choice of wavelengths, which in these experiments was 515 and 660 nm. By evaluating the absorption coefficient at two wavelengths, tissue information such as chromophore concentration can be determined. Oxyhaemoglobin (HbO_2) and deoxyhaemoglobin (Hb) are important tissue properties because they can detect perfusion, which enables differentiation between malignant and benign tumours [30]. *Mazhar et al.* have shown wavelengths of 670 and 850 nm are commonly used for accurate retrieval of HbO_2 and Hb information [34]. The system has two constraints which make it challenging to extend to the NIR e.g. 850 nm. First, the micro camera module has an IR filter that blocks light in this range, but future versions may remove this. Secondly, the fiber array was designed for 660 nm, and therefore the ratio of power from the coupler into the fiber array to power emanating from fiber tip when using a 850 nm laser was $200:1$, i.e. $< 1\%$ efficiency. In the future, a fiber array could be designed to operate successfully at both 660 and 850 nm. Fiber arrays with low-coupling between cores that operate well into the NIR (1550 nm) are routinely used in telecommunications [227].

The second limitation is the need for real time operation for use in clinical applications. In the system, the projected spatial frequency pattern often cycles through a period, giving the required 3 phases, in a short period of time (< 1 s), as shown in Sect 4.4.2. These fringes can be suitably captured by a camera operating at 10 fps. Though this gives an effective SFDI frame rate of at most 3.3 fps, faster frame-rate cameras could likely improve this: > 100 fps cameras are widely available. An SFDI frame rate of 10 fps is desired to be compatible with conventional imaging, which would be achievable using a camera with a higher frame rate of just 30 fps. However, the phase tracking algorithm is currently relatively slow (on the order of several minutes), so does not allow for real-time operation. This could be addressed by implementing the algorithm on a fast GPU that processes images as they arrive. Alternatively, images with non-optimal phases could be used for sinusoid fitting instead of waiting for 3 equispaced phases [228].

The third limitation is image quality, which is somewhat reduced by the non-ideal illumination patterns produced by the fiber array. The image quality here could be improved by using AI [185] or building custom LUTs based on non-ideal projection patterns [140].

4.5.3 Potential advances

Current polarisers are manually cut to size which can be challenging on miniature scales. Further miniaturisation of the device could look at the use of metasurfaces for polarisers on the fiber tip [229], or the use mechanical dicing to create high-quality polarisers down to scale [216]. Various fiber tip filters could also be placed to image different reflected wavelengths over separating camera colour channels [230].

For wide field lumen optical property mapping *in-vivo*, a patterned surface could be placed on a bare fiber to produce a concentric circle illumination pattern required for wide-field imaging inside tubular lumen, as discussed in Chapter 3.

This device also has potential to be used in additive manufacturing for investigating difficult to reach parts in machinery [212].

4.6 Conclusion

This chapter shows the capability of an ultra-miniature (3 mm diameter) SFDI system to detect quantifiable variances in absorption and reduced scattering coefficients in tissue mimicking phantoms with errors of 15% and 6% respectively, compared to a conventional bench top SFDI system. The system has the capability to project two wavelengths simultaneously, enabling extraction of additional properties such as tissue chromophore information. Tissue-mimicking phantoms simulating typical gastrointestinal condition of squamous cell carcinoma adjacent to healthy oesophageal tissue were fabricated, where the absorption coefficient of squamous cell carcinoma is much greater than that of healthy tissue and the reduced scattering coefficient is lower. Successful imaging of this variation with the system at both one and two wavelengths simultaneously has been shown, providing enhanced contrast between the two tissue types. It is envisaged that this system could be used for cost-effective endoscopic screening of gastrointestinal cancers, providing earlier detection and reducing the mortality rate.

Chapter 5

Future works & conclusion

This thesis presents the initial steps in the development of an ultra-miniature spatial frequency domain imaging (SFDI) system, capable of potential endoscopic deployment for early stage gastrointestinal cancer detection. Future work is required on the ultra-miniature SFDI prototype, proposed in Chapter 4, before successful deployment in a clinical setting. Here, potential future work to advance further development of this device, through both simulation work and hardware and software advancement, is discussed. With these future potentials in mind, a conclusion is drawn on the work as a whole and a proposition for the future of this device is presented.

5.1 Potential future work

5.1.1 Simulation of miniature system in Blender

It is envisaged that the SFDI simulation tool developed in *Blender* (presented in Chapter 3) will be used as an aid for future SFDI systems to speed up the design and development process. This is due to the fact that *Blender* has the capability to simulate realistic lighting conditions, such as use of various colours of incident light, various incident power intensities, and various spatial frequencies of projection. It also has the capability to simulate realistic imaging geometries, as was demonstrated in Chapter 3 by imaging inside a tube, simulating a lumen.

As discussed in Chapter 3, the simulation was used to investigate constraints inherit with miniaturisation of SFDI systems, such as smaller projector-camera angles. The effect of non-planar projection on optical property extraction was also investigated. These results were then used in the development of the ultra-miniature system in Chapter 4. Simulation of the actual ultra-miniature SFDI imaging system in *Blender* is desired to further develop the prototype. The fiber array could be simulated by use of pre-existing shader simulating glass, and illumination may be simulated by altering the colour of the incident light. Simulation of the fringes with speckle noise may also be possible. A visual representation of the proposed fiber simulation in *Blender* is shown in Fig 5.1.

This simulation would be advantageous for several reasons. Firstly, recreation of the interference patterns produced by the ultra-miniature system in *Blender* would allow for a direct comparison in optical property retrieval between the simulated bench top and ultra-miniature systems *and* the physical bench top and ultra-

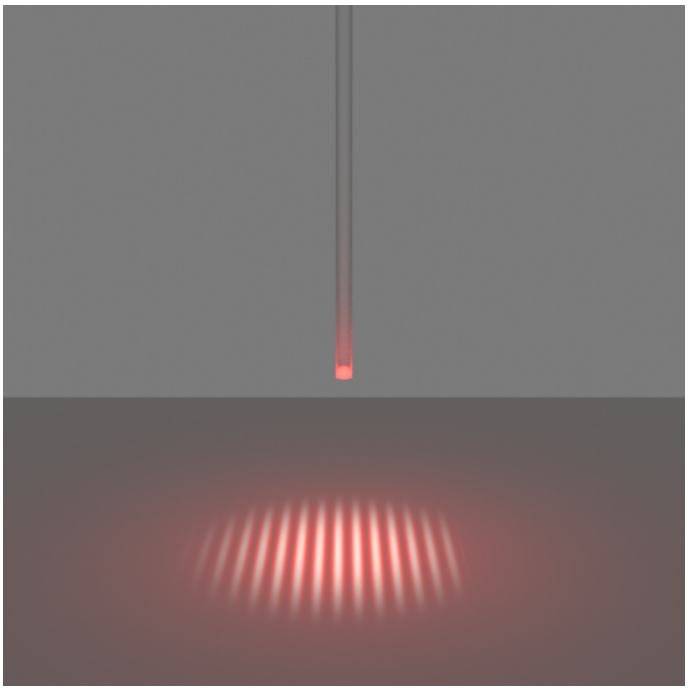

Figure 5.1: Example of simulated fiber array in ultra-miniature SFDI imaging system in *Blender* projecting an interference pattern. This will allow custom LUT development for more accurate optical property measurements

miniature systems. This may then highlight where errors are arising in the physical ultra-miniature system, resulting in the capability to resolve issues and therefore an increase in accuracy of optical property measurement.

Secondly, *Blender* has the capability to simulate large quantities of data. By accurate simulation of the ultra-miniature SFDI system, one could simulate vast quantities of data for varying material optical properties, thus allowing the generation of a custom look-up table (LUT) for the ultra-miniature system. The capabilities of *Blender* mean several LUTs for different spatial frequencies, wavelengths, and working distances (for example) can be developed at ease. This could then be incorporated with the physical ultra-miniature system for increased accuracy in optical property measurement.

For this to be possible, several improvements to the existing simulation model are required. The first is the expansion of the range of optical properties from which SFDI and double integrating sphere results agree. The current model is accurate for absorption coefficients within the range $0.05 - 0.25$ mm^{-1} and reduced scattering coefficients within the range $1.5 - 6.5$ mm^{-1}. Exploring the lower range of both absorption and reduced scattering coefficients possible with the SFDI simulation is desired. Lowering the minimum absorption and reduced scattering coefficient may require the development of a simulation other than a double integrating sphere to characterise the material, as this may not be returning accurate results due to loss of light rays at the sample-sphere interface.

5.1.2 Increasing accuracy in tubular geometry measurements

A novel illumination pattern for wide field optical property mapping within a tubular geometry was presented in Chapter 3. This pattern has shown accurate optical

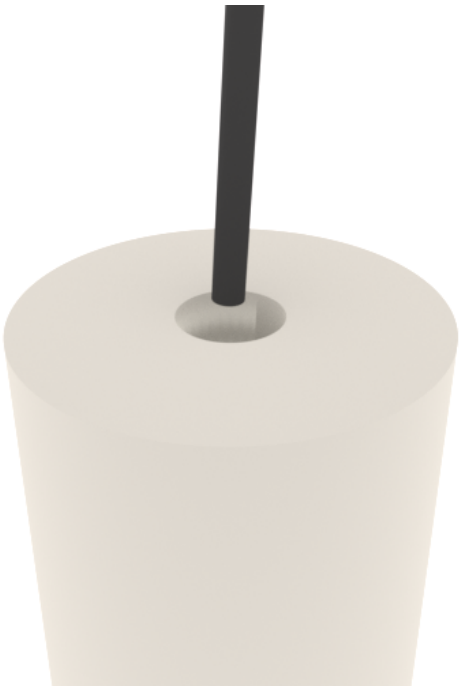

Figure 5.2: Visual schematic of a simulated probe entering tube. There is potential to use animation in *Blender* to investigate optical property extraction at different distances as the probe is in motion.

property retrieval when both the camera and projector are placed 110 mm above the proximal opening of the tube. Knowledge of how accurate this projection pattern is at optical property retrieval as the projector and camera, packaged together as a probe, advance into the tube is desired. *Blender* has the capability to advance the simulated probe into the tube by use of the animation feature, and in doing so measuring the resultant optical properties on the inner tube wall as the probe progresses throughout the tube length. This would be advantageous for understanding how optical properties vary at different depths within the tube. Different probe-tube distances may return inaccuracies in optical properties, and a relationship between captured phase and distance from probe to tube wall may be required to correct for these inaccuracies, for example. Custom LUTs for different depths within the tube may also be required.

Another proposed idea is to determine shape information of objects placed within the tube at varying depths using the novel illumination scheme. Chapter 3 presented the successful reconstruction of object shape in up-close, planar geometries. However, the acquisition of object shape in a wide field, tubular geometry is yet to be explored. As previously discussed, obtaining the height and shape information of an object with fringe profilometry requires knowledge of the specific system geometry. Therefore, determining object height within a tube at an unknown distance from object to probe is challenging and will have to be investigated.

The use of endoscopic imaging in tubular geometries has been explored for manufacturing applications to aid in the detection of faults in difficult to reach areas [212, 231]. This simulation tool in *Blender* may also be used to accelerate development of such devices, where shape information can be used to assess three dimensional defects.

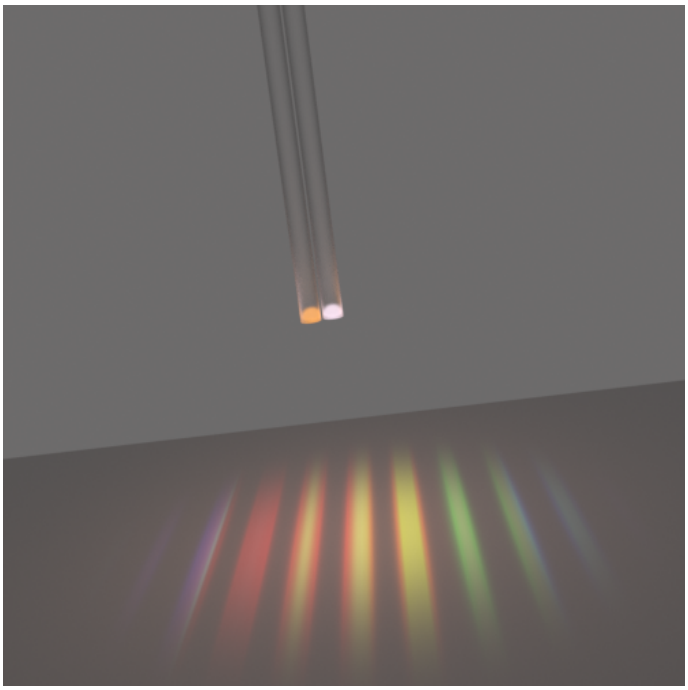

Figure 5.3: Example of fiber producing a multispectral sinusoidal pattern and adjacent fiber providing therapeutic light

5.1.3 Complementary imaging with ultra-miniature system

The current ultra-miniature SFDI system presented in Chapter 4 has the capability to perform optical property mapping at two wavelengths (515 and 660 nm), which has the potential to extend to chromophore mapping of biological tissue samples. There are several other imaging techniques that have the capability to be complimentary to miniature, endoscopic SFDI, which will be discussed here.

First, the incorporation of fringe profilometry with the ultra-miniature system, as successfully demonstrated with the bench top system in Chapter 2, is desired. Shape information can be an important factor in staging colorectal cancer polyps [76], and therefore it is highly desired for an *in-vivo* gastrointestinal imaging tool. Obtaining shape information with the current system may involve the use of high spatial frequencies to ensure sufficient fringes pass over the object of interest. Phantoms smaller than the hemispherical phantoms fabricated in Chapter 2 will be required to be fabricated to test the system for height and optical property recovery.

Further advances could combine a secondary fiber to deliver therapeutic light to a sample, as depicted in Fig 5.3. *Kress et al.* present of a dual channel endoscope consisting of two fibers, one to image reflectance to infer tissue properties and the second to deliver therapeutic light [232]. Mid-infrared wavelengths ($3 - 50$ μm) can ablate soft and hard tissues due to the strong absorption of tissue molecules such as water, proteins and lipids at these wavelengths [233, 234]. This strong absorption results in substantial heating which can precisely excise biological tissue at a shallow absorption depth of $10 - 100$ μm [235]. By detecting abnormal tissue with SFDI and ablating it with a therapeutic fiber in the same procedure, typical gastrointestinal procedures where biopsy is required would have reduced wait times. This is because patients requiring screening could have their procedure in a point of care environment rather than a hospital, reducing cost and increasing number of

patients seen.

Another advance of this device could be to incorporate the use of laser speckle imaging (LSI) [105]. LSI, as discussed in Sect 1.3.2 is the imaging of random speckle patterns from a coherent laser to image blood flow [64]. *Chen et al.* have shown that the random speckle illumination produced from a laser diode can be used to sample the modulation transfer function of a sample of interest at known spatial frequencies, enabling the successful extraction of sample optical properties, a technique termed speckle illumination spatial frequency domain imaging (si-SFDI) [52]. *Milstein et al.* have shown the capability of the technique in detecting ischemic areas on gastric tube reconstructions following oesophagectomy [106]. As the apparatus required for LSI are non-bulky in nature, it is possible that it could be incorporated into the miniature device to image optical properties and perfusion simultaneously within the gastrointestinal tract, improving disease diagnosis. It would also be possible to investigate the speckle illumination pattern produced by the laser, projected from the fiber array for it's potential to be used for LSI instead of additional components.

In some clinical imaging, such as imaging skin or muscle, knowing the orientation of the scattering is advantageous in early detection of disease diagnosis. *Konecky et al.* predict that in a turbid medium, the attenuation of a projected sinusoidal pattern will vary depending on it's orientation with respect to the subsurface scattering structures within the medium [236]. Therefore, by rotating the projected pattern on the medium and measuring it's attenuation and phase shift, one can image the spatially varying orientation of the medium and therefore determine the direction of scattering structures. This is possible with the proposed system as different channel illumination pairs project spatial frequencies at different angles. The addition of this technique could provide additional information to aid in disease diagnosis.

Also, as previously discussed in Sect 4.5, if the monitoring of Hb and HbO_2 in a sample is to be done efficiently, a fiber array would need to be fabricated that operates effectively in the NIR. The possibility to fabricating a fiber array capable to operate efficiently at multiple wavelengths, including the NIR should be investigated, as depicted in Fig 5.3. This may involve fibers optimised for 660 and 850 nm within the same array. Multi wavelength imaging is advantageous for extracting additional sample information which can be indicative of disease state.

5.1.4 Reduction of acquisition & processing speeds

Further work is needed in increasing the acquisition and reducing the processing speeds of the ultra-miniature SFDI device if it is to be deployed in a clinical setting. The current time from commencement of video capture to final optical property maps is on the order of several minutes, which is not feasible in a clinical environment. The reason for this extended time from initial acquisition to final optical property maps is for several reasons. First, the process is currently not automated, and hence time is lost between image acquisition and image input to processing code. The next step should therefore be automation of the system, from initial video capture to resultant optical property maps.

The second step lies in optimisation of the processing code, currently written in *Python*. The most time consuming part of the code is the phase tracking algorithm, presented in Sect 4.3.3. This code cycles through all frames within the video and selects frames equally shifted in phase from one another. As discussed in Chapter

4, the fiber array is essentially an interferometer and shifts through multiple periods in a short amount of time, shifting phases to 120° and 240° in < 1 s. However, the chosen camera has a frame rate of just 10 frames per second. Therefore, the video capture may not exactly capture the 120° and 240° phase shifts in < 1 s, and several seconds of video are typically required to extract the equiphase shifted frames. It is thought that a camera with an increased framerate would therefore reduce the acquisition speeds by several seconds. The processing code may also be increased by use of a fast GPU.

As discussed in Chapter 1, groups have shown decrease in optical property map generation time to < 1 s by use of AI [60, 61, 63]. Combining these techniques with the system may enable more processing times feasible for use within a clinical setting.

At quicker acquisition speeds, the imaging of clinical samples, possibly resected colon polyps or resected areas of Barrett's Oesophagus, will then be desired as a clinical proof of concept. The updated system may then be prototyped to a clinical device ready for endoscopic deployment.

5.1.5 Further prototype development

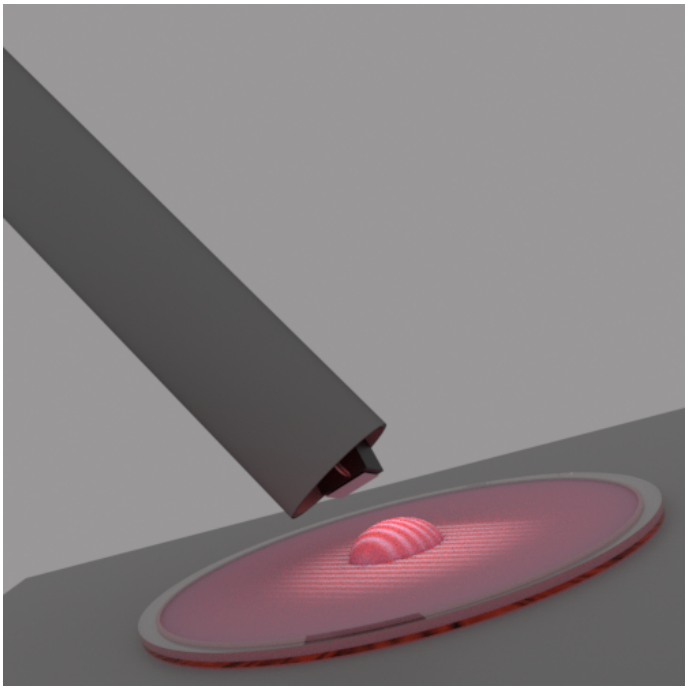

Figure 5.4: Visual of fiber array and micro camera encapsulated in flexible tubing, imaging an *ex-vivo* sample of gastrointestinal tissue.

The proposed prototype has sufficient diameter to fit in the instrument channel of a conventional endoscope or colonoscopes (3 mm), and such could be used to accompany conventional white light imaging as an additional contrast. As discussed in Chapter 4, the current rigid length of the proposed prototype is 70 mm. This length, due to the rigid nature of the distal end of the fiber array, is not feasible for *in-vivo* gastrointestinal imaging and needs to be reduced.

It is thought that further tapering the tip of the fiber array will create a flexible tip. The maximum desired length of fiber rigidity is 2 mm, which is the height of

the micro camera. This should allow flexible movement of the device. The current steel tubing used will also have to be replaced with a more flexible material. Typical endoscopes are made flexible by use of different polymers [237].

Alternatively, a device could be fabricated in which the fiber array is projected at an angle from the side of the distal end of the scope, such that the projection pattern is incident on the gastrointestinal tract wall. The scope would then have to be rotated to image the entire lumen, or the use of two fiber arrays each projecting out opposites sides of the scope is possible. This type of device would likely be used in solitude, without going down the instrument channel of an existing endoscope or colonoscope.

The current input power of the laser light at 660 nm is $\leq$ 5 mW, as stated in Chapter 4. Increasing this low power needs to be investigated, while keeping the device in accordance with the maximum permissible exposure of laser radiation on tissue. In the UK, this British Standard BS EN 60825-1:2014+A11:2021 forms part of the International Standard IEC 60825 on laser radiation, which indicates the maximum permissible exposure permitted on tissue, depending on the incident wavelength and exposure time. This standard must be taken into account when advancing the development of this device.

As discussed in Sect 1.4, tethered capsule endoscopy has shown promise as a less-invasive technique for imaging upper gastrointestinal conditions. Packaging the device into a tethered capsule may allow for advances in use in screening potential, reducing the amount of patients awaiting endoscopy. If regions of interest are identified on initial screening, the patient may then be referred for an endoscopy. However if nothing suspicious is detected, the patient would not require an endoscopy procedure. This would be advantageous for patients who require regular endoscopic screening, such as for monitoring Barrett's Oesophagus.

It is estimated that taking a medical device from concept to commercialisation such that it is available to the public is $3 - 7$ years [238]. There are several steps involved in this time frame to get a regulatory approved device. First, the classification of the medical device must be determined, where the higher the risk to the patient, the higher the class. According to the UK Medical Device Regulations, there are four main classes of medical devices: class I, class II and class III, where class III devices require the most regulatory control [239, 240]. According to the US Food and Drug Administration, endoscopes are classified as class II medical devices, where the associated photographic accessories can be classified as class I [241].

To get the device presented in Chapter 4 to market, it will need to be properly regulated. For the UK market, this means acquiring UKCA (UK Conformity Assessed) marking. To obtain a UKCA mark on a device, a conformity test is required to be completed by a regulatory body, such as the MHRA (Medicines and Healthcare products Regulatory Agency), which assesses the relevant requirements for UKCA marking. However, UKCA marking is not recognised by the EU and such CE marking is required for the EU market, for which a conformity test must be performed by a European regulatory agency. These procedures are required for class II and class II medical devices, however manufacturers of class I medical devices can declare the conformity of their medical devices themselves [242].

5.2 Conclusion

This thesis presents work on the development of a cost-effective, ultra-miniature SFDI system with the aim of endoscopic deployment for improved gastrointestinal cancer detection. First, in Chapter 2, a conventional bench top SFDI system was constructed with the aim to characterise the optical properties and shape of tissue-mimicking phantoms. A phantom protocol developed by collaborators at the University of Cambridge was followed to fabricate phantoms of desired optical properties. These phantoms were imaged in the bench top SFDI system with accuracy of 19% and 11% respectively for absorption and reduced scattering coefficients, compared to expected values from double integrating sphere measurements. Phantoms mimicking typical optical property variation seen in gastrointestinal tissues were also imaged for their optical properties and shape. This chapter represents the capability of a cost-effective bench top SFDI system to successfully image typical gastrointestinal condition phantoms.

To miniaturise this bench top SFDI system, several design points such as projector-camera angle, illumination conditions, and imaging in non-planar geometries had to be considered. To aid in the investigation of these constraints, a model of an SFDI system was simulated in *Blender*, discussed in Chapter 3. The simulated material was characterised to have specific absorption and reduced scattering coefficients through simulating a double integrating sphere set up. It was found that smaller projector camera angles (4°) allowed accurate optical property measurements on a sample of material simulating healthy oesophageal tissue. Imaging wide field of view in a tubular geometry proved a challenge and conventional sinusoidal pattern illumination resulted in non-uniform spatial frequencies throughout the tube length. A novel illumination scheme was then developed to correct for this, such that the projected pattern has uniform spatial frequency throughout the length of the tube, allowing for wide field optical property mapping within tubular lumen, such as an oesophagus. It was also found that the tube had to be sectioned in length to different look-up tables for more accurate optical property measurement. This work showed the capability of the graphics software *Blender* to be used in diffuse optical system design.

Taking what was learnt from the SFDI simulation study, an ultra-miniature system was developed as discussed in Chapter 4. The novel use of an interfering fiber array for optical property measurement was tested to replace bulky projectors, typical in conventional SFDI systems. Phantoms were again fabricated as before and imaged in both the bench top and ultra-miniature system, with 15% and 6% accuracy between systems for absorption and reduced scattering coefficients respectively. The capability of the ultra-miniature system to successfully differentiate between adjacent phantoms of variable optical properties was also presented.

This work presents the first step in the development of a cost-effective, high contrast imaging device for deployment in population based screening for gastrointestinal cancers. SFDI has shown to provide enhanced contrast over typical white light endoscopy, even at the miniature scale. By using this system to detect gastrointestinal cancers at an early stage, treatment can be obtained and survival rates should increase drastically.

Chapter 6

Supplementary: Investigating aerosol generation during gastrointestinal procedures

Due to the Covid-19 pandemic, clinical collaborators became interested in the generation of aerosols during gastrointestinal procedures. Aerosols are classified as particles < 5 μm that are airborne, linger in the area of production, and are capable of transmitting virus particles [243]. Upper gastrointestinal (GI) procedures are classed as aerosol generating procedures (AGP), meaning that certain protocols must be followed if a persistent virus is present e.g. Covid-19. Firstly, all clinical staff are required to wear full personal protective equipment (PPE). Secondly, after each endoscopy procedure, the room in which the procedure took place must be left free for 20 minutes to allow the aerosol particles to settle. This is called 'fallow time'. Finally, the room in which the procedure took place must be fully disinfected before the clinicians can re-enter the room and start on the next patient. This means that fewer patients can be seen in a session as there are longer wait times between procedures. This fallow time was not necessary for lower GI procedures, as they are not classified as AGPs. The aim of the study presented here was to quantify aerosol generation during upper and lower GI procedures. The work presented here is based on [142, 143]. This authors contribution included study design, some initial data collection, and whole data collation and processing, which was then sent to Dr. Gordon for statistical analysis. Statistical analysis of results presented here is not work by this author.

6.1 Study design

For this prospective, observational study, Health Research Authority and ethical approval was granted by the Wales Research Ethics Committee before the start of the study. Consent was obtained from all patients. Patients undergoing routine upper GI and lower GI endoscopy on the lists of 13 different participating endoscopists at the Endoscopy Unit of the Nottingham University Hospitals NHS Trust Treatment Centre were included, between October 2020 and March 2021. Inclusion criteria were patients > 18 years of age with the capacity to consent. For reasons of practicality, entire lists were selected for recruitment, and all those on each list who met the inclusion criteria were invited to participate. Procedures were performed as they

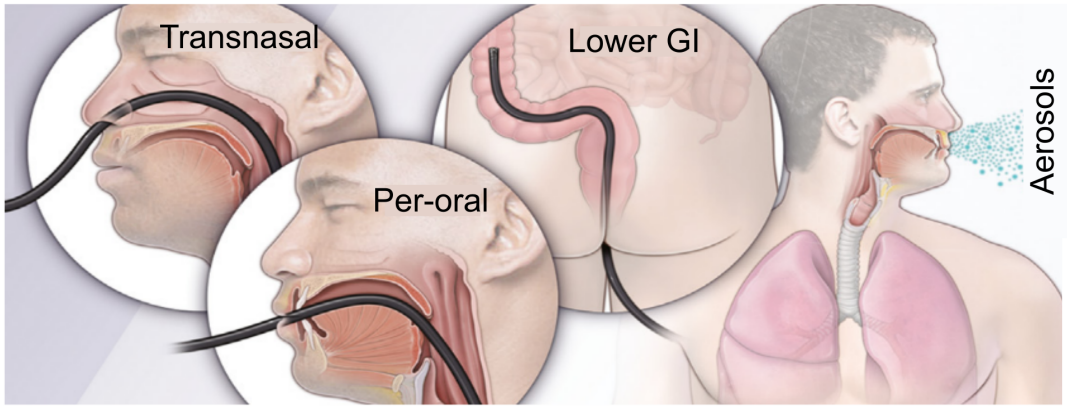

Figure 6.1: Depiction of upper GI transnasal and per-oral procedures, as well as lower GI colonoscopy or flexible sigmoidoscoy procedure. Adapted from [142]

normally would be in clinical practice. To standardise procedures, endoscopy rooms within the same endoscopy suite were used, which all had room ventilation set at $15-17$ air changes per hour and were of a similar size, air temperature, and humidity level. Unnecessary airflow was minimised by not allowing the room doors to be opened during the procedures and only allowing 1 additional person (the research nurse) in the room. All present in the room wore enhanced PPE that minimised additional human aerosol sources.

Both upper GI and lower GI procedures were recorded. Two types of upper GI procedures were recorded: per-oral and transnasal. Per-oral is a typical endoscopic procedure, whereas a transnasal procedure enters the oesophagus through the nasal cavity instead of the mouth, as shown in Fig 6.1. Patients have shown preference to transnasal procedures over conventional per-oral procedures [244]. Two types of lower GI procedures were also recorded: colonoscopy and flexible sigmoidoscopy. Both procedures enter the gastrointestinal tract through the anus. A colonoscopy examines the entire bowel, whereas a flexible sigmoidoscopy examines just the rectum and lower part of the bowel [245].

6.2 Study methodology

6.2.1 Instruments

Two pieces of equipment were used to measure particle sizes. The first was an Aerotrak portable particle counter (Model 9500-01, *TSI*, United States), shown in Fig 6.2 (a), which measured particle diameters in 6 ranges: ($0.5-0.7$ μm, $0.7-1.0$ μm, $1.0-3.0$ μm, $3.0-5.0$ μm, $5.0-10.0$ μm, and $10.0-25.0$ μm). A 2 m tube connected the particle counter to an isokinetic head, which was connected onto an articulating arm, mounted onto side of the procedure trolley. For upper GI procedures, the isokinetic head was placed $\sim$ 10 cm from the patient's mouth and for lower GI procedures, it was placed $\sim$ 20 cm from the patient's anus. Thesis distances were chosen for their compatibility with previously published studies [246], and represented an acceptable trade off between practicality (such as access to scope and need to change patient position) and maximising aerosol capture (known to be

Figure 6.2: Instruments used for aerosol and droplet generation (a) Aerotrak [248] (b) VisiSize [249]

reduced significantly by 2 m in a room with high background particles [247]). The operator's hands are kept $>$ 50 cm from the isokinetic head to avoid interference from leakage through the endoscope's suction, air and water controls.

The second piece of equipment used was a VisiSize spray characterisation tool (Model N60, *Oxford Lasers*, UK), shown in Fig 6.2 (b). This instrument allowed sizing of particles from $\sim$ 10 μm to 3.5 mm in diameter, much larger than the suspected aerosol range. It is important to consider these larger size ranges because respiratory aerosols are believed to be polydisperse, with 2 size peaks at around 1 μm and 100 μm in diameter [247]. The instrument images particles that pass through a small volume located between a laser head and a camera of dimensions $12.6 \times 7.2 \times 50$ mm $= 4536$ mm^3). The instrument is placed such that this volume is located $\sim$ 10 cm from the mouth of the patient, for reasons previously discussed.

6.2.2 Data collection

During the procedure, an observation camera with a timestamp feature was used to record audio and video for synchronisation purposes. The camera was used to record the time displayed by the clocks on the particle counter, the spray characteriser, and the endoscope. This meant that the feed could later be synchronised to within 1 s and correlated with recorded event timings. For each procedure, an experienced research nurse recorded information on a case report form containing demographics (age, sex, body mass index, smoker) and variables determined during the procedure (sedation type, degree of discomfort, use of CO_2 or water for lower GI procedures, subjective 3-tier estimate of anal tone taken during the pre procedure digital rectal examination and representing pressure required for insertion, and presence of hiatus hernia). During the procedure, the times of relevant events, beginning when the patient entered the room and ending after the patient left the room, were recorded alongside the time of the event to the nearest second. Times were then synchronised from the videos recorded by the camera, the case report forms were transcribed into CSV format, and any discrepancies (e.g. inaccurate timings, ambiguous terminology, etc.) were resolved using the videos. Periods of time when there were no significant events (e.g. lengthy examinations without patient movement) were identified and marked as 'null reference' events in the final data files.

6.2.3 Data processing

Whole procedure

First, the total particle count for each procedure for 2 particle diameter ranges; $0.5-5$ μm (aerosols) and $5-25$ μm (droplets) were considered. The time period considered commenced from either anaesthetic spray (for upper GI procedures) or intubation (for lower GI procedures), and ended at extubation (for both procedures). This particle count was compared with a reference period before the procedure began. It was thought that the fallow period of 20 minutes between procedures should minimise interference from residual particles, but for comparison an alternative method was also considered. This method used a background removal technique based on smoothing to estimate particle counts.

Causal event-based

The causal event–based model was next applied, which essentially takes a difference in particle counts before and after an annotated event (e.g. cough) to estimate the number of particles produced by the event. For each annotated event, the room background particle count immediately before the event was first estimated by smoothing the data over a 105 s period. This background was then subtracted from the raw particle count immediately after the event and averaged over a period of $15-30$ s. To validate this background subtraction approach, it was also applied to several periods when there was no annotated event, and such the expected difference was to be ~ 0.

6.3 Results

A total of 96 procedures were recorded: 48 upper GI procedures (37 per-oral, 11 transnasal) and 48 lower GI procedures (37 colonoscopies, 11 flexible sigmoidoscopies). Of the upper GI procedures, 17 patients were asked to perform a voluntary cough and 12 to perform deep breathing and speaking before the commencement of the procedure. This was to be used as a reference against non-voluntary events during the procedure. Of the total 96 patients, 52 were men and 44 were women, with a median age of 62 years and median body mass index of 25.5 kg/m^2. 14 patients reported themselves as a smoker, whereas 82 did not.

6.3.1 Whole procedure analysis

The particle counts were normalised to procedure duration, relative to the reference background, and the results are shown in Fig 6.3. Over the full range of particle sizes ($0.5-25$ μm), it was found that both per-oral and transnasal upper GI procedures produced significantly higher particle counts than the reference background, $\times 1.96$ and $\times 2$ respectively, However, when directly comparing per-oral and transnasal procedures, it was found that per-oral procedures produced significantly more particles ($\times 1.99$).

Lower GI procedures also produced particles that were significantly higher than the reference background ($\times 1.34$). By considering the absolute number of particles,

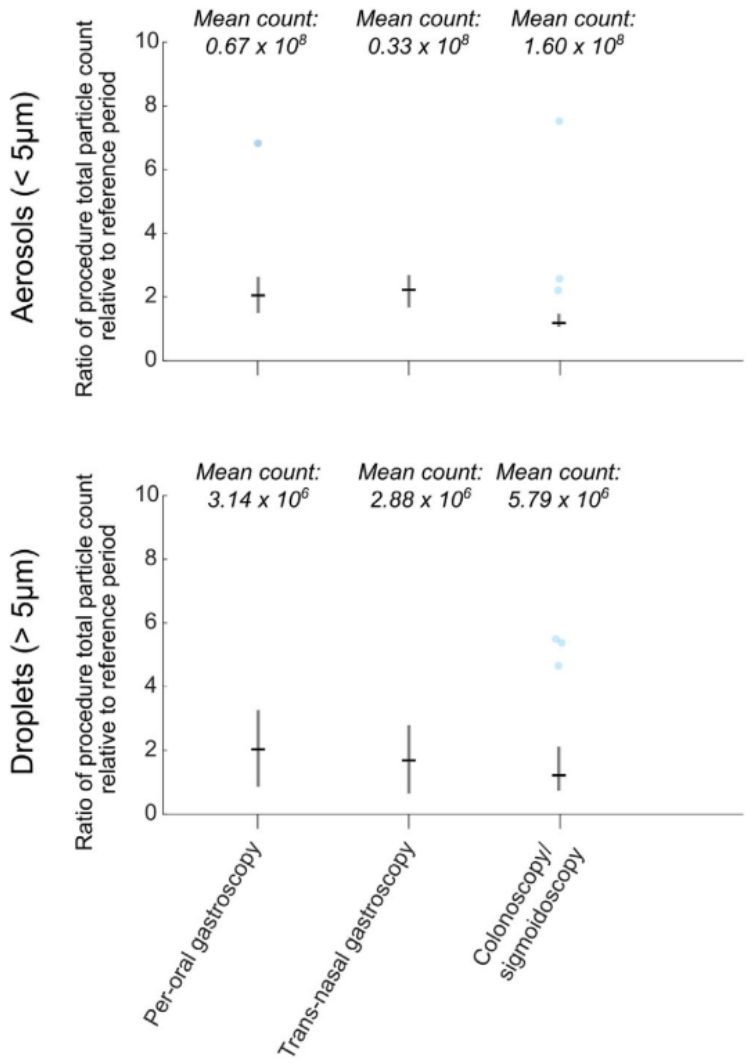

Figure 6.3: Ratios of particle counts over entire procedures relative to a reference period before the start of the procedure (normalised to procedure duration).

lower GI procedures produced a greater number of particles (1.69×10^8) than per-oral procedures (0.71×10^8), as shown in Fig 6.3. However, for this study the median duration of lower GI procedures was 24.7 minutes and for upper GI procedures was 7.2 minutes. Therefore, lower GI procedures produced *less* particles per unit time at a rate of 8.8×10^6 per minute/m^3, while per-oral upper GI procedures produced particles at a rate of 13.9×10^6 per minute/m^3. For particles > 5 μm in diameter it was found that lower GI procedures were no longer significant relative to the background.

The only significant result for lower GI procedures was that patient discomfort rated as high on the case report form resulted in more particles being generated than when patient discomfort was rated as low. For upper GI procedures there was a small, statistically significant ($P < .05$) negative correlation between particle count and age, implying that the number of particles generated during an upper GI procedure decreases with increasing patient age.

6.3.2 Causal event-based analysis

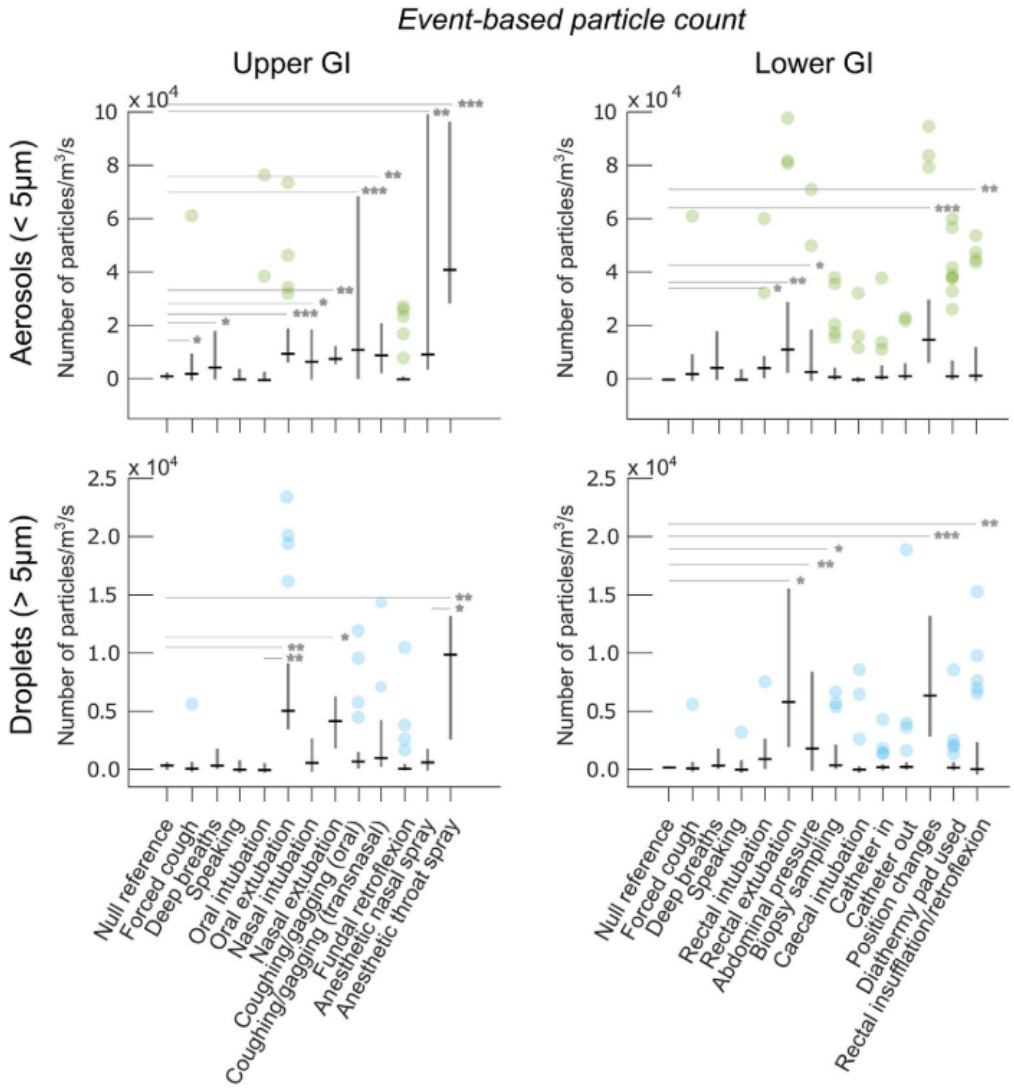

Figure 6.4: Particle production by individual events measured during upper and lower GI procedures. Numbers of recorded events are shown. Black dashes represent medians.

Fig 6.4 shows the particles generated during individual events throughout upper and lower GI procedures. For upper GI procedures, several events were found to be significant relative to the room background particle count. These were nasal intubation (×10.9), oral extubation (×37.5), nasal extubation (×32.0), coughing or gagging during per-oral endoscopy (×25.8), coughing or gagging during transnasal endoscopy (×20.0), voluntary forced coughing (×7.5), voluntary deep breathing (×15.7), anesthetic nasal spray application (×40.1), and anesthetic throat spray application (×150.0). Oral intubation and speaking at low volume were not found to produce significant particles, which is consistent with previous studies [250].

For lower GI procedures, several events were found to be significant relative to the room background particle count. These were rectal intubation (×9.9), rectal extubation (×27.2), application of abdominal pressure (×9.6), patient position changes (×34.9), and rectal insuflation or retroflexion (×7.7). It was observed that rectal

extubation produced significantly more particles than intubation (×3.3). Biopsy sampling, insertion and removal of catheters, water injection, and use of diathermy cutting were not found to produce a significant number particles relative to the room background particle count.

6.3.3 Particle size

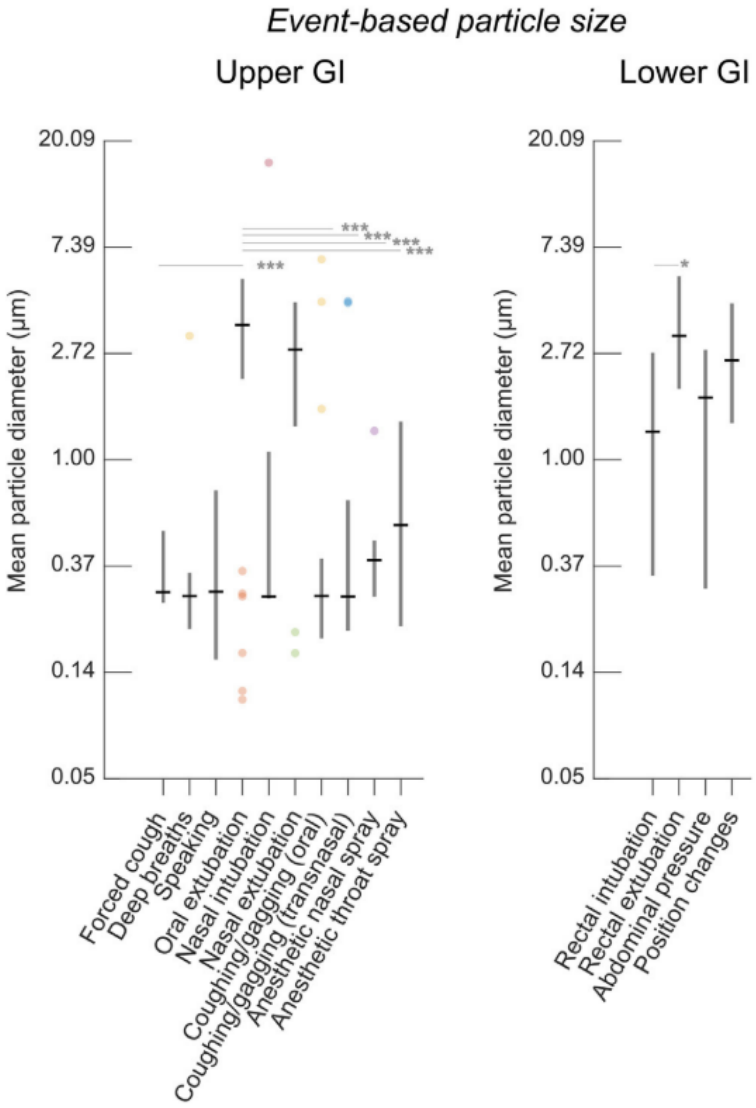

Figure 6.5: Particle size distribution for a selection of statistically significant particle generating events.

The size range of particles associated with each event is shown in Fig 6.5. For upper GI procedures, oral extubation produced particle sizes significantly larger (2.2 μm) than voluntary coughing (0.32 μm). Involuntary coughing or gagging produced particles on similar size scales to voluntary coughing (0.44 μm for per-oral and 0.68 μm for transnasal). The application of both anaesthetic throat spray and nasal spray produced particles statistically similar in size to those produced when coughing. For lower GI procedures, rectal extubation produced particles of a similar mean size as oral extubation (2.0 μm). Patient position changes produced particles comparable with rectal extubation (1.7 μm).

For particles > 25 μm measured with the VisiSize, it was found that oral extubation and fundal retroflexion produced particles up to 300 μm in diameter, with mean particle diameter of 32 μm. Coughing or gagging did not produce detectable particles in this range. The limited cases of particles recorded resulted in insufficient data for a complete statistical analysis.

6.4 Discussion

This is the first study to report that both transnasal endoscopy and lower GI endoscopy are aerosol and droplet generating procedures. It is also the first to report on defined particle-generating events and associated particle sizes within procedures performed through the mouth, nose, and rectum. Both per-oral and transnasal endoscopy should therefore be classed as AGPs, whereas the classification of lower GI endoscopy depends on the definition particle size associated with AGPs used.

With regard to per-oral endoscopy, these results confirm those of previous studies showing this is an AGP, producing particles at double the background level. The most significant contributing event is local anesthetic throat spray application, which generates $\times 10$ the number of particles compared with a voluntary cough, with an average particle size in the aerosol range.

The particles recorded with throat spray application are potentially infectious, because they would have rebounded from the patient's oropharynx or occasionally from coughing induced by the throat spray. There is additional risk because the throat spray is applied face-on with the patient. It is therefore important that barrier methods such as face shields or goggles are used while applying throat and nasal spray. Extubation is the second most particle generating event in per-oral endoscopy and is also significantly more particle generating than voluntary coughing. However, a higher proportion of particles is in the droplet range, which has a lower risk for airborne transmission. This is understandable because both insufflation in the oesophagus and movement of the wet shaft of the endoscope on extubation generate particles [251]. Coughing or gagging is also a significant generator of particles and is predictably comparable with the level of particles produced by voluntary coughing

Transnasal endoscopy has been suggested by some as a non-AGP method for performing upper GI endoscopy [252]. However, these results show that transnasal endoscopy *is* an AGP, producing particles predominantly in the aerosol range (≤ 5 μm). Nasal spray application, nasal intubation, and nasal extubation were all associated with significant spikes of particles. Transnasal endoscopy generates approximately half the level of particles of per-oral endoscopy. Therefore, if used with additional mitigating strategies (avoidance of nasal spray and use of barrier methods), transnasal endoscopy could potentially become a non-AGP procedure. With regard to lower GI procedures, this study shows the absolute levels of particles produced are greater than upper GI procedures but are about one-third lower when taken per unit of time. Although there would be a greater exposure to aerosols in lower GI procedures because of longer procedure times, these are therefore more likely to be cleared in well-ventilated rooms. It is recognised that COVID-19 is primarily a respiratory pathogen, and fecal–oral transmission has not been proven. The risk from lower GI procedures is likely to be considerably lower than equivalent aerosols generated by upper GI procedures.

6.5 Conclusion

In this study, aerosol and droplet generation from the endoscopic procedures performed through the mouth, nose, or rectum were characterised. For upper GI procedures, these results suggest that aerosols can be greatly reduced by avoiding throat spray and through performing transnasal endoscopy over per-oral endoscopy. However, transnasal endoscopy is still an AGP and further mitigating strategies should be applied. Lower GI procedures were found to produce more particles per procedure but less particles per unit time. It is emphasised that the detected aerosols may not necessarily contain viable virus material, and so their generation does not equate to infectivity of the procedures themselves. This depends on multiple factors, including from which part of the patient the particles are generated. Particles from the oral and nasal cavities are likely to have a much higher potential infectivity risk compared with those from the large bowel. Because the infectivity of procedures is not established, it is therefore suggested that adequate PPE (including high-efficiency masks) and sanitisation of floors and surfaces (to prevent re-suspension of aerosols) are used for all GI endoscopy where there is a high population prevalence of Covid-19. More studies are needed to evaluate mitigation strategies and to characterise the infectivity of these procedures themselves.

Appendix A

Solving the Helmholtz equation for fluence rate

Inserting Eqns 1.2 and 1.3 into Eqn 1.1 one gets:

$$\nabla^2\Big(\varphi_0(z)\cos(k_x x+\alpha)\cos(k_y y+\beta)\Big)-\mu_{eff}^2\Big(\varphi_0(z)\cos(k_x x+\alpha)\cos(k_y y+\beta)\Big) \\ =-3\mu_{tr}\Big(q_0(z)\cos(k_x x+\alpha)\cos(k_y y+\beta)\Big)$$

This is expanded by:

$$\frac{\partial^2}{\partial x^2}\Big(\varphi_0(z)\cos(k_x x+\alpha)\cos(k_y y+\beta)\Big)+\frac{\partial^2}{\partial y^2}\Big(\varphi_0(z)\cos(k_x x+\alpha)\cos(k_y y+\beta)\Big) \\ +\frac{\partial^2}{\partial z^2}\Big(\varphi_0(z)\cos(k_x x+\alpha)\cos(k_y y+\beta)\Big)-\mu_{eff}^2\varphi_0(z)\cos(k_x x+\alpha)\cos(k_y y+\beta) \\ =-3\mu_{tr}q_0(z)\cos(k_x x+\alpha)\cos(k_y y+\beta)$$

Using the fact that:

$$\frac{d}{dx}\cos(x)=-\sin(x) \qquad\qquad \frac{d}{dx}\sin(x)=\cos(x)$$

One gets

$$\varphi_0(z)k_x^2\Big(-\cos(k_x x+\alpha)\cos(k_y y+\beta)\Big)+\varphi_0(z)k_y^2\Big(\cos(k_x x+\alpha)(-\cos(k_y y+\beta))\Big) \\ +\frac{\partial^2}{\partial z^2}\varphi_0(z)\Big(\cos(k_x x+\alpha)\cos(k_y y+\beta)\Big)-\mu_{eff}^2\varphi_0(z)\Big(\cos(k_x x+\alpha)\cos(k_y y+\beta)\Big) \\ =-3\mu_{tr}q_0(z)\Big(\cos(k_x x+\alpha)\cos(k_y y+\beta)\Big)$$

Dividing across by $\cos(k_x x+\alpha)\cos(k_y y+\beta)$ one gets

$$\frac{\partial^2}{\partial z^2}\varphi_0(z)-(k_x^2+k_y^2)\varphi_0(z)-\mu_{eff}^2\varphi_0(z)=-3\mu_{tr}q_0(z) \\ \Rightarrow \frac{\partial^2}{\partial z^2}\varphi_0(z)-(\mu_{eff}^2+k_x^2+k_y^2)\varphi_0(z)=-3\mu_{tr}q_0(z)$$

where one can substitute a scalar attenuation coefficient of the propagating wave, $\mu\prime_{eff}$, as

$$\mu\prime_{eff}=(\mu_{eff}^2+k_x^2+k_y^2)^{1/2}$$

Providing the final equation of:

$$\frac{\partial^2}{\partial z^2}\varphi_0(z) - \mu_{eff}'^2\varphi_0(z) = -3\mu_{tr}q_0(z)$$

Appendix B

Deriving a solution for the fluence rate of an angularly isotropic source introduced via scattering of a collimated, forward-directed beam

Looking at Eqn 1.4, it is noted that this is a second order differential equation of form:

$$\varphi_0''(z) + w\varphi_0'(z) + v\varphi_0(z) = f(z) \tag{B.1}$$

where $w = 0$, v is a constant, and $f(z)$ is some function dependent on z. As this equation is non-homogeneous, i.e. $f(z) \neq 0$, two solutions are required: a complementary solution $\varphi_{00}(z)$ and a particular solution $\varphi_{01}(z)$ such that

$$\varphi_0(z) = \varphi_{00}(z) + \varphi_{01}(z) \tag{B.2}$$

To find the complementary solution, a homogenous solution is assumed and Eqn B.1 is written as

$$\varphi_{00}''(z) + v\varphi_{00}(z) = 0 \tag{B.3}$$

To solve, one looks at $f(z)$, where

$$f(z) = -3\mu_{tr}P_0\mu_s e^{-\mu_{tr}z} \tag{B.4}$$

and one can therefore assume an undetermined coefficient for Eqn B.3 of $\varphi_{00}(z) = e^{pz}$, where p is a constant. Therefore, Eqn B.3 becomes:

$$\frac{d^2}{dz^2}e^{pz} + ve^{pz} = 0 \tag{B.5}$$

$$p^2 + v = 0$$

$$\Rightarrow p^2 = -v$$

From Eqn 1.4, one knows that $v = -\mu'^2_{eff}$ and such $p = \pm\mu'_{eff}$. Therefore, the complementary solution can be given as:

$$\varphi_{00}(z) = C_1 e^{\mu'_{eff} z} + C_2 e^{-\mu'_{eff} z} \tag{B.6}$$

where C_1 and C_2 are constants from differentiation. Next, to find the particular solution, it is assumed that because $f(z)$ is of the form Ae^{qz}, where A and q are constants, that the solution to the particular solution must be of the same form where $\varphi_{01}(z) = A'e^{qz}$. Inserting this into Eqn B.1 one gets:

$$\varphi''_{01}(z) + v\varphi_{01}(z) = Ae^{qz} \tag{B.7}$$

$$\Rightarrow \frac{d^2}{dz^2} A'e^{qz} + vA'e^{qz} = Ae^{qz}$$

$$\Rightarrow q^z A' + vA' = A$$

It is known from Eqn B.4 that $A = -3\mu_{tr} P_0 \mu'_s$ and $q = -\mu_{tr}$, and from Eqn 1.4 that $v = -\mu'^2_{eff}$, and therefore one can find A':

$$A' = \frac{A}{q^2 + v}$$

$$A' = \frac{-3\mu_{tr} P_0 \mu'_s}{\mu^2_{tr} - \mu'^2_{eff}}$$

$$\Rightarrow A' = \frac{3P_0 a'}{(1 - (\mu'_{eff}/\mu_{tr})^2)} \tag{B.8}$$

where the reduced albedo, $a' = \mu'_s/\mu_{tr}$. Therefore, the particular solution is given by:

$$\varphi_{01}(z) = \frac{3P_0 a'}{(1 - (\mu'_{eff}/\mu_{tr})^2)} e^{\mu_{tr} z} \tag{B.9}$$

Combining these two solutions, a solution is obtained for $\varphi_0(z)$ from Eqn B.2 of:

$$\varphi_0(z) = C_1 e^{-\mu'^2_{eff} z} + \frac{3P_0 a'}{(1 - (\mu'_{eff}/\mu_{tr})^2)} e^{\mu_{tr} z} \tag{B.10}$$

Appendix C

Determining the coefficient of M_{AC} for 3 equiphase shifted captures

Neil et al. states the image intensity of a sample illuminated by a mask can be written as [253]:

$$I(t,w) = I_0 + I_c \cos\phi_0 + I_s \sin\phi_0 \tag{C.1}$$

where I_0 represents a conventional, wide field image and I_c and I_s represent the images due to the masks of $m\cos(ft_0)$ and $m\sin(ft_0)$ respectively, where m is the modulation depth. These definitions suggest that

$$I_p = (I_c^2 + I_s^2)^{1/2} \tag{C.2}$$

would remove the grid patter from the image by taking three images I_1, I_2 and I_3 with relative spatial phases of $\phi_0 = 0, 2\pi/3$ and $4\pi/3$ respectively. An optically sectioned image can therefore be obtained without I_0 with:

$$I_p = [(I_1 - I_2)^2 + (I_1 - I_3)^2 + (I_2 - I_3)^2]^{1/2} \tag{C.3}$$

which is analogous to square law detection in communication systems. There exists a coefficient of the right hand side of Eqn C.3, which is determined here. From Eqn C.1 one can write I_1, I_2 and I_3 (with relative spatial phases of $\phi_0 = 0, 2\pi/3$ and $4\pi/3$ respectively) as:

$$I_1 = I_0 + I_c \tag{C.4}$$

$$I_2 = I_0 - \frac{1}{2}I_c + \frac{\sqrt{3}}{2}I_s \tag{C.5}$$

$$I_3 = I_0 - \frac{1}{2}I_c - \frac{\sqrt{3}}{2}I_s \tag{C.6}$$

Filling these into Eqn C.3 one gets:

$$I_p = \left[\left(\frac{3}{2}I_c + \frac{\sqrt{3}}{2}I_s\right)^2 + \left(\frac{3}{2}I_c - \frac{\sqrt{3}}{2}I_s\right)^2 + \left(\sqrt{3}I_s\right)^2\right]^{1/2} \tag{C.7}$$

$$\rightarrow I_p = \left[\frac{9}{2}\left(I_c^2 + I_s^2\right)\right]^{1/2} = \frac{3}{\sqrt{2}}(I_c^2 + I_s^2)^{1/2} \tag{C.8}$$

Subbing in Eqns C.2 and C.3 one gets:

$$[(I_1 - I_2)^2 + (I_1 - I_3)^2 + (I_2 - I_3)^2]^{1/2} = \frac{3}{\sqrt{2}} I_p \tag{C.9}$$

$$\rightarrow I_p = M_{AC} = \frac{\sqrt{2}}{3}[(I_1 - I_2)^2 + (I_1 - I_3)^2 + (I_2 - I_3)^2]^{1/2} \tag{C.10}$$

Appendix D

Derivation of height equation via Fourier Transform Profilometry

When no object is present, the resultant image of a deformed fringe pattern (assuming telecentricity of projection and imaging system) will have the form:

$$g_0(x,y) = \sum_{n=-\infty}^{\infty} A_n \exp(i[2\pi n f_0 x + n\phi_0(x,y)]) \tag{D.1}$$

where A_n and f_0, represent the amplitude and fundamental frequency of the observed fringe pattern respectively, and $\phi(x,y)$ is given by:

$$\phi(x,y) = 2\pi f_0 s(x,y) \tag{D.2}$$

where $s(x,y) = \overline{AD}$, shown in Fig D.1. When an object of height h is present, Eqn D.1 becomes:

$$g(x,y) = r(x,y) \sum_{n=-\infty}^{\infty} A_n \exp(i[2\pi n f_0 x + n\phi(x,y)]) \tag{D.3}$$

where $r(x,y)$ is the amplitude variation caused by the presence of an object. This equation represents multiple signals with spatial carrier frequencies nf_0 that are modulated in phase by $\phi(x,y)$ and in amplitude by $r(x,y)$. The phase, $\phi(x,y)$, needs to be extracted in order to calculate the height. To do this, Eqn D.3 can be simplified by setting $q_n = A_n r(x,y)\exp(in\phi(x,y))$ performing a 1D Fourier transform on Eqn D.3:

$$G(f,y) = \int_{-\infty}^{\infty} g(x,y)\exp(-2\pi i f x)dx = \sum_{n=-\infty}^{\infty} Q_n(f - nf_0, y) \tag{D.4}$$

where $G(f,y)$ and $Q_n(f,y)$ are the Fourier spectra of $g(x,y)$ and $q_n(x,y)$ respectively. By selecting a single spectrum from $Q_n(f - nf_0, y)$ for $n = 1$ and computing it's inverse Fourier transform, Eqn D.4 becomes:

$$\hat{g}(x,y) = q_1(x,y)\exp(2\pi i f_0 x) = A_1 r(x,y)\exp(i[2\pi f_0 x + \phi(x,y)]) \tag{D.5}$$

Repeating the same steps for a planar sample, Eqn D.1 becomes:

$$\hat{g}_0(x,y) = A_1 \exp(i[2\pi f_0 x + \phi_0(x,y)]) \tag{D.6}$$

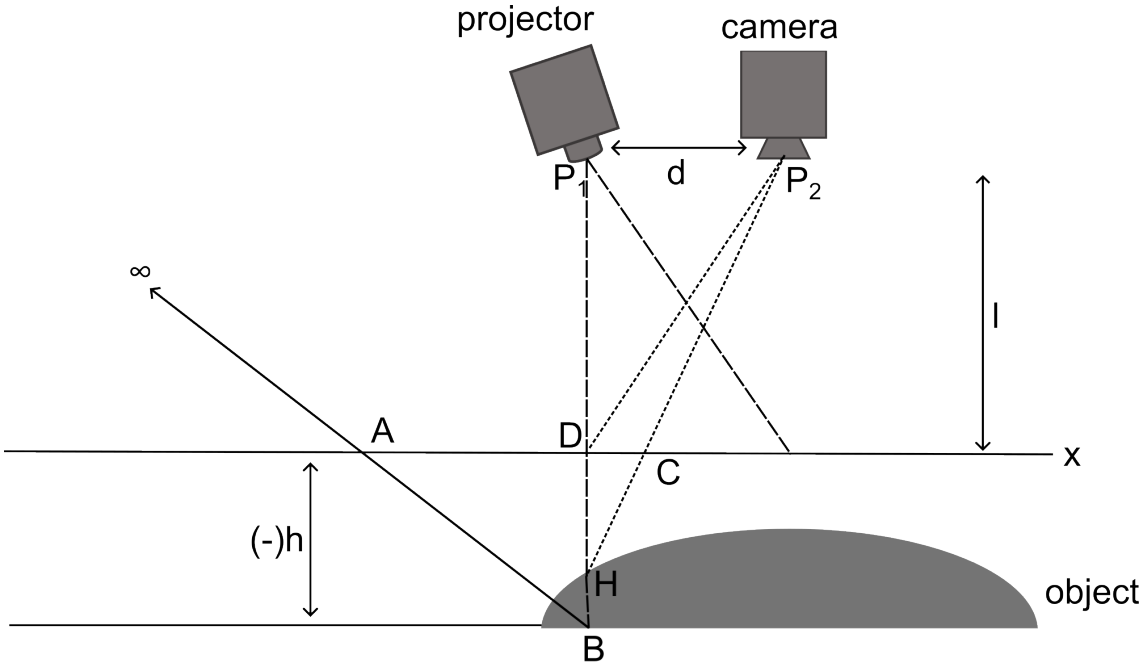

Figure D.1: Schematic of FTP for a crossed optical axis geometry. Adapted from [81].

In a mathematical equivalence to shifting in the Fourier domain, the signal from an object of height h, Eqn D.5, is multiplied with the conjugate of the signal from $h = 0$, Eqn D.6, to get:

$$\hat{g}(x,y) \cdot \hat{g}_0^*(x,y) = |A_1|^2 r(x,y) \exp(i\Delta\phi(x,y)) \tag{D.7}$$

where the phase modulation due to the presence of an object of height h is:

$$\Delta\phi(x,y) = \phi(x,y) = \phi_0(x,y) = 2\pi f_0(\overline{AC} - \overline{AD}) = 2\pi f_0 \overline{DC} \tag{D.8}$$

By computing the complex logarithm of Eqn D.7, the phase can be isolated from the imaginary part, exploiting logarithm rules $\log(A \cdot B) = \log(A) + \log(B)$:

$$\log[\hat{g}(x,y) \cdot \hat{g}_0^*(x,y)] = \log[|A_1|^2 r(x,y)] + i\Delta\phi(x,y) \tag{D.9}$$

One must now derive an equation for height. Looking at Fig D.1, $\triangle P_1 H P_2 \wedge \triangle DHC$. Therefore,

$$\overline{DC} = \frac{-dh(x,y)}{l - h(x,y)} \tag{D.10}$$

where d and l are the distances between the camera and projector, and between the camera and reference plane respectively. Subbing this into Eqn D.8, an equation for height in terms of phase remains:

$$h(x,y) = \frac{\Delta\phi(x,y) l}{\Delta\phi(x,y) - 2\pi d f_0} \tag{D.11}$$

Appendix E

N phase shift measurement

SFDI and fringe profilometry at N equiphase shifted images is considered. To do this, an intensity image I is thought of as the sum of the AC and DC modulation amplitudes such that

$$I = M_{AC}\sin(2\pi ft + \phi) + M_{DC} \tag{E.1}$$

where the AC modulation amplitude is scaled by a sinusoidal pattern of frequency f and phase ϕ. Using the double angle formula where:

$$\sin(A + B) = \sin A\cos B + \cos A\sin B \tag{E.2}$$

enabling Eqn E.1 to be rewritten as:

$$I = M_{AC}\sin(2\pi ft)\cos(\phi) + M_{AC}\cos(2\pi ft)\sin(\phi) + M_{DC} \tag{E.3}$$

Knowing that the period of the sinusoidal pattern $T = 1/f$, a fraction $t/T \leq 1$ exists which is the fraction of the present period. Given that:

$$ft = 0, \frac{1}{N}, \ldots \frac{n-1}{N} \tag{E.4}$$

where N is the number of images within the period and n is an integer value from 1 to N. Therefore, from a sample of N images over one period, for one pixel $x_1, x_2, x_3 ... x_N$ in the resultant intensity image I, Eqn E.3 can be written as:

$$\begin{bmatrix} M_{AC}\sin(0) \\ M_{AC}\sin(2\pi) \\ \vdots \\ M_{AC}\sin(2\pi\frac{N-1}{N}) \end{bmatrix}\cos(\phi) + \begin{bmatrix} M_{AC}\cos(0) \\ M_{AC}\cos(2\pi) \\ \vdots \\ M_{AC}\cos(2\pi\frac{N-1}{N}) \end{bmatrix}\sin(\phi) + \begin{bmatrix} M_{DC} \\ M_{DC} \\ \vdots \\ M_{DC} \end{bmatrix} = \begin{bmatrix} x_1 \\ x_2 \\ \vdots \\ x_N \end{bmatrix}$$

Writing this in matrix form:

$$\begin{bmatrix} \sin(0) & \cos(0) & 1 \\ \sin(2\pi) & \cos(2\pi) & 1 \\ \vdots & \vdots & \\ \sin(2\pi\frac{N-1}{N}) & \cos(2\pi\frac{N-1}{N}) & 1 \end{bmatrix}\begin{bmatrix} M_{AC}\cos(\phi) \\ M_{AC}\sin(\phi) \\ M_{DC} \end{bmatrix} = \begin{bmatrix} x_1 \\ x_2 \\ \vdots \\ x_N \end{bmatrix} \tag{E.5}$$

where the resultant $N \times 1$ matrix is for a single pixel across all images. In order to consider all pixels from the image:

$$\begin{bmatrix} \sin(0) & \cos(0) & 1 \\ \sin(2\pi) & \cos(2\pi) & 1 \\ \vdots & \vdots & \\ \sin(2\pi\frac{N-1}{N}) & \cos(2\pi\frac{N-1}{N}) & 1 \end{bmatrix} \begin{bmatrix} M_{AC,1}\cos(\phi_{x,1}) & M_{AC,2}\cos(\phi_{x,2}) & \dots & M_{AC,R}\cos(\phi_{x,R}) \\ M_{AC,1}\sin(\phi_{x,1}) & M_{AC,2}\sin(\phi_{x,2}) & \dots & M_{AC,R}\sin(\phi_{x,R}) \\ M_{DC,1} & M_{DC,2} & \dots & M_{DC,R} \end{bmatrix}$$

$$= \begin{bmatrix} x_{11} & x_{12} & \dots & x_{1R} \\ x_{21} & x_{22} & \dots & x_{2R} \\ \vdots & \vdots & \ddots & \vdots \\ x_{N1} & x_{N2} & \dots & x_{NR} \end{bmatrix} \tag{E.6}$$

where R is the number of pixels in a single image. Solving the center matrix will give M_{AC} and M_{DC} for N equally phase shifted images. As the number of input images N is known and hence the phase shift of each image, the left hand side matrix from Eqn E.6 is also known. To obtain the matrix on the right hand side of Eqn E.6 via *Python*, the function *numpy.ndarray.flatten()* is first used to flatten the input images and then the function *numpy.vstack()* to vertically stack the images. Finally, to obtain the center matrix, a least squares solver function *numpy.linalg.lstsq()* is used. From this the phase ϕ, M_{AC}, and M_{DC} may be extracted.

Appendix F

Utilising Blender SFDI model

Data files for using this model are available at [254]. There are 3 files to use for the *Blender* SFDI model:

1. Blender_bulkMaterial.blend
2. Blender_Tube.blend
3. Blender_DIS.blend

accompanied by 4 *Python* files for image analysis:

(A) Density_calc.ipynb

(B) SFDI_calc.ipynb

(C) Shape_calc.ipynb

(D) SFDI_calc_tube.ipynb

F.1 Blender_bulkMaterial.blend

This software has the bulk material which one can change the optical properties of, a projector to project any desired illumination pattern and a camera to capture the reflection/transmission of this illumination pattern. This file is used to generate images of the phase shifted pattern on the material of interest, which can then be input into custom *Python* SFDI code (SFDI_calc.ipynb above) to determine optical properties of the material.

F.1.1 File contents

Upon opening the file, one will see the several items that can be present in the scene. The first is *BulkMaterial*. This is the main material of which the optical properties may be altered. It uses the add shader node to add a volume absorption and a volume scattering node and outputs the result to volume material output. The glass BSDF shader outputs to the surface material output. The absorption density, scattering density, anisotropy factor, and refractive index of this material may be altered. The next item is the *camera*. This captures an image of the projected illumination pattern on the bulk material. The next items are *Material_BO* and *Material_HT*

which are two separate, adjacent blocks of bulk material simulating material with the specific optical properties of Barrett's Oesophagus (BO) and healthy oesophageal tissue (HT). *Projector Basic* is a projector which projects a single selected image onto the bulk material. *Projector with animation* is set up to project different phase shifted patterns in an animation such that the camera captures each projected image in a sequence. *Red Sphere Test* is used to determine the limitations of the system i.e. when the bulk material is transparent enough such that one can see the red sphere through the material, those specific material properties are not valid. Finally, *Spheroid_SCC* is a sphere scaled down to simulate a polyp with optical properties of squamous cell carcinoma (SCC).

To make an object visible in the scene, one needs to select the eye icon to the right of the object one wants to appear. To make the object visible in the render, the camera icon adjacent to the eye icon also needs to be selected.

F.1.2 Using the material

In the shader tab at the top of *Blender* file, select the material of which properties you want to alter. You will see Fig 3.3 in the lower panel of the screen. To change the absorption density of the material, you change the value of 'Absorption Density' and to change the scattering density of the material you change the 'Scattering Density' by clicking on the existing number and typing in the desired value. The anisotropy, g, of the material may be changed with the 'Anisotropy' parameter in the same manner. To change the refractive index, you change the value of index of refraction (IOR) in the glass BSDF node.

If one wants to make a particular shape with this material, you can use shift+A to add a new object to the scene. Once added, in the shader tab you need to add a material to the new object by hitting the +New button. Then, one can then copy and paste the Node Tree from the bulk material into the new material and attach the shader on the right of the Node Tree to the volume of the output material. Ensure to also copy the glass BSDF shader so the material has a refractive index. Ensure that the new material is scaled in x, y, z equivalent the bulk material.

To determine what absorption density and scattering density will give exact optical properties of interest, the script *Density_calc.ipynb* can be used.

F.1.3 Using the projector

The projector nodes are shown in Fig 3.5. To change the desired projection of interest, change the input image in the image texture node. Ensure the colour space is always set to linear after inputting a new image.

To capture an image of the projected pattern on the material, click the render button in the top left of *Blender* file and select *Render Image*. This will render the viewpoint of the camera. Select the 0 key to go in and out of camera view while setting up the scene to see what the camera will view. If an animation has been set up, select *Render Animation* directly below *Render Image*. This will render the first projected pattern first, save it to a folder, and then run the render for the second projected pattern. It's helpful to use this when generating large datasets as you can leave the software running over a long period of time. For SFDI when three images are required of a single phase shifted pattern, it's advantageous to render the three

phases sequentially for each set of material properties. The blender file is set up to do this currently. It's important to know where the rendered images are being saved. In the right hand side icons, click on output properties and scroll down to output. Clicking on the folder icon right under output allows you to select which folder one wants the renders to go into once complete.

F.1.4 Using accompanying Python code

The first cell in *SFDI_calc.ipynb* code generates optical property maps using a Monte Carlo look-up table and the second cell generates optical property maps using empirically derived look-up table. In cell 1, one can alter absorption density (ad), scattering density (sd) and exposure (exp) to other values previously rendered, present in the accompanying folder *bulkMaterial*. In cell 2, one can alter ad_test, sd_test, exp_test to other values previously rendered. *Shape_calc.ipynb* calculats a height map of the rendered polyp in the accompanying folder *bulkMaterial/polyp*.

F.2 Blender_Tube.blend

This software has the bulk material which one can change the optical properties of in a tubular geometry, as well as a projector to project any desired illumination pattern and a camera to capture the reflection/transmission of this illumination pattern. This file is used to create the concentric circle illumination pattern needed for imaging in a tubular geometry and to generate images of this pattern phase shifted within a tube with any material of interest, which can then be input into *Python* SFDI code to determine optical properties of the material throughout the tube.

F.2.1 File contents

Upon opening the file, one will see the several items that can be present in the scene. The first is *Camera* which is placed directly above the tube and captures the projection pattern down the tube. Next is *Camera for tube side view* which is a camera placed orthogonal to the tube, and when viewed with *Tube_half for side view* it can visualise how the illumination pattern is propagating through the length of the tube. *Oesophagus_BOregion* is a quarter of the total tube with the specific optical properties of BO. *Oesophagus_HTregion* is three quarters of the tube with the specific optical properties of healthy oesophageal tissue. *Projector Basic* is a projector that projects a single image into the tube and *Projector with Animation* projects multiple images simultaneously down the tube, analogous to previously described with the *bulk material* set up. *Red Sphere Test* determines the limitations of the optical properties of the tube. *Spheroids 1-4* are spheres that are mimicking colon polyps with the optical properties of squamous cell carcinoma. *Tube* is the main tube/lumen material to work with. This material has same material properties and the *bulk material* previously described. *Point Sources down tube* is a folder consisting of 41 point sources placed equally throughout the length of the tube. Their purpose is to uniformly illuminate the tube when capturing the wrapped sinusoidal pattern inside the tube to generate the concentric circle projection patterns.

F.2.2 Switching between cameras

To change between active cameras, one can simply right click on a camera present in the scene and set it as an active camera. Alternatively, click on scene properties and then select the camera desired to be active. To view what the active camera is viewing, select 0 on the keypad.

F.2.3 Unwrapping object to generate illumination patterns for non-planar geometries

In the layout tab, the material that is desired to get the illumination pattern for, in this case the tube, is selected. A selected object will appear orange. Then click on the UV editing tab. The left hand side the screen shows the unwrapped selected mesh and the right hand side shows the object as a whole with the selected vertices showing in orange. As only the inside of the tube needs to be selected, the right panel is deselected and grabbed over the region of interest. Certain vertices may be selected and deselected by holding the shift key down and clicking on a vertices with the mouse pad. The respective selected vertices on the right panel will show up on the left panel unwrapped. A desired sinusoidal pattern is added here at the top of the left panel via the +New button. Once applied, the material is then wrapped, such that the inside of the tube now has a uniform spatial frequency throughout its length. The point sources are then switched to be visible. Using the camera placed above the top of the tube, a rendered image is then captured of the concentric circle illumination pattern. This image was then exported to *Python* where a normalisation was applied to ensure that the sinusoid pixel values vary across the maximum range for projection $0 - 255$. This image can then be projected from the projector above the tube onto a tube of the bulk material previously described. If patterns of three phases of the same spatial frequency are created and then projected, the optical properties within the tube can be calculated using Python code.

F.2.4 Using accompanying Python code

Lines 241 and 242 in *SFDI_calc_tube.ipynb* allow to alter the absorption density and scattering density of the material whose optical properties are desired to be determined.

F.3 Blender_DIS.blend

This software has a double integrating sphere (DIS) used to calibrate the optical properties of the bulk material. This file is used to generate reflectance and transmission images of the reflected and transmitted light through the bulk material. These values can then be input to an inverse-adding doubling algorithm (IAD) to determine the optical properties of the bulk material for specific absorption density and scattering density values.

F.3.1 File contents

Upon opening the file, one will see the several items that can be present in the scene. The first are *Baffle_reflection* and *Baffle_transmission* which are present to block the specularly reflected light from entering the detector. *Beam blocker* is present to block the source of incident light, if desired. *Cam_reflection* is the camera, or detector, placed at the base of the reflection sphere and *Cam_transmission* is the detector at the base of the transmission sphere. *Light source* is the input light source entering through the reflection sphere entry port, passing through the material, and then either getting absorbed, back scattered, or entering the transmission sphere. *Sample* is material with the same bulk material properties as previously described, where the absorption and scattering density, as well as anisotropy parameters can be altered. *Sphere_reflection* and *Sphere_transmission* are the highly reflective reflection and transmission spheres.

F.3.2 Switching from reflection to transmission measurements

Switching between reflection and transmission measurements simply involves switching which camera is active, as discussed in F.2.2.

F.3.3 Changing the camera exposure

To change the exposure, click on the camera icon for render properties and scroll down to colour management. The exposure here can be altered for each render, as long as it is corrected using Eqn 3.2.

F.3.4 Using the IAD software

The software and accompanying manual can be downloaded from [255].

Appendix G

Calculating desired fiber spacing

To determine the minimum spacing required to produce spatial frequency patterns of $0.15 - 0.3$ mm^{-1} at a working distance, z, of 50 mm at a wavelength, λ, of 660 nm, one looks at Eqn 4.1 and Fig 4.2. For $m = 1$, Eqn 4.1 becomes:

$$\lambda = d \sin\theta \tag{G.1}$$

where

$$\sin\theta = \frac{x}{\sqrt{z^2 + x^2}} \tag{G.2}$$

Therefore, the spacing d is given by:

$$d = \frac{\lambda\sqrt{z^2 + x^2}}{x} \tag{G.3}$$

where the desired spatial frequency is given by $1/x$. Therefore, for a desired spatial frequency of 0.15 mm^{-1}, the spacing d is given by:

$$d = \frac{660 \times 10^{-6}\sqrt{(50)^2 + (\frac{1}{0.15})^2}}{\frac{1}{0.15}} = 4.9938 \times 10^{-3} \text{ mm} = 4.99\ \mu\text{m} \tag{G.4}$$

and for a spatial frequency of 0.3 mm^{-1}, the spacing d is given by:

$$d = \frac{660 \times 10^{-6}\sqrt{(50)^2 + (\frac{1}{0.3})^2}}{\frac{1}{0.3}} = 9.9220 \times 10^{-3} \text{ mm} = 9.92\ \mu\text{m} \tag{G.5}$$

Bibliography

[1] André Liemert and Alwin Kienle. "Exact and efficient solution of the radiative transport equation for the semi-infinite medium". In: *Scientific Reports* 3 (2013). ISSN: 20452322. DOI: 10.1038/srep02018.

[2] David J. Cuccia et al. "Quantitation and mapping of tissue optical properties using modulated imaging". In: *Journal of Biomedical Optics* 14.2 (2009), p. 024012. ISSN: 10833668. DOI: 10.1117/1.3088140.

[3] Lars O. Svaasand et al. "Reflectance measurements of layered media with diffuse photon-density waves: A potential tool for evaluating deep burns and subcutaneous lesions". In: *Physics in Medicine and Biology* 44.3 (Mar. 1999), pp. 801–813. ISSN: 00319155. DOI: 10.1088/0031-9155/44/3/020.

[4] Richard C. Haskell et al. "Boundary conditions for the diffusion equation in radiative transfer". In: *Journal of the Optical Society of America A* 11.10 (Oct. 1994), p. 2727. ISSN: 1084-7529. DOI: 10.1364/josaa.11.002727.

[5] Steven L. Jacques and Brian W. Pogue. "Tutorial on diffuse light transport". In: *Journal of Biomedical Optics* 13.4 (2008), p. 041302. ISSN: 10833668. DOI: 10.1117/1.2967535.

[6] K M Yoo, Feng Liu, and R R Alfano. *When Does the Diffusion Approximation Fail to Describe Photon Transport in Random Media?* Tech. rep. 1990.

[7] Joshua B. Fishkin et al. "Gigahertz photon density waves in a turbid medium: Theory and experiments". In: *Physical Review E - Statistical Physics, Plasmas, Fluids, and Related Interdisciplinary Topics* 53.3 (1996), pp. 2307–2319. ISSN: 1063651X. DOI: 10.1103/PhysRevE.53.2307.

[8] Robert L. Harrison. "Introduction to Monte Carlo simulation". In: *AIP Conference Proceedings*. Vol. 1204. 2009, pp. 17–21. ISBN: 9780735407411. DOI: 10.1063/1.3295638.

[9] Winston Haynes. *Encyclopedia of Systems Biology*. Ed. by Werner Dubitzky et al. Springer New York, 2013, pp. 1752–1754.

[10] B. C. Wilson and G. Adam. "A Monte Carlo model for the absorption and flux distributions of light in tissue". In: *Medical Physics* 10.6 (1983), pp. 824–830. ISSN: 00942405. DOI: 10.1118/1.595361.

[11] Lihong Wang, Steven L Jacques, and Liqiong Zheng. "MCML - Monte Carlo modeling of light transport in multi-layered tissues". In: *Computer Methods and Programs in Biomedicine* 47 (1995), pp. 131–146.

[12] Carole K. Hayakawa et al. "MCCL: an open-source software application for Monte Carlo simulations of radiative transport". In: *Journal of Biomedical Optics* 27.08 (Apr. 2022). ISSN: 15602281. DOI: 10.1117/1.jbo.27.8.083005.

[13] Murat Canpolat and Judith R Mourant. *High-angle scattering events strongly affect light collection in clinically relevant measurement geometries for light transport through tissue*. Tech. rep. 2000, pp. 1127–1140.

[14] L Henyey and J Greenstein. "Diffuse radiation in the Galaxy". In: 93 (Jan. 1941), pp. 70–83. DOI: 10.1086/144246.

[15] T. Binzoni et al. "The use of the Henyey-Greenstein phase function in Monte Carlo simulations in biomedical optics". In: *Physics in Medicine and Biology* 51.17 (Sept. 2006). ISSN: 00319155. DOI: 10.1088/0031-9155/51/17/N04.

[16] Adam R Gardner and Vasan Venugopalan. *Accurate and efficient Monte Carlo solutions to the radiative transport equation in the spatial frequency domain*. Tech. rep. 2011.

[17] Erik Alerstam, Stefan Andersson-Engels, and Tomas Svensson. "White Monte Carlo for time-resolved photon migration". In: *Journal of Biomedical Optics* 13.4 (2008), p. 041304. ISSN: 10833668. DOI: 10.1117/1.2950319.

[18] Alwin Kienle and Michael S Patterson. *Determination of the optical properties of turbid media from a single Monte Carlo simulation*. Tech. rep. 1996, p. 2221.

[19] Tim A. Erickson et al. "Lookup-table method for imaging optical properties with structured illumination beyond the diffusion theory regime". In: *Journal of Biomedical Optics* 15.3 (2010), p. 036013. ISSN: 10833668. DOI: 10.1117/1.3431728.

[20] Arnold D Kim. *Transport theory for light propagation in biological tissue*. Tech. rep. 2004.

[21] K.M. Case and P.W. Zweifel. *Linear transport theory*. Reading, MA. : Addison-Wesley Pub. Co., 1967, pp. 24–26.

[22] Anouk L. Post, Dirk J. Faber, and Ton G van Leeuwen. "Model for the diffuse reflectance in spatial frequency domain imaging". In: *Journal of Biomedical Optics* 28.4 (2023). DOI: https://doi.org/10.1117/1.JBO.28.4.046002.

[23] Tuchin. *Tissue Optics Third Edition*. 2015. URL: http://ebooks.spiedigitallibrary.org/.

[24] Nikiforos Kollias and From Wellman. *The Physical Basis of Skin Color and Its Evaluation*. Tech. rep.

[25] Thomas Wriedt. "A Review of Elastic Light Scattering Theories". In: *Particle and Particle Systems Characterization* 15.2 (1998), pp. 67–74. ISSN: 09340866. DOI: 10.1002/(SICI)1521-4117(199804)15:2<67::AID-PPSC67>3.0.CO;2-F.

[26] Guang S. He, Hai Yan Qin, and Qingdong Zheng. "Rayleigh, Mie, and Tyndall scatterings of polystyrene microspheres in water: Wavelength, size, and angle dependences". In: *Journal of Applied Physics* 105.2 (2009). ISSN: 00218979. DOI: 10.1063/1.3068473.

[27] Christopher M Sorensen. "Rayleigh scattering". In: *Light Scattering and Absorption by Particles*. IOP Publishing, Dec. 2022, pp. 6–1. DOI: 10.1088/978-0-7503-5157-7ch6.

[28] Scott Prahl. *Optical absorption of haemoglobin*. URL: https://omlc.org/spectra/hemoglobin/.

[29] B. Beauvoit, T. Kitai, and B. Chance. "Contribution of the mitochondrial compartment to the optical properties of the rat liver: a theoretical and practical approach". In: *Biophysical Journal* 67.6 (1994), pp. 2501–2510. ISSN: 00063495. DOI: 10.1016/S0006-3495(94)80740-4.

[30] Nrusingh C Biswal, Yan Xu, and Quing Zhu. *Imaging Tumor Oxyhemoglobin and Deoxyhemoglobin Concentrations with Ultrasound-Guided Diffuse Optical Tomography*. Tech. rep.

[31] Amal Jubran. "Pulse oximetry". In: *Critical Care* 19.1 (July 2015). ISSN: 1466609X. DOI: 10.1186/s13054-015-0984-8.

[32] WG Zijlstra, A Buursma, and WP Meeuwsen-van der Roest. "Absorption spectra of human fetal and adult oxyhemoglobin, deoxyhemoglobin, carboxyhemoglobin, and methemoglobin". In: *Clinical Chemistry* (1991), pp. 1633–8.

[33] R. L. P. van Veen et al. "Determination of visible near-IR absorption coefficients of mammalian fat using time- and spatially resolved diffuse reflectance and transmission spectroscopy". In: *Journal of Biomedical Optics* 10.5 (2005), p. 054004. ISSN: 10833668. DOI: 10.1117/1.2085149.

[34] Amaan Mazhar et al. "Wavelength optimization for rapid chromophore mapping using spatial frequency domain imaging". In: *Journal of Biomedical Optics* 15.6 (2010), p. 061716. ISSN: 10833668. DOI: 10.1117/1.3523373.

[35] Hiroki Sato et al. "Practicality of wavelength selection to improve signal-to-noise ratio in near-infrared spectroscopy". In: *NeuroImage* 21.4 (Apr. 2004), pp. 1554–1562. ISSN: 10538119. DOI: 10.1016/j.neuroimage.2003.12.017.

[36] Christoph Holmer et al. "Optical properties of adenocarcinoma and squamous cell carcinoma of the gastroesophageal junction". In: *Journal of Biomedical Optics* 12.1 (2007), p. 014025. ISSN: 10833668. DOI: 10.1117/1.2564793.

[37] S Mullangi and M Lekkala. "Adenocarcinoma ". In: *[Updated 2022 Sep 26]. In StatPearls [Internet]. Treasure Island (FL):StatPearls Publishing* (2023).

[38] "SEER Training Modules, Epithelial Tissue". In: *U.S. National Institutes of Health, National Cancer Institute.* ().

[39] G. Paolo Dotto and Anil K. Rustgi. *Squamous Cell Cancers: A Unified Perspective on Biology and Genetics*. May 2016. DOI: 10.1016/j.ccell.2016.04.004.

[40] Merja I Auvinen et al. "Incipient Angiogenesis in Barrett's Epithelium and Lymphangiogenesis in Barrett's Adenocarcinoma". In: *Journal of Clinical Oncology* 20.13 (2022), pp. 2971–2979. DOI: 10.1200/JCO.2002.09.011. URL: https://doi.org/10.1200/JCO.2002.09.011.

[41] Diem-Phuong D Dao and Patrick H. Le. *Histology, Goblet Cells*. 2023. URL: https://www.ncbi.nlm.nih.gov/books/NBK553208/.

[42] Rajeswari Anaparthy and Prateek Sharma. "Progression of Barrett oesophagus: Role of endoscopic and histological predictors". In: *Nature Reviews Gastroenterology and Hepatology* 11.9 (2014), pp. 525–534. ISSN: 17595053. DOI: 10.1038/nrgastro.2014.69. URL: http://dx.doi.org/10.1038/nrgastro.2014.69.

[43] William M. Grady et al. "Barrett's esophagus and esophageal adenocarcinoma biomarkers". In: *Cancer Epidemiology Biomarkers and Prevention* 29.12 (Dec. 2020), pp. 2486–2494. ISSN: 15387755. DOI: 10.1158/1055-9965.EPI-20-0223.

[44] Wayne A. Phillips et al. *Barrett's esophagus*. 2011. DOI: 10.1111/j.1440-1746.2010.06602.x.

[45] CRUK. *Barrett's oesophagus*. 2023. URL: https://www.cancerresearchuk.org/about-cancer/other-conditions/barretts-oesophagus/.

[46] Nadhi Thekkek, Sharmila Anandasabapathy, and Rebecca Richards-Kortum. *Optical molecular imaging for detection of Barrett's-associated neoplasia*. 2011. DOI: 10.3748/wjg.v17.i1.53.

[47] Jordan A. Sweer et al. "Wide-field optical property mapping and structured light imaging of the esophagus with spatial frequency domain imaging". In: *Journal of Biophotonics* (2019). ISSN: 18640648. DOI: 10.1002/jbio.201900005.

[48] Prateek Sharma et al. "The American Society for Gastrointestinal Endoscopy PIVI (Preservation and Incorporation of Valuable Endoscopic Innovations) on imaging in Barrett's Esophagus". In: *Gastrointestinal Endoscopy* 76.2 (2012), pp. 252–254. ISSN: 10976779. DOI: 10.1016/j.gie.2012.05.007.

[49] David J. Cuccia et al. "Modulated imaging: quantitative analysis and tomography of turbid media in the spatial-frequency domain". In: *Optics Letters* 30.11 (2005), p. 1354. ISSN: 0146-9592. DOI: 10.1364/ol.30.001354.

[50] Sylvain Gioux, Amaan Mazhar, and David J. Cuccia. "Spatial frequency domain imaging in 2019: principles, applications, and perspectives". In: *Journal of Biomedical Optics* 24.07 (June 2019), p. 1. DOI: 10.1117/1.jbo.24.7.071613.

[51] Kyle P Nadeau et al. *Multifrequency synthesis and extraction using square wave projection patterns for quantitative tissue imaging*. Tech. rep. 2015. URL: https://www.spiedigitallibrary.org/terms-of-use.

[52] Mason T. Chen, Melina Papadakis, and Nicholas J. Durr. "Speckle illumination SFDI for projector-free optical property mapping". In: *Optics Letters* 46.3 (Feb. 2021), p. 673. ISSN: 0146-9592. DOI: 10.1364/ol.411187.

[53] Sylvain Gioux et al. "First-in-human pilot study of a spatial frequency domain oxygenation imaging system". In: *Journal of Biomedical Optics* 16.8 (2011), p. 086015. ISSN: 10833668. DOI: 10.1117/1.3614566.

[54] Samuel J. Waldron et al. "Experimental evidence suggests that specular reflectance and glossy appearance help amplify warning signals". In: *Scientific Reports* 7.1 (2017). ISSN: 20452322. DOI: 10.1038/s41598-017-00217-5.

[55] Jean Vervandier and Sylvain Gioux. "Single snapshot imaging of optical properties". In: *Biomedical Optics Express* 4.12 (Dec. 2013), p. 2938. ISSN: 2156-7085. DOI: 10.1364/boe.4.002938.

[56] Martijn van de Giessen, Joseph P. Angelo, and Sylvain Gioux. "Real-time, profile-corrected single snapshot imaging of optical properties". In: *Biomedical Optics Express* 6.10 (Oct. 2015), p. 4051. ISSN: 2156-7085. DOI: 10.1364/boe.6.004051.

[57] Kyle P Nadeau, Anthony J Durkin, and Bruce J Tromberg. *Advanced demodulation technique for the extraction of tissue optical properties and structural orientation contrast in the spatial frequency domain*. Tech. rep. 2014.

[58] Enagnon Aguénounon and Foudil Dadouche. "Single snapshot of optical properties image quality improvement using anisotropic two-dimensional windows filtering". In: *Journal of Biomedical Optics* 24.07 (Mar. 2019), p. 1. DOI: 10.1117/1.jbo.24.7.071611.

[59] Jonathan M. Blackledge. *Digital Image Processing*. 2005, pp. 464–481.

[60] Mason T. Chen et al. "GANPOP: Generative Adversarial Network Prediction of Optical Properties from Single Snapshot Wide-field Images". In: *IEEE Transactions on Medical Imaging* (2019), pp. 1–10. ISSN: 1558254X. DOI: 10.1109/TMI.2019.2962786.

[61] Enagnon Aguénounon et al. "Real-time, wide-field and high-quality single snapshot imaging of optical properties with profile correction using deep learning". In: *Biomedical Optics Express* 11.10 (2020), p. 5701. ISSN: 2156-7085. DOI: 10.1364/boe.397681.

[62] Yanyu Zhao et al. "Deep learning model for ultrafast multifrequency optical property extractions for spatial frequency domain imaging". In: *Optics Letters* 43.22 (2018), p. 5669. ISSN: 0146-9592. DOI: 10.1364/ol.43.005669.

[63] Swapnesh Panigrahi and Sylvain Gioux. "Machine learning approach for rapid and accurate estimation of optical properties using spatial frequency domain imaging". In: *Journal of Biomedical Optics* 24.07 (2018), p. 1. ISSN: 1560-2281. DOI: 10.1117/1.jbo.24.7.071606.

[64] Wido Heeman et al. "Clinical applications of laser speckle contrast imaging: a review". In: *Journal of Biomedical Optics* 24.08 (Aug. 2019), p. 1. ISSN: 15602281. DOI: 10.1117/1.jbo.24.8.080901.

[65] Andrew K Dunn et al. *Dynamic Imaging of Cerebral Blood Flow Using Laser Speckle*. Tech. rep. 2001, pp. 195–201.

[66] Sam Eriksson et al. "Laser speckle contrast imaging for intraoperative assessment of liver microcirculation: A clinical pilot study". In: *Medical Devices: Evidence and Research* 7.1 (July 2014), pp. 257–261. ISSN: 11791470. DOI: 10.2147/MDER.S63393.

[67] Yasuhiro Tamaki et al. "Real-time measurement of human optic nerve head and choroid circulation, using the laser speckle phenomenon". In: *Japanese Journal of Ophthalmology* 41.1 (Jan. 1997), pp. 49–54. ISSN: 00215155. DOI: 10.1016/S0021-5155(96)00008-1.

[68] Michael Ghijsen et al. "Real-time simultaneous single snapshot of optical properties and blood flow using coherent spatial frequency domain imaging (cSFDI)". In: *Biomedical Optics Express* 7.3 (2016), p. 870. ISSN: 2156-7085. DOI: 10.1364/boe.7.000870.

[69] Matthew B. Applegate and Darren Roblyer. "High-speed spatial frequency domain imaging with temporally modulated light". In: *Journal of Biomedical Optics* 22.7 (July 2017), p. 076019. ISSN: 1083-3668. DOI: 10.1117/1.jbo.22.7.076019.

[70] Scott R. Domingue, David G. Winters, and Randy A. Bartels. "Hyperspectral imaging via labeled excitation light and background-free absorption spectroscopy". In: *Optica* 2.11 (Nov. 2015), p. 929. ISSN: 23342536. DOI: 10.1364/optica.2.000929.

[71] Mohammad Torabzadeh et al. "Hyperspectral imaging in the spatial frequency domain with a supercontinuum source". In: *Journal of Biomedical Optics* 24.07 (July 2019), p. 1. ISSN: 15602281. DOI: 10.1117/1.jbo.24.7.071614.

[72] Ali Mansouri. "Methemoglobinemia". In: *The American Journal of the Medical Sciences* 289.5 (1985), pp. 200–209. DOI: https://doi.org/10.1097/00000441-198505000-00004.

[73] Vivian Pera et al. "Optical property uncertainty estimates for spatial frequency domain imaging". In: *Biomedical Optics Express* 9.2 (Feb. 2018), p. 661. ISSN: 2156-7085. DOI: 10.1364/boe.9.000661.

[74] Carole K. Hayakawa et al. "Optical sampling depth in the spatial frequency domain". In: *Journal of Biomedical Optics* 24.07 (2018), p. 1. ISSN: 15602281. DOI: 10.1117/1.jbo.24.7.071603.

[75] David M. McClatchy et al. "Wide-field quantitative imaging of tissue microstructure using sub-diffuse spatial frequency domain imaging". In: *Optica* 3.6 (2016), p. 613. ISSN: 2334-2536. DOI: 10.1364/optica.3.000613.

[76] Douglas K. Rex, Aasma Shaukat, and Michael B. Wallace. "Optimal Management of Malignant Polyps, From Endoscopic Assessment and Resection to Decisions About Surgery". In: *Clinical Gastroenterology and Hepatology* 17.8 (2019), pp. 1428–1437. ISSN: 15427714. DOI: 10.1016/j.cgh.2018.09.040. URL: https://doi.org/10.1016/j.cgh.2018.09.040.

[77] Wenbo Du et al. "Application of 3D surface profilometer in single cut sample inspection". In: *Journal of Physics: Conference Series*. Vol. 2220. 1. IOP Publishing Ltd, Mar. 2022. DOI: 10.1088/1742-6596/2220/1/012014.

[78] Joe Eastwood, Danny Sims-Waterhouse, and Samanta Piano. "Machine learning approaches". In: *Advances in Optical Form and Coordinate Metrology* (2020), pp. 1–26. DOI: 10.1088/978-0-7503-2524-0ch6.

[79] Sylvain Gioux et al. "Three-dimensional surface profile intensity correction for spatially modulated imaging". In: *Journal of Biomedical Optics* 14.3 (2009), p. 034045. ISSN: 10833668. DOI: 10.1117/1.3156840.

[80] Xianyu Su and Wenjing Chen. "Fourier transform profilometry: a review". In: *Optics and Lasers in Engineering* 35.5 (2001), pp. 263–284. ISSN: 01438166. DOI: 10.1016/S0143-8166(01)00023-9.

[81] Mitsuo Takeda and Kazuhiro Mutoh. "Fourier transform profilometry for the automatic measurement of 3-D object shapes". In: *Applied Optics* 22.24 (1983), p. 3977. ISSN: 0003-6935. DOI: 10.1364/ao.22.003977.

[82] Lu-Rong Guo, Xian-Yu Su, and Jian Li. "Improved Fourier transform profilometry for the automatic measurement of 3D object shapes". In: *Optical Engineering* 29.12 (1990), p. 1439. ISSN: 00913286. DOI: 10.1117/12.55746.

[83] Beiwen Li, Yatong An, and Song Zhang. "Single-shot absolute 3D shape measurement with Fourier transform profilometry". In: *Applied Optics* 55.19 (2016), p. 5219. ISSN: 0003-6935. DOI: 10.1364/ao.55.005219.

[84] *Modulim*. 2023. URL: https://modulim.com.

[85] Ahmed B. Ayoub and Demetri Psaltis. "High speed, complex wavefront shaping using the digital micro-mirror device". In: *Scientific Reports* 11.1 (Dec. 2021). ISSN: 20452322. DOI: 10.1038/s41598-021-98430-w.

[86] Amaan Mazhar et al. "Noncontact imaging of burn depth and extent in a porcine model using spatial frequency domain imaging". In: *Journal of Biomedical Optics* (2014). DOI: 10.1117/1.

[87] Matthew B Applegate et al. "OpenSFDI : an open-source guide for constructing a spatial frequency domain imaging system". In: *Journal of Biomedical Optics* 25.1 (2020). DOI: 10.1117/1.JBO.25.1.016002.

[88] Rolf B. Saager et al. "Portable (handheld) clinical device for quantitative spectroscopy of skin, utilizing spatial frequency domain reflectance techniques". In: *Review of Scientific Instruments* 88.9 (2017), pp. 1–9. ISSN: 10897623. DOI: 10.1063/1.5001075. URL: http://dx.doi.org/10.1063/1.5001075.

[89] Mohsen Erfanzadeh et al. "Low-cost compact multispectral spatial frequency domain imaging prototype for tissue characterization". In: *Biomedical Optics Express* 9.11 (2018), p. 5503. ISSN: 2156-7085. DOI: 10.1364/boe.9.005503.

[90] Gordon T Kennedy et al. "Spatial frequency domain imager based on a compact multiaperture camera: testing and feasibility for noninvasive burn severity assessment". In: *Journal of Biomedical Optics* 26.08 (Aug. 2021). ISSN: 15602281. DOI: 10.1117/1.jbo.26.8.086001.

[91] Joseph P. Angelo, Martijn van de Giessen, and Sylvain Gioux. "Real-time endoscopic optical properties imaging". In: *Biomedical Optics Express* 8.11 (Nov. 2017), p. 5113. ISSN: 2156-7085. DOI: 10.1364/boe.8.005113.

[92] M.B. Applegate. *OpenSFDI*. URL: http://opensfdi.org.

[93] Rolf B. Saager et al. "Method for depth-resolved quantitation of optical properties in layered media using spatially modulated quantitative spectroscopy". In: *Journal of Biomedical Optics* 16.7 (2011), p. 077002. ISSN: 10833668. DOI: 10.1117/1.3597621.

[94] Joseph P Angelo, Martjin van de Giessen, and Sylvain Gioux. "Real-time endoscopic oxygenation imaging using single snapshot of optical properties (SSOP) imaging (Conference Presentation)". In: *Proc. SPIE 9696, Molecular-Guided Surgery: Molecules, Devices, and Applications II, 969605*. 2016.

[95] Mohammad Torabzadeh et al. "Compressed single pixel imaging in the spatial frequency domain". In: *Journal of Biomedical Optics* 22.3 (2017), p. 030501. ISSN: 1083-3668. DOI: 10.1117/1.jbo.22.3.030501.

[96] Enagnon Aguénounon et al. "Single snapshot imaging of optical properties using a single-pixel camera: a simulation study". In: *Journal of Biomedical Optics* 24.07 (2019), p. 1. ISSN: 1560-2281. DOI: 10.1117/1.jbo.24.7.071612.

[97] Ben O. L. Mellors et al. "Applications of compressive sensing in spatial frequency domain imaging". In: *Journal of Biomedical Optics* 25.11 (Nov. 2020). ISSN: 15602281. DOI: 10.1117/1.jbo.25.11.112904.

[98] Samuel S. Streeter et al. "Active line scan with spatial gating for sub-diffuse reflectance imaging of scatter microtexture". In: *Optics Letters* 45.23 (Dec. 2020), p. 6378. ISSN: 0146-9592. DOI: 10.1364/ol.404415.

[99] Marco Visentini-Scarzanella et al. "A structured light laser probe for gastrointestinal polyp size measurement: a preliminary comparative study". In: *Endoscopy International Open* 06.05 (2018), E602–E609. ISSN: 2364-3722. DOI: 10.1055/a-0577-2798.

[100] Dong Hu, Renfu Lu, and Yibin Ying. "Spatial-frequency domain imaging coupled with frequency optimization for estimating optical properties of two-layered food and agricultural products". In: *Journal of Food Engineering* 277 (July 2020). ISSN: 02608774. DOI: 10.1016/j.jfoodeng.2020.109909.

[101] María Rita Rodríguez-Luna et al. "Quantification of bowel ischaemia using real-time multispectral Single Snapshot Imaging of Optical Properties (SSOP)". In: *Surgical Endoscopy* (Nov. 2022). ISSN: 0930-2794. DOI: 10.1007/s00464-022-09764-z. URL: https://link.springer.com/10.1007/s00464-022-09764-z.

[102] Alistair D. Bounds and John M. Girkin. "Early stage dental caries detection using near infrared spatial frequency domain imaging". In: *Scientific Reports* 11.1 (Dec. 2021). ISSN: 20452322. DOI: 10.1038/s41598-021-81872-7.

[103] S. Nandy et al. "Label-free quantitative optical assessment of human colon tissue using spatial frequency domain imaging". In: *Techniques in Coloproctology* 22.8 (2018), pp. 617–621. ISSN: 1128045X. DOI: 10.1007/s10151-018-1841-y.

[104] Adrien Ponticorvo et al. "Quantitative assessment of graded burn wounds in a porcine model using spatial frequency domain imaging (SFDI) and laser speckle imaging (LSI)". In: *Biomedical Optics Express* 5.10 (Oct. 2014), p. 3467. ISSN: 2156-7085. DOI: 10.1364/boe.5.003467.

[105] Adrien Ponticorvo et al. "Evaluating clinical observation versus Spatial Frequency Domain Imaging (SFDI), Laser Speckle Imaging (LSI) and thermal imaging for the assessment of burn depth". In: *Burns* 45.2 (2019), pp. 450–460. ISSN: 18791409. DOI: 10.1016/j.burns.2018.09.026. URL: https://doi.org/10.1016/j.burns.2018.09.026.

[106] Dan M.J. Milstein et al. "Laser speckle contrast imaging identifies ischemic areas on gastric tube reconstructions following esophagectomy". In: *Medicine (United States)* 95.25 (June 2016). ISSN: 15365964. DOI: 10.1097/MD.0000000000003875.

[107] Dale J. Waterhouse et al. *Emerging optical methods for endoscopic surveillance of Barrett's oesophagus*. May 2018. DOI: 10.1016/S2468-1253(18)30030-X.

[108] J. W. Tang et al. *Observing and quantifying airflows in the infection control of aerosol- and airborne-transmitted diseases: An overview of approaches*. 2011. DOI: 10.1016/j.jhin.2010.09.037.

[109] *Olympus EVIS X1*. URL: https://www.olympus-europa.com/medical/en/Products-and-Solutions/Products/Product/EVIS-X1.html.

[110] *Medtronic PillCam*. URL: https://www.medtronic.com/covidien/en-gb/products/capsule-endoscopy/pillcam-capsules/pillcam-sb-3-capsule.html.

[111] Michalina J. Gora et al. "Tethered capsule endomicroscopy enables less invasive imaging of gastrointestinal tract microstructure". In: *Nature Medicine* 19.2 (Feb. 2013), pp. 238–240. ISSN: 10788956. DOI: 10.1038/nm.3052.

[112] CRUK. *Cytosponge: A 'sponge on a string' test to detect oesophageal cancer earlier*. URL: https://news.cancerresearchuk.org/2020/07/31/a-sponge-on-a-string-test-to-detect-oesophageal-cancer-earlier/.

[113] A. Swager, W. L. Curvers, and J. J. Bergman. *Diagnosis by endoscopy and advanced imaging*. Feb. 2015. DOI: 10.1016/j.bpg.2014.11.011.

[114] *IQ Endoscopes*. URL: https://www.iqendoscopes.com/our-technology/.

[115] Jae Young Jang. "The past, present, and future of image-enhanced endoscopy". In: *Clinical Endoscopy* 48.6 (2015), pp. 466–475. ISSN: 22342443. DOI: 10.5946/ce.2015.48.6.466.

[116] Roberto De Franchis et al. "Esophageal capsule endoscopy for screening and surveillance of esophageal varices in patients with portal hypertension". In: *Hepatology* 47.5 (2008), pp. 1595–1603. ISSN: 02709139. DOI: 10.1002/hep.22227.

[117] J. R. Olliver et al. "Chromoendoscopy with methylene blue and associated DNA damage in Barrett's oesophagus". In: *Lancet* 362.9381 (Aug. 2003), pp. 373–374. ISSN: 01406736. DOI: 10.1016/S0140-6736(03)14026-3.

[118] Stuart J. Spechler et al. *American gastroenterological association technical review on the management of Barrett's esophagus*. 2011. DOI: 10.1053/j.gastro.2011.01.031.

[119] Nirav Thosani et al. "ASGE Technology Committee systematic review and meta-analysis assessing the ASGE Preservation and Incorporation of Valuable Endoscopic Innovations thresholds for adopting real-time imaging-assisted endoscopic targeted biopsy during endoscopic surveillance of Barrett's esophagus". In: *Gastrointestinal Endoscopy* 83.4 (Apr. 2016), pp. 684–698. ISSN: 10976779. DOI: 10.1016/j.gie.2016.01.007.

[120] Sandra Barbeiro et al. "Narrow-Band Imaging: Clinical Application in Gastrointestinal Endoscopy". In: *GE Portuguese Journal of Gastroenterology* 26.1 (Dec. 2018), pp. 40–53. ISSN: 23414545. DOI: 10.1159/000487470.

[121] Hiroyuki Osawa et al. "Blue laser imaging provides excellent endoscopic images of upper gastrointestinal lesions". In: *Video Journal and Encyclopedia of GI Endoscopy* 1.3-4 (Jan. 2014), pp. 607–610. ISSN: 22120971. DOI: 10.1016/j.vjgien.2014.01.001.

[122] Monalisa Filip et al. "Autofluorescence imaging and magnification endoscopy". In: *World Journal of Gastroenterology* 17.1 (2011), pp. 9–14. ISSN: 10079327. DOI: 10.3748/wjg.v17.i1.9.

[123] K Ragunath. "Autofluorescence endoscopy - not much gain after all?" In: (2007). DOI: 10.1055/s2007966986.

[124] David Huang et al. *Optical Coherence Tomography*. Tech. rep. 5035. 1991, pp. 1178–1181.

[125] Muna Bhende et al. "Optical coherence tomography: A guide to interpretation of common macular diseases". In: *Indian Journal of Ophthalmology* 66.1 (2018), p. 20. ISSN: 0301-4738. DOI: 10.4103/ijo.ijo{_}902{_}17.

[126] Michalina J. Gora et al. "Endoscopic optical coherence tomography: technologies and clinical applications [Invited]". In: *Biomedical Optics Express* 8.5 (May 2017), p. 2405. ISSN: 2156-7085. DOI: 10.1364/boe.8.002405.

[127] Elisabet A. Rank et al. "Miniaturizing optical coherence tomography". In: *Translational Biophotonics* (Mar. 2022). ISSN: 2627-1850. DOI: 10.1002/tbio.202100007.

[128] *NinePoint Medical, The NvisionVLE® Imaging System, with Real-time Targeting™*. URL: https://ninepointmedical.com/nvisionvle-imaging-system.

[129] George Zonios et al. "Diffuse reflectance spectroscopy of human adenomatous colon polyps in vivo". In: *Applied Optics* 38.31 (1999), p. 6628. ISSN: 0003-6935. DOI: 10.1364/ao.38.006628.

[130] Shanthi Prince and S Malarvizhi. "An Automated System for Optical Imaging to Characterize Tissue based on Diffuse Reflectance Spectroscopy". In: *Proceedings of the 2nd Biennial IEEE/RAS-EMBS International Conference on Biomedical Robotics and Biomechatronics* (2008).

[131] Polina S. Tseregorodtseva et al. "Single-fiber diffuse reflectance spectroscopy and spatial frequency domain imaging in surgery guidance: a study on optical phantoms". In: *Materials* 14.24 (Dec. 2021). ISSN: 19961944. DOI: 10.3390/ma14247502.

[132] Alexandre Douplik et al. "Diffuse reflectance spectroscopy in Barrett's Esophagus: Developing a large field-of-view screening method discriminating dysplasia from metaplasia". In: *Journal of Biophotonics* 7.5 (2014), pp. 304–311. ISSN: 18640648. DOI: 10.1002/jbio.201200114.

[133] Ioannis Gkouzionis et al. "Real-time tracking of a diffuse reflectance spectroscopy probe used to aid histological validation of margin assessment in upper gastrointestinal cancer resection surgery". In: *Journal of Biomedical Optics* 27.02 (Feb. 2022). ISSN: 15602281. DOI: 10.1117/1.jbo.27.2.025001.

[134] Michalina J. Gora et al. "Tethered capsule endomicroscopy: from bench to bedside at a primary care practice". In: *Journal of Biomedical Optics* 21.10 (2016), p. 104001. ISSN: 1083-3668. DOI: 10.1117/1.jbo.21.10.104001.

[135] Kaicheng Liang et al. "Ultrahigh speed en face OCT capsule for endoscopic imaging". In: *Biomedical Optics Express* 6.4 (Apr. 2015), p. 1146. ISSN: 2156-7085. DOI: 10.1364/boe.6.001146.

[136] Kaicheng Liang et al. "Tethered capsule en face optical coherence tomography for imaging Barrett's oesophagus in unsedated patients". In: *BMJ Open Gastroenterology* 7.1 (Sept. 2020). ISSN: 20544774. DOI: 10.1136/bmjgast-2020-000444.

[137] Gargi Sharma et al. "Smartphone-based multimodal tethered capsule endoscopic platform for white-light, narrow-band, and fluorescence/autofluorescence imaging". In: *Journal of Biophotonics* 14.2 (Feb. 2020). ISSN: 18640648. DOI: 10.1002/jbio.202000324.

[138] Rebecca C. Fitzgerald et al. "Cytosponge-trefoil factor 3 versus usual care to identify Barrett's oesophagus in a primary care setting: a multicentre, pragmatic, randomised controlled trial". In: *The Lancet* 396.10247 (2020), pp. 333–344. ISSN: 1474547X. DOI: 10.1016/S0140-6736(20)31099-0.

[139] J Crowley and G S D Gordon. "Simulating medical applications of tissue optical property and shape imaging using open-source ray tracing software". In: *Proceedings of SPIE* 1165707.March (2021). DOI: 10.1117/12.2576779.

[140] Jane Crowley and George Gordon. "Designing and simulating realistic spatial frequency domain imaging systems using open-source 3D rendering software". In: *Biomedical Optics Express* (Apr. 2023). ISSN: 2156-7085. DOI: 10.1364/BOE.484286.

[141] Jane Crowley and George Gordon. "Ultra-miniaturised spatial frequency domain imaging for improved early detection of gastrointestinal cancers". In: *Biomedical Applications of Light Scattering XIII*. Ed. by Adam Wax and Vadim Backman. SPIE, Mar. 2023, p. 2. ISBN: 9781510658912. DOI: 10.1117/12.2648766. URL: https://doi.org/10.1117/12.2648766.

[142] Frank Phillips et al. "Aerosol and droplet generation in upper and lower GI endoscopy: whole procedure and event-based analysis". In: *Gastrointestinal Endoscopy* 96.4 (Oct. 2022), pp. 603–611. ISSN: 10976779. DOI: 10.1016/j.gie.2022.05.018.

[143] Frank Phillips et al. "Air filtration mitigates aerosol levels both during and after endoscopy procedures". In: *DEN Open* 3.1 (Apr. 2023). ISSN: 2692-4609. DOI: 10.1002/deo2.231. URL: https://onlinelibrary.wiley.com/doi/10.1002/deo2.231.

[144] *Raspberry Pi Documentation, About the Camera Modules*. URL: https://www.raspberrypi.com/documentation/accessories/camera.html.

[145] *LG Minibeam PH150g HD ready mini projector*. URL: https://www.lg.com/uk/projectors/lg-PH150G.

[146] *Raspberry 'picamera' module documentation*. URL: https://picamera.readthedocs.io/en/release-1.13/.

[147] Peter Wilson. "High Speed Video Application". In: *Design Recipes for FPGAs*. Elsevier, 2016, pp. 67–77. DOI: 10.1016/b978-0-08-097129-2.00007-6.

[148] Charlotte J. Maughan Jones and Peter R. T. Munro. "Stability of gel wax based optical scattering phantoms". In: *Biomedical Optics Express* 9.8 (Aug. 2018), p. 3495. ISSN: 2156-7085. DOI: 10.1364/boe.9.003495.

[149] Paul Lemaillet et al. "Double-integrating-sphere system at the National Institute of Standards and Technology in support of measurement standards for the determination of optical properties of tissue-mimicking phantoms". In: *Journal of Biomedical Optics* 20.12 (Oct. 2015), p. 121310. ISSN: 1083-3668. DOI: 10.1117/1.jbo.20.12.121310.

[150] Larry A Dewerd and Michael Kissick. *Biological and Medical Physics, Biomedical Engineering The Phantoms of Medical and Health Physics Devices for Research and Development*. Tech. rep. URL: http://www.springer.com/series/3740.

[151] Enrique Villa et al. "Bimodal microwave and ultrasound phantoms for non-invasive clinical imaging". In: *Scientific Reports* 10.1 (Dec. 2020). ISSN: 20452322. DOI: 10.1038/s41598-020-77368-5.

[152] A. Cafarelli et al. "Speed of sound in rubber-based materials for ultrasonic phantoms". In: *Journal of Ultrasound* 19.4 (2016), pp. 251–256. ISSN: 18767931. DOI: 10.1007/s40477-016-0204-7.

[153] Rolf B. Saager et al. "Low-cost tissue simulating phantoms with adjustable wavelength-dependent scattering properties in the visible and infrared ranges". In: *Journal of Biomedical Optics* 21.6 (2016), p. 067001. ISSN: 1083-3668. DOI: 10.1117/1.jbo.21.6.067001.

[154] Phuong Diep et al. "Three-dimensional printed optical phantoms with customized absorption and scattering properties". In: *Biomedical Optics Express* 6.11 (2015), p. 4212. ISSN: 2156-7085. DOI: 10.1364/boe.6.004212.

[155] Laura A. Dempsey et al. "Geometrically complex 3D-printed phantoms for diffuse optical imaging". In: *Biomedical Optics Express* 8.3 (Mar. 2017), p. 1754. ISSN: 2156-7085. DOI: 10.1364/boe.8.001754.

[156] Gage J. Greening et al. "Characterization of thin poly(dimethylsiloxane)-based tissue-simulating phantoms with tunable reduced scattering and absorption coefficients at visible and near-infrared wavelengths". In: *Journal of Biomedical Optics* 19.11 (2014), p. 115002. ISSN: 1083-3668. DOI: 10.1117/1.jbo.19.11.115002.

[157] Georges Wagnì et al. *An optical phantom with tissue-like properties in the visible for use in PDT and fluorescence spectroscopy*. Tech. rep. 1997, pp. 1415–1426.

[158] Brian W. Pogue and Michael S. Patterson. "Review of tissue simulating phantoms for optical spectroscopy, imaging and dosimetry". In: *Journal of Biomedical Optics* 11.4 (2006), p. 041102. ISSN: 10833668. DOI: 10.1117/1.2335429.

[159] Lina Hacker et al. "A copolymer-in-oil tissue-mimicking material with tuneable acoustic and optical characteristics for photoacoustic imaging phantoms". In: *IEEE Transactions on Medical Imaging* (2021). ISSN: 1558254X. DOI: 10.1109/TMI.2021.3090857.

[160] Zhizhong Sun et al. *Spatial-frequency domain imaging: An emerging depth-varying and wide-field technique for optical property measurement of biological tissues*. May 2021. DOI: 10.3390/photonics8050162.

[161] Dong Hu et al. "Numerical simulation on spatial-frequency domain imaging for estimating optical absorption and scattering properties of two-layered horticultural products". In: *Applied Sciences (Switzerland)* 11.2 (Jan. 2021), pp. 1–16. ISSN: 20763417. DOI: 10.3390/app11020617.

[162] Peter Mcculloch, Jeremy Ward, and Paris P Tekkis. *Papers Mortality and morbidity in gastro-oesophageal cancer surgery: initial results of ASCOT multicentre prospective cohort study*. Tech. rep.

[163] Noam Shussman and Steven D. Wexner. *Colorectal polyps and polyposis syndromes*. Feb. 2014. DOI: 10.1093/gastro/got041.

[164] *unwrap 0.1.1*. URL: https://pypi.org/project/unwrap/.

[165] Cheng Chen et al. *A primary method for determination of optical parameters of turbid samples and application to intralipid between 550 and 1630nm*. Tech. rep. 7. 2006, pp. 1317–1351. URL: http://omlc.ogi.edu/spectra/intralipid/index.html..

[166] Dong Hu, Renfu Lu, and Yibin Ying. "A two-step parameter optimization algorithm for improving estimation of optical properties using spatial frequency domain imaging". In: *Journal of Quantitative Spectroscopy and Radiative Transfer* 207 (Mar. 2018), pp. 32–40. ISSN: 00224073. DOI: 10.1016/j.jqsrt.2017.12.022.

[167] Steven L. Jacques. *Optical properties of biological tissues: A review*. July 2013. DOI: 10.1088/0031-9155/58/14/5007.

[168] *Titanium oxide(IV) anatase*. URL: https://www.sigmaaldrich.com/GB/en/product/aldrich/232033.

[169] Frederick Ayers et al. "Fabrication and characterization of silicone-based tissue phantoms with tunable optical properties in the visible and near infrared domain". In: *Design and Performance Validation of Phantoms Used in Conjunction with Optical Measurements of Tissue*. Vol. 6870. SPIE, Feb. 2008, p. 687007. ISBN: 9780819470454. DOI: 10.1117/12.764969.

[170] *Absorption (Nigrosin)*. URL: https://www.aatbio.com/absorbance-uv-visible-spectrum-graph-viewer/nigrosin.

[171] Ronald M. Summers. *Polyp size measurement at CT colonography: What do we know and what do we need to know?* June 2010. DOI: 10.1148/radiol.10090877.

[172] Joseph Angelo et al. "Ultrafast optical property map generation using lookup tables". In: *Journal of Biomedical Optics* 21.11 (2016), p. 110501. ISSN: 1083-3668. DOI: 10.1117/1.jbo.21.11.110501.

[173] Scott Prahl. *Everything I think you should know about Inverse Adding-Doubling*. Tech. rep. 503. 2011, pp. 821–1344. URL: http://omlc.org.

[174] Rebekah Drezek, Andrew Dunn, and Rebekah Richards-Kortum. *Light scattering from cells: finite-difference time-domain simulations and goniometric measurements*. Tech. rep. 1999.

[175] Suzette Lee et al. "SFDI biomarkers provide a quantitative ulcer risk metric and can be used to predict diabetic foot ulcer onset". In: *Journal of Diabetes and its Complications* 34.9 (Sept. 2020). ISSN: 1873460X. DOI: 10.1016/j.jdiacomp.2020.107624.

[176] José Ribeiro, Sara Nóbrega, and António Cunha. "Polyps Detection in Colonoscopies". In: *Procedia Computer Science*. Vol. 196. Elsevier B.V., 2021, pp. 477–484. DOI: 10.1016/j.procs.2021.12.039.

[177] *Zemax*. URL: https://www.zemax.com/.

[178] *Lumerical*. URL: https://www.lumerical.com/.

[179] Martin Schweiger and Simon Arridge. "The Toast++ software suite for forward and inverse modeling in optical tomography". In: *Journal of Biomedical Optics* 19.4 (Apr. 2014), p. 040801. ISSN: 1083-3668. DOI: 10.1117/1.jbo.19.4.040801.

[180] Aleksi A Leino, Aki Pulkkinen, and Tanja Tarvainen. "ValoMC: a Monte Carlo software and MATLAB toolbox for simulating light transport in biological tissue". In: *OSA Continuum* 2.3 (Mar. 2019), p. 957. ISSN: 2578-7519. DOI: 10.1364/osac.2.000957.

[181] Yuming Liu et al. "OptogenSIM: a 3D Monte Carlo simulation platform for light delivery design in optogenetics". In: *Biomedical Optics Express* 6.12 (Dec. 2015), p. 4859. ISSN: 2156-7085. DOI: 10.1364/boe.6.004859.

[182] Jeffrey Cassidy et al. "High-performance, robustly verified Monte Carlo simulation with FullMonte". In: *Journal of Biomedical Optics* 23.08 (Aug. 2018), p. 1. ISSN: 1560-2281. DOI: 10.1117/1.jbo.23.8.085001.

[183] Joe Eastwood et al. "Smart photogrammetry for three-dimensional shape measurement". In: *Proceedings of SPIE* April (2020), p. 11. DOI: 10.1117/12.2556462.

[184] Yuxuang Zhang and Qianqian Fang. "BlenderPhotonics: an integrated open-source software environment for three-dimensional meshing and photon simulations in complex tissues". In: *Journal of Biomedical Optics* 27.08 (Apr. 2022). ISSN: 1083-3668. DOI: 10.1117/1.JBO.27.8.083014. URL: https://www.spiedigitallibrary.org/journals/journal-of-biomedical-optics/volume-27/issue-08/083014/BlenderPhotonics--an-integrated-open-source-software-environment-for-three/10.1117/1.JBO.27.8.083014.full.

[185] Ahmed Osman, Jane Crowley, and George Gordon. "Training Generative Adversarial Networks for Optical Property Mapping using Synthetic Image Data". In: *Biomedical Optics Express* (Oct. 2022). ISSN: 2156-7085. DOI: 10.1364/boe.458554.

[186] Nimmi Ramanujam David A. Boas Constantinos Pitris. *HANDBOOK OF BIOMEDICAL OPTICS*. CRC Press, 2011, pp. 130–131.

[187] *Blender source code*. 2022. URL: https://github.com/PierrickKoch/blender/blob/master/intern/cycles/kernel/kernel_projection.h.

[188] Daniele Contini, Fabrizio Martelli, and Giovanni Zaccanti. *Photon migration through a turbid slab described by a model based on diffusion approximation. I. Theory*. Tech. rep. Dipartimento di Fisica dell'Universita'degli Studi di Firenze, 1997.

[189] *Blender Manual, Color Management*. 2023. URL: https://docs.blender.org/manual/en/2.93/render/color_management.html.

[190] John W. Pickering et al. "Double-integrating-sphere system for measuring the optical properties of tissue". In: *Journal of Applied Optics* (1993), pp. 399–410.

[191] B. Bernad et al. "Deviation of white diffuse reflectance standards from perfect reflecting diffuser at visible and near-infrared spectral ranges". In: *Metrologia* 56.5 (Aug. 2019). ISSN: 16817575. DOI: 10.1088/1681-7575/ab3351.

[192] Scott A. Prahl, Martin J. C. van Gemert, and Ashley J. Welch. "Determining the optical properties of turbid media by using the adding–doubling method". In: *Applied Optics* 32.4 (1993), p. 559. ISSN: 0003-6935. DOI: 10.1364/ao.32.000559.

[193] G De Vries et al. "The Effect of Light Losses in Double Integrating Spheres on Optical Properties Estimation". In: *IEEE JOURNAL OF SELECTED TOPICS IN QUANTUM ELECTRONICS* 5.4 (1999).

[194] Dan Zhu et al. "Effect of light losses of sample between two integrating spheres on optical properties estimation". In: *Journal of Biomedical Optics* 12.6 (2007), p. 064004. ISSN: 10833668. DOI: 10.1117/1.2815691.

[195] Aziz ul Rehman, Iftikhar Ahmad, and Shahzad Ahmad Qureshi. *Biomedical Applications of Integrating Sphere: A Review*. Sept. 2020. DOI: 10.1016/j.pdpdt.2020.101712.

[196] Suresh N. Thennadil and Yi Chieh Chen. "Alternative measurement configurations for extracting bulk optical properties using an integrating sphere setup". In: *Applied Spectroscopy* 71.2 (Feb. 2017), pp. 224–237. ISSN: 19433530. DOI: 10.1177/0003702816665124.

[197] Chao Zuo et al. "Phase shifting algorithms for fringe projection profilometry : A review". In: *Optics and Lasers in Engineering* 109.200 (2018), pp. 23–59. ISSN: 0143-8166. DOI: 10.1016/j.optlaseng.2018.04.019. URL: https://doi.org/10.1016/j.optlaseng.2018.04.019.

[198] Shijie Feng et al. "Fringe pattern analysis using deep learning". In: *Advanced Photonics* 1.02 (Feb. 2019), p. 1. DOI: 10.1117/1.ap.1.2.025001.

[199] *The Five Layers of the Esophageal Lining*. URL: https://educationaldimensions.com/eLearn/barretts/layers.php.

[200] Wouter Saeys et al. "Optical properties of apple skin and flesh in the wavelength range from 350 to 2200 nm". In: *Applied Optics* 47.7 (Mar. 2008), pp. 908–919. ISSN: 15394522. DOI: 10.1364/AO.47.000908.

[201] Nico Bodenschatz et al. "Sources of errors in spatial frequency domain imaging of scattering media". In: *Journal of Biomedical Optics* 19.7 (Jan. 2014), p. 071405. ISSN: 1083-3668. DOI: 10.1117/1.jbo.19.7.071405.

[202] Syeda Tabassum et al. "Feasibility of spatial frequency domain imaging (SFDI) for optically characterizing a preclinical oncology model". In: *Biomedical Optics Express* 7.10 (Oct. 2016), p. 4154. ISSN: 2156-7085. DOI: 10.1364/boe.7.004154.

[203] "Burn wound classification model using spatial frequency-domain imaging and machine learning". In: *Journal of Biomedical Optics* 24.05 (May 2019), p. 1. ISSN: 15602281. DOI: 10.1117/1.jbo.24.5.056007.

[204] Melina Arnold et al. "Global Burden of 5 Major Types of Gastrointestinal Cancer". In: *Gastroenterology* 159.1 (July 2020), pp. 335–349. ISSN: 15280012. DOI: 10.1053/j.gastro.2020.02.068.

[205] Wen Qiang Wei et al. "Long-term follow-up of a community assignment, one-time endoscopic screening study of esophageal cancer in China". In: *Journal of Clinical Oncology* 33.17 (June 2015), pp. 1951–1957. ISSN: 15277755. DOI: 10.1200/JCO.2014.58.0423.

[206] Shengbing Zhao et al. "Magnitude, Risk Factors, and Factors Associated With Adenoma Miss Rate of Tandem Colonoscopy: A Systematic Review and Meta-analysis". In: *Gastroenterology* 156.6 (May 2019), pp. 1661–1674. ISSN: 15280012. DOI: 10.1053/j.gastro.2019.01.260.

[207] Shyam Varadarajulu et al. "GI endoscopes". In: *Gastrointestinal Endoscopy* 74.1 (2011), pp. 1–6. ISSN: 10976779. DOI: 10.1016/j.gie.2011.01.061.

[208] Hanh N. D. Le et al. "Demonstration of a laparoscopic structured-illumination three-dimensional imaging system for guiding reconstructive bowel anastomosis". In: *Journal of Biomedical Optics* 23.05 (2018), p. 1. ISSN: 1560-2281. DOI: 10.1117/1.jbo.23.5.056009.

[209] Timothy N. Ford, Daryl Lim, and Jerome Mertz. "Fast optically sectioned fluorescence HiLo endomicroscopy". In: *Journal of Biomedical Optics* 17.02 (Mar. 2012), p. 1. ISSN: 10833668. DOI: 10.1117/1.jbo.17.2.021105.

[210] Omkar D. Supekar et al. "Miniature structured illumination microscope for in vivo 3D imaging of brain structures with optical sectioning". In: *Biomedical Optics Express* 13.4 (Apr. 2022), p. 2530. ISSN: 2156-7085. DOI: 10.1364/boe.449533.

[211] Christoph Ohrt, Markus Kästner, and Eduard Reithmeier. "High resolution measurements of filigree, inner geometries with endoscopic micro fringe projection". In: *Optical Measurement Systems for Industrial Inspection VIII*. Vol. 8788. SPIE, May 2013, p. 878817. ISBN: 9780819496041. DOI: 10.1117/12.2020440.

[212] Andreas Pösch et al. "Rigid and flexible endoscopes for three dimensional measurement of inside machine parts using fringe projection". In: *Optics and Lasers in Engineering* 89 (Nov. 2016), pp. 178–183. ISSN: 01438166. DOI: 10.1016/j.optlaseng.2016.05.023.

[213] Steffen Matthias et al. "Fringe projection profilometry using rigid and flexible endoscopes". In: *Technisches Messen* 84.2 (Feb. 2017), pp. 123–129. ISSN: 21967113. DOI: 10.1515/teme-2016-0054.

[214] Fukai Zhang and Fan Feng. "Fiber-optic project-fringe interferometry with sinusoidal phase modulating system". In: *Optical Engineering 52(6)* (2013).

[215] Antonios Perperidis et al. "Image computing for fibre-bundle endomicroscopy: A review". In: *Medical Image Analysis* 62 (May 2020). ISSN: 13618423. DOI: 10.1016/j.media.2019.101620.

[216] Lorenzo Niemitz et al. "Microcamera Visualisation System to Overcome Specular Reflections for Tissue Imaging". In: *Micromachines* 14.5 (May 2023). ISSN: 2072666X. DOI: 10.3390/mi14051062.

[217] Xianpei Chen, Kristen Lantz Reichenbach, and Chris Xu. "Experimental and theoretical analysis of core-to-core coupling on fiber bundle imaging". In: *Optics Express* 16.26 (2008).

[218] Junjie Yao and Lihong V. Wang. "Photoacoustic microscopy". In: *Laser and Photonics Reviews* 7.5 (Sept. 2013), pp. 758–778. ISSN: 18638880. DOI: 10.1002/lpor.201200060.

[219] Mason T. Chen and Nicholas J. Durr. "Rapid tissue oxygenation mapping from snapshot structured-light images with adversarial deep learning". In: *arXiv* 25.November (2020), pp. 1–12. ISSN: 15602281. DOI: 10.1117/1.jbo.25.11.112907.

[220] Oeystein Ivar Helle et al. "Structured illumination microscopy using a photonic chip". In: *Nature Photonics* (2020). ISSN: 17494893. DOI: 10.1038/s41566-020-0620-2.

[221] Vivek Venugopal et al. "Design and characterization of an optimized simultaneous color and near-infrared fluorescence rigid endoscopic imaging system". In: *Journal of Biomedical Optics* 18.12 (Dec. 2013), p. 1. ISSN: 10833668. DOI: 10.1117/1.jbo.18.12.126018.

[222] Verena Kaynig et al. "Fully automatic stitching and distortion correction of transmission electron microscope images". In: *Journal of Structural Biology* 171.2 (Aug. 2010), pp. 163–173. ISSN: 10478477. DOI: 10.1016/j.jsb.2010.04.012.

[223] Zhengyou Zhang. *A Flexible New Technique for Camera Calibration*. Tech. rep. 2008. URL: http://research.microsoft.com/œzhanghttp://research.microsoft.com/œzhang.

[224] Quanzeng Wang et al. "Endoscope field of view measurement". In: *Biomedical Optics Express* 8.3 (Mar. 2017), p. 1441. ISSN: 2156-7085. DOI: 10.1364/boe.8.001441.

[225] K Kinnstaetter et al. "Accuracy of phase shifting interferometry". In: *Applied Optics* 27.24 (1988).

[226] *Imaging Resolution, Thorlabs*. URL: https://www.thorlabs.com/newgrouppage9.cfm?objectgroup_id=4338.

[227] R. G.H. Van Uden et al. "Ultra-high-density spatial division multiplexing with a few-mode multicore fibre". In: *Nature Photonics* 8.11 (Nov. 2014), pp. 865–870. ISSN: 17494893. DOI: 10.1038/nphoton.2014.243.

[228] J E Greivenkamp. *Generalized data reduction for heterodyne interferometry*. Tech. rep. 4. 1984, pp. 350–352. URL: https://www.spiedigitallibrary.org/terms-of-use.

[229] Rita S. Rodrigues Ribeiro et al. "Fabrication of Fresnel plates on optical fibres by FIB milling for optical trapping, manipulation and detection of single cells". In: *Scientific Reports* 7.1 (Dec. 2017). ISSN: 20452322. DOI: 10.1038/s41598-017-04490-2.

[230] Moohyuk Kim et al. "Multilayer all-polymer metasurface stacked on optical fiber via sequential micro-punching process". In: *Nanophotonics* (2023). ISSN: 21928614. DOI: 10.1515/nanoph-2022-0762.

[231] Armando G Albertazzi et al. *Photogrammetric endoscope for measurement of inner cylindrical surfaces using fringe projection*. Tech. rep. 2008.

[232] Jeremy Kress et al. "A dual-channel endoscope for quantitative imaging, monitoring, and triggering of doxorubicin release from liposomes in living mice". In: *Scientific Reports* 7.1 (2017), pp. 1–13. ISSN: 20452322. DOI: 10.1038/s41598-017-15790-y. URL: http://dx.doi.org/10.1038/s41598-017-15790-y.

[233] Kevin Ke et al. "Mid-infrared absorption spectroscopy and differential damage in vitro between lipids and proteins by an all-fiber integrated supercontinuum laser". In: *Optics Express* 17.15 (2009).

[234] Eric Larson et al. "Mid-infrared absorption by soft tissue sarcoma and cell ablation utilizing a mid-infrared interband cascade laser". In: *Journal of Biomedical Optics* 26.04 (Apr. 2021). ISSN: 15602281. DOI: 10.1117/1.jbo.26.4.043012.

[235] V. S. Serebryakov et al. "Mid_IR laser for high-precision surgery". In: *Journal of Optical Technology* 82.12 (2015), pp. 781–788. DOI: https://doi.org/10.1364/JOT.82.000781.

[236] Soren D. Konecky. "Imaging scattering orientation with spatial frequency domain imaging". In: *Journal of Biomedical Optics* 16.12 (Dec. 2011), p. 126001. ISSN: 1083-3668. DOI: 10.1117/1.3657823.

[237] Shinhi Hayakawa and Kensaku Ueki. *Flexible tube for endoscope, material used for producing outer cover of the flexible tube, and production method of the flexible tube*. 2003.

[238] Kyle M. Fargen et al. *The FDA approval process for medical devices: An inherently flawed system or a valuable pathway for innovation?* July 2013. DOI: 10.1136/neurintsurg-2012-010400.

[239] *The Medical Devices Regulations 2002*. URL: https://www.legislation.gov.uk/uksi/2002/618/contents/made.

[240] Sumatha Kondabolu. *The 3 FDA medical device classes: differences and examples explained*. 2023. URL: https://www.qualio.com/blog/fda-medical-device-classes-differences.

[241] *U.S. Food and Drug Administration, Code of Federal Regulations Title 21, Gastroenterology - Urology Devices*. URL: https://www.accessdata.fda.gov/scripts/cdrh/cfdocs/cfcfr/CFRSearch.cfm?fr=876.1500.

[242] *Regulating medical devices in the UK*. 2023. URL: https://www.gov.uk/guidance/regulating-medical-devices-in-the-uk.

[243] A. Bak et al. *SARS-CoV-2 routes of transmission and recommendations for preventing acquisition: joint British Infection Association (BIA), Healthcare Infection Society (HIS), Infection Prevention Society (IPS) and Royal College of Pathologists (RCPath) guidance*. 2021. DOI: 10.1016/j.jhin.2021.04.027.

[244] Al Karawi et al. "Comparison between per-oral and ultrathin transnasal endoscopy in unsedated patients". In: *Saudi Journal of Gastroenterology* 7.1 (2001), pp. 26–29.

[245] *Flexible sigmoidoscopy*. URL: https://www.cancerresearchuk.org/about-cancer/bowel-cancer/getting-diagnosed/tests/flexible-sigmoidoscopy.

[246] Ian M. Gralnek et al. *ESGE and ESGENA Position Statement on gastrointestinal endoscopy and COVID-19: An update on guidance during the post-lockdown phase and selected results from a membership survey*. Oct. 2020. DOI: 10.1055/a-1213-5761.

[247] Florence K.A. Gregson et al. "Analytical challenges when sampling and characterising exhaled aerosol". In: *Aerosol Science and Technology* 56.2 (2021), pp. 160–175. ISSN: 15217388. DOI: 10.1080/02786826.2021.1990207.

[248] *AeroTrak Portable Particle Counter 9500*. URL: https://tsi.com/discontinued-products/aerotrak-portable-particle-counter-9500/.

[249] "VisiSize N60 Spray: Characterisation - Particle and droplet measurement in fast moving sprays". In: (). URL: https://www.oxfordlasers.com/laser-imaging/visisize-n60-and-n60max.

[250] Nick Wilson, Stephen Corbett, and Euan Tovey. *Airborne transmission of covid-19*. Aug. 2020. DOI: 10.1136/bmj.m3206.

[251] Michael Klompas, Meghan Baker, and Chanu Rhee. *What Is an Aerosol-Generating Procedure?* Feb. 2021. DOI: 10.1001/jamasurg.2020.6643.

[252] Vanessa Y.J. Tan et al. "Respiratory droplet generation and dispersal during nasoendoscopy and upper respiratory swab testing". In: *Head and Neck* 42.10 (Oct. 2020), pp. 2779–2781. ISSN: 10970347. DOI: 10.1002/hed.26347.

[253] M A A Neil, R Juškaitis, and T Wilson. *Method of obtaining optical sectioning by using structured light in a conventional microscope*. Tech. rep. 24. 1997.

[254] Jane Crowley and George S.D. Gordon. *Dataset for designed and simulating realistic spatial frequency domain imaging systems using open-source 3D rendering software*. 2023. URL: 10.17639/nott.7298.

[255] Scott Prahl. *Inverse Adding Doubling*. URL: https://omlc.org/software/iad/.